

# Course AE4431-23 Aircraft Noise

An introduction to general  
acoustics and aircraft noise

Prof. dr. D.G. Simons  
Prof. dr. ir. M. Snellen  
August 2023

---

## Contents

Introduction.....	3
Chapter 1 Basics of acoustics .....	4
1.1 Sound waves.....	4
1.2 Reflection, refraction and diffraction.....	8
1.3 The decibel scale – sound pressure level .....	13
1.4 Interference – standing waves .....	17
1.5 Doppler effect.....	20
1.6 Directionality .....	23
Exercises .....	25
Chapter 2 The wave equation and its basic solutions.....	28
2.1 Conservation of mass, momentum and energy .....	28
2.2 Wave equation .....	31
2.3 Plane waves - acoustic resistance .....	32
2.4 Spherical waves - acoustic impedance .....	35
Exercises .....	38
Chapter 3 Propagation of sound in the atmosphere .....	40
3.1 Spherical spreading .....	40
3.2 Sound absorption due to friction and molecular relaxation .....	41
3.3 Reflection, refraction and transmission .....	44
3.4 Non-homogeneous atmosphere – ray tracing .....	48
3.5 Ground effect .....	56
Exercises .....	67
Chapter 4 Sound propagation – special situations.....	70
4.1 Sound propagation through a layer – mass law.....	70
4.2 Propagation in enclosures - room acoustics.....	76
4.3 Propagation in ducts – acoustics filters.....	90
4.4 Noise barriers .....	101
Exercises .....	106
Chapter 5 Acoustic signal analysis.....	110
5.1 Fourier transform – continuous and discrete .....	110
5.2 Power spectral density and spectrum level .....	112
5.3 Octave band and 1/3-octave band analysis .....	114
5.4 Overall sound pressure level .....	118

5.5	Spectrogram .....	119
5.6	Aircraft noise measurements - examples.....	120
5.7	Microphones.....	126
	Exercises .....	133
	Chapter 6 Noise metrics .....	134
6.1	Equal loudness contours and overall loudness .....	134
6.2	Equal noisiness contours and perceived noise level .....	136
6.3	A-weighting and overall A-weighted sound pressure level.....	138
6.4	Sound exposure level* .....	140
6.5	Day-night average level.....	143
6.6	Noise contours.....	147
6.7	Dutch aircraft noise model NRM* .....	151
6.8	Psychoacoustic Annoyance and Sound Quality Metrics.....	166
	Exercises .....	168
	Chapter 7 Directional acoustic sources.....	172
7.1	Monopole, dipole and quadrupole source.....	172
7.2	Line array of monopoles and the continuous line array .....	177
7.3	Rayleigh integral and loudspeakers.....	182
	Exercises .....	186
	Chapter 8 Acoustic imaging* .....	187
8.1	Principle of beamforming* .....	188
8.2	1D beamforming * .....	191
8.3	2D beamforming* .....	202
8.4	Imaging aircraft noise data* .....	206
	Exercises .....	209
	Chapter 9 Aircraft noise sources .....	211
9.1	General properties of piston engine and propeller noise .....	211
9.2	General properties of turbo-engine noise.....	214
9.3	General properties of airframe noise.....	216
9.4	Aircraft noise modelling* .....	217
9.5	Aero-acoustics .....	223
	Exercises .....	231

## **Introduction**

These are the lecture notes for the MSc course AE4431-23 “Aircraft Noise”. It is set up in such a way that it provides an introduction to both general acoustics and aircraft noise.

One of the aims of the course is to provide students with a basic understanding of the relationship between aviation and the noise footprint on the ground, particularly around airports.

In the MSc project AE4463P-23 “Advanced Aircraft Noise Modelling and Measurement” you will practice with this material using measured aircraft noise data. The relevant sections for this are denoted with a \*.

Prior knowledge required are the courses on physics and calculus, both of the first year of the BSc of AE. Important equations, sometimes the result of a long mathematical derivation, are highlighted.

The course is assessed by a written exam (maximum 8 points) and a programming assignment about noise contour modelling of a specific aircraft flyover (maximum 2 points). All chapters contain a set of exercises, the difficulty of which are at the examination level. Many questions are taken from previous exams.

D.G. Simons  
M. Snellen  
August, 2023

Section Aircraft Noise and Climate Effects  
Department Control & Operations  
Faculty of Aerospace Engineering  
Delft University of Technology  
The Netherlands

## Chapter 1 Basics of acoustics

### 1.1 Sound waves

Sound is a propagating pressure disturbance. Usually, noise is ‘defined’ as sound that is unwanted by the observer. Considering noise problems in aerospace engineering a distinction is made between interior noise (e.g. cabin noise) and exterior noise (community noise). The emphasis in this course is on exterior noise. Three factors determine the resulting noise levels at the observer: the sound source characteristics (e.g. the aircraft), the propagation medium (atmosphere, terrain, obstacles) and the receivers of the noise (microphones, human beings). All these are subsequently treated in these lecture notes. In this section some basic notions concerning sound are briefly discussed. In later chapters these topics are treated in more detail.

A sound wave is a longitudinal wave, i.e. the displacement of the particles in the medium is in the direction of the wave propagation, see figure 1.1 where the regions of compressed air and expanded air are propagating to the right. The speed of propagation of these pressure (hence density) disturbances equals 340 m/s (at standard temperature and ambient pressure), i.e. the speed of sound. We note that the speed of the air molecules around their equilibrium position is much smaller, see chapter 2.

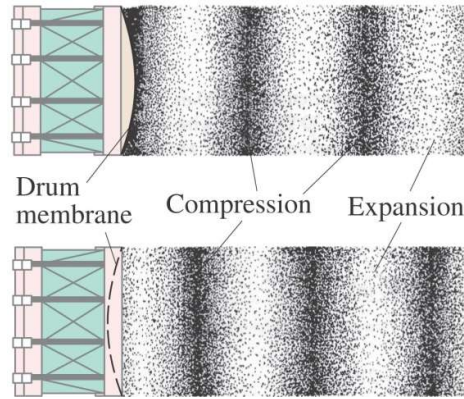


Figure 1.1: Areas of compressed and expanded air due to a propagating longitudinal sound wave.

In case the sound source is a point source radiating sound at a single frequency, a so-called harmonic wave is created for which the sound pressure at time  $t$  and distance  $r$  is given by

$$p'(r,t) = \frac{A}{r} \cos[\omega(t - r/c)] \quad (1.1)$$

with  $A$  the amplitude at 1 m from the source,  $c$  the sound speed and  $\omega = 2\pi f$  the radial frequency (and  $f$  the frequency in Hz). We use the notation  $p'$  for sound pressure, since a sound wave is a very small pressure disturbance on the static pressure ( $10^5$  Pa).

We will derive in chapter 2 the  $1/r$  – dependence of the amplitude for the case of a point source. In complex notation the sound pressure for this situation can also be written as

$$p'(r,t) = \operatorname{Re} \left[ \frac{A}{r} e^{i\omega(t-r/c)} \right] \quad (1.2)$$

where ‘Re’ means ‘real part of’ (which is usually omitted in further calculations) and  $i^2 = -1$ . Figure 1.2 depicts the sound pressure as a function of position for two time instances, i.e.  $t = 0$  and a time  $t$  later. (The  $1/r$  – dependence is not shown for the sake of simplicity). At time  $t$  the function has shifted to the right by a distance  $vt$  with  $v$  the wave speed (equal to  $c$  in the case of a sound wave).

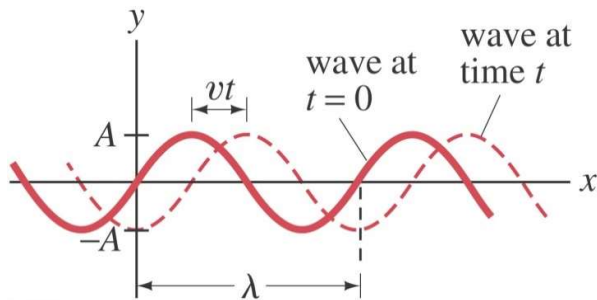


Figure 1.2: Sound pressure (on the y-axis) as a function of position  $x$  for time  $t = 0$  and a time  $t$  seconds later.

Also indicated in the figure is the wavelength  $\lambda$ , which is distance the wave has travelled in one period  $T$  where the period is related to the frequency according to  $T = \frac{1}{f}$ . Hence,

$$\lambda = cT = \frac{c}{f}. \quad (1.3)$$

A measure for the strength of a sound wave is given by the so-called ‘effective sound pressure’ given as

$$p_e = \left[ \frac{1}{T} \int_0^T [p'(t)]^2 dt \right]^{1/2} \quad (1.4)$$

with  $T$  now a sufficiently long integration time (not the period of a harmonic wave). This formula takes care of the fact that sound pressure is both positive and negative. In the case of a harmonic wave originating from a point source, it is easily shown that the effective sound pressure becomes

$$p_e = \frac{A}{r\sqrt{2}}. \quad (1.5)$$

We note that, in contrast to longitudinal waves, also transverse waves exist. The displacement of the particles in the medium is then perpendicular to the direction of the wave propagation. A wave on a violin or piano string is an example of this. In the case of surface waves on a liquid and so-called Rayleigh surface waves on a solid, the particle motion is a superposition of a motion parallel and a motion perpendicular to the direction of wave propagation.

We will derive in chapter 2 that the sound speed in air is given by

$$c = \sqrt{\gamma RT} \quad (1.6)$$

with  $R$  the specific gas constant (in  $\text{m}^2/(\text{s}^2 \text{ K})$ ),  $T$  the temperature in K and  $\gamma$  the ratio of the specific heat at constant pressure and constant volume. For air  $R = 287.05 \text{ m}^2/(\text{s}^2 \text{ K})$  and  $\gamma = 1.4$ , so that at  $15^\circ\text{C}$  ( $= 288.15 \text{ K}$ ) the sound speed becomes  $c = 340.3 \text{ m/s}$ .

Sound is audible if the frequency is in the range 20 to 20,000 Hz. Below 20 Hz, the sound is called infrasound, above 20,000 Hz it is called ultrasound, see figure 1.3.

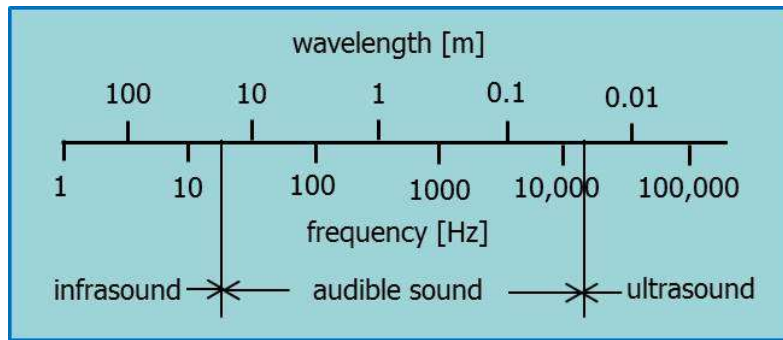


Figure 1.3: Frequency ranges of infrasound, audible sound and ultrasound.

Waves can be represented by wave fronts, which are surfaces on which, at a given time, the particle displacement is everywhere the same. Lines perpendicular to the wave fronts are called rays; they point in the direction of propagation of the wave. Figure 1.4 (left part) depicts the wave fronts of the wave originating from a point source. The wave fronts are spheres, hence such a wave is called a spherical wave (for which the sound pressure amplitude varies as  $1/r$  with  $r$  the distance from the source). The corresponding rays are radial lines pointing outward from the source. The right part of the figure shows the wave fronts of a plane wave. Actually, it is a one-dimensional wave, the parameters of the wave being only dependent on one coordinate, i.e. the direction of the wave. The wave fronts are infinite parallel planes and the corresponding rays are parallel lines.

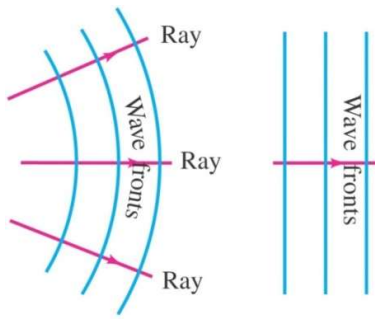


Figure 1.4: Wave fronts of a spherical wave (left) and a plane wave (right).

So far we have only discussed the harmonic (or single-frequency) wave. Basically, there are two types of sound: periodic or discrete sound (shown in figure 1.5) and random or broadband sound (shown in figure 1.6). Examples of periodic sound are a pure tone (i.e. the harmonic wave), a musical tone and propeller noise. Periodic sound has a line spectrum (see chapter 5 for a detailed explanation of the ‘spectrum’). Examples of broadband noise are white noise and the noise due to the jet exhaust of a turbofan engine. The spectrum of broadband noise exhibits no lines. In practice, all noise sources, aircraft in particular, are a mixture of broadband and periodic noise, e.g., the spectrum of the noise from a turbofan engine shows broadband noise due to the jet and periodic noise due to the fan at the same time.

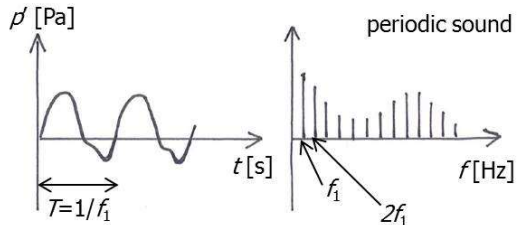


Figure 1.5: Periodic sound in the time domain (left) and frequency domain (right).

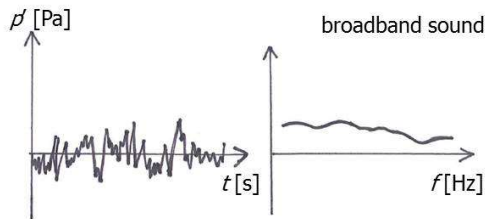


Figure 1.6: Broadband sound in the time domain (left) and frequency domain (right).

Another distinction between types of sound can be made, i.e. stationary and non-stationary. For stationary noise the effective sound pressure  $p_e$ , see equation 1.4, remains constant over time. For non-stationary noise  $p_e$  varies with time. Noise from an aircraft flyover is an example of non-stationary noise.

## 1.2 Reflection, refraction and diffraction

The wave fronts and corresponding sound rays shown in figure 1.4 are for a homogenous medium, i.e. sound speed is the same everywhere in the medium and there are no boundaries. Then the sound propagation is along straight lines and the rays are also straight lines. In this section we briefly discuss the effect of a non-homogeneous medium with a varying sound speed on the propagation. We first consider the simplified situation sketched in figure 1.7 where two media with different sound speed (and density) are separated by a plane interface. A plane wave (indicated by the corresponding ray) in medium 1 is arriving at the interface at a grazing angle  $\theta_1$ . Due to the different medium properties part of the wave energy is reflected and part of it is ‘refracted’ into medium 2. The reflected plane wave is at the same grazing angle  $\theta_1$  as that of the incoming angle, whereas the grazing angle  $\theta_2$  of the refracted wave is different.

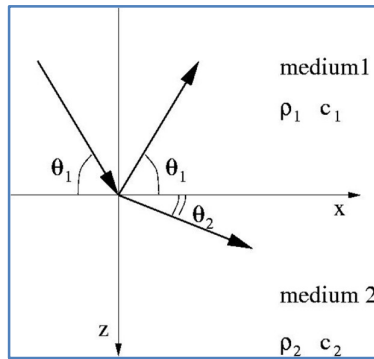


Figure 1.7: Incoming, reflected and refracted ray at the interface between two media.

The relation between the two angles is given by Snell’s law, which reads

$$\frac{\cos \theta_2}{c_2} = \frac{\cos \theta_1}{c_1} \quad (1.7)$$

with  $c_1$  and  $c_2$  the sound speed in medium 1 and medium 2, respectively. Snell’s law will be derived in section 3.3.

According to equation 1.6 the sound speed in air is dependent on temperature. As will be explained in section 3.4, the atmosphere is a medium with a continuously varying temperature. Hence, the atmosphere also exhibits a continuously varying sound speed. This situation is sketched in the right part of figure 1.8, where sound speed is increasing with height. If the medium is divided up into very small layers of constant sound speed and if we apply Snell's law in the subsequent layers (see figure 1.9), we see that the sound ray seems curved (although still straight in each layer).

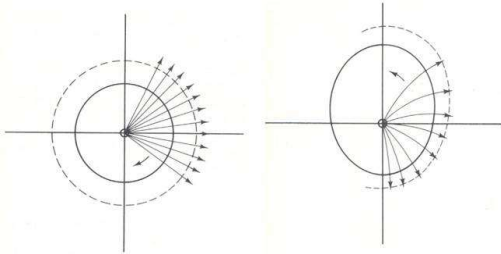


Figure 1.8: Sound rays originating from a point source in a medium with a constant sound speed (left) and a medium with linearly increasing sound speed (right).

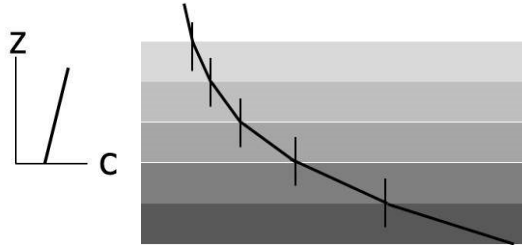


Figure 1.9: Medium divided up in small layers of constant sound speed and a sound ray calculated by applying Snell's law at each interface.

The middle part of figure 1.8 shows the curved sound rays originating from a point source in an atmosphere with a continuously increasing sound speed with height. To compare, the left part of the figure shows the straight rays for a medium with a constant sound speed.

The fact that in a real atmosphere sound rays are no longer straight lines but curved, has a profound effect on the intensity of the sound at a certain distance from the source. This is illustrated in figure 1.10. In the upper part of the figure, temperature, and thus sound speed, decreases with height. Consequently, sound rays are refracted upwards, which results in the formation of so-called 'shadow zones' (where sound intensity is zero in principle). In the lower part of the figure temperature increases with height. Sound rays are now refracted downwards to the ground and there is no formation of zones of silence. The method for calculating the shadow zone distance is discussed in detail in section 3.4.

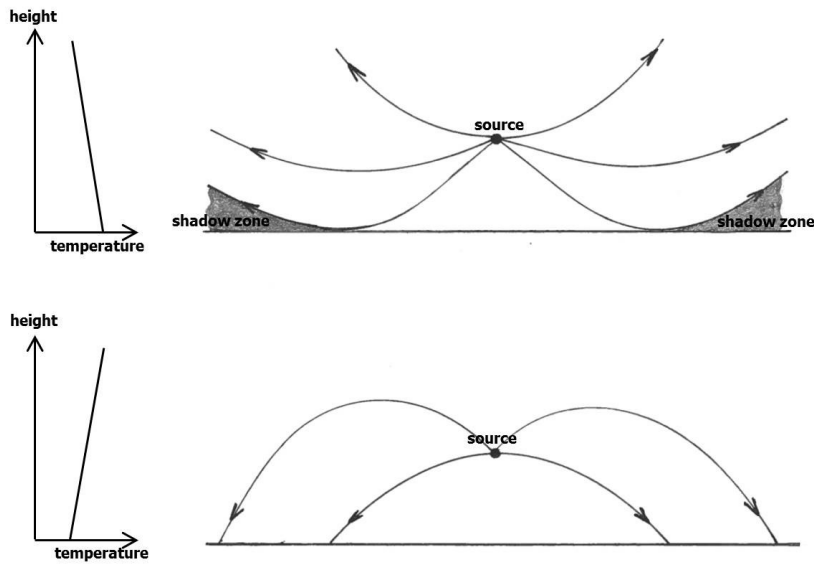


Figure 1.10: Sound rays emanating from a point source in an atmosphere with decreasing temperature with height (top figure) and increasing temperature with height (bottom figure).

A wind speed gradient has a similar effect on the sound propagation, but now the direction of the wind with respect to the direction of propagation is important too. This is illustrated in figure 1.11. For ‘upwind’ conditions (wind direction and propagation direction are opposite), sound speed decreases with height and hence a shadow zone is formed. For ‘downwind’ conditions (wind and propagation in the same direction), sound speed increases with height and there is no shadow zone.

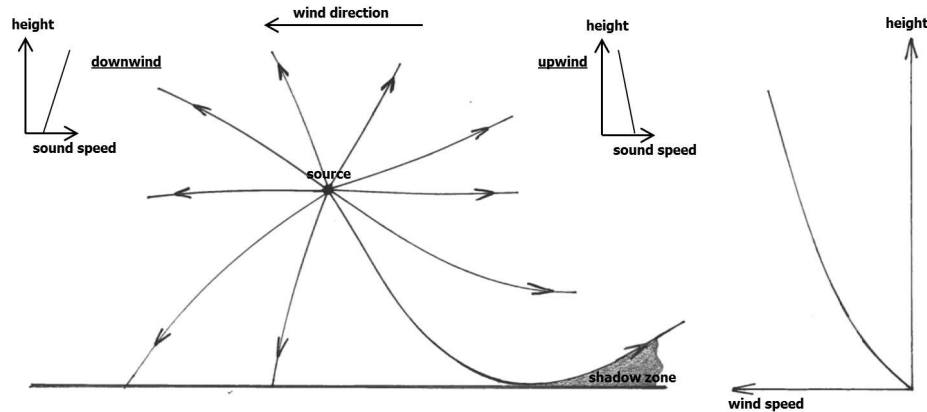


Figure 1.11: Sound rays emanating from a point source in an atmosphere with a wind speed gradient (temperature gradient assumed to be zero).

When a wave encounters an obstacle, it bends around it and passes into the region behind the obstacle. This is called ‘diffraction’, not to be confused with refraction (in both cases the wave direction changes). As a consequence, sound can be heard behind an obstacle.

Diffraction is shown for water surface waves in figure 1.12: the waves, coming from the upper left, pass the obstacle and bend around it into the shadow region behind the obstacle.

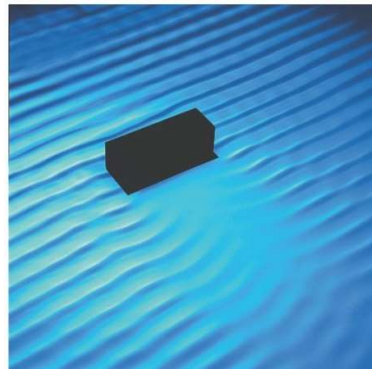


Figure 1.12: Diffraction of a wave by an obstacle.

The amount of diffraction depends on the ratio of the wavelength and the dimension of the object. If the wavelength is much larger than the object, the wave will bend around it as if the object were not there, i.e. there is a lot of diffraction. Conversely, when the object is much larger than the wavelength, there is not much diffraction and there is a clear shadow region behind the object. Consequently, sound screens are only effective at high frequencies (see section 4.4).

The rule is: when the wavelength is (much) smaller than the object, then there is a significant shadow region, i.e. hardly no diffraction. This rule also applies to reflection from an obstacle: when the wavelength is (much) smaller than the object, only then there is a significant reflection.

Diffraction can be modelled by the Huygens-Fresnel principle, which states that each point of a wave front is considered as a new source of a spherical wave. The new wave front is the envelope of the wave fronts of all these new spherical waves. The principle is illustrated in figure 1.13, both for a plane wave and a spherical wave.

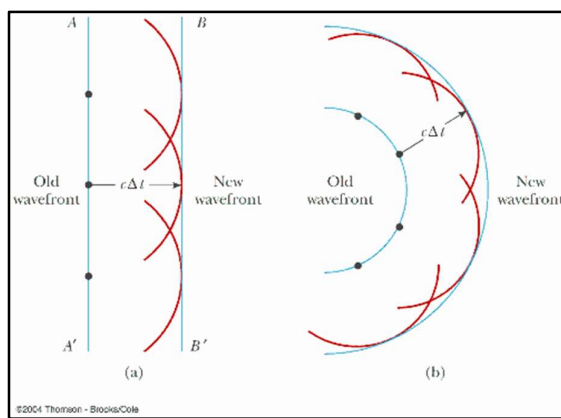


Figure 1.13: Huygens-Fresnel principle for propagation of a plane wave (left) and a spherical wave (right).

In figure 1.14 we illustrate the Huygens-Fresnel principle for diffraction of a plane wave at an aperture. The plane wave (in blue) is approaching the aperture from above. The new sources in the aperture (indicated in yellow) generate spherical waves. The new wave front below the aperture is the envelope of the wave fronts of these new spherical waves. In the figure two wave fronts are shown in green for two subsequent times.

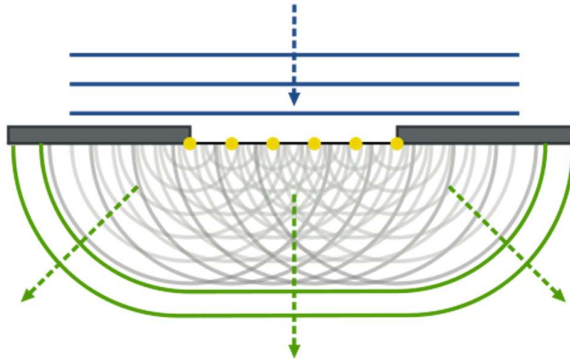


Figure 1.14: Huygens-Fresnel principle for diffraction of a plane wave at an aperture.

Figure 1.15 shows model calculations using the Huygens-Fresnel principle for three circular apertures. (Note the colour scale is a dB scale, see next section). In the most left figure the radius  $R$  of the aperture is only  $\lambda/5$  and the aperture seems to act as a single point source generating a spherical wave. In this case the diffraction is maximal. In the most right figure the aperture is much larger compared to the wavelength, i.e. the radius  $R$  of the aperture equals  $5\lambda$ . Now there are clear shadow regions below and above a beam of high sound intensity. The middle figure shows the intermediate case of  $R = \lambda$ .

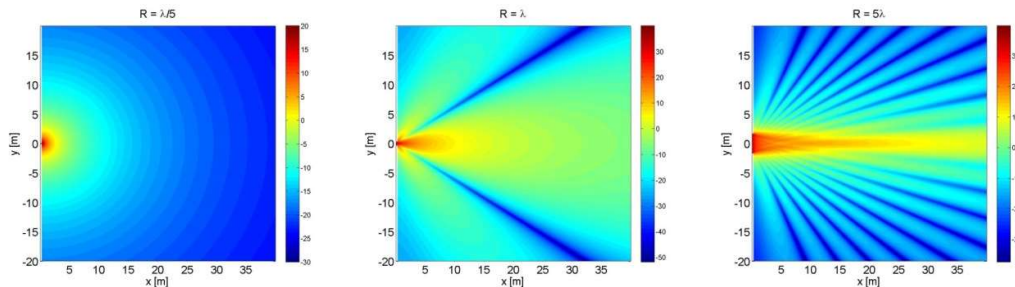


Figure 1.15: Huygens-Fresnel simulation of diffraction of a plane wave at a circular aperture of radius  $\lambda/5$  (left),  $\lambda$  (middle) and  $5\lambda$  (right).

As already mentioned above, diffraction is important for designing effective sound screens (see section 4.4). Also, the amount of aircraft noise shielding, e.g. shielding of engine noise by the aircraft wings, is governed by diffraction.

### 1.3 The decibel scale – sound pressure level

The acoustic power  $W$  of a source (in Watt) is equal to the amount of sound energy emitted per unit time. The range of  $W$  values is enormous, i.e. typically from  $10^{-12}$  to  $10^8$  Watt. The Power Watt Level PWL in dB is defined as<sup>1</sup>

$$\text{PWL} = 10 \log \left( \frac{W}{W_0} \right) \quad (1.8)$$

with  $W_0 = 10^{-12}$  Watt. Figure 1.16 lists the typical acoustic power (both in Watt and dB) for various acoustic sources.

Power [Watt]	Power watt level [dB]	
$10^8$	200	Saturn rocket
$10^6$	180	
$10^4$	160	jet transport
$10^2$	140	small propeller-driven airplane
1	120	large orchestra
$10^{-2}$	100	piano
$10^{-4}$	80	shouted speech
$10^{-6}$	60	conversational speech
$10^{-8}$	40	whisper
$10^{-10}$	20	
$10^{-12}$	0	

Figure 1.16: Typical acoustic power, both in Watt and dB, for various acoustic sources.

We note that the acoustic power of aircraft, although significant, is only a small fraction of the total power of the vehicle.

The sound intensity  $I$  is the sound energy per unit time per unit area. The unit of  $I$  is thus  $\text{W/m}^2$ . For a point source with acoustic power  $W$  in a homogeneous atmosphere, the intensity at a distance  $r$  from the source is given by

$$I(r) = \frac{W}{4\pi r^2} \quad (1.9)$$

which simply follows from the principle of conservation of energy. Here we have assumed free field conditions, i.e. no obstacles or boundaries.

---

<sup>1</sup> A log is always a  $^{10}\log$  (i.e. base 10) unless otherwise stated

The Sound Intensity Level SIL in dB is defined as

$$SIL = 10 \log \left( \frac{I}{I_0} \right) \quad (1.10)$$

with  $I_0 = 10^{-12}$  Watt/m<sup>2</sup>. Figure 1.17 lists typical acoustic intensities (both in Watt/m<sup>2</sup> and dB) encountered in practice.

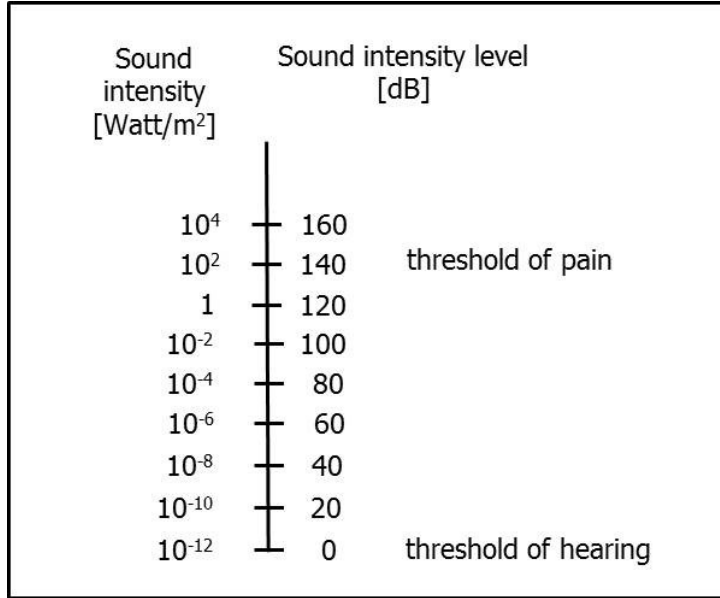


Figure 1.17: Typical acoustic intensity values, both in Watt and dB, encountered in practice.

The threshold of hearing (the minimum intensity perceptible by the human ear) corresponds to a SIL value of 0 dB ( $10^{-12}$  Watt/m<sup>2</sup>), whereas the threshold of pain is at 140 dB (100 Watt/m<sup>2</sup>). Note that 0 dB does not mean an absence of sound, but a sound with an intensity equal to the reference intensity  $I_0$ .

In general, the instantaneous intensity at a distance  $r$  from the source is given by (see figure 1.18)

$$I' = \frac{p' dA dr}{dt dA} \quad (1.11)$$

with  $p'$  the instantaneous sound pressure at distance  $r$  from the source.

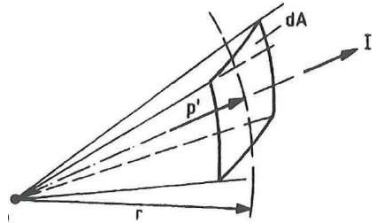


Figure 1.18: Instantaneous sound intensity at a distance  $r$  from a point source.

The particle velocity is  $v_r = \frac{dr}{dt}$ , thus  $I' = p' v_r$ . The sound intensity is the time averaged value of  $I'$ . Hence,

$$I = \frac{1}{T} \int_0^T p' v_r dt \quad (1.12)$$

with  $T$  a sufficiently long integration time. According to this equation, only the component of the particle velocity that is in phase with the sound pressure gives a contribution to the intensity. This is the ‘active part’ of the sound field. The ‘reactive part’ of the sound field, for which the particle velocity is out of phase with sound pressure, does not contribute to the intensity. In a reactive sound field intensity is zero, i.e. there is no net flow of acoustic energy. A standing wave is an example of a reactive sound field, see section 1.4.

The Sound Pressure Level in dB is defined according to

$$SPL = 10 \log \left( \frac{p_e^2}{p_{e0}^2} \right) \quad (1.13)$$

with  $p_e$  the effective sound pressure and  $p_{e0}$  the reference effective pressure equal to  $2 \times 10^{-5}$  N/m<sup>2</sup>. Figure 1.19 lists the typical sound pressure levels encountered in practice.

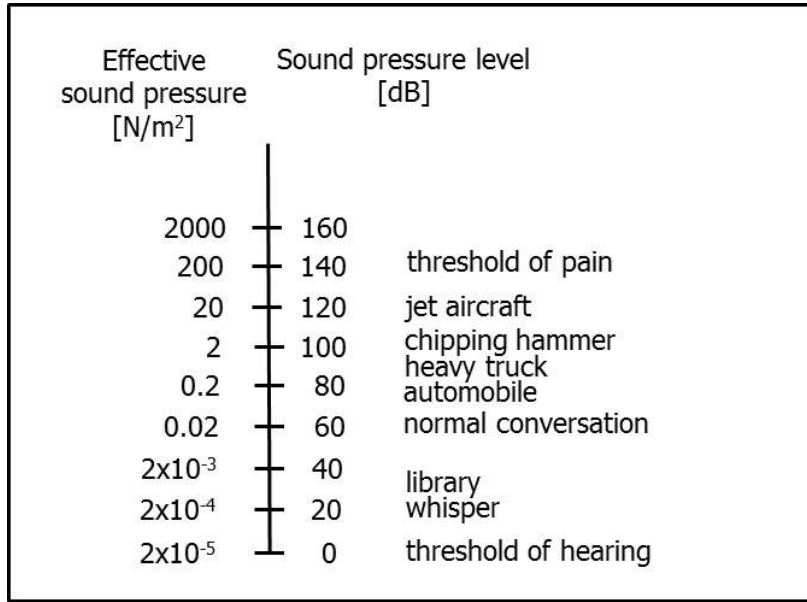


Figure 1.19: Typical effective sound pressure (in N/m<sup>2</sup>) and corresponding sound pressure level in dB for various acoustic sources.

We note that a change of 1 dB in SPL can just be discerned by the human ear and that a 10 dB change in SPL appears to be twice as loud. Consequently, providing accuracies better than 1 dB is meaningless.

In chapter 2 we will derive that in the free field the relation between intensity  $I$  and effective pressure  $p_e$  is given by

$$I = \frac{p_e^2}{\rho_\infty c} \quad (1.14)$$

with  $\rho_\infty$  the static density and  $c$  the sound speed. The quantity  $\rho_\infty c$  is called the characteristic acoustic resistance (see chapter 2). At standard sea level conditions,  $\rho_\infty = 1.225 \text{ kg/m}^3$  and  $c = 340.29 \text{ m/s}$ . Hence  $\rho_\infty c = 416.86 \text{ kg/(m}^2 \text{s)}$ .

From this equation and the definitions of SIL and SPL we find

$$\text{SPL} = \text{SIL} + 10 \log \left( \frac{I_0 \rho_\infty c}{p_{e_0}^2} \right). \quad (1.15)$$

Filling in the value for  $\rho_\infty c$  and those for the reference values, we obtain

$$\text{SPL} = \text{SIL} + 0.2 \text{ dB}. \quad (1.16)$$

When the prevailing  $\rho_\infty c$  value deviates from the standard sea level conditions, we have to add a correction term, resulting in the following relation between SPL and SIL:

$$\text{SPL} = \text{SIL} + 0.2 + 10 \log \left( \frac{\rho_\infty c}{(\rho_\infty c)_0} \right). \quad (1.17)$$

Here,  $(\rho_\infty c)_0$  denotes the acoustic resistance for the standard sea level conditions. Under virtually all atmospheric conditions (relevant for aircraft noise), the difference between SPL and SIL remains within 1 dB. Hence, practically  $\text{SPL} = \text{SIL}$ .

#### 1.4 Interference – standing waves

We consider two interfering sound sources, each emitting a pure tone with angular frequency  $\omega_1$  and  $\omega_2$ , respectively. We observe the total sound pressure  $p'_m(t)$  at a distance  $r_1$  and  $r_2$  from sound source 1 and source 2, respectively. For the moment we assume  $\omega_1 \neq \omega_2$ . The total sound pressure is given by

$$p'_m(t) = p'_1(t) + p'_2(t) = \frac{A}{r_1} \cos(\omega_1(t - r_1/c)) + \frac{B}{r_2} \cos(\omega_2(t - r_2/c)) \quad (1.18)$$

with  $A$  and  $B$  arbitrary constants (subscript  $m$  stands for microphone). The square of the total effective sound pressure is

$$\begin{aligned} p_{e_m}^2 &= \frac{1}{T} \int_0^T \left[ \frac{A}{r_1} \cos(\omega_1(t - r_1/c)) \right]^2 dt + \frac{1}{T} \int_0^T \left[ \frac{B}{r_2} \cos(\omega_2(t - r_2/c)) \right]^2 dt + \\ &+ \frac{1}{T} \int_0^T \left[ \frac{2AB}{r_1 r_2} \cos(\omega_1(t - r_1/c)) \cos(\omega_2(t - r_2/c)) \right] dt \end{aligned} \quad (1.19)$$

with  $T$  a sufficiently long integration time.

Using the trigonometric relation  $\cos x \cos y = \frac{1}{2} [\cos(x+y) + \cos(x-y)]$  we see that the third integral of this equation is zero, so that

$$p_{e_m}^2 = \left( \frac{A}{r_1 \sqrt{2}} \right)^2 + \left( \frac{B}{r_2 \sqrt{2}} \right)^2 = p_{e_1}^2 + p_{e_2}^2. \quad (1.20)$$

The total sound pressure level then becomes

$$SPL_m = 10 \log \left[ \frac{p_{e_1}^2 + p_{e_2}^2}{p_{e_0}^2} \right] = 10 \log \left[ 10^{SPL_1/10} + 10^{SPL_2/10} \right] \quad (1.21)$$

with  $SPL_1$  and  $SPL_2$  the sound pressure level of source 1 and source 2, respectively, given by

$$SPL_1 = 10 \log \left[ \frac{p_{e_1}^2}{p_{e_0}^2} \right] \quad \text{and} \quad SPL_2 = 10 \log \left[ \frac{p_{e_2}^2}{p_{e_0}^2} \right]. \quad (1.22)$$

In the case of  $N$  sources we have

$$SPL_m = 10 \log \left[ \sum_{i=1}^N 10^{SPL_i/10} \right]. \quad (1.23)$$

Examples:

- When  $SPL_1$  and  $SPL_2$  are both 80 dB ( $p_{e_1} = p_{e_2}$ ), the total sound pressure level  $SPL_m$  becomes 83 dB, i.e. only 3 dB higher than the individual SPL values.
- To produce a 10 dB higher sound pressure level, ten equally strong sources must operate together.

Assuming  $\omega_1 = \omega_2$  then the total sound pressure level  $SPL_m$  becomes dependent on the phase difference between the two sound waves as they arrive at the observation point. Now, we obtain

$$SPL_m = 10 \log \left[ \frac{p_{e_1}^2 + p_{e_2}^2 + 2p_{e_1}p_{e_2} \cos\left(\frac{\omega\Delta r}{c}\right)}{p_{e_0}^2} \right] \quad (1.24)$$

with  $\Delta r = r_2 - r_1$ .

If the sources are in phase (at the observation point), then  $\cos\left(\frac{\omega\Delta r}{c}\right) = 1$ , which gives

$$SPL_m = 10 \log \left[ \frac{p_{e_1}^2 + p_{e_2}^2 + 2p_{e_1}p_{e_2}}{p_{e_0}^2} \right] = 10 \log \left[ \frac{(p_{e_1} + p_{e_2})^2}{p_{e_0}^2} \right]. \quad (1.25)$$

If the sources are in out-of-phase (at the observation point), then  $\cos\left(\frac{\omega\Delta r}{c}\right) = -1$ , which gives

$$SPL_m = 10 \log \left[ \frac{p_{e_1}^2 + p_{e_2}^2 - 2p_{e_1}p_{e_2}}{p_{e_0}^2} \right] = 10 \log \left[ \frac{(p_{e_1} - p_{e_2})^2}{p_{e_0}^2} \right]. \quad (1.26)$$

Considering the situation that  $SPL_1$  and  $SPL_2$  are equal (hence  $p_{e_1} = p_{e_2}$ ), then the total sound pressure can be 6 dB higher than the individual  $SPL$  values (sources in phase) or the total  $SPL$  can become  $-\infty$  (sources out of phase).

A special case of interfering sound sources having the same frequency is that of a so-called ‘standing wave’, which results from the reflection of a plane wave from a plane, rigid boundary placed normal to the direction of propagation of the incoming wave. The sum of the two sound pressures, incoming plus reflected, is

$$p'_m(x, t) = A \cos(\omega(t - x/c)) + B \cos(\omega(t + x/c)). \quad (1.27)$$

The second term in this equation contains a plus in the argument of the cosine as the reflected wave travels in the opposite direction of that of the incoming wave.

Suppose that perfect reflection occurs, i.e.  $B = A$ , then again using  $\cos x \cos y = \frac{1}{2}[\cos(x+y) + \cos(x-y)]$  we obtain

$$p'_m(x, t) = 2A \cos(\omega t) \cos\left(\frac{\omega x}{c}\right) = 2A \cos\left(\frac{2\pi t}{T}\right) \cos\left(\frac{2\pi x}{\lambda}\right). \quad (1.28)$$

Note that now  $T = \frac{1}{f} = \frac{2\pi}{\omega}$  is the period of the wave.

The last equation shows that at any position on the  $x$ -axis sound pressure varies as  $\cos\left(\frac{2\pi t}{T}\right)$ . The amplitude along the  $x$ -axis, however, varies as  $2A \cos\left(\frac{2\pi x}{\lambda}\right)$ . Hence, this is not a propagating wave, but a standing wave. At the points  $x = \left(n + \frac{1}{2}\right)\frac{\lambda}{2}$ ,  $n = 0, 1, 2, \dots$ , the sound pressure is zero, independent of time. These points are the nodes of the standing wave. At the points  $x = n\frac{\lambda}{2}$ ,  $n = 0, 1, 2, \dots$  (the antinodes of the standing wave) the amplitude of the sound pressure is maximal. Figure 1.20 shows a sketch of the standing wave at different times. At the boundary, at  $x = 0$ , the pressure is also maximal.

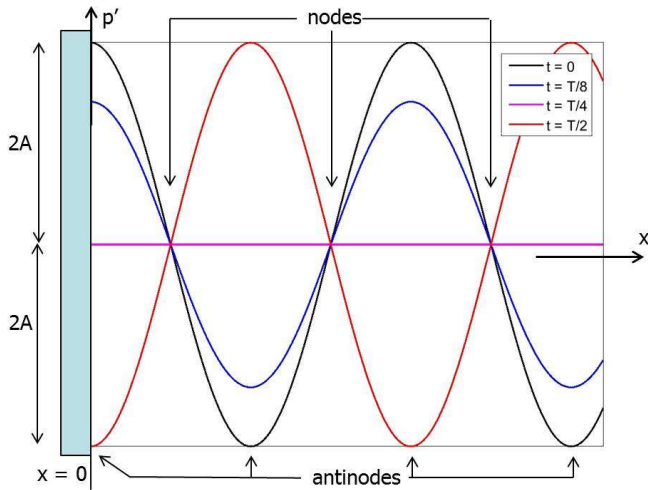


Figure 1.20: A standing wave at various time instances.

Application of Euler's equation,  $v_x = -\frac{1}{\rho} \int \frac{\partial p'}{\partial x} dt$  (derived in chapter 2), yields for the particle velocity of the standing wave

$$v_x(x, t) = -\frac{2A}{\rho c} \sin(\omega t) \sin\left(\frac{\omega x}{c}\right) = -\frac{2A}{\rho c} \sin\left(\frac{2\pi t}{T}\right) \sin\left(\frac{2\pi x}{\lambda}\right) \quad (1.29)$$

i.e. for a standing wave particle velocity is  $90^\circ$  out of phase with the sound pressure. Hence, a standing wave is an example of a reactive sound field where sound intensity is zero everywhere (see general equation for intensity in section 1.3), i.e. there is no propagation of acoustic energy.

## 1.5 Doppler effect

When a sound source is moving towards or from a stationary observer a different frequency than that emitted by the source is perceived. This is known as the Doppler effect. In this section we will derive a formula for the Doppler shifted frequency of a tone as emitted by an aircraft in flyover conditions, see figure 1.21.

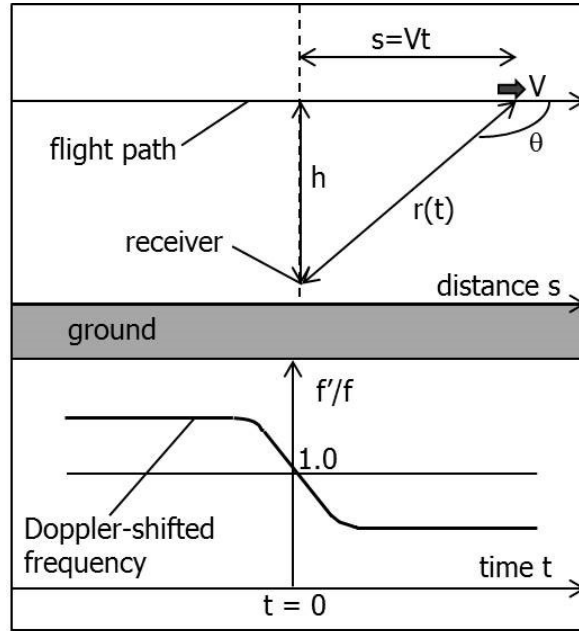


Figure 1.21: Aircraft flyover flight path (upper figure) and corresponding Doppler shifted frequency (relative to the true frequency) (bottom figure).

For a sound source moving towards a stationary observer, the perceived frequency is given by

$$f' = \frac{f}{1 - \frac{v}{c}} \quad (1.30)$$

with  $f$  the true frequency of the source and  $v$  the source speed magnitude. If the source is moving away from the observer the perceived frequency becomes

$$f' = \frac{f}{1 + \frac{v}{c}}. \quad (1.31)$$

For the aircraft flyover geometry we have

$$\frac{f'}{f} = \frac{1}{1 + \frac{dr/dt}{c}} \quad (1.32)$$

with  $r(t) = \sqrt{h^2 + (Vt)^2}$  the instantaneous distance of the aircraft to the observer,  $h$  the aircraft altitude and  $V$  its speed. Hence, the rate of change  $\frac{dr}{dt}$  can be written as

$$\frac{dr}{dt} = \frac{d}{dt} \left( \sqrt{h^2 + V^2 t^2} \right) = \frac{V^2 t}{r}. \quad (1.33)$$

Also, the cosine of the angle  $\theta$ , see figure 1.21, is given by  $\cos \theta = -\frac{Vt}{r}$ . Thus, the Doppler shifted frequency (relative to the true frequency) is

$$\frac{f'}{f} = \frac{1}{1 + \frac{V^2 t}{rc}} = \frac{1}{1 - \frac{V^2 t \cos \theta}{Vtc}}. \quad (1.34)$$

Introducing the Mach number  $M = \frac{V}{c}$ , this can be written as

$$\frac{f'}{f} = \frac{1}{1 - M \cos \theta}. \quad (1.35)$$

Figure 1.22 shows a so-called ‘spectrogram’ of the noise emitted by a small propeller-driven aircraft. How to make a spectrogram from noise data is explained in detail in chapter 5. Here, it suffices to state that a spectrogram provides the sound pressure level as a function of time and frequency. The red lines in the figure are the Doppler shifted propeller tone and its higher harmonics, which follow exactly equation 1.35.

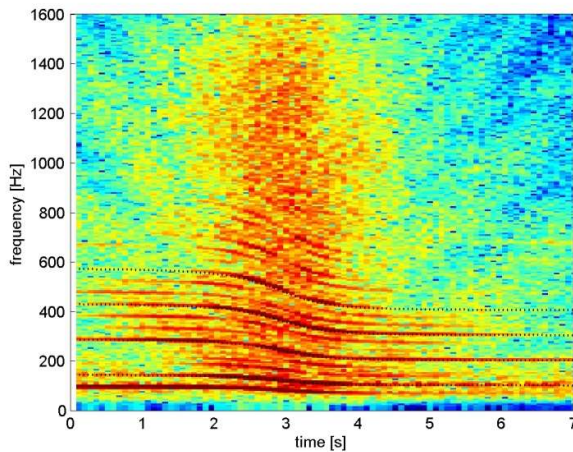


Figure 1.22: Spectrogram of the noise emitted by a small propeller-driven aircraft.

For a sound source moving faster than the speed of sound, a shock wave is created. The source is said to have a supersonic speed with Mach number  $M > 1$ . The effect is illustrated in figure 1.23.

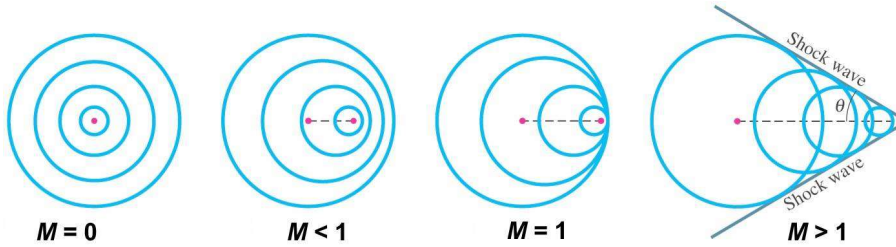


Figure 1.23: Wave fronts emanating from a point source moving at various speeds (compared to the speed of sound).

The situation of subsonic speed,  $M < 1$ , is treated above and the left part of the figure shows the wave fronts. The higher frequency perceived by an observer to the right of the source is reflected by the fact that the wave fronts are closer together than in the case the source would be stationary. In the right part of the figure where  $M > 1$ , the source is outrunning the waves it produces and the wave fronts pile up on one another along the sides. The shock wave is the result of constructive interference of a large number of wave fronts. When the shock wave passes an observer it is heard as a loud 'sonic boom'. For aircraft the sonic boom can consist of several booms formed at the front, the rear and the wings of the aircraft.

It is easily shown that the angle  $\alpha$  of the cone the shock wave consists of is given by

$$\sin \alpha = \frac{c}{V}. \quad (1.36)$$

## 1.6 Directionality

So far we only considered point sources. When a sound source is large compared to the wavelength it emits, then the source tends to be directional. Directionality of a sound source is quantified by the so-called directivity index DI, which is defined as the difference between the sound pressure level in a specified direction  $\theta$  and the average sound pressure level at the same distance  $r$ . Hence,

$$DI(\theta) = SPL(\theta, r) - SPL_{av}(r) \quad (1.37)$$

which to very good approximation is equal to

$$DI(\theta) = SPL(r, \theta) - 10 \log \left( \frac{W / 4\pi r^2}{I_0} \right). \quad (1.38)$$

In chapter 7 we will treat this topic elaborately. Here we only mention that aircraft noise sources show a marked directionality. This is clearly illustrated in figure 1.24 for a turbojet

engine (left) and turbofan engine (right). Note the strong directionality of the various noise sources.

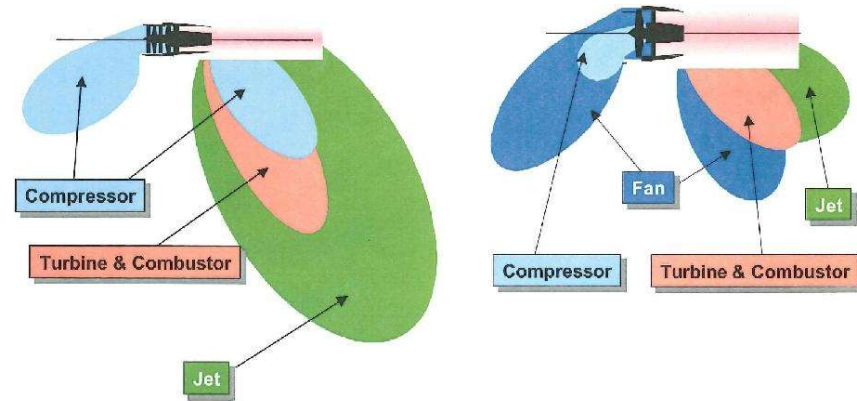


Figure 1.24: Directionality of the various noise sources for a turbojet engine (left) and a turbofan engine (right).

### Exercises

#### Question 1

You drop a stone down a well that is 9.5 m deep. How long does it take before you hear the splash? Take 340 m/s for the sound speed in air.

#### Question 2

Consider a harmonic sound wave in air with a frequency of 2000 Hz and amplitude 0.5 Pa.

- (a) Calculate the wavelength of this sound.
- (b) Assume this sound is produced at the ground. Is the sound effectively blocked by a screen of 100 m wide and 10 m high?
- (c) When does the screen become more effective: in downwind (wind blows in direction from source to observer) or upwind conditions?
- (d) Calculate the sound pressure level SPL of the sound wave.
- (e) What is the corresponding sound intensity level SIL ?
- (f) Consider a second harmonic sound wave from an independent source with frequency 1500 Hz and amplitude 0.25 Pa. Find the total sound pressure level.
- (g) Is the total sound discrete or broadband?
- (h) Are the sounds audible?
- (i) Suppose the 2000 Hz harmonic wave is produced by a distant aircraft moving towards an observer with a speed of 200 km/hour. Calculate the observed frequency, wavelength and Doppler shift.

#### Question 3

A wave is described by the function  $y(x,t) = (2.00 \text{ m}) \cos \left\{ (3.00 \text{ m}^{-1})x + (5.00 \text{ s}^{-1})t \right\}$   
Find the period, the wavelength and the speed of this wave.

Question 4

For the situation where the source speed  $V$  is higher than the speed of sound  $c$ , a Mach cone develops. Derive that the Mach cone angle  $\alpha$  is given by  $\sin \alpha = \frac{c}{V}$ .

Question 5

A bat emits a sound at a frequency of 30 kHz as it approaches a wall. The bat detects the frequency of the echo to be 900 Hz higher than the frequency the bat is emitting. At what speed is the bat flying?

Question 6

Calculate the speed of the aircraft for a tonal for which  $f_{\text{approach}} = 430$  Hz and  $f_{\text{depart}} = 310$  Hz (as observed in figure 1.22).

Question 7

A supersonic plane passes overhead at a speed of 500 m/s. If you hear the shock wave 4.00 s after the plane is directly overhead, at what altitude is the plane flying?

Question 8

Some animals use a form of radar with sound waves ('audio radar') to detect their prey. In order to detect an object with (sound) waves, the object (in this case the prey) must be sufficiently large compared to the used wavelength so that reflection occurs. Therefore, assume that the object or prey must be at least equal to five times the used wavelength in order to sufficiently avoid diffraction around the object.

- (a) Certain bats use an audio radar frequency of around 70 kHz, i.e. in the supersonic range. What is the minimum size of the insects that the bat can catch?
- (b) Porpoises also use audio radar (in this case called 'sonar') at a similar frequency of around 70 kHz. What is the minimum size of the small fish that the porpoise can catch? Note that the sound speed in water is considerably higher than that in air. It depends on parameters like temperature and salinity, but for this calculation you may take 1500 m/s.

This exercise has shown that, apparently, these creatures survive by knowing the underlying physics.

Question 9

We consider two stationary sound sources radiating at a frequency of 2000 Hz. The sources have different distances to an observer. Switching on only source 1, a SPL of 70 dB is measured at the observer. When switching on only source 2, a SPL of 65 dB is measured at the observer.

- (a) What is the total SPL at the observer in the situation that both sources are switched on and that the phase difference of the signals due to the two sources is  $90^\circ$  at the observer?
- (b) And when the phase difference is  $180^\circ$ ?

## Chapter 2 The wave equation and its basic solutions

The main topic of this chapter is to derive the acoustic wave equation from basic physics principles. The three basic laws from the field of ‘mechanics of continuous media’, i.e. conservation of mass, momentum and energy, form the basis of this chapter. From these the wave equation is derived. Subsequently, plane waves and spherical waves are investigated as basic solutions of this equation. From this, the concepts of acoustic resistance and acoustic impedance is introduced. The assumptions made throughout this chapter are that viscous effects are negligible and that sound is a very weak disturbance of the fluid (air), i.e. the equations can be linearized.

### 2.1 Conservation of mass, momentum and energy

We consider an elemental (and infinitesimally small) volume of a flowing fluid in a Cartesian coordinate system  $(x, y, z) = (x_1, x_2, x_3)$ , see figure 2.1. Let  $\vec{v} = (v_1, v_2, v_3)^T$  be the velocity vector of the fluid particles at time  $t$  ( $T$  denotes the transpose). Each component of  $\vec{v}$  is dependent on the three coordinates and time. Let  $\rho(x_1, x_2, x_3, t)$  be the local fluid density at time  $t$ .

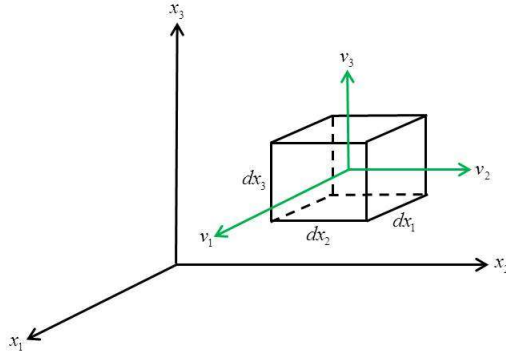


**Figure 2.1: Elemental volume of a flowing fluid in 3D space. Also indicated are the three components of its velocity.**

By imposing that the density in the elemental volume, i.e. the local density, can only change due to a corresponding net mass flow through the elemental volume, we obtain

$$\frac{\partial \rho}{\partial t} + \frac{\partial}{\partial x_1}(\rho v_1) + \frac{\partial}{\partial x_2}(\rho v_2) + \frac{\partial}{\partial x_3}(\rho v_3) = 0. \quad (2.1)$$

This is the well-known ‘equation of continuity’, also called the law of conservation of mass.

We can write

$$\rho = \rho_\infty + \rho' \quad (2.2)$$

with  $\rho_\infty$  the static density and  $\rho'$  the small density change due to a sound wave. Assuming  $\rho' \ll \rho_\infty$  and  $\vec{v}$  to be also very small, equation 2.1 becomes

$$\frac{\partial \rho'}{\partial t} + \rho_\infty \frac{\partial v_1}{\partial x_1} + \rho_\infty \frac{\partial v_2}{\partial x_2} + \rho_\infty \frac{\partial v_3}{\partial x_3} = 0$$

which is a linearization of equation 2.1. It can also be written in more compact form as

$$\frac{\partial \rho'}{\partial t} + \rho_\infty \nabla \cdot \vec{v} = 0 \quad (2.3)$$

where  $\nabla \cdot \vec{v}$  is the divergence of  $\vec{v}$ , i.e. the inner product of the 'nabla' operator  $\left( \frac{\partial}{\partial x_1}, \frac{\partial}{\partial x_2}, \frac{\partial}{\partial x_3} \right)^T$  and  $\vec{v} = (v_1, v_2, v_3)^T$ .

We will now derive a second conservation law. Again consider the elemental volume of a flowing fluid as shown in figure 2.1. In the absence of external and viscous forces, only pressure forces act on the volume, see figure 2.2.

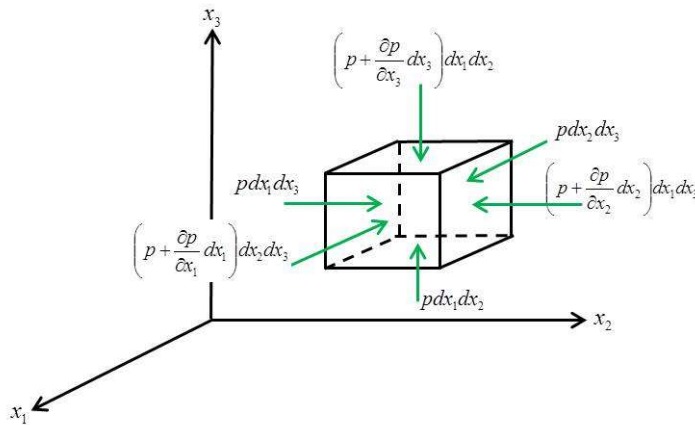


Figure 2.2: The six pressure forces acting on an elemental volume of a flowing fluid.

Then Newton's second law states

$$\frac{dv_i}{dt} = -\frac{1}{\rho} \frac{\partial p}{\partial x_i} \quad \text{for } i = 1, 2, 3 \quad (2.4)$$

where the acceleration  $\frac{dv_i}{dt}$  is given by the total derivative

$$\frac{dv_i}{dt} = \frac{\partial v_i}{\partial t} + \frac{\partial v_i}{\partial x_1} \frac{dx_1}{dt} + \frac{\partial v_i}{\partial x_2} \frac{dx_2}{dt} + \frac{\partial v_i}{\partial x_3} \frac{dx_3}{dt} \quad \text{for } i=1,2,3 \quad (2.5)$$

which can be written as

$$\frac{dv_i}{dt} = \frac{\partial v_i}{\partial t} + v_1 \frac{\partial v_i}{\partial x_1} + v_2 \frac{\partial v_i}{\partial x_2} + v_3 \frac{\partial v_i}{\partial x_3} \quad \text{for } i=1,2,3 \quad (2.6)$$

Combining equations 2.4 and 2.6 we obtain the so-called Euler equations:

$$\frac{\partial v_i}{\partial t} + \frac{\partial v_i}{\partial x_1} v_1 + \frac{\partial v_i}{\partial x_2} v_2 + \frac{\partial v_i}{\partial x_3} v_3 + \frac{1}{\rho} \frac{\partial p}{\partial x_i} = 0 \quad \text{for } i=1,2,3 \quad (2.7)$$

Using  $\rho = \rho_\infty + \rho'$  (with  $\rho' \ll \rho_\infty$ ) and  $p = p_\infty + p'$  ( $p' \ll p_\infty$ ,  $p_\infty$  being the static pressure) and neglecting quadratic terms in disturbances, Euler's equations become

$$\rho_\infty \frac{\partial v_i}{\partial t} + \frac{\partial p'}{\partial x_i} = 0 \quad \text{for } i=1,2,3 \quad (2.8)$$

i.e., the linearized version of equation 2.7. In vector form this can be written as

$$\rho_\infty \frac{\vec{\partial} \vec{v}}{\partial t} + \nabla p' = 0. \quad (2.9)$$

Note that the second term in this equation is the gradient of  $p'$  and not the divergence as appearing in the mass conservation law.

Finally, a third equation is needed. The basis for this is the first law of thermodynamics, i.e. conservation of energy, and the ideal gas law  $p = \rho RT$ .  $R$  is the *specific* gas constant being 287 J/(kg K) for air and  $T$  is the temperature in K. Assuming isentropic flow, i.e. the process is reversible and adiabatic, we obtain the Poisson relation

$$\frac{p}{\rho^\gamma} = \text{constant} \quad (2.10)$$

with  $\gamma = \frac{c_p}{c_v}$  the ratio of the specific heat at constant pressure ( $c_p$ ) and at constant volume ( $c_v$ ).

We have  $c_p = c_v + R$  and for air  $\gamma = 1.4$ .

Note: Usually, the ideal gas law is written as  $pV = nR_0T$  with  $n$  the number of moles,  $V$  the volume and  $R_0$  the *universal* gas constant (equal to 8.314 J/(mol K)). Since  $\rho = \frac{m}{V}$ ,  $m$  being the mass of the gas, we obtain  $R = R_0 \frac{n}{m} = \frac{R_0}{M}$  with  $M$  the molar mass of the gas in

kg/mol. For air  $M = 29 \times 10^{-3}$  kg mol<sup>-1</sup>, hence the specific gas constant is  $8.314/29 \times 10^{-3} = 287$  J/(kg K).

Equation 2.10 can be written as

$$\frac{p}{\rho^\gamma} = \frac{p_\infty}{\rho_\infty^\gamma}. \quad (2.11)$$

Using again  $\rho = \rho_\infty + \rho'$  and  $p = p_\infty + p'$  this can be rewritten as

$$1 + \frac{p'}{p_\infty} = \left[ 1 + \frac{\rho'}{\rho_\infty} \right]^\gamma. \quad (2.12)$$

With  $\rho' \ll \rho_\infty$  the right-hand side of this equation is well approximated by  $1 + \gamma \frac{\rho'}{\rho_\infty}$ .

Hence, we obtain a simple linear relation between  $p'$  and  $\rho'$ :

$$p' = \gamma \frac{p_\infty}{\rho_\infty} \rho'. \quad (2.13)$$

Introducing the constant  $c$  by

$$c^2 = \gamma \frac{p_\infty}{\rho_\infty} = \gamma RT \quad (2.14)$$

gives Poisson's equation as

$$p' = c^2 \rho'. \quad (2.15)$$

In section 2.3 it will become apparent that  $c$  is the sound speed.

## 2.2 Wave equation

In this section we derive the wave equation from the three conservation laws developed in the previous section. Using Poisson's relation we write conservation of mass, equation 2.3, as

$$\frac{1}{c^2} \frac{\partial p'}{\partial t} + \rho_\infty \nabla \cdot \vec{v} = 0. \quad (2.16)$$

Taking the time derivative and using the property that the operators  $\frac{\partial}{\partial t}$  and  $\nabla \cdot$  are commutative we obtain

$$\frac{1}{c^2} \frac{\partial^2 p'}{\partial t^2} + \rho_\infty \nabla \cdot \frac{\vec{\partial v}}{\partial t} = 0. \quad (2.17)$$

Next we take the divergence  $\nabla \cdot$  of Euler's equation, which yields

$$\rho_\infty \nabla \cdot \frac{\vec{\partial v}}{\partial t} + \nabla \cdot \nabla p' = 0 \quad (2.18)$$

with  $\nabla \cdot \nabla = \nabla^2 = \frac{\partial^2}{\partial x_1^2} + \frac{\partial^2}{\partial x_2^2} + \frac{\partial^2}{\partial x_3^2}$  the Laplace operator. Eliminating the term  $\rho_\infty \nabla \cdot \frac{\vec{\partial v}}{\partial t}$  in

equations 2.17 and 2.18 we obtain the 3D wave equation

$$\nabla^2 p' - \frac{1}{c^2} \frac{\partial^2 p'}{\partial t^2} = 0. \quad (2.19)$$

When eliminating  $p'$  instead of  $\rho'$  we get

$$\nabla^2 \rho' - \frac{1}{c^2} \frac{\partial^2 \rho'}{\partial t^2} = 0. \quad (2.20)$$

### 2.3 Plane waves - acoustic resistance

We consider plane wave solutions of the wave equation with  $p'$  being a function of only one spatial coordinate, i.e.  $p' = p'(x, t)$  with  $x = x_1$ . Equation 2.19 reduces to the 1D wave equation

$$\frac{1}{c^2} \frac{\partial^2 p'}{\partial t^2} - \frac{\partial^2 p'}{\partial x^2} = 0. \quad (2.21)$$

The general solution, found by d'Alembert, is

$$p'(x, t) = f_1(x - ct) + f_2(x + ct) \quad (2.22)$$

i.e., the superposition of two arbitrary waves  $f_1$  and  $f_2$  traveling with speed  $c$  in opposite direction, both without changing shape. Indeed,  $c$  is the speed with which the waves travel, i.e.  $c$  defined as  $c = \sqrt{\gamma RT}$  in section 2.1, is the sound speed. Figure 2.3 shows the wave  $p'(x, t) = f_1(x - ct)$  as a function of position  $x$  at two instances in time, i.e.  $t = 0$  and a time  $t$  later. In that time the wave has travelled a distance  $ct$  in the positive  $x$  direction.

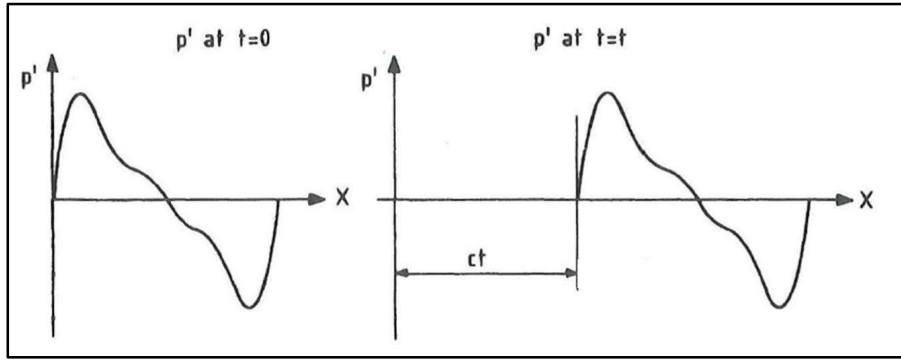


Figure 2.3: An arbitrary 1D wave as a function of position at time  $t = 0$  and a time  $t$  later.

The plane harmonic wave  $p'(x,t) = A \cos[\omega(t - x/c)]$  is also a solution of the 1D wave equation. Using Euler's equation,  $\rho_\infty \frac{\partial v}{\partial t} + \frac{\partial p'}{\partial x} = 0$ , we obtain for the corresponding particle velocity

$$v = -\frac{1}{\rho_\infty c} \int \frac{\partial p'}{\partial x} dt \quad (2.23)$$

which yields

$$v = \frac{A}{\rho_\infty c} \cos[\omega(t - x/c)] = \frac{p'}{\rho_\infty c} \quad (2.24)$$

i.e., for a plane harmonic wave pressure and particle velocity are in phase. The ratio between  $p'$  and  $v$  is called the characteristic acoustic resistance and is given by  $\rho_\infty c$  for a plane harmonic wave. The equation

$$\frac{p'}{v} = \rho_\infty c \quad (2.25)$$

is the acoustic analogy of Ohm's law in electricity.

Using equation 1.12,  $I = \frac{1}{T} \int_0^T p' v dt$ , we obtain for the intensity

$$I = \frac{1}{T} \int_0^T \frac{[p']^2}{\rho_\infty c} dt = \frac{p_e^2}{\rho_\infty c} \quad (2.26)$$

with  $p_e$  the effective pressure (defined by equation 1.4). We note that equations 2.25 and 2.26 are valid for all types of plane waves, not only the plane harmonic waves.

As an example we calculate the particle velocity amplitude for a plane harmonic wave with an effective pressure of 2 Pa. Then  $v_{\max} = \frac{\sqrt{2} p_e}{\rho_\infty c} = \frac{2\sqrt{2}}{1.225 \times 340.29} = 0.0068 \text{ m/s}$ , i.e. a very small value compared to the sound speed  $c = \sqrt{\gamma RT} = \sqrt{\gamma \frac{p_\infty}{\rho_\infty}} = \sqrt{1.4 \frac{101325}{1.225}} = 340.29 \text{ m/s}$ . It is interesting to compare both speeds to the so-called molecular speed, i.e. the mean speed of random motion of the particles (in the absence of a sound wave). The speed of random motion of the molecules in a gas is distributed according to the Maxwell-Boltzmann probability density function given by

$$f(v) = 4\pi \sqrt{\left(\frac{m}{2\pi k_B T}\right)^3 v^2} \exp\left[\frac{-mv^2}{2k_B T}\right] \quad (2.27)$$

with  $k_B = 1.38 \times 10^{-23} \text{ J/K}$  the Boltzmann constant and  $m$  the mass of a molecule. This function is graphically depicted in figure 2.4 for 15 °C ( $T = 288.15 \text{ K}$ ) and  $m = 2 \times 14 \times 1.7 \times 10^{-27} \text{ kg}$  (assuming N<sub>2</sub> molecules only).

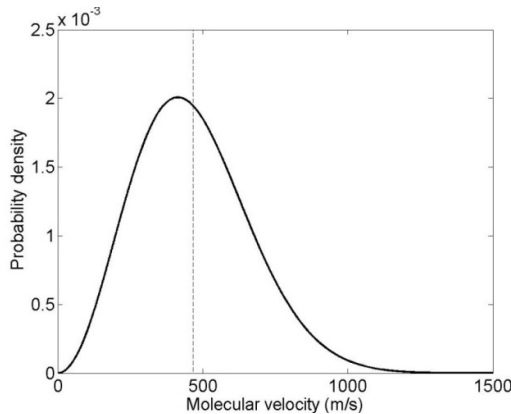


Figure 2.4: Molecular velocity distribution of air at a temperature of 15 °C.

The mean speed, indicated in the figure by the vertical dashed line, is given by

$$\bar{v} = \sqrt{\frac{8k_B T}{\pi m}} = \sqrt{\frac{8p_\infty}{\pi\rho_\infty}} = \sqrt{\frac{8}{\pi\gamma}} c = 1.35 c \quad (2.28)$$

At 15 °C,  $\bar{v} = 458 \text{ m/s}$ , i.e. of the same order of magnitude as the speed of sound, but very large compared to the particle velocity of a sound wave.

## 2.4 Spherical waves - acoustic impedance

We consider spherical wave solutions of the wave equation with  $p'$  being only a function of radial distance from the point source and time, i.e.  $p' = p'(r, t)$  with  $r = \sqrt{x_1^2 + x_2^2 + x_3^2}$ . The wave equation 2.19, is

$$\frac{\partial^2 p'}{\partial x_1^2} + \frac{\partial^2 p'}{\partial x_2^2} + \frac{\partial^2 p'}{\partial x_3^2} = \frac{1}{c^2} \frac{\partial^2 p'}{\partial t^2} \quad (2.29)$$

which, when converted to spherical coordinates, becomes

$$\frac{1}{r} \frac{\partial^2}{\partial r^2} (rp') + \frac{1}{r^2 \sin \theta} \frac{\partial}{\partial \theta} \left( \sin \theta \frac{\partial p'}{\partial \theta} \right) + \frac{1}{r^2 \sin^2 \theta} \frac{\partial^2 p'}{\partial \phi^2} = \frac{1}{c^2} \frac{\partial^2 p'}{\partial t^2}. \quad (2.30)$$

The solution is only dependent on  $r$ , hence this equation reduces to

$$\frac{1}{r} \frac{\partial^2}{\partial r^2} (rp') = \frac{1}{c^2} \frac{\partial^2 p'}{\partial t^2} \quad (2.31)$$

or

$$\frac{\partial^2}{\partial r^2} (rp') = \frac{1}{c^2} \frac{\partial^2 (rp')}{\partial t^2}. \quad (2.32)$$

This is essentially the 1D wave equation, the solution of which is again the d'Alembert equation, i.e.

$$p'(r, t) = \frac{1}{r} [f_1(r - ct) + f_2(r + ct)] \quad (2.33)$$

i.e., a superposition of an outward and inward traveling spherical wave (for which the amplitude behaves as  $1/r$ ). In open space the inward wave is physically impossible, hence we restrict ourselves to the solution

$$p'(r, t) = \frac{1}{r} f_1(r - ct). \quad (2.34)$$

This restriction is also known as the Sommerfeld radiation condition.

As a special case, the spherical harmonic wave  $p'(r, t) = \frac{A}{r} \cos[\omega(t - r/c)]$  is also a solution to equation 2.32. According to equation 1.5 its effective pressure is  $p_e = \frac{A}{r\sqrt{2}}$ .

Using Euler's equation in the  $r$ -direction,  $\rho_\infty \frac{\partial v_r}{\partial t} + \frac{\partial p'}{\partial r} = 0$ , we obtain for the corresponding particle velocity (in the  $r$ -direction)

$$v_r(r,t) = -\frac{1}{\rho_\infty} \int \frac{\partial p'}{\partial r} dt = \frac{A}{r} \frac{1}{\rho_\infty c} \left[ \cos(\omega(t-r/c)) + \frac{c}{\omega r} \sin(\omega(t-r/c)) \right]. \quad (2.35)$$

Now the sound pressure and particle velocity are not in phase. The first term in the equation for particle velocity is in phase with the sound pressure (the active part of the sound field), whereas the second term is out of phase with sound pressure (the reactive part of the sound field). Hence, using equation 1.12 for the intensity, we can ignore the second term and obtain

$$I = \frac{1}{T} \int p' v_r dt = \frac{A^2}{r^2 \rho_\infty c} \frac{1}{T} \int_0^T \cos^2[\omega(t-r/c)] dt. \quad (2.36)$$

The average of the  $\cos^2$ -function equals  $\frac{1}{2}$  so that

$$I = \frac{A^2}{2r^2 \rho_\infty c} = \frac{p_e^2}{\rho_\infty c} \quad (2.37)$$

which is the same expression as that for the plane wave (see equation 2.26). Note that this result is valid for all  $r$ . Also, note that the second term in equation 2.35, i.e. the reactive part, behaves as  $1/r^2$ . Hence, sound pressure and particle velocity become more and more in phase when  $r$  increases.

We can also start with the spherical harmonic wave in complex notation, i.e.  $p'(r,t) = \frac{A}{r} e^{i\omega(t-r/c)}$ . Then particle velocity is given as

$$v_r(r,t) = -\frac{1}{\rho_\infty} \int \frac{\partial p'}{\partial r} dt = \frac{1}{\rho_\infty c} \frac{A}{r} e^{i\omega(t-r/c)} \left[ 1 + \frac{c}{i\omega r} \right]. \quad (2.38)$$

This equation can be rewritten as

$$v_r(r,t) = \frac{1}{\rho_\infty c} p'(r,t) \left[ 1 + \frac{c}{i\omega r} \right]. \quad (2.39)$$

Now the ratio of sound pressure and particle velocity is

$$\frac{p'(r,t)}{v_r(r,t)} = \frac{\rho_\infty c}{\left[ 1 + \frac{c}{i\omega r} \right]} = \rho_\infty c \frac{1 + i \frac{c}{\omega r}}{1 + \left( \frac{c}{\omega r} \right)^2} \quad (2.40)$$

which is called the characteristic acoustic ‘impedance’ (instead of resistance as now it is a complex quantity). Introducing the wavenumber  $k = \frac{\omega}{c} = \frac{2\pi}{\lambda}$ , the impedance can be written as

$$\frac{p'(r,t)}{v_r(r,t)} = \frac{\rho_\infty c}{\left[1 + \frac{1}{ikr}\right]} \quad (2.41)$$

from which it is obvious that sufficiently far away, i.e.  $kr \gg 1$  ( $r \gg \frac{\lambda}{2\pi}$ ), the spherical wave is behaving as a plane wave (i.e. wave fronts are nearly plane and  $\frac{p'(r,t)}{v_r(r,t)} = \rho_\infty c$ ).

## Exercises

### Question 1

Consider the wave equation  $A \frac{\partial^2 p(x,t)}{\partial x^2} = B \frac{\partial^2 p(x,t)}{\partial t^2}$  with  $A$  and  $B$  positive constants.

What is the speed of the waves described by this equation?

### Question 2

Show that  $p'(x,t) = f_1(x - ct) + f_2(x + ct)$  is the general solution to the 1D wave equation.

### Question 3

- (a) Consider a plane harmonic wave in air with frequency  $f = 2000$  Hz and SPL = 60 dB. Calculate the corresponding pressure amplitude  $p'_{\max}$ .
- (b) Calculate the amplitude of the corresponding particle velocity.
- (c) Calculate the amplitude of the corresponding particle displacement.
- (d) Now consider a plane harmonic wave in air at the same frequency but SPL = 0 dB (i.e. at the threshold of hearing). Calculate again the amplitude of the corresponding particle velocity and particle displacement.
- (e) Compare your last answer for the amplitude of the particle displacement with the Bohr radius of the hydrogen atom (in its lowest energy state).

### Question 4

A plane harmonic sound wave in air (at standard sea level conditions) has a frequency of 500 Hz and a sound pressure level of 67 dB. Calculate the maximum change in density that accompanies this wave. Also calculate the maximum particle displacement of this wave.

### Question 5

In the physics classes of your BSc you have learned that the speed of longitudinal waves (sound) in fluids, i.e. gases and liquids, is given by  $c = \sqrt{\frac{B}{\rho}}$ . Here,  $B$  is the bulk modulus defined as  $B = -V \frac{dp}{dV}$  with  $V$  the volume and  $p$  the (static) pressure.  $\rho$  is the density.

For gases,  $B$  depends on the type of process, i.e. a distinction must be made between an isothermal process ( $B = B_T$ ) and a adiabatic process ( $B = B_S$ ). For liquids and solids  $B_T \approx B_S$ .

- (a) Show that for an isothermal process in an ideal gas  $B_T = p$ . (Use Boyle's law  $pV = \text{constant}$  and the definition of  $B$ ).
- (b) Show that for an adiabatic process in an ideal gas  $B_S = \gamma p$ . (Use the equation  $pV^\gamma = \text{constant}$ ,  $\gamma$  being the ratio of specific heats, see also equation 2.10).
- (c) Assuming that sound is an adiabatic process, show that for an ideal gas  $c = \sqrt{\frac{\gamma p}{\rho}} = \sqrt{\gamma RT}$ ,  $R$  being the specific gas constant.
- (d) Calculate the sound speed in Nitrogen gas and Helium gas with the formula derived in question (c) (at standard sea level conditions). Note that for diatomic molecules  $\gamma = 1.4$  and for monatomic molecules  $\gamma = 1.67$  (see lectures on thermodynamics). Also give the corresponding (adiabatic) bulk modulus values. The densities of N<sub>2</sub> gas and He are 1.25 kg/m<sup>3</sup> and 0.164 kg/m<sup>3</sup>, respectively.
- (e) The bulk modulus and density of water (at standard sea level conditions) is 2.2 GPa and 1000 kg/m<sup>3</sup>. Calculate the sound speed of water.
- (f) For a long solid rod the speed of longitudinal waves (sound) is given by the similar formula  $c = \sqrt{\frac{E}{\rho}}$  with  $E$  Young's modulus. For steel  $E \approx 200$  GPa and  $\rho \approx 8 \times 10^3$  kg/m<sup>3</sup>. Calculate the sound speed in steel.

## Chapter 3 Propagation of sound in the atmosphere

We first consider the atmosphere to be homogeneous (constant temperature, no wind) without any boundaries. In this simplified situation propagation of sound is governed by spherical spreading and absorption due to friction.

### 3.1 Spherical spreading

We derived the expression for the effective pressure of a spherical wave due to a point source:

$$p_e(r) = \frac{A}{r\sqrt{2}} \quad (3.1)$$

with  $A$  a constant and  $r$  the distance from the point source. This is known as the inverse distance law. The sound pressure level difference between distance  $r_1$  and  $r_2$  is given as

$$\text{SPL}(r_1) - \text{SPL}(r_2) = 10 \log \left( \frac{p_e^2(r_1)}{p_{e_0}^2} \right) - 10 \log \left( \frac{p_e^2(r_2)}{p_{e_0}^2} \right) \quad (3.2)$$

which can be written as

$$\text{SPL}(r_1) - \text{SPL}(r_2) = 20 \log \left( \frac{p_e(r_1)}{p_e(r_2)} \right) = 20 \log \left( \frac{r_2}{r_1} \right). \quad (3.3)$$

Taking  $r_1 = 1 \text{ m}$  and  $r_2 = r$  we obtain

$$\text{SPL}(r) = \text{SPL}(r_1 = 1 \text{ m}) - 20 \log(r). \quad (3.4)$$

We also derived previously for the intensity of the spherical acoustic wave that

$$I(r) = \frac{W}{4\pi r^2} \quad (3.5)$$

with  $W$  the power (in Watt) of the acoustic source. From this and the definition of power watt level PWL, the sound intensity level is

$$\text{SIL}(r = 1 \text{ m}) = \text{PWL} - 11.0 \quad (3.6)$$

We also derived that  $\text{SPL} = \text{SIL} + 0.2$ , hence

$$\text{SPL}(r = 1 \text{ m}) = \text{PWL} - 10.8 \quad (3.7)$$

The sound pressure level at distance  $r$  is thus

$$\text{SPL}(r) = \text{PWL} - 10.8 - 20 \log(r). \quad (3.8)$$

For a directional sound source with directivity index DI we have

$$\text{SPL}(r, \theta) = \text{PWL} - 10.8 - 20 \log(r) + \text{DI}(\theta). \quad (3.9)$$

### 3.2 Sound absorption due to friction and molecular relaxation

In addition to geometrical or spherical spreading, absorption due to friction (which in turn is governed by the fluid's viscosity) attenuates the acoustic wave. Also, relaxation processes of the oxygen, nitrogen and water vapour molecules attenuate the sound, as some of the energy carried by the sound wave causes these molecules to vibrate and rotate, thus taking away energy from the wave.

Introducing the sound absorption coefficient  $\alpha$  (with units  $\text{m}^{-1}$ ), the effective pressure of a spherical wave due to a point source becomes

$$p_e(r) = \frac{A}{r\sqrt{2}} e^{-\alpha r}. \quad (3.10)$$

The absorption coefficient is a strong function of frequency and also depends on temperature  $T$  and relative humidity  $RH$ .

The sound pressure level at distance  $r$  now becomes

$$\text{SPL}(r, \theta) = \text{PWL} - 10.8 - 20 \log(r) + \text{DI}(\theta) - \alpha r \quad (3.11)$$

with  $\alpha$  the absorption coefficient in units  $\text{dB/m}$ . It can easily be shown that (see exercises, question 1)

$$\alpha [\text{dB/m}] = 8.686 \alpha [\text{m}^{-1}]. \quad (3.12)$$

Note that this attenuation is introduced here after the wave equation was derived.

Values for the absorption coefficient in the audible frequency range (at the octave band centre frequencies, see chapter 5) are given in table 3.1. The coefficient is given in  $\text{dB/km}$ , hence to obtain the value in  $\text{dB/m}$ , one has to divide these numbers by  $10^3$ .

Table 3.1

Temperature (°C)	Relative humidity (%)	63 Hz	125 Hz	250 Hz	500 Hz	1000 Hz	2000 Hz	4000 Hz	8000 Hz
30	20	0.212	0.717	1.86	3.40	6.00	14.6	47.6	167
	50	0.0904	0.346	1.24	3.56	7.03	11.7	24.7	74.2
	80	0.0573	0.223	0.852	2.90	7.41	13.3	23.3	56.4
20	20	0.259	0.706	1.39	2.59	6.55	21.6	74.9	218
	50	0.122	0.440	1.31	2.73	4.67	9.90	29.7	106
	80	0.0788	0.298	1.04	2.76	5.15	9.01	21.4	69.6
10	20	0.271	0.576	1.19	3.27	11.0	36.4	92.1	155
	50	0.160	0.481	1.05	1.89	4.27	13.3	47.2	157
	80	0.108	0.373	1.02	1.96	3.57	8.80	29.0	105
0	20	0.256	0.609	1.84	6.15	17.8	34.8	47.2	58.4
	50	0.180	0.408	0.818	2.08	6.84	23.9	71.6	148
	80	0.138	0.376	0.756	1.51	4.07	13.9	49.3	148

Figure 3.1 shows the absorption coefficient (in dB/m) as a function of frequency for a temperature of 10 °C and a relative humidity equal to 20, 50 and 80 %.

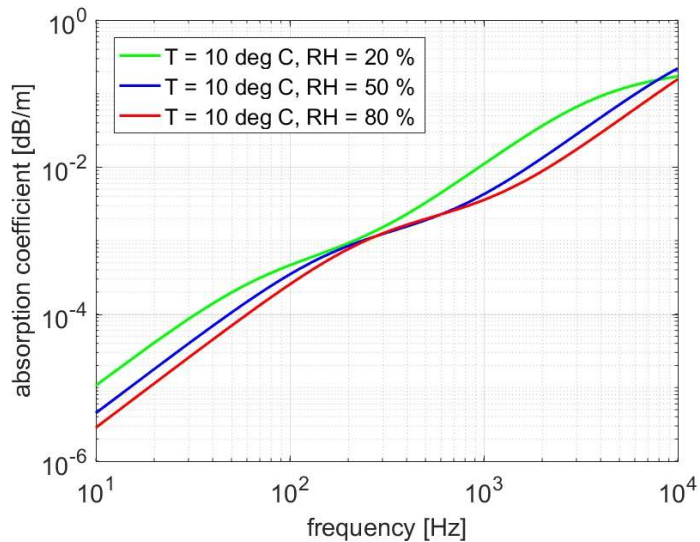


Figure 3.1: Absorption coefficient of air (in dB/m) as a function of frequency (in Hz) for a temperature of 10 °C and three values of the relative humidity.

The dependence of  $\alpha$  on  $T$  and  $RH$  is illustrated in figure 3.2 for a fixed frequency of 1000 Hz.

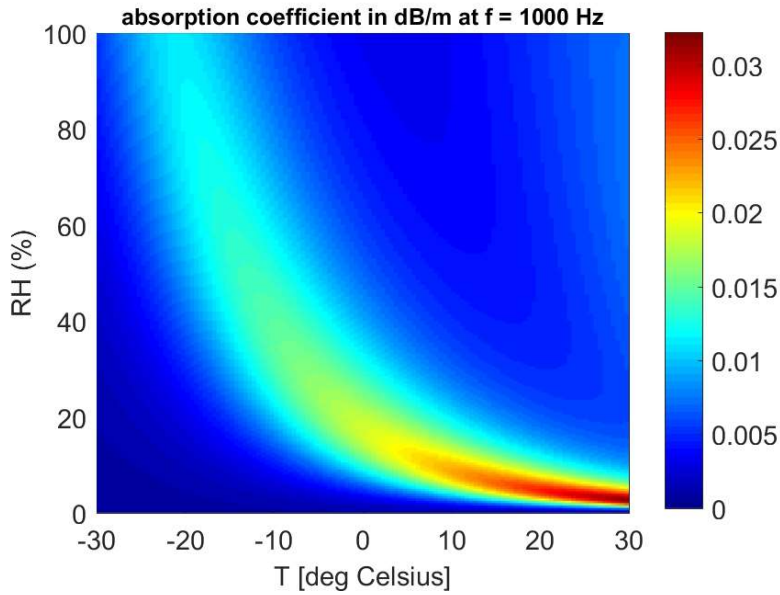


Figure 3.2: Absorption coefficient of air (in dB/m) as a function of temperature and relative humidity at a fixed frequency of 1 kHz.

Figure 3.3 gives the sound pressure level SPL (in dB) as a function of distance  $r$  from a point source ( $\text{DI} = 0 \text{ dB}$ ) of  $\text{PWL} = 80 \text{ dB}$ , operating at the frequencies 100, 1000 and 10,000 Hz. Note that at 100 Hz sound absorption is negligible and the SPL versus  $r$  curve follows the geometrical spreading law, whereas at 10,000 Hz the sound is heavily attenuated by absorption. Consequently, high frequency noise, e.g. from aircraft, becomes unimportant after several hundred meters of propagation.

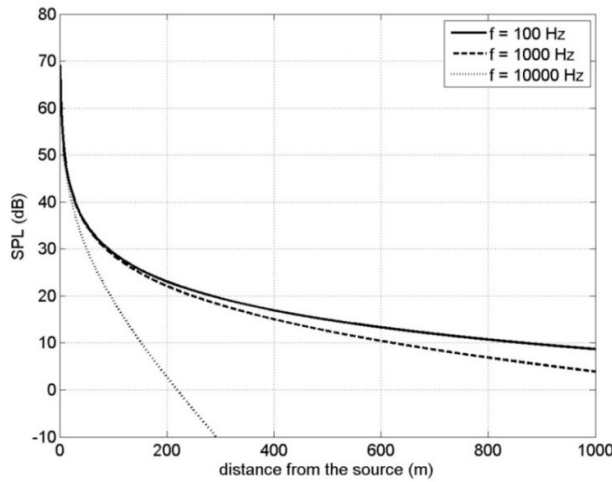


Figure 3.3: Sound pressure level as a function of distance from a point source, operating at the frequencies 100, 1000 and 10,000 Hz.

In the next sections we consider a non-homogeneous atmosphere with boundaries.

### 3.3 Reflection, refraction and transmission

The basics for sound propagation in a real atmosphere (non-homogeneous, with boundaries) is solving the problem of a sound ray arriving at a plane interface between two (air) layers with different sound speed and density. This situation is sketched in figure 3.4.

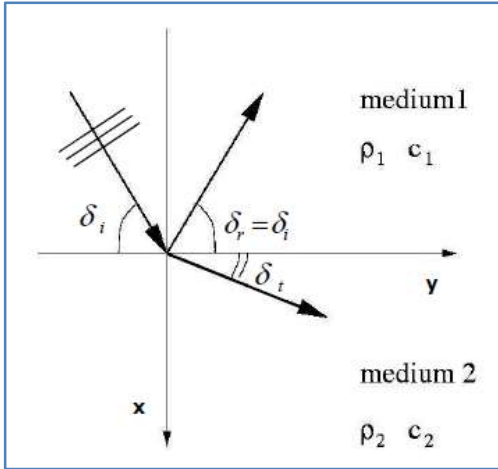


Figure 3.4: Incoming, reflected and refracted ray at the interface between two media.

The incoming harmonic plane wave, making an angle  $\delta_i$  with the interface, is given as

$$p'_i(x, y, z, t) = p'_i(\vec{r}, t) = A e^{i(\omega t - \vec{k} \cdot \vec{r})} \quad (3.13)$$

with

$$\vec{k} \cdot \vec{r} = k_x x + k_y y + k_z z \quad (3.14)$$

where we have introduced the wave number vector  $\vec{k} = (k_x, k_y, k_z)^T$ .  $\omega$  is the radial frequency and  $A$  is the (arbitrary) amplitude of the wave. The abrupt change in density and sound speed at the interface results in a reflected and transmitted plane wave. The three plane waves are situated in 3D space where the interface is at  $x = 0$  and the problem is independent of the  $z$ -coordinate.

The incoming, reflected and transmitted plane wave are given as

$$p'_i = A e^{i(\omega t - x(\sin \delta_i) \omega/c_1 - y(\cos \delta_i) \omega/c_1)} \quad (3.15)$$

$$p'_r = C e^{i(\omega t + x(\sin \delta_r) \omega/c_1 - y(\cos \delta_r) \omega/c_1)} \quad (3.16)$$

$$p'_t = B e^{i(\omega t - x(\sin \delta_t) \omega/c_2 - y(\cos \delta_t) \omega/c_2)} \quad (3.17)$$

with  $c_1$  and  $c_2$  the sound speed above and below the interface, respectively.  $\delta_r (= \delta_i)$  is the (grazing) angle of reflection and  $\delta_t$  is the angle of transmission. The amplitudes  $B$  and  $C$  of the transmitted and reflected waves are allowed to be complex numbers (as a phase change might occur). Note that there is no change in frequency when going from medium 1 (above the interface) to medium 2 (below the interface). However, the wavelength does change due to the change in sound speed.

At the interface  $x=0$  we impose the boundary condition of continuity of pressure, i.e.  $p'_i + p'_r = p'_t$ . Omitting the time dependence we obtain

$$(A+C)e^{i(-y\cos\delta_i\omega/c_1)} = Be^{i(-y\cos\delta_t\omega/c_2)} \quad (3.18)$$

which can be rewritten as

$$(A+C) = Be^{i\omega(\cos\delta_i/c_1 - \cos\delta_t/c_2)y}. \quad (3.19)$$

The right-hand side of this equation is dependent on coordinate  $y$ , whereas the left-hand side is not. This can only be true if

$$\cos\delta_i/c_1 - \cos\delta_t/c_2 = 0 \quad (3.20)$$

which can be written as

$$\frac{\cos\delta_t}{c_2} = \frac{\cos\delta_i}{c_1}. \quad (3.21)$$

This is Snell's law. At the same time we have found the following relation between the amplitudes of the plane waves:

$$A+C = B. \quad (3.22)$$

We need a second boundary condition (at  $x=0$ ) to solve for the relative amplitudes of the reflected and transmitted waves. Continuity of the normal component of the particle velocity, i.e. in the  $x$ -direction, gives

$$(v_x)_i + (v_x)_r = (v_x)_t. \quad (3.23)$$

Application of Euler's equation,  $v_x = -\frac{1}{\rho} \int \frac{\partial p'}{\partial x} dt$ , to  $p'_i$ ,  $p'_r$  and  $p'_t$  and using Snell's law

gives

$$\left( \frac{A \sin \delta_i}{\rho_1 c_1} \right) - \left( \frac{C \sin \delta_i}{\rho_1 c_1} \right) = \left( \frac{B \sin \delta_t}{\rho_2 c_2} \right)$$

with  $\rho_1$  and  $\rho_2$  the density above and below the interface, respectively. This equation can be rewritten as

$$A - C = B \frac{\rho_1 c_1 \sin \delta_i}{\rho_2 c_2 \sin \delta_t}. \quad (3.24)$$

Together with  $A + C = B$  we obtain the reflection coefficient  $R$  and the transmission coefficient  $T$  (both for the amplitude):

$$\begin{aligned} R &= \frac{C}{A} = \frac{Z_2 - Z_1}{Z_2 + Z_1} \\ T &= \frac{B}{A} = \frac{2Z_2}{Z_2 + Z_1} \end{aligned} \quad (3.25)$$

with  $Z_1$  and  $Z_2$  the so-called ‘generalised impedances’ given by  $Z_1 = \frac{\rho_1 c_1}{\sin \delta_i}$  and  $Z_2 = \frac{\rho_2 c_2}{\sin \delta_t}$

, respectively. Note that  $1 + R = T$  and not  $R + T = 1$ , which might suggest a violation of conservation of energy. However, there is no such law as conservation of amplitude in physics (moreover, both  $R$  and  $T$  can be complex numbers). Conservation of energy holds for the intensities (see exercises, question 3) of the three plane waves, i.e.  $I_i = I_r + I_t$  with

$I_i = \frac{1}{\rho_1 c_1}$ ,  $I_r = \frac{|R|^2}{\rho_1 c_1}$  and  $I_t = \frac{|T|^2}{\rho_2 c_2}$  (taking  $A = \sqrt{2}$  Pa for convenience). The amplitude reflection coefficient can be written as

$$R = \frac{\rho_2 c_2 \sin \delta_i - \rho_1 c_1 \sin \delta_t}{\rho_2 c_2 \sin \delta_i + \rho_1 c_1 \sin \delta_t}. \quad (3.26)$$

Similarly,

$$T = \frac{2\rho_2 c_2 \sin \delta_i}{\rho_2 c_2 \sin \delta_i + \rho_1 c_1 \sin \delta_t}. \quad (3.27)$$

It can be shown (see exercises, question 3) that if  $c_2 > c_1$ , which is often the case,  $|R| = 1$  (and  $R$  is a complex number) for grazing incoming angles  $0 < \delta_i < (\delta_i)_c$  with

$$(\delta_i)_c = \cos^{-1} \left( \frac{c_1}{c_2} \right) \quad (3.28)$$

the so-called critical angle. This is known as total internal reflection. For  $\delta_i > (\delta_i)_c$  the amplitude reflection coefficient  $R < 1$  (and a real number).

In table 3.2 the density and sound speed values are listed for a few relevant materials.

Table 3.2

medium	sound speed $c$ [m/s]	density $\rho$ [kg/m <sup>3</sup> ]	$\rho c$ [kg/(m <sup>2</sup> s)]
air (15 °C)	340	1.225	417
water (20 °C)	1481	998	1.5x10 <sup>6</sup>
cork	500	250	0.13x10 <sup>6</sup>
concrete	3100	2600	8.0x10 <sup>6</sup>
aluminium	6300	2700	17x10 <sup>6</sup>

We observe that in all cases the  $\rho c$ -value is much larger than that of air, the consequence of which is that all these materials are good reflectors, i.e. practically  $|R|=1$  for all incoming angles. In figure 3.5 the calculated  $|R|$  versus incoming angle  $\delta_i$  is given for cork with  $(\delta_i)_c = \cos^{-1}\left(\frac{340}{500}\right) = 47^\circ$ . Note that even at  $\delta_i = 90^\circ$  (normal incidence),  $R$  is very close to 1.

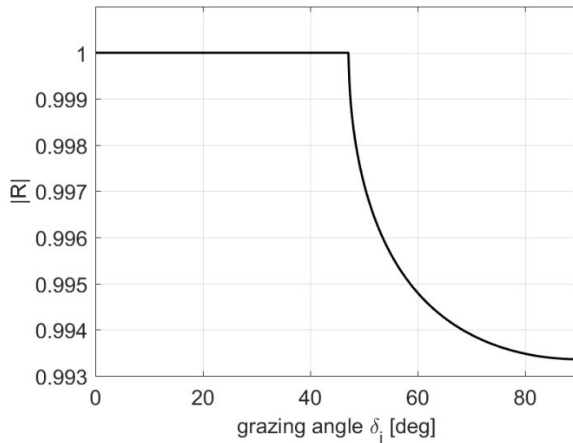


Figure 3.5: Absolute value of the reflection coefficient versus incoming angle for an air-cork interface.

For concrete (with a  $\rho c$  value even higher than that of cork), the critical angle is close to normal incidence, i.e.  $(\delta_i)_c = \cos^{-1}\left(\frac{340}{3100}\right) = 84^\circ$ . For a plane wave in air reflecting off a concrete wall, the reflection coefficient is then very close to (and practically equal to) 1 for all incoming angles.

Note: The gel used in medical ultrasonic imaging helps transfer acoustic energy from the source to the body and back again. Without the gel the impedance (i.e.  $\rho c$ ) mismatch from source to air and from air to body results in reflection of almost all acoustic energy, leaving very little to go into the body.

### 3.4 Non-homogeneous atmosphere – ray tracing

In this section we will apply Snell's law for propagation of sound in a non-homogeneous atmosphere, i.e. an atmosphere with a continuously varying temperature. Because of the temperature dependence of sound speed according to  $c = \sqrt{\gamma RT}$ , such an atmosphere also exhibits a continuously varying sound speed. We only consider variations of  $T$  and  $c$  in one dimension, i.e. in the  $z$  coordinate (height in the atmosphere is in the  $-z$  direction).

First, we recall the concepts of wave fronts and corresponding sound rays. In the most left part of figure 3.6 we see the wave front and corresponding rays of a plane wave. Wave fronts are planes and rays are parallel in this case. The middle part of the figure shows a spherical wave originating from a point source in a homogeneous medium. The medium properties are indicated by the sound speed  $c$  versus  $z$  graph, where  $c$  is independent of  $z$  here. Wave fronts are spheres and the corresponding rays, always perpendicular to the wave fronts, go radially outwards and are still straight lines.

Now consider a medium where  $c$  is changing with  $z$  in a linear fashion, as shown in the most right part of figure 3.6. Since propagation is now faster above the point source as compared to that below the point source, wave fronts are now non-spherical, but ellipsoid in shape. The corresponding rays, still always perpendicular to the wave fronts, are now curved.

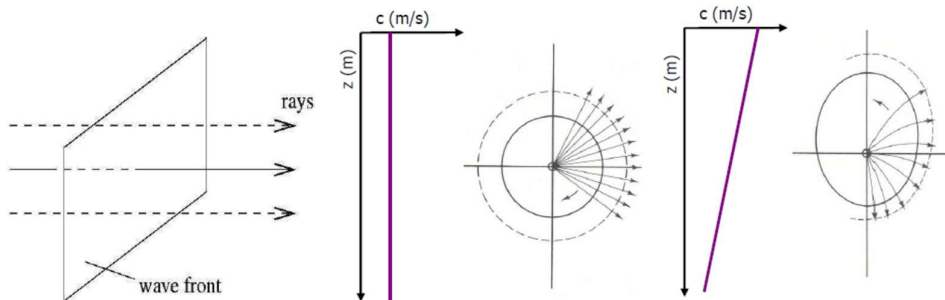


Figure 3.6: Rays and wave fronts emanating from a point source in a medium with a constant sound speed (middle) and a medium with a linearly decreasing sound speed (right). For comparison, the left part of the figure shows the rays and wave fronts for a plane wave.

The typical temperature variation with height for the whole atmosphere is shown in the left part of figure 3.7. The right part of the figure zooms in on the lower 20 km of the atmosphere. We note that the atmosphere can be considered as a layered system where in each layer temperature behaves linearly with height. Usually, temperature decreases linearly with height in the troposphere (defined as the lower 11 km of the atmosphere). In the first part of the stratosphere, temperature is virtually constant. After that it increases linearly with height due to the fact that the sun's ultraviolet radiation is absorbed by the ozone layer.

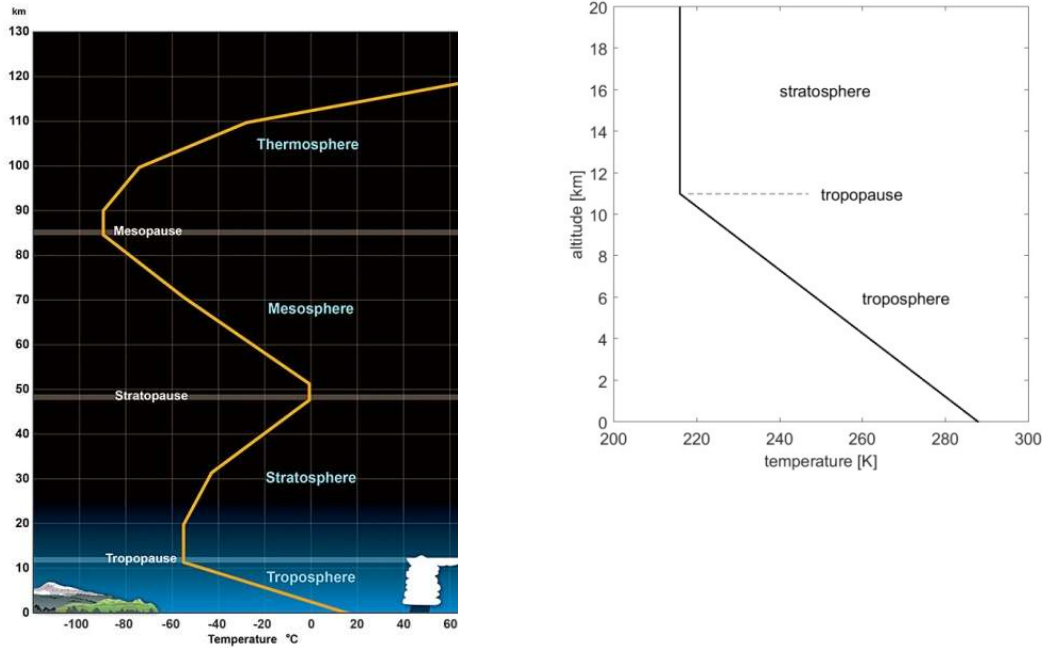


Figure 3.7: Typical temperature variation with height for the entire atmosphere (left). The right part of the figure zooms in on the lower 20 km of the atmosphere.

For aircraft noise, only the troposphere is of importance and we model its temperature variation by the linear function

$$T = T_0 + \lambda H \quad (3.29)$$

with  $T_0$  the atmosphere temperature at the ground in K,  $H$  the height in m and  $\lambda$  the temperature gradient in K/m.

Note: In this section  $\lambda$  is the temperature gradient and not the wavelength.

Typically,  $\lambda = \frac{dT}{dH} = -0.0065 \text{ K/m}$  and  $T_0 = 288.15 \text{ K}$  in the standard atmosphere. Using  $c = \sqrt{\gamma RT}$ , we show that, to a very good approximation, the sound speed also behaves as a linear function with height. Since the gradient  $\lambda$  is small, we can write

$$c = [\gamma R(T_0 + \lambda H)]^{1/2} = c_0 \left(1 + \frac{\lambda H}{T_0}\right)^{1/2} \approx c_0 + \frac{c_0 \lambda H}{2T_0} = c_0 + \frac{dc}{dH} H \quad (3.30)$$

where use has been made of the first order Taylor series approximation

$$\sqrt{1+x} \approx 1 + \frac{1}{2}x \quad \text{for } x \ll 1. \quad (3.31)$$

The tropospheric sound speed gradient is typically

$$\frac{dc}{dH} = -\frac{dc}{dz} = \frac{\lambda c_0}{2T_0} = \frac{-0.0065 \times 340.29}{2 \times 288.15} = -0.00384 \text{ s}^{-1}. \quad (3.32)$$

Let us now consider an atmosphere with sound speed varying linearly with  $z$  or  $H$ , see figure 3.8. In the figure the coordinate system is such that  $x$  is the horizontal direction and  $z = -H$  is the vertical direction. We consider a single sound ray, launched at position  $x = 0$  and  $z = -H_1$  with horizontal angle  $\delta_1$ . The sound ray is curved and at the position indicated by the arrow, the radius of curvature is equal to  $R$  (meaning that locally the sound ray is a small part of a circle with radius  $R$ ).

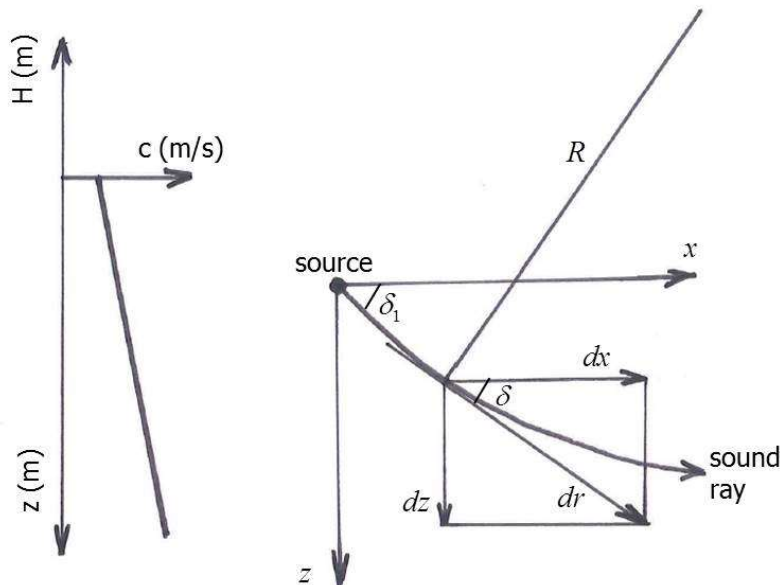


Figure 3.8: Geometry of a sound ray (right) in an atmosphere with decreasing sound speed with height (left).

We consider an infinitesimal part  $dr = R d\delta$  of the sound ray at the position of the arrow, where the ray makes an angle  $\delta < \delta_1$  with the horizontal.  $d\delta$  is the local change in horizontal angle of the ray. The corresponding infinitesimal changes in  $x$  and  $z$  are

$$dx = \cos \delta dr = R \cos \delta d\delta \quad (3.33)$$

and

$$dz = \sin \delta dr = R \sin \delta d\delta \quad (3.34)$$

respectively.

Along the sound ray at all positions, Snell's law applies, i.e.

$$\frac{c(z)}{\cos(\delta(z))} = \frac{c_1}{\cos \delta_1} \quad (3.35)$$

with  $c_1$  the sound speed at the source, i.e. at  $z = -H_1$ . Differentiating this equation with respect to  $z$ , we obtain

$$\frac{dc}{dz} = -\frac{c_1}{\cos \delta_1} \sin \delta(z) \frac{d\delta}{dz} \quad (3.36)$$

which can be rewritten as

$$d\delta = -\frac{\cos \delta_1}{c_1} \frac{dc}{\sin \delta(z)} = -\frac{\cos \delta(z)}{\sin \delta(z)} \frac{dc}{c(z)} \quad (3.37)$$

where we have again used Snell's law. The radius of curvature  $R$  is now given as

$$R = \frac{dr}{d\delta} = -\frac{\frac{dz}{\sin \delta}}{\frac{\cos \delta}{dc} \frac{dc}{c}} = -\frac{c(z)}{\cos \delta(z)} \frac{1}{\frac{dc}{dz}}. \quad (3.38)$$

With Snell's law this can be written as

$$R = -\frac{c_1}{\cos \delta_1} \frac{dc}{\frac{dz}{\sin \delta}}. \quad (3.39)$$

Note that  $c_1$  and  $\delta_1$  are constants and that if the sound speed gradient  $\frac{dc}{dz}$  is a constant too, then radius of curvature  $R$  is also a constant. This would mean that when  $c(z)$  is a linear function, the entire ray would be a circle. Still, note that  $R$  is dependent on the launch angle  $\delta_1$ . Also, note that if  $\frac{dc}{dz} > 0$  then  $R < 0$ , i.e. an 'upward refracting' ray.

The lengths of the ray in the  $x$  and  $z$  direction, in the case of constant  $\frac{dc}{dz}$ , are now given by

$$\Delta x = \int_{\delta_1}^{\delta} dx = R \int_{\delta_1}^{\delta} \cos \delta d\delta = R (\sin \delta - \sin \delta_1) \quad (3.40)$$

and

$$\Delta z = \int_{\delta_1}^{\delta} dz = R \int_{\delta_1}^{\delta} \sin \delta d\delta = R (\cos \delta_1 - \cos \delta) \quad (3.41)$$

respectively. Here  $\delta_l$  and  $\delta$  are the begin angle (launch angle) and end angle, respectively. In figure 3.9 we show a set of four upward refracting rays with increasing launch angle  $\delta_l$  at the source at height  $H_1$ . All rays are circles with radius depending on  $\delta_l$ . The sound speed at the source and at the ground are  $c_1$  and  $c_0 > c_1$ , respectively.

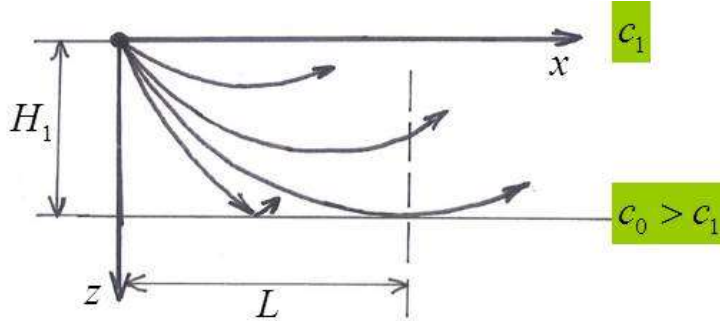


Figure 3.9: Upward refracting sound rays for various values of launch angle at the source.

Depending on  $\delta_l$  the rays either do not hit the ground, just hit the ground or reflect off the ground. The ray that just hits the ground is called the ‘limiting ray’. At  $x = L$ ,  $\delta = 0^\circ$  for this ray. Beyond  $x = L$  rays cannot appear, hence  $L$  is denoted ‘shadow zone’ distance. For  $x > L$  there is a zone of silence.

Substituting this in the above formulas for  $\Delta x$  and  $\Delta z$ , we obtain

$$\Delta x = -R \sin \delta_l = L \quad (3.42)$$

and

$$\Delta z = R(\cos \delta_l - 1) = H_1 \quad (3.43)$$

with

$$R = -\frac{c_1}{\cos \delta_l \frac{dc}{dz}} = -\frac{c_0}{\cos 0 \frac{dc}{dz}} = c_0 \frac{2T_0}{c_0 \lambda} = \frac{2T_0}{\lambda} < 0 \quad (3.44)$$

where we have used  $\frac{dc}{dz} = -\frac{\lambda c_0}{2T_0} > 0$  (see above).

From the equation  $R(\cos \delta_l - 1) = H_1$ , we can solve  $\delta_l$  and substitute this into  $L = -R \sin \delta_l$  to obtain the shadow zone distance.

Due to the fact the  $\frac{dc}{dz} \ll 1$ , launch angles are small. Hence, we may use the first order

Taylor series approximations for the sine and the cosine, i.e.

$$\sin x \approx x \text{ and } \cos x \approx 1 - \frac{1}{2}x^2 \quad \text{for } x \ll 1 \quad (3.45)$$

provided  $x$  to be in radians. Hence, the equations for  $H_1$  and  $L$  become

$$H_1 = R(\cos \delta_1 - 1) \approx -R\left(\frac{1}{2}\delta_1^2\right) \quad (3.46)$$

and

$$L = -R \sin \delta_1 \approx -R\delta_1 \quad (3.47)$$

with  $R = \frac{2T_0}{\lambda} < 0$ . From this we obtain a very practical formula for the shadow zone distance, i.e.

$$L = \sqrt{-\frac{4T_0 H_1}{\lambda}}. \quad (3.48)$$

From figure 3.10, showing a plot of  $L$  versus source height  $H_1$  (and  $\lambda = -0.0065 \text{ K/m}$ ), we see that  $L$  is typically a few km for source heights of a few 100 m.

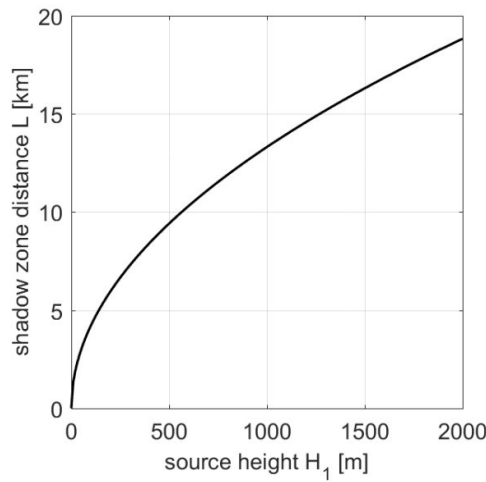


Figure 3.10: Shadow zone distance as a function of source height for an atmosphere with a temperature gradient equal to  $\lambda = -0.0065 \text{ K/m}$ .

Figure 3.11 shows a detailed ray calculation for the same temperature gradient  $\lambda = -0.0065 \text{ K/m}$  and source height  $H_1 = 800 \text{ m}$ . In this situation the shadow zone distance is

$$L = \sqrt{-\frac{4T_0 H_1}{\lambda}} = \sqrt{-\frac{4 \times 288.15 \times 800}{-0.0065}} \approx 12 \text{ km}. \quad (3.49)$$

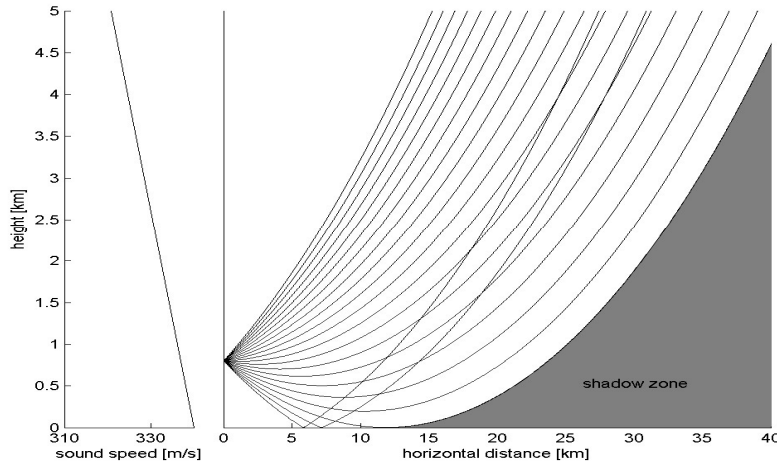


Figure 3.11: Upward refracting sound rays calculated for an atmosphere with a temperature gradient equal to  $\lambda = -0.0065 \text{ K/m}$ .

Given the right atmospheric conditions, the vertical temperature gradient can invert such that temperature and therefore sound speed increases with height (i.e. decreases with  $z$ ,  $\frac{dc}{dz} < 0, \frac{dc}{dH} > 0$ ). Figure 3.12 shows a detailed ray calculation for  $T_0 = 253.15 \text{ K}$  and  $\lambda = +5 \times 10^{-3} \text{ K/m}$ . A source height of  $H_1 = 10 \text{ m}$  is chosen. Rays are launched from the source for  $\delta_i$  values from  $-10^\circ$  to  $+10^\circ$  in steps of  $1^\circ$ . Note that there is no formation of a shadow zone as the rays are now bent to the ground and hence ground-reflected. In contrast with a zone of silence, this results in a reinforcement of sound.

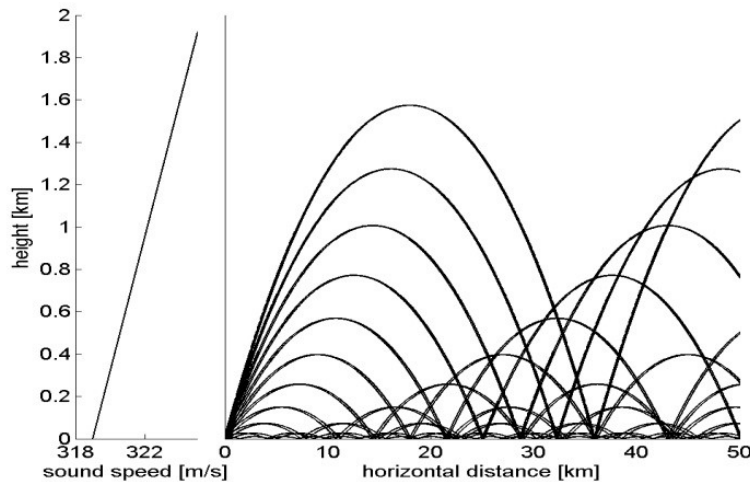


Figure 3.12: Downward refracting sound rays calculated for an atmosphere with a temperature gradient equal to  $\lambda = +0.005 \text{ K/m}$ .

The above formulas for  $\Delta x$  and  $\Delta z$  in the case of constant  $\frac{dc}{dz}$ , equations 3.40 and 3.41, offer the possibility of a simulation technique called ‘ray tracing’. Then the full sound speed profile  $c(z)$  is approximated by linear pieces and in the resulting layers with constant  $\frac{dc}{dz}$ , the formulas for  $\Delta x$  and  $\Delta z$  are subsequently applied. The rays then consist of consecutive parts of circles with different radius of curvatures.

An example of such a ray tracing simulation is given in figure 3.13, where rays are calculated for the full atmosphere up a height of 150 km (i.e., up to the thermosphere) and for horizontal distances up to 1000 km. Note that the rays converge at regular distances called ‘convergence zones’ (zones of high sound intensity).

These long-range propagation calculations are shown for two stratospheric conditions, i.e. for a sound speed gradient of  $0.0010 \text{ s}^{-1}$  and for a gradient of  $0.0015 \text{ s}^{-1}$  (depending on the temperature structure of the stratosphere). It is observed that the convergence zone distance depends on this gradient, i.e. 400 km for  $0.0010 \text{ s}^{-1}$  and 300 km for  $0.0015 \text{ s}^{-1}$ , respectively. Conversely, measurement of the convergence zone distance can provide information about the properties of the higher layers of the atmosphere, which in this example is the temperature gradient of the stratosphere. This is an example of ‘inverse modelling’, i.e. determining the input parameters of the model using measurements that are assumed to be equal to the model output. In this specific case, the inversion is called ‘acoustic remote sensing’.

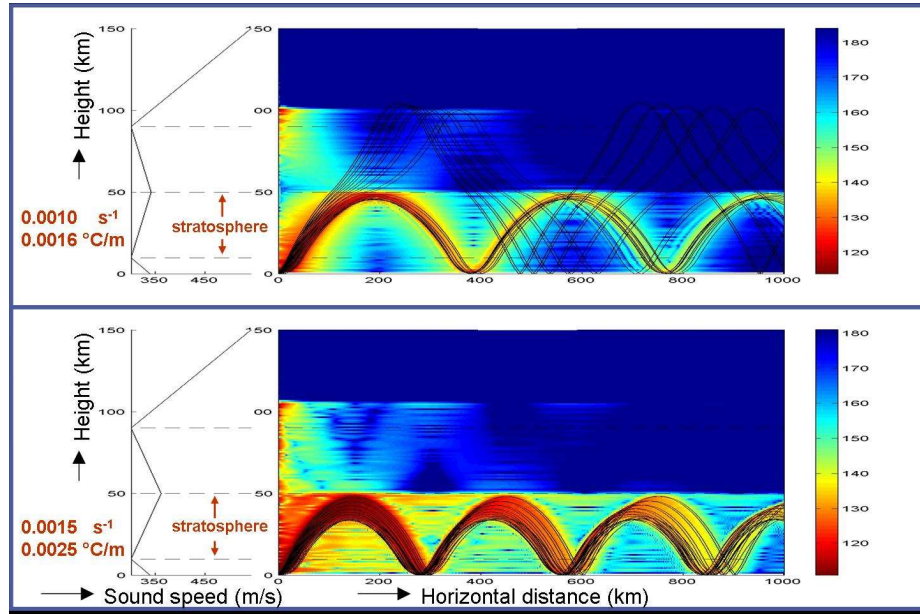


Figure 3.13: Long-range sound propagation calculations for two values of the stratospheric sound speed gradient:  $+0.0010 \text{ s}^{-1}$  (upper figure) and  $+0.0015 \text{ s}^{-1}$  (lower figure).

Notes:

- Also indicated in figure 3.13 is a measure for the sound intensity (in dB) as a function of distance and height (red = high intensity, low transmission loss, blue = low intensity, high transmission loss). This was obtained by solving the wave equation numerically.
- Obtaining information about the higher layers of the atmosphere requires long-range propagation, i.e. several 100 km. Due to the strongly increasing sound absorption coefficient with frequency, a low frequency sound source is required (below approximately 20 Hz).
- Retrieving information about the properties of the higher layers of the atmosphere, such as the temperature (and wind) structure of the stratosphere and higher, is very difficult and usually done by weather balloons (and satellites). Here, results from acoustic remote sensing can provide complementary data.

### 3.5 Ground effect

The effects of ground reflected sound can complicate the interpretation of noise measurements, for aircraft noise in particular. The geometry of the problem treated in this section is given in figure 3.14.

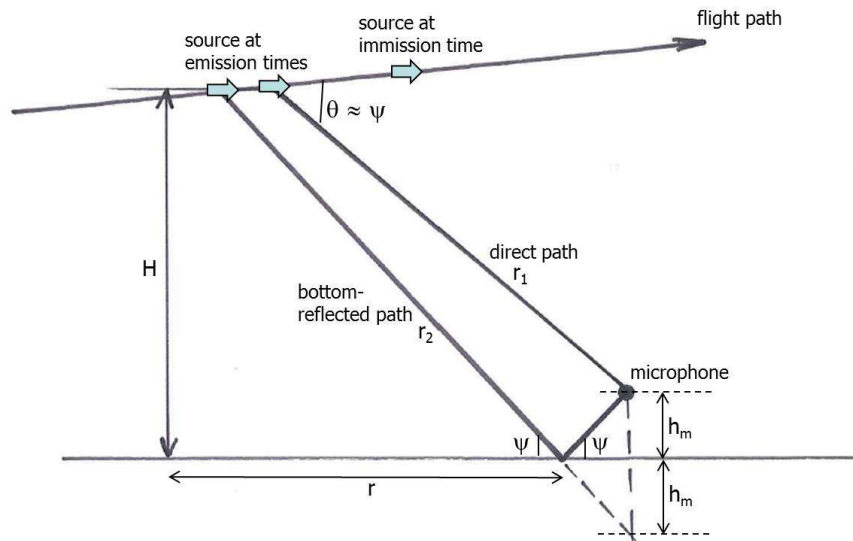


Figure 3.14: Direct and ground-reflected sound path.

The following assumptions are made:

- as an acoustic source, the aircraft is a point source;

- the atmosphere is homogeneous;
- the ground reflection is specular, i.e. irregularities in the ground surface are small compared to the wavelength of the aircraft sound.

At a given emission time  $t_e$  the aircraft is at the position indicated in the figure (at height  $H$ ). Then,  $\theta$  is the emission angle to the observer or microphone. The direct sound ray arrives at the microphone at an immission time  $t = t_e + \frac{r_1}{c}$  with  $r_1$  the length of the direct path and  $c$  the sound speed. At the same time a ground-reflected sound ray arrives at the microphone (path length  $r_2$ ). This reflected sound is emitted slightly earlier by a time given by  $\Delta t = \frac{r_2 - r_1}{c}$ .

We further assume that the small displacement of the source, i.e. the aircraft, in this time interval  $\Delta t$  is negligible.

At radial frequency  $\omega = 2\pi f$ , the sound pressure at the observer in complex notation is given by

$$p_m(r, t) = \frac{A}{r_1} e^{i\omega(t-r_1/c)} + Q \frac{A}{r_2} e^{i\omega(t-r_2/c)} \quad (3.50)$$

with  $A$  the amplitude of the sound pressure at 1 m from the source,  $r$  the horizontal distance from the source to the microphone and  $Q$  the amplitude reflection coefficient of the ground. In complex notation  $Q$  can be written as  $Q = |Q| e^{i\phi}$  with  $\phi$  the phase change at reflection.

In section 1.4 we derived for this interference problem that the total effective sound pressure is given as

$$p_{e_m}(r) = \left[ \left( \frac{A}{r_1 \sqrt{2}} \right)^2 + |Q|^2 \left( \frac{A}{r_2 \sqrt{2}} \right)^2 + |Q| \frac{A^2}{r_1 r_2} \cos \left( \frac{\omega \Delta r}{c} + \phi \right) \right]^{1/2} \quad (3.51)$$

with  $\Delta r = r_2 - r_1$ . The first term in this equation is the effective sound pressure squared of the direct path ( $p_{e_d}^2$ ). Hence, the total effective sound pressure can be written as

$$p_{e_m}(r) = p_{e_d}(r) \left[ 1 + \left( \frac{r_1}{r_2} \right)^2 |Q|^2 + 2 \left( \frac{r_1}{r_2} \right) |Q| \cos \left( \frac{\omega \Delta r}{c} + \phi \right) \right]^{1/2}. \quad (3.52)$$

The ground effect  $\Delta SPL(r, \theta)$  is defined as the difference between the measured  $SPL_m(r, \theta)$  and  $SPL_d(r, \theta)$  that would occur in the free field, i.e. without the ground boundary. Hence,

$$\Delta \text{SPL}(r, \theta) = \text{SPL}_m(r, \theta) - \text{SPL}_d(r, \theta) = 10 \log \left[ 1 + \left( \frac{r_1}{r_2} \right)^2 |Q|^2 + 2 \left( \frac{r_1}{r_2} \right) |Q| \cos \left( \frac{\omega \Delta r}{c} + \phi \right) \right]$$

(3.53)

Here, atmospheric absorption is neglected as  $\Delta r \ll r_1, r_2$ .

We will have a closer look at  $\Delta r = r_2 - r_1$  now. We have

$$r_1 = \sqrt{r^2 + (H - h_m)^2} \quad \text{and} \quad r_2 = \sqrt{r^2 + (H + h_m)^2} \quad (3.54)$$

with  $h_m$  the microphone height. As  $H \gg h_m$  and  $H \gg \Delta r$  a good approximation for  $\Delta r$  is  $\Delta r = 2h_m \sin \psi$ . The ground effect thus becomes

$$\Delta \text{SPL}(r, \theta) = 10 \log \left[ 1 + \left( \frac{r_1}{r_2} \right)^2 |Q|^2 + 2 \left( \frac{r_1}{r_2} \right) |Q| \cos \left( \frac{4\pi f}{c} h_m \sin \psi + \phi \right) \right]. \quad (3.55)$$

Figure 3.15 shows the ground effect as a function of frequency  $f$ . The assumptions made are

- hard boundary, for which we can approximate  $|Q| \approx 1$ ;
- $r_1 \approx r_2$ ;
- no phase shift, i.e.  $\phi = 0$ ;
- microphone height  $h_m = 1.2$  m;
- aircraft is overhead i.e.  $\psi = 90^\circ$ .

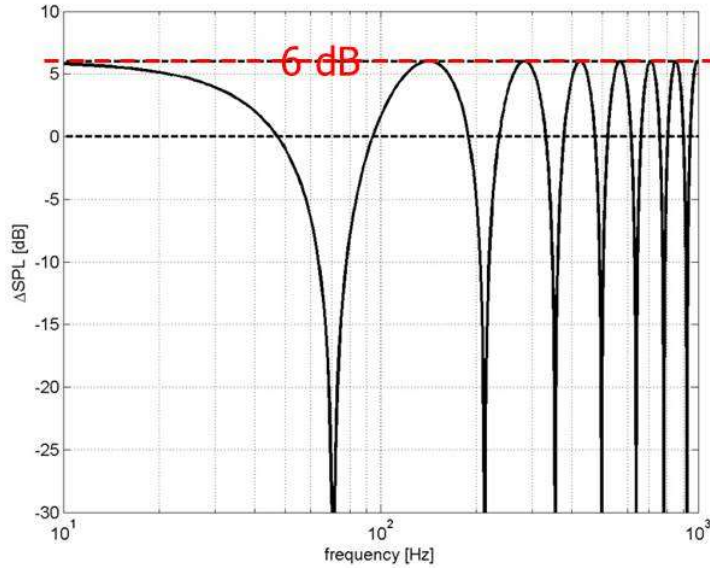


Figure 3.15: Ground effect as a function of frequency for a hard boundary (with microphone height = 1.2 m and aircraft overhead).

As already seen in section 1.9, the ground interference effect can change the measured SPL by a value between 6 dB and  $-\infty$ . Cancellation (ground effect  $\Delta\text{SPL} = -\infty$ ) occurs at the frequencies

$$f = \frac{c(n+1/2)}{2h_m}, \quad n = 0, 1, 2, \dots \quad (3.56)$$

Substituting the values for  $c$  and  $h_m$ , this is at  $f = 70, 213, 354, 496, 638, 779, 921, \dots$  Hz. Generally, at arbitrary  $\psi$  the frequencies at which cancellation occurs are

$$f = \frac{c(n+1/2)}{2h_m \sin \psi}, \quad n = 0, 1, 2, \dots \quad (3.57)$$

The ground effect on the aircraft noise spectrum, measured for two emission angles ( $\theta \approx \psi = 90^\circ, 150^\circ$ ), is shown in figure 3.16.

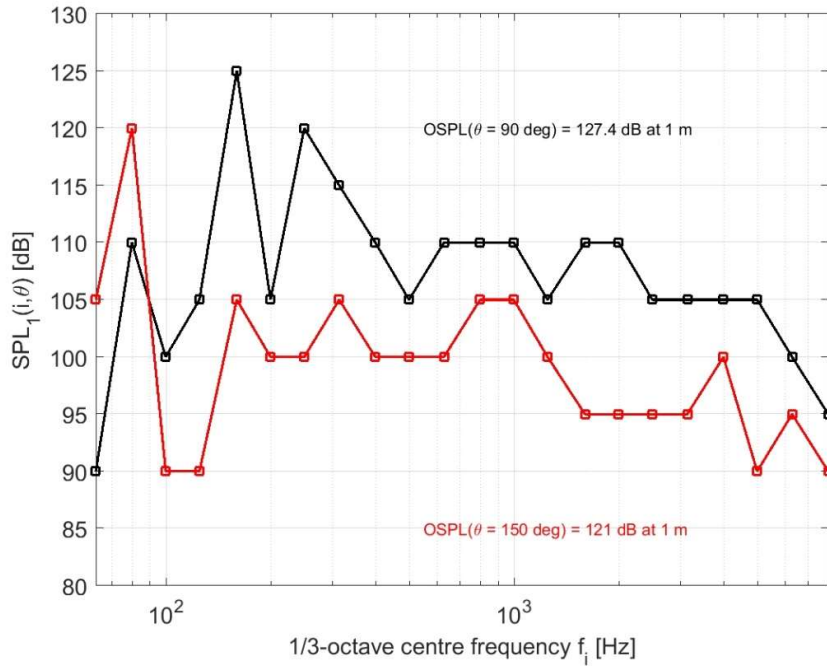


Figure 3.16: A noise spectrum for a single aircraft measured at two different emission angles, showing the profound effect of the ground reflection.

The figure shows SPL values measured in 1/3-octave bands. The details about such a frequency analysis are given in chapter 5. Here, it suffices to say that the figure shows SPL as a function of frequency and that the ground reflection has a profound effect on it due to the subsequent reinforcement (+6 dB) and cancellation effects, which in turn are dependent on the emission angle.

We will now examine the reflection coefficient  $Q$  in more detail. For sufficiently large  $r_1$  (and  $r_2$ )  $Q$  is a plane wave reflection coefficient, hence denoted  $Q_p$ . As illustrated in figure 3.17 we can distinguish two ground media, one that can transmit sound in the lateral direction and one that cannot. The first type of medium is treated elaborately in section 3.3. The second type of medium, called ‘locally reacting’, is not able to propagate sound in the direction parallel to the surface. The latter medium commonly applies to airplane noise testing situations.

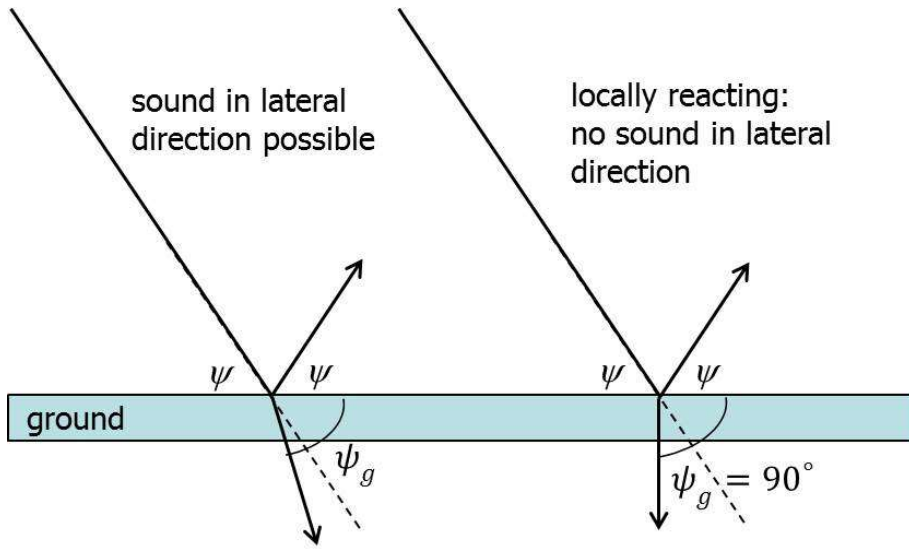


Figure 3.17: A ground medium that can transmit sound in the lateral direction (left) and a ground medium that cannot transmit sound in the lateral direction (right).

Recall the plane wave reflection coefficient derived in section 3.3:

$$R = \frac{\rho_2 c_2 \sin \delta_i - \rho_1 c_1 \sin \delta_t}{\rho_2 c_2 \sin \delta_i + \rho_1 c_1 \sin \delta_t}. \quad (3.58)$$

Now  $\rho_1 c_1 = \rho_\infty c$  is the specific resistance for air and  $\rho_2 c_2 = Z_g$  is that of the ground. In the notation of this section the plane wave reflection coefficient becomes

$$Q_p = \frac{\frac{Z_g}{\rho_\infty c} \sin \psi - \sin \psi_g}{\frac{Z_g}{\rho_\infty c} \sin \psi + \sin \psi_g} \quad (3.59)$$

with  $\psi = \delta_i$  and  $\psi_g = \delta_t$ . For a locally reacting ground we have  $\psi_g = 90^\circ$  and  $Z_g$  becomes  $Z_n$ , the so-called ‘normal surface impedance’. Then  $Q_p$  is

$$Q_p = |Q_p| e^{i\beta} = \frac{\frac{Z_n}{\rho_\infty c} \sin \psi - 1}{\frac{Z_n}{\rho_\infty c} \sin \psi + 1}. \quad (3.60)$$

For the specific normal surface impedance (i.e. relative to  $\rho_\infty c$ ) usually the model of Delany and Bazley is used, i.e.

$$\frac{Z_n}{\rho_\infty c} = \left[ 1 + 9.08 \left( \frac{\sigma}{f} \right)^{0.75} \right] + i \left[ 11.9 \left( \frac{\sigma}{f} \right)^{0.73} \right] \quad (3.61)$$

with  $f$  the frequency in Hz. This model applies to ‘fibrous absorbent’ materials and has only one parameter, the flow resistivity  $\sigma$  in units  $\text{kPa s m}^{-2}$ . Figure 3.18 presents the real and imaginary part of  $\frac{Z_n}{\rho_\infty c}$  as a function of  $f$ .

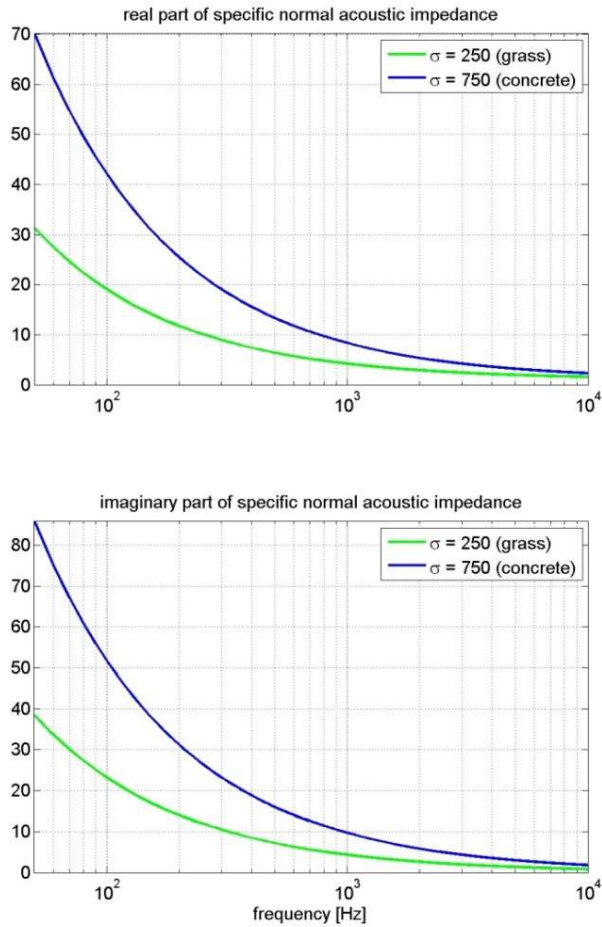


Figure 3.18: Real and imaginary part of the specific normal surface impedance for grass and concrete according to the model of Delany and Bazley.

The surface impedance of two relevant ground media are shown: grass ( $\sigma = 250 \text{ kPa s m}^{-2}$ ) and concrete ( $\sigma = 750 \text{ kPa s m}^{-2}$ ). Figure 3.19 shows the absolute value and phase  $\beta$  of the corresponding plane wave reflection coefficient for these two media at a frequency of 1000 Hz.

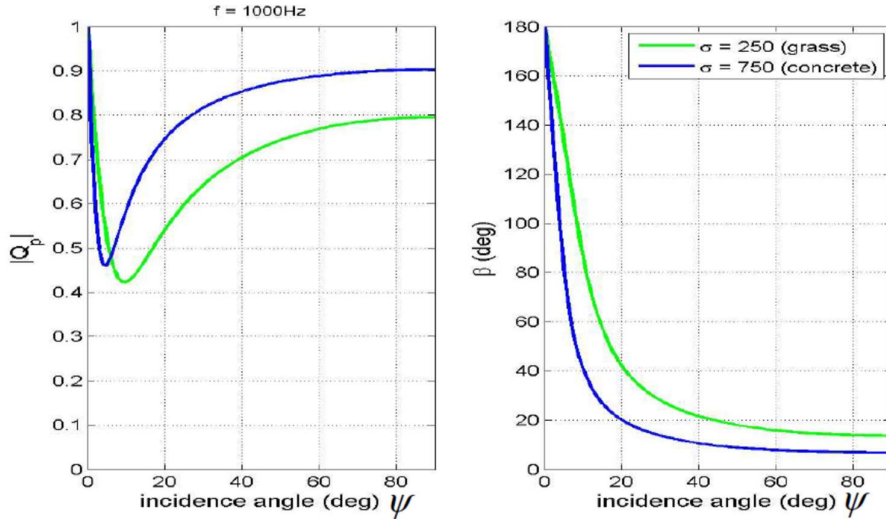


Figure 3.19: Absolute value and phase of the plane wave reflection coefficient for grass and concrete as a function of incidence angle (Delany and Bazley model). Results are shown for a fixed frequency of 1000 Hz

Figure 3.20 shows the ground reflection coefficient as a function of frequency, again for grass and concrete. A set of incidence angle values between  $\psi = 5^\circ$  and  $\psi = 90^\circ$  has been chosen. We conclude from this figure that, except at small incidence angles, real grounds (soils) are almost perfect reflectors of acoustic energy, especially at low frequencies.

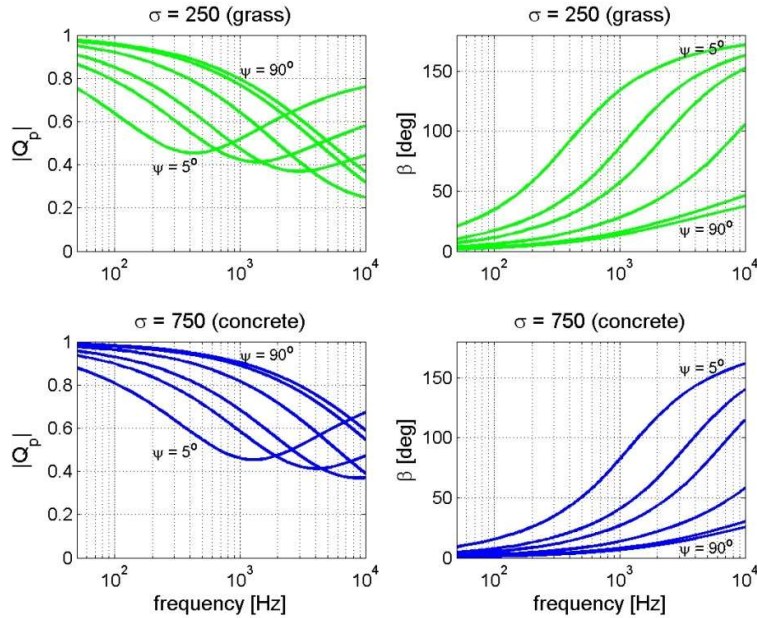


Figure 3.20: Absolute value and phase of the plane wave reflection coefficient for grass and concrete as a function of frequency (Delany and Bazley model). Results are shown for a set of incidence angle values in between  $5^\circ$  and  $90^\circ$ .

We can now simulate the full ground effect  $\Delta SPL$  using equation 3.55 with  $Q = Q_p$  and  $\phi = \beta$  with the formula

$$\Delta \text{SPL}(r, \theta) = 10 \log \left[ 1 + \left( \frac{r_1}{r_2} \right)^2 |Q_p|^2 + 2 \left( \frac{r_1}{r_2} \right) |Q_p| \cos \left( \frac{4\pi f}{c} h_m \sin \psi + \beta \right) \right]. \quad (3.62)$$

Figure 3.21 shows the ground effect as a function of frequency up to 1000 Hz for three values of the emission (incidence) angle, i.e.  $\theta \approx \psi = 15^\circ, 30^\circ$  and  $89^\circ$ , and a microphone height  $h_m$  of 1.2 m. Results are shown for concrete (upper three graphs) and grass (lower three graphs). We note that these natural surfaces produce ground reflection effects very similar to those produced by a hard solid ground (see figure 3.15).

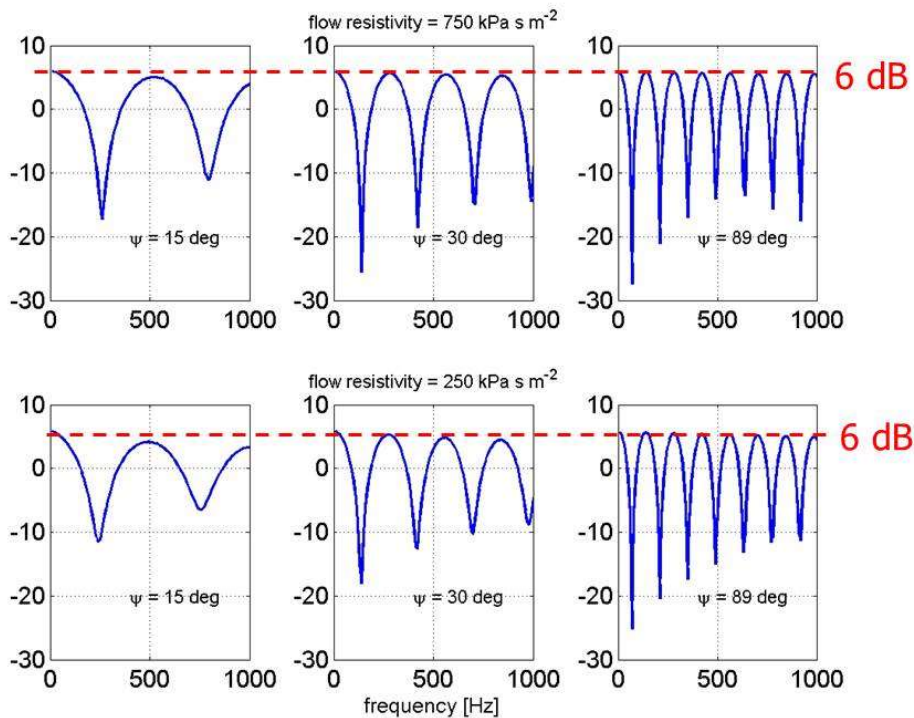


Figure 3.21: Calculated ground effect as a function of frequency for grass (lower figures) and concrete (upper figures). Results are shown for three values of the incidence angle. The microphone height equals 1.2 m.

Figure 3.22 shows the calculated ground effect, but now for a flush-mounted microphone, i.e.  $h_m$  equal to 0 m. We observe that for this case the ground effect simply results in a pressure doubling ( $\Delta \text{SPL} \approx 6 \text{ dB}$ ), i.e. the conversion to free field levels simply requires a subtraction of 6 dB.

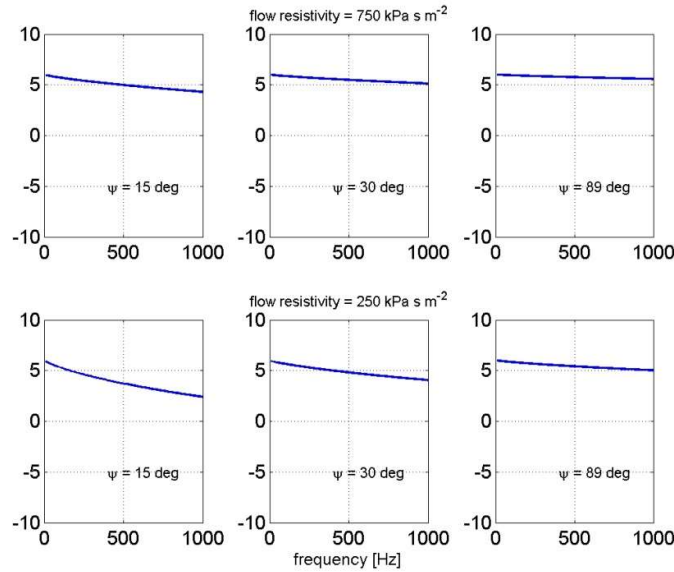


Figure 3.22: Calculated ground effect as a function of frequency for grass (lower figures) and concrete (upper figures). Results are shown for three values of the incidence angle. The microphone height equals 0 m.

For an aircraft flyover the observed sound pressure level as a function of (horizontal) distance  $r$  and frequency  $f$  can now be written as (adding a subscript  $G$  for ground)

$$\text{SPL}(r, f) = \text{PWL} - 10.8 - 20 \log r_1 - \alpha(f)r_1 + \Delta\text{SPL}_G(r, f) \quad (3.63)$$

where, for spherical spreading and atmospheric absorption, we have assumed that  $r_1 \approx r_2$ . This formula contains all environmental effects for the situation of a homogeneous atmosphere, i.e. no temperature and no wind gradients. For an aircraft flyover around airports this equation is sufficiently accurate for distances up to several 100 m (no ray curvature yet).

Figure 3.23 shows  $\text{SPL}(r, f)$  in dB for a concrete ground and microphone heights of 1.2 and 0 m, respectively. A value of 160 dB has been adopted for the power watt level PWL of the (point) source being at a height of 100 m. Further, the source is assumed to move sufficiently slow so that we can ignore Doppler effects. The left figure ( $h_m = 1.2$  m) clearly shows the interference pattern due to the ground effect, whereas in the right figure ( $h_m = 0$  m) this is absent and the ground effect is reduced to a simple 5 to 6 dB addition. In both plots the effect of atmospheric absorption is clearly seen at the higher frequencies and the longer ranges  $r$ .

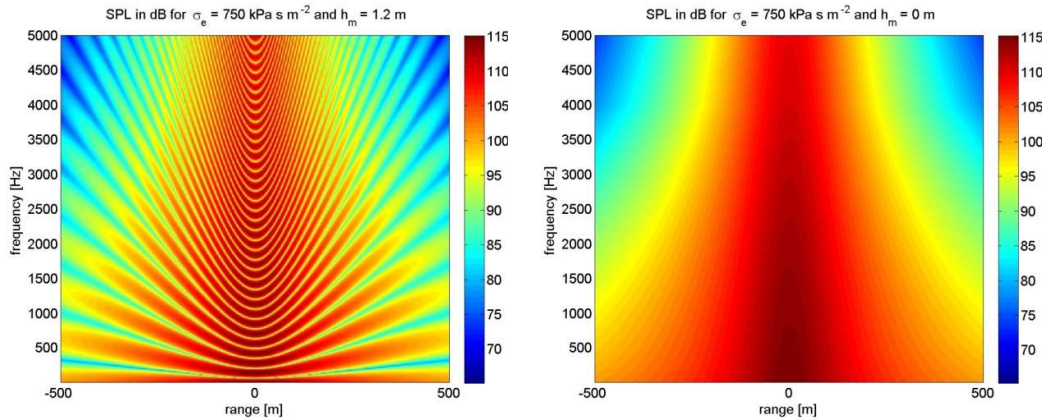


Figure 3.23: Simulated sound pressure level SPL as a function distance (range) and frequency for a slowly moving point source at a height of 100 m above a concrete ground. The left figure is for a microphone height of 1.2 m, whereas for the right figure the microphone height is 0 m.

The results shown in figure 3.23 are similar to that of a so-called 'spectrogram', i.e. SPL as a function of time and frequency (where time can be obtained from the horizontal distance  $r$  using the geometry of figure 1.21 and the aircraft velocity). Chapter 5 describes in detail how a spectrogram is derived from the sound pressure as a function of time as measured by a microphone. For now it suffices to say that a spectrogram is obtained from the measured pressure time series by subsequent Fourier transforming consecutive time intervals of the data. Figure 3.24 shows an example of a measured spectrogram for a flyover of an airplane equipped with a jet engine. At around 15 s the airplane is at overhead position. The interference pattern due to the ground effect is clearly observed. A Doppler-shifted fan tone (at a frequency of about 3000 Hz at overhead) is also visible in the spectrogram.

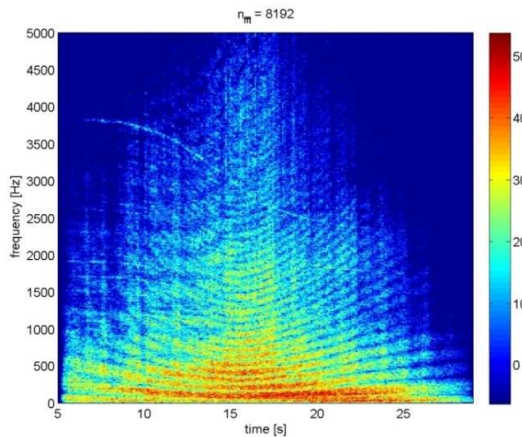


Figure 3.24: Measured spectrogram (i.e. SPL versus time and frequency) for a flyover of an airplane equipped with a jet engine. Notice the clear interference pattern due to the ground effect.

## Exercises

### Question 1

Show that for the atmospheric sound attenuation coefficient  $\alpha$  (due to friction)  $\alpha [\text{dB/m}] = 8.686 \alpha [\text{m}^{-1}]$ .

### Question 2

- (a) Consider a non-directional acoustic source with acoustic power  $W = 10 \text{ mW}$  in an atmosphere at a temperature of  $15^\circ\text{C}$  and relative humidity 50 %. Calculate the Sound Pressure Level SPL (in dB) at distances 10 m, 100 m, 1 km and 10 km from this source for the frequencies 10 Hz, 100 Hz, 1 kHz and 10 kHz.

		range from source			
frequency	$\alpha$	10 m	100 m	1 km	10 km
10 Hz	$10^{-4} \text{ dB/m}$				
100 Hz	$5 \times 10^{-4} \text{ dB/m}$				
1 kHz	$5 \times 10^{-3} \text{ dB/m}$				
10 kHz	0.1 dB/m				

- (b) Make a plot of your results of the previous question (SPL in dB on  $y$ -axis and range from source on a logarithmic  $x$ -axis for the 4 frequencies).

### Question 3

- (a) By using the expression for acoustic intensity of a plane wave, verify that the sum of the reflected and transmitted intensity equals the incoming intensity. To simplify things, perform this check only for normal incidence:  $\delta_i = 90^\circ$ .
- (b) Consider an interface between two media for which  $c_2 > c_1$ . Show that for incidence angles less than the critical angle the absolute value of the reflection coefficient equals 1, i.e.  $|R| = 1$ .
- (c) Consider a plane interface between media water ( $\rho_1 = 1000 \text{ kg/m}^3$ ,  $c_1 = 1480 \text{ m/s}$ ) and aluminium ( $\rho_2 = 2700 \text{ kg/m}^3$ ,  $c_2 = 6300 \text{ m/s}$ ). Calculate the critical angle and

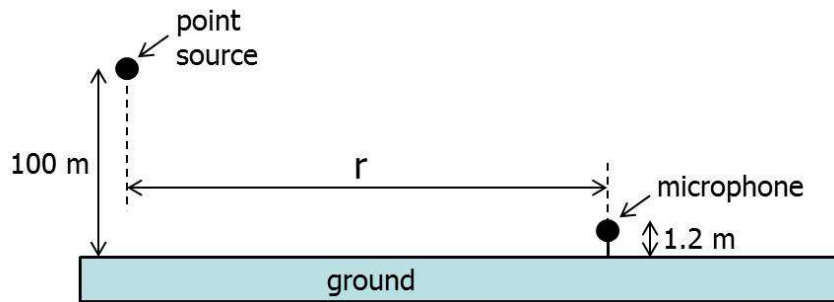
the plane wave reflection coefficient  $R$  at normal incidence. Make a sketch of  $|R|$  as a function of incidence angle.

Question 4

- (a) Consider a troposphere where temperature decreases with increasing height. The temperature gradient value amounts to  $-0.0065 \text{ } ^\circ\text{Cm}^{-1}$ . The temperature just above the ground is  $20^\circ\text{C}$ . Calculate the corresponding sound speed just above the ground and the sound speed gradient in this troposphere.
- (b) An airplane is flying at a height of 1200 m. The airplane may be considered a point source. Calculate the launch angle (i.e. the angle with the horizontal at the source position) of the sound ray that travels from the position of the aircraft in the direction of the ground, such that this ray *just* hits the ground. (Rays with larger launch angles reflect off the ground and rays with smaller launch angles do not reach the ground). Also calculate the corresponding horizontal position on the ground at which this ray hits the ground.
- (c) Make a sketch of this sound ray and indicate the shadow zone.
- (d) Now an observer is standing on the ground at a horizontal distance of 18 km from the sound source. Does this person perceive any sound coming from the airplane? And what if the gradient would be reversed, i.e. the sound speed increases with height? Motivate your answer.
- (e) Suppose in the evening the temperature gradient in the troposphere has decreased with a factor of two to  $-0.0033 \text{ } ^\circ\text{Cm}^{-1}$ . Calculate again the horizontal position where the shadow zone starts.

Question 5

A point source in a homogenous atmosphere radiates sound at a frequency of 100 Hz. The Power Watt Level of the source is  $\text{PWL} = 160 \text{ dB}$ . The source is at a height of 100 m above a perfectly *absorbing* ground. A microphone at a height of 1.2 m above the ground is moved from a *horizontal* distance  $r = 0 \text{ m}$  to  $r = 1000 \text{ m}$  from the source, see figure. Note that  $r = 0 \text{ m}$  corresponds to the source being directly above the microphone. Sound absorption due to friction and molecular relaxation can be neglected.



- (a) Calculate the Sound Pressure Level SPL as a function of horizontal distance from  $r = 0$  m to  $r = 1000$  m. Make a plot of the calculated SPL as a function of  $r$ .
- (b) Calculate again SPL versus  $r$  (from  $r = 0$  m to  $r = 1000$  m), but now for a perfectly reflecting ground. No phase shift occurs during reflecting of the sound at the air-ground interface. Plot your calculated SPL values in the same graph as that of (a). You may assume that source height is much greater than microphone height and that source height is much greater than the difference in path length of the direct and bottom-reflected sound.

## Chapter 4 Sound propagation – special situations

### 4.1 Sound propagation through a layer – mass law

In this section we consider the sound transmission through a layer having acoustic properties (i.e.  $\rho$  and  $c$ ) different from that of the medium on both sides of that layer. This is of interest when we want to have an estimate of how much sound is transmitted through e.g. a 2 mm thick aluminium layer (aircraft fuselage) or a 10 cm concrete wall.

We start by approaching the problem in a very general way, i.e. we consider three media all having different acoustic properties as shown in figure 4.1 below. The middle layer has a thickness  $h_2$  and acoustic properties  $\rho_2$  and  $c_2$ . On both sides of the layer there are half-infinite spaces with acoustic properties  $\rho_1$  and  $c_1$  and  $\rho_3$  and  $c_3$ , respectively. The three media are infinitely long in the horizontal direction and the direction perpendicular to the plane of drawing.

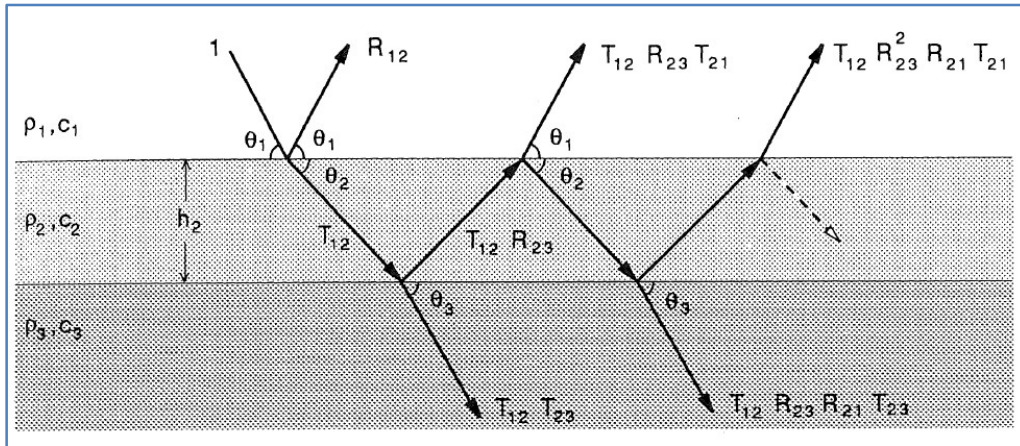


Figure 4.1: Reflection and refraction of a sound ray in a three-layer system. The layers have different acoustic properties and the incoming ray is in medium 1.

A plane harmonic wave in medium 1 with amplitude 1 impinges on the second medium at a grazing angle of  $\theta_1$ . This wave is reflected at an angle  $\theta_1$  and transmitted at an angle  $\theta_2$ . The relation between the two angles is determined by Snell's law. The transmitted wave is again reflected and transmitted at the interface between medium 2 and medium 3. But the latter reflected wave is again reflected and transmitted at the interface between medium 2 and medium 1, and so on. This results in an infinite series of waves emerging in medium 1 and also an infinite series of transmitted waves in medium 3. The latter is of interest here. The amplitudes of all plane waves are indicated in the figure. The amplitude reflection coefficients  $R_{12}$ ,  $R_{23}$  and  $R_{21}$  are given by the equations developed in section 3.3. This also holds for the amplitude transmission coefficients  $T_{12}$ ,  $T_{23}$  and  $T_{21}$ .

The total (amplitude) transmission coefficient  $T$  is given by

$$T = T_{12}T_{23}e^{i\phi_2} + T_{12}R_{23}R_{21}T_{23}e^{3i\phi_2} + T_{12}R_{23}^2R_{21}^2T_{23}e^{5i\phi_2} + T_{12}R_{23}^3R_{21}^3T_{23}e^{7i\phi_2} + \dots \quad (4.1)$$

which can be written as

$$T = T_{12}T_{23}e^{i\phi_2} \left( 1 + R_{23}R_{21}e^{2i\phi_2} + R_{23}^2R_{21}^2e^{4i\phi_2} + R_{23}^3R_{21}^3e^{6i\phi_2} + \dots \right). \quad (4.2)$$

Here  $\phi_2$  is the phase delay between two subsequent transmitted rays (due to the extra propagation in medium 2). That part of this equation in parentheses is a geometric series, hence  $T$  is given by

$$T = \frac{T_{12}T_{23}e^{i\phi_2}}{1 - R_{23}R_{21}e^{2i\phi_2}}. \quad (4.3)$$

Using  $R_{21} = -R_{12}$  we have

$$T = \frac{T_{12}T_{23}e^{i\phi_2}}{1 + R_{12}R_{23}e^{2i\phi_2}}. \quad (4.4)$$

Similarly one can derive the total reflection coefficient

$$R = \frac{R_{12} + R_{23}e^{2i\phi_2}}{1 + R_{12}R_{23}e^{2i\phi_2}}. \quad (4.5)$$

We will now derive a formula for the phase delay in terms of the properties of medium 2 and the incoming angle. Consider figure 4.2 below.

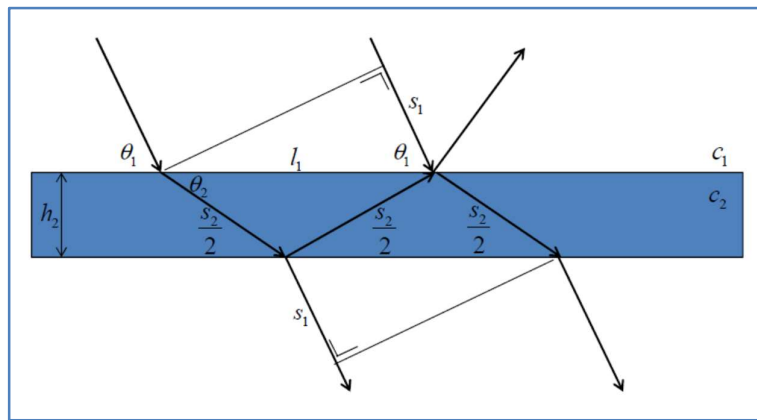


Figure 4.2: Geometry for determining the phase delay between two subsequent transmitted rays due to the extra propagation in medium 2.

In terms of the distance  $s_1$  and  $s_2$ , twice the phase delay is given by

$$2\phi_2 = \frac{2\pi s_2}{\lambda_2} - \frac{2\pi s_1}{\lambda_1} = \frac{\omega s_2}{c_2} - \frac{\omega s_1}{c_1} \quad (4.6)$$

with  $\omega$  the radial frequency of the incoming plane wave considered and  $\lambda_1$  and  $\lambda_2$  the wavelengths in medium 1 and 2, respectively. Distance  $s_2$  is given by

$$s_2 = \frac{2h_2}{\sin \theta_2}. \quad (4.7)$$

Further, distance  $l_1 = s_2 \cos \theta_2$  and distance  $s_1 = l_1 \cos \theta_1$ , from which we obtain

$$s_1 = s_2 \cos \theta_1 \cos \theta_2. \quad (4.8)$$

Substituting this into the equation for  $2\phi_2$  we get

$$2\phi_2 = \frac{\omega}{c_2} \frac{2h_2}{\sin \theta_2} - \frac{\omega}{c_1} \frac{2h_2}{\sin \theta_2} \cos \theta_2 \frac{c_1}{c_2} \cos \theta_2 \quad (4.9)$$

which can be written as

$$2\phi_2 = \frac{\omega}{c_2} \frac{2h_2}{\sin \theta_2} (1 - \cos^2 \theta_2) = \frac{\omega}{c_2} \frac{2h_2}{\sin \theta_2} \sin^2 \theta_2. \quad (4.10)$$

Hence,

$$\phi_2 = \frac{\omega h_2}{c_2} \sin \theta_2 \quad (4.11)$$

i.e. only dependent on  $c_2$  and not on  $\rho_2$ .  $\theta_2$  can be expressed in terms of  $\theta_1$  with Snell's law.

Basically, we have now solved the problem, but in order to obtain a very practical engineering result, let us make a few assumptions and approximations.

First, we only consider normal incidence sound. From section 3.3 we know that

$$R_{12} = \frac{\rho_2 c_2 - \rho_1 c_1}{\rho_2 c_2 + \rho_1 c_1} = -R_{21} \quad (4.12)$$

and

$$T_{12} = \frac{2\rho_2 c_2}{\rho_2 c_2 + \rho_1 c_1}. \quad (4.13)$$

The phase delay is then simply  $\phi_2 = \frac{\omega h_2}{c_2} = k_2 h_2$  with  $k_2$  the wavenumber in medium 2.

Let us also consider transmission through a wall or layer with the same medium on both sides of it, i.e.,  $\rho_3 c_3 = \rho_1 c_1$ . Further, let us also assume the layer to be made of a material for which  $\rho_2 c_2 \gg \rho_1 c_1$ , which is usually the case for materials like concrete, wood or a metal with on both sides air, see table in section 3.3. Using the first order Taylor series approximation

$$(1+x)^{-1} \approx 1-x \quad \text{for } x \ll 1 \quad (4.14)$$

we can write

$$R_{12} = -R_{23} = \frac{\rho_2 c_2 - \rho_1 c_1}{\rho_2 c_2 + \rho_1 c_1} \approx \left(1 - \frac{\rho_1 c_1}{\rho_2 c_2}\right)^2, \quad (4.15)$$

$$T_{12} = \frac{2\rho_2 c_2}{\rho_2 c_2 + \rho_1 c_1} \approx 2 \left(1 - \frac{\rho_1 c_1}{\rho_2 c_2}\right) \quad (4.16)$$

and

$$T_{23} = \frac{2\rho_3 c_3}{\rho_2 c_2 + \rho_3 c_3} = \frac{2\rho_1 c_1}{\rho_2 c_2 + \rho_1 c_1} \approx 2 \frac{\rho_1 c_1}{\rho_2 c_2} \left(1 - \frac{\rho_1 c_1}{\rho_2 c_2}\right). \quad (4.17)$$

Now the total transmission coefficient can be written as

$$T \approx \frac{2(1-x)2x(1-x)e^{i\phi_2}}{1-(1-x)^2(1-x)^2e^{2i\phi_2}} \quad \text{with} \quad x = \frac{\rho_1 c_1}{\rho_2 c_2}. \quad (4.18)$$

Neglecting terms of order  $x^2$  or higher, we can further simplify this to

$$T \approx \frac{4x(1-2x)}{e^{-i\phi_2} - (1-4x)e^{i\phi_2}}. \quad (4.19)$$

Applying Euler's equation  $e^{i\phi} = \cos \phi + i \sin \phi$  we obtain

$$T \approx \frac{4x(1-2x)}{\cos \phi_2 - i \sin \phi_2 - (1-4x)(\cos \phi_2 + i \sin \phi_2)} \quad (4.20)$$

which can be written as

$$T \approx \frac{2(1-2x)}{2 \cos \phi_2 + i \left(2 - \frac{1}{x}\right) \sin \phi_2}. \quad (4.21)$$

A further approximation is obtained by neglecting first order terms in  $x$ :

$$T \approx \frac{2}{2 \cos \phi_2 - \frac{i}{x} \sin \phi_2} = \frac{2}{2 \cos(k_2 h_2) - i \frac{\rho_2 c_2}{\rho_1 c_1} \sin(k_2 h_2)}. \quad (4.22)$$

The absolute value of the total transmission coefficient squared is

$$|T|^2 = \frac{4}{4 \cos^2(k_2 h_2) + \left(\frac{\rho_2 c_2}{\rho_1 c_1}\right)^2 \sin^2(k_2 h_2)} \quad (4.23)$$

and the transmission loss (in dB) or so-called insulation is  $TL = -10 \log(|T|^2)$ .

The last formula for  $|T|^2$  is very accurate as the only approximation made so far is  $\rho_2 c_2 \gg \rho_1 c_1$ , which is always the case in practice. In principle no further approximations are needed.

Now suppose that the layer thickness is small compared to the wavelength, i.e.  $k_2 h_2 \ll 1$ , then

$$\cos^2(k_2 h_2) \approx 1 \quad \text{and} \quad \sin^2(k_2 h_2) \approx (k_2 h_2)^2 \quad (4.24)$$

and hence

$$\frac{1}{|T|^2} \approx 1 + \frac{1}{4} \left( \frac{\rho_2 c_2}{\rho_1 c_1} \right)^2 (k_2 h_2)^2. \quad (4.25)$$

Using  $k_2 c_2 = \omega$  and introducing  $\sigma = \rho_2 h_2$ , the mass of the layer or wall per unit area (in  $\text{kg/m}^2$ ), the transmission loss or insulation in dB becomes

$$TL = 10 \log \left( \frac{1}{|T|^2} \right) = 10 \log \left( 1 + \left( \frac{2\pi f \sigma}{2\rho_1 c_1} \right)^2 \right) \approx 20 \log \left( \frac{2\pi f \sigma}{2\rho_1 c_1} \right). \quad (4.26)$$

This is the so-called ‘mass law’, a quite practical formula for a quick engineering estimation of the insulation of a wall as a function of frequency. Note the  $\rho_1 c_1$  in the formula, i.e. the acoustic properties of the medium outside the plate. The plate properties are contained in  $\sigma$ , the mass of the layer per unit area, hence the name ‘mass law’. TL turns out to be independent of  $c_2$ .

Figure 4.3 shows TL as a function of frequency for an infinite aluminium plate of thickness 1 mm and 10 mm, respectively.

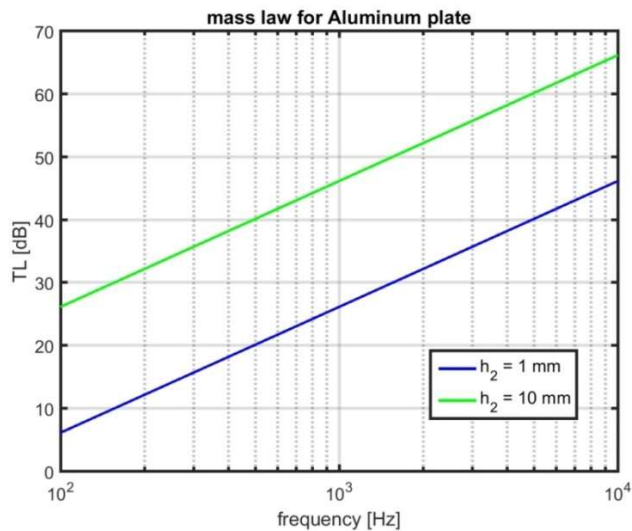


Figure 4.3: Transmission loss as a function of frequency for an infinite aluminium plate of thickness 1 mm and 10 mm (calculated according to the mass law).

The difference between the two curves is  $20\log_{10} = 20$  dB, independent of frequency. Also, a factor of 10 increase in frequency gives a 20 dB increase in insulation.

In figure 4.4 we show TL versus  $f$  for a 10 cm and a 25 cm concrete wall, calculated according to the mass law (equation 4.26) and calculated according to equation 4.23 with the only approximation  $\rho_2 c_2 \gg \rho_1 c_1$ . In this figure the solid lines indicate the mass law approximations, whereas the dashed lines indicate the calculations according to equation 4.23. From this it can be concluded that for 10 cm the mass-law-approximation seems acceptable, which is definitely not the case for 25 cm thickness.

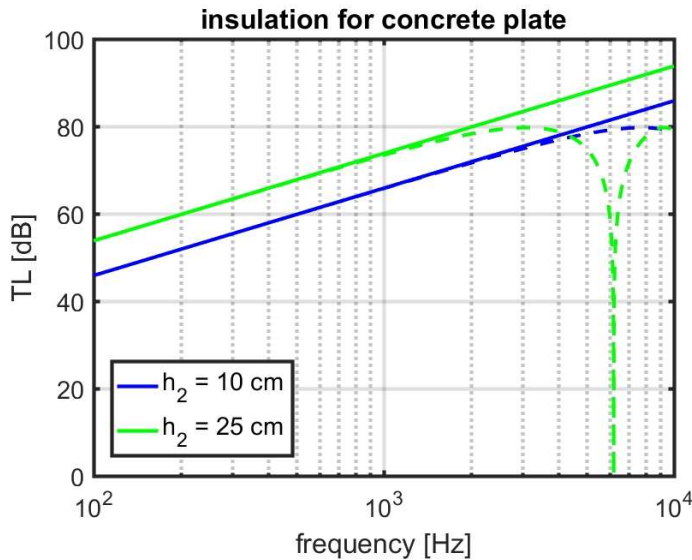


Figure 4.4: Transmission loss calculations for 10 cm and 25 cm concrete, calculated according to the mass law (equation 4.26) and calculated according to the more accurate equation 4.23.

For the aluminium cases of figure 4.3, the mass-law-approximation is valid.

We note (and do not derive here) that the mass law for plane waves making a grazing angle  $\theta_1$  with the wall (see figure 4.1), is given as

$$TL = 10 \log \left( 1 + \left( \frac{2\pi f \sigma \sin \theta_1}{2\rho_i c_i} \right)^2 \right)$$

i.e. the insulation becomes less with decreasing  $\theta_1$ . TL even approaches 0 dB when  $\theta_1 \rightarrow 0^\circ$ .

For a sound field with random grazing angles of incidence (e.g. the diffuse sound field introduced in the next section), the insulation is  $TL_{\text{random}} \approx TL_{90^\circ} - 5 \text{ dB}$  with  $TL_{90^\circ}$  the normal incidence insulation calculated according to the mass law, equation 4.26.

## 4.2 Propagation in enclosures - room acoustics

The sound field in an enclosure, e.g. a room (from lecture rooms to concert halls) or a passenger cabin of an airplane, is governed by reflections from the enclosure's walls. At every interaction of sound with the enclosing walls, partial reflection and absorption occurs.

So, in addition to the direct sound (from source to receiver), there is a significant amount of reflected sound, see figure 4.5.

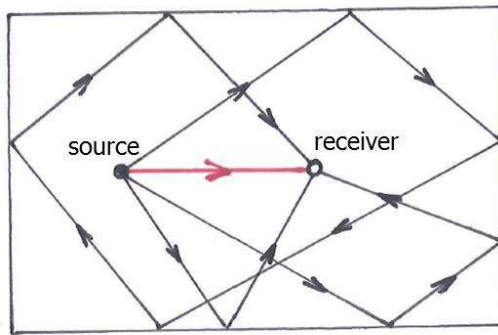


Figure 4.5: Direct sound ray (red arrow) and a few reflected sound rays (black arrows) from the walls of an enclosure.

The sound pressure level of the direct sound is given by (see section 3.2, equation 3.11)

$$SPL_d = PWL - 10.8 - 20 \log r - \alpha r + DI(\theta) \quad (4.27)$$

with  $r$  the distance from the source (with power watt level  $PWL$  and directivity  $DI$ ). Because of the short distances considered in this section we will ignore the absorption term  $\alpha r$  and also assume a non-directional source ( $DI = 0$ ). In general there is a very large number of reflections coming from all directions. Consequently, the reflected sound field, also called reverberant sound field, becomes a 'diffuse field'. For a diffuse sound field, the sound pressure and particle velocity are uncorrelated. Also, the sound pressure and the energy are uniform and unequal to zero throughout the diffuse sound field. (For continuous sound sources, the absorption at the walls prevents the sound pressure level to become infinite).

Figure 4.6 shows the typical sound pressure level in an enclosure as a function of distance  $r$  from the source. A distinction is made between the direct sound pressure level  $SPL_d$  (black line) and the reverberant sound pressure level  $SPL_r$  (blue line). The latter is independent of  $r$ . Also indicated is the total sound pressure level  $SPL_t$  (pink line), which is given by

$$SPL_t = 10 \log \left[ 10^{\frac{SPL_d}{10}} + 10^{\frac{SPL_r}{10}} \right]. \quad (4.28)$$

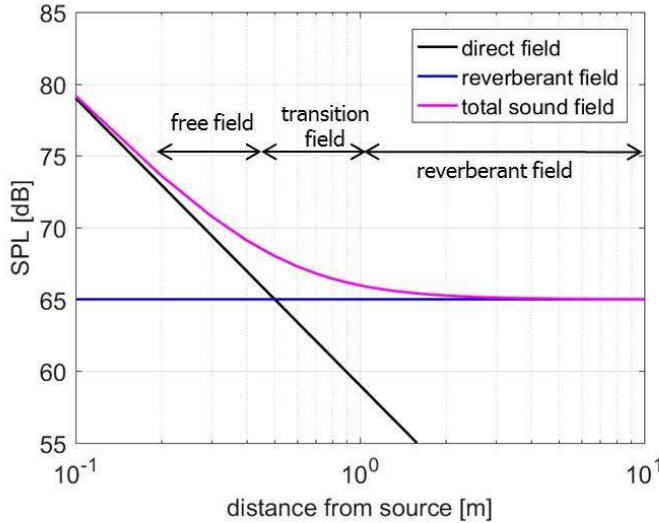


Figure 4.6: Typical sound pressure level versus distance behaviour in an enclosure (pink line). Also indicated is the direct sound pressure level (black line) and the reverberant sound pressure level (blue line), both as a function of distance.

Obviously, a distinction can be made between the free field (where direct sound dominates) and the reverberant field (where diffuse sound dominates). There is a transition field in between where both are important.

In this section we will study the properties of the diffuse sound field according to the theory of W.C. Sabine (1868-1919). Among other things we will derive a formula for  $SPL_r$ .

First, we introduce the concept of energy density (unit  $J/m^3$ ) of a sound field. With the aid of figure 4.7 we determine the relation between intensity  $I$  and energy density  $e$  of a plane wave, i.e. the simplest sound field.

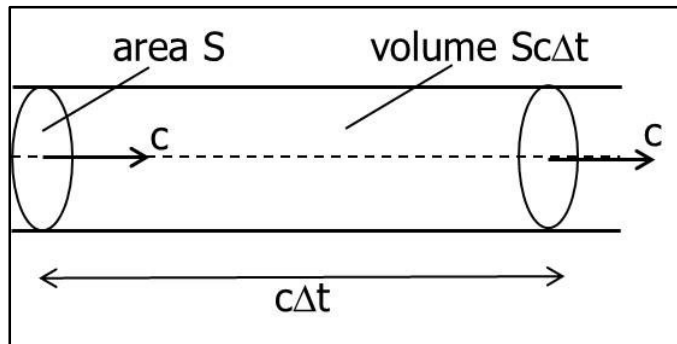


Figure 4.7: Geometry for the derivation of the relation between intensity and energy density for a plane wave.

The acoustic energy  $E$  passing through an area  $S$  perpendicular to the propagation direction of the plane wave (in a time  $\Delta t$ ) is given by

$$E = IS\Delta t . \quad (4.29)$$

This energy is per definition equal to  $E = eV$  with volume  $V$  equal to  $Sc\Delta t$  (see figure 4.7). Hence the relation between intensity and energy density for a plane wave is

$$I = ec \quad (4.30)$$

or

$$e = \frac{I}{c} = \frac{p_e^2}{\rho_\infty c^2}. \quad (4.31)$$

We will now derive the relation between intensity and energy density for a diffuse sound field. Inside the enclosure the sound energy is now distributed in all directions instead of just one direction as in the case of a plane wave. We consider a small part  $dA$  of a wall of the enclosure, see figure 4.8 (left part).

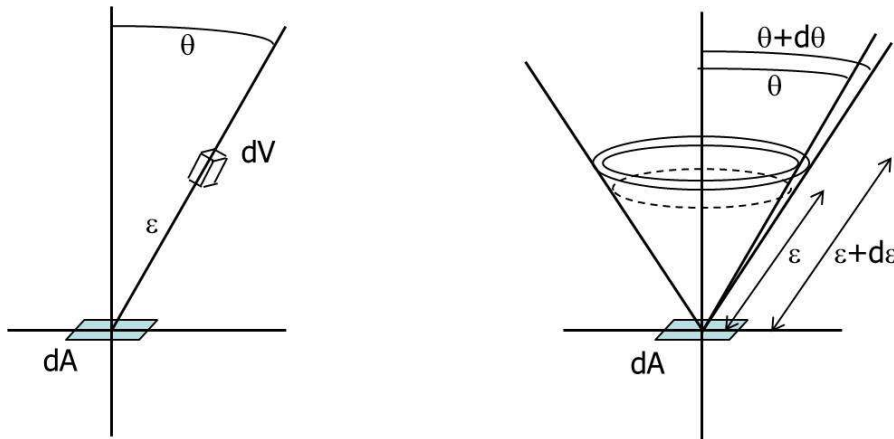


Figure 4.8: Geometry for deriving the relation between intensity and energy density for a diffuse sound field.

We further consider a small volume  $dV$  at a distance  $\varepsilon$  from  $dA$  with  $\theta$  the angle between the normal to  $dA$  and the line connecting  $dV$  and  $dA$ . According to the definition of  $e$ , the sound energy contained in this volume is  $edV$ . The elemental volume  $dV$  radiates sound energy in all directions with velocity  $c$ . At a distance  $\varepsilon$  the energy is spread over an area  $4\pi\varepsilon^2$ . Hence, the energy from  $dV$  reaching surface  $dA$  is given by

$$\frac{edV(\cos\theta dA)}{4\pi\varepsilon^2}. \quad (4.32)$$

We now assume that  $dV$  is part of a hemispherical shell with radius  $\varepsilon$  and thickness  $d\varepsilon$  (see figure 4.8, right part), which has a volume of

$$(2\pi\varepsilon \sin\theta)(\varepsilon d\theta)d\varepsilon = 2\pi\varepsilon^2 \sin\theta d\varepsilon d\theta. \quad (4.33)$$

Hence, all energy impinging on  $dA$  at an angle  $\theta$  (still from a distance  $\varepsilon$ ) is given by

$$\frac{edAd\varepsilon}{2} \sin \theta \cos \theta d\theta \quad (4.34)$$

i.e. independent of  $\varepsilon$ .

To obtain all energy  $\Delta E$  impinging on  $dA$ , we have to integrate over  $\theta$ , i.e.

$$\Delta E = \frac{edAd\varepsilon}{2} \int_0^{\pi/2} \sin \theta \cos \theta d\theta = \frac{edAd\varepsilon}{4}. \quad (4.35)$$

This energy falls on  $dA$  in the time interval  $\Delta t = \frac{d\varepsilon}{c}$ . Hence, the total energy per unit time on  $dA$  is

$$\frac{\Delta E}{\Delta t} = \frac{ec dA}{4}. \quad (4.36)$$

Thus the intensity of a diffuse sound field with energy density  $e$  on the walls of an enclosure is given by

$$I = \frac{\Delta E}{\Delta t dA} = \frac{ec}{4} \quad (4.37)$$

i.e. one quarter of that of a plane unidirectional wave with the same energy density  $e$  that impinges perpendicularly on the wall.

Having a formula for the sound intensity  $I$  on the walls, the total sound power absorbed by the walls can be written as

$$W_a = I \sum_{i \text{ (wall area)}} \alpha_i S_i \quad (4.38)$$

with  $S_i$  the area of wall  $i$  of the enclosure (summation is over all walls of the enclosure) and  $\alpha_i$  the corresponding (dimensionless) absorption coefficient of that wall. We define the so-called 'open window area'  $S_a$  according to

$$S_a = \sum_{i \text{ (wall area)}} \alpha_i S_i \quad (4.39)$$

i.e.  $S_a$  is an equivalent area for the entire enclosure with an absorption coefficient equal to 1 (hence 'open window'). The total sound power absorbed by the walls thus becomes

$$W_a = \frac{ec}{4} S_a. \quad (4.40)$$

We now consider a source with power  $W$  (in Watts) placed in an enclosure. The rate of change of the total sound energy in the enclosure is given by

$$V \frac{de(t)}{dt} = W - \frac{e(t)c}{4} S_a. \quad (4.41)$$

With the initial condition  $e(t=0) = 0$ , the solution of this first-order non-homogeneous differential equation is

$$e(t) = \frac{4W}{cS_a} \left[ 1 - e^{-\frac{S_a c}{4V} t} \right]. \quad (4.42)$$

The corresponding intensity is

$$I(t) = \frac{W}{S_a} \left[ 1 - e^{-\frac{t}{\tau}} \right] \quad (4.43)$$

with time constant

$$\tau = \frac{4V}{S_a c}. \quad (4.44)$$

Figure 4.9 shows this temporal behaviour of the diffuse sound intensity.

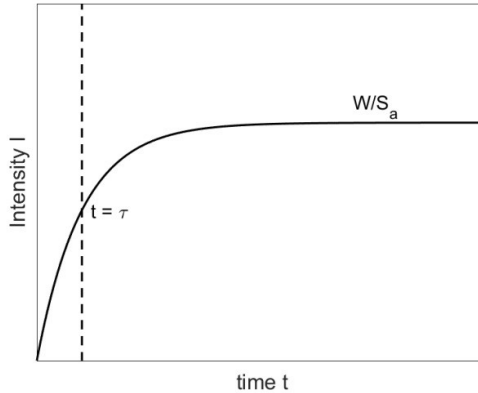


Figure 4.9: Temporal behaviour of the diffuse sound intensity (source switched on at  $t = 0$ ).

Figure 4.10 shows the temporal behaviour of the diffuse sound intensity in an enclosure in the situation that the source is switched on and somewhat later switched off. The blue curve is for the situation that  $S_a$  is large (i.e.  $\tau$  small and  $\frac{W}{S_a}$  low), whereas the pink curve is for the situation that  $S_a$  is made smaller (i.e.  $\tau$  larger and  $\frac{W}{S_a}$  higher).

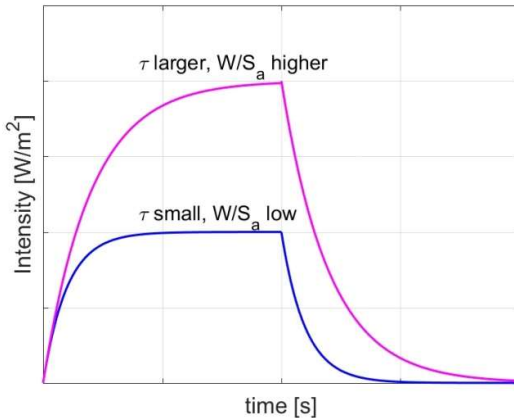


Figure 4.10: A schematic of the temporal behaviour of the diffuse sound intensity in an enclosure in the situation that a source is switched on and somewhat later switched off. The blue curve is for a relatively large value of the open window area, whereas the pink curve is for a smaller value of the open window area.

We will have a closer look at the temporal behaviour of the intensity after the source has been switched off. Then  $W = 0$  and the differential equation for  $e(t)$  becomes

$$V \frac{de}{dt} = -\frac{e(t)c}{4} S_a. \quad (4.45)$$

With initial condition  $e(t=0) = \frac{W}{S_a}$ , the solution is

$$I(t) = \frac{W}{S_a} e^{-\frac{t}{\tau}} \quad (4.46)$$

with  $\tau$  the same as above, i.e.  $\tau = \frac{4V}{S_a c}$ . We define the 'reverberation time'  $T_{60}$  as the time

up to a 60 dB drop in sound pressure level after switching off the sound source, see figure 4.11. This time is given as

$$T_{60} = \tau \ln 10^6 = \frac{4V}{c S_a} \ln 10^6. \quad (4.47)$$

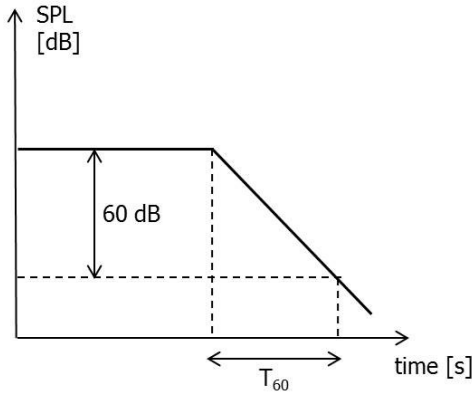


Figure 4.11: Definition of reverberation time  $T_{60}$ , i.e. the time up to a 60 dB drop in sound pressure level after switching off the sound source.

Using  $\ln 10^6 = 13.8$  and  $c = 340 \text{ m/s}$  we obtain

$$T_{60} \approx \frac{V}{6S_a}. \quad (4.48)$$

This simple formula is known as Sabine's law for room (or architectural) acoustics.

As an example we consider a room  $5\text{m} \times 3\text{m} \times 2.6\text{ m}$ , i.e.  $V = 39 \text{ m}^3$ . Assume that the open window area  $S_a$  equals  $10 \text{ m}^2$  (out of the  $71.6 \text{ m}^2$  total area of the walls). At  $t = 0$  we switch on a source of  $W = 10 \mu\text{W}$  ( $\text{PWL} = 70 \text{ dB}$ ) and we switch it off 0.5 seconds later. The left part of figure 4.12 shows the sound intensity as a function of time, whereas the right part of the figure shows the SPL decay from the time the source is switched off. For this situation

$$\frac{W}{S_a} = \frac{10^{-5}}{10} = 10^{-6} \text{ Watt/m}^2 \text{ and the reverberation time is } T_{60} = \frac{V}{6S_a} = \frac{39}{6 \times 10} = 0.65 \text{ s}$$

$$\left( \tau = \frac{4V}{S_a c} = 0.046 \text{ s} \right).$$

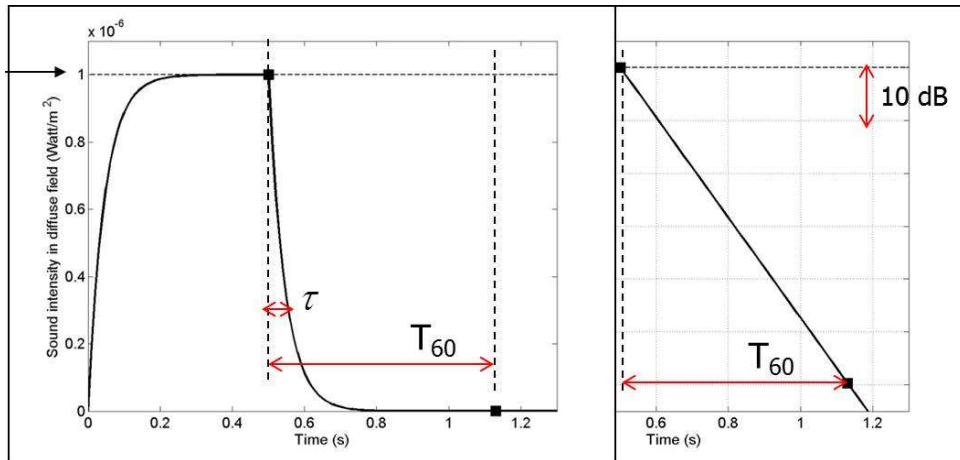


Figure 4.12: Left: sound intensity as a function of time for the situation that a source is switched on at  $t = 0$  and switched off 0.5 seconds later. Right: sound pressure level decay from the time the source is switched off.

Sabine, the founder of architectural acoustics, states the following about the right reverberation times for an enclosure: good concert halls have reverberation times of 2-2.3 seconds (with shorter reverberation times, a music hall seems too "dry" to the listener), while good lecture halls have reverberation times of slightly under 1 second (to maintain good speech intelligibility). Figure 4.13 provides the desired reverberation time ranges for various enclosures, based on Sabine's statement.

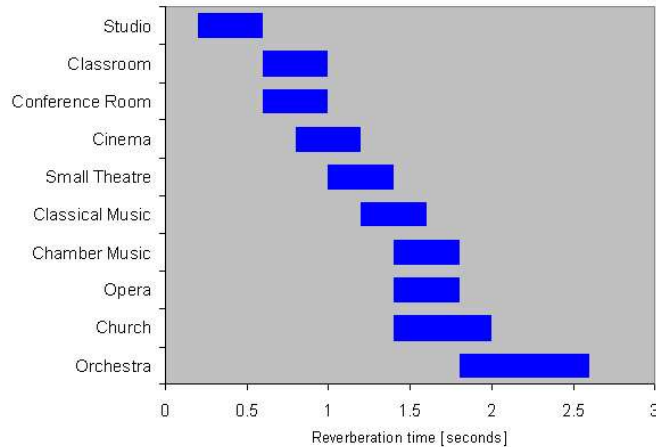


Figure 4.13: Desired reverberation time ranges for various enclosures according to Sabine.

In fact, a certain enclosure can be adapted in such a way that it has the right reverberation time for its purpose, i.e. change  $S_a$  by choosing the proper wall material until, according to Sabine's law (equation 4.48), the right  $T_{60}$  is obtained. To this end, typical values for the absorption coefficient of various wall materials are given in figure 4.14. Note that this dimensionless absorption coefficient is frequency dependent.

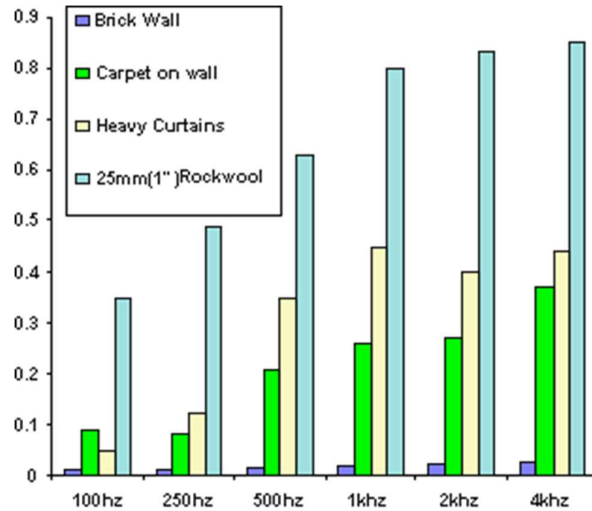


Figure 4.14: Typical values for the dimensionless absorption coefficient of various wall materials.

Figure 4.15 shows two famous enclosures in The Netherlands, i.e. the ‘Concertgebouw’ ( $V = 19,500 \text{ m}^3$ ) and the ‘Tweede Kamer’ ( $V = 4200 \text{ m}^3$ ). The reverberation time of the Concertgebouw is 2.55 s when empty. With all the 2100 seats occupied the reverberation time drops to 2.15 s (due to the extra absorption of clothes). The reverberation time of the Tweede Kamer is 1.05 s. We note that both enclosures have a reverberation time in the right ballpark.



Figure 4.15: Concertgebouw (left) and ‘Tweede Kamer’ (right).

Finally, we return to figure 4.6 and derive a formula for the distance at which the sound pressure level of the direct sound equals that of the reverberant sound. This distance is known as the ‘reverberation distance’ and is a good measure of the distance of the transition field where the free field transitions into the reverberant field.

For a non-directional source the sound pressure level of the direct sound is

$$SPL_d = PWL - 10.8 - 20 \log r = PWL - 10 \log(4\pi) + 0.2 - 20 \log r. \quad (4.49)$$

The sound pressure level of the reverberant field is

$$SPL_r = 10 \log \left( \frac{p_e^2}{p_{e_0}^2} \right) \quad \text{with} \quad p_e^2 = 4I\rho c. \quad (4.50)$$

Hence,

$$SPL_r = 10 \log \left( \frac{4\rho c I}{p_{e_0}^2} \right) = 10 \log(4) + 10 \log \left( \frac{W / S_a}{p_{e_0}^2 / \rho c} \right). \quad (4.51)$$

Using  $10 \log \left( \frac{W_0 \rho c}{p_{e_0}^2} \right) = 0.2 \text{ dB}$  (with  $W_0 = 10^{-12} \text{ dB}$  and  $p_{e_0} = 2 \times 10^{-5} \text{ Pa}$ ) we can write this as

$$SPL_r = 10 \log(4) + PWL + 0.2 - 10 \log(S_a). \quad (4.52)$$

By imposing  $SPL_r = SPL_d$  for  $r = D$  we obtain

$$10 \log(4 / S_a) = -10 \log(4\pi D^2) \quad (4.53)$$

i.e. the reverberation distance  $D$  is given by the simple formula

$$D = \sqrt{\frac{S_a}{16\pi}}. \quad (4.54)$$

Figure 4.16 shows the sound pressure level (direct, reverberant and total) as a function of distance for the previous example (volume =  $39 \text{ m}^3$ , total area of room =  $71.6 \text{ m}^2$ , PWL of source = 70 dB) for three values of the open window area  $S_a$  (being 10, 20 and 40  $\text{m}^2$ ). Note that in all cases the reverberation distance is less than 1 m from the source, i.e. already fairly close to the source the reverberant field is dominant.

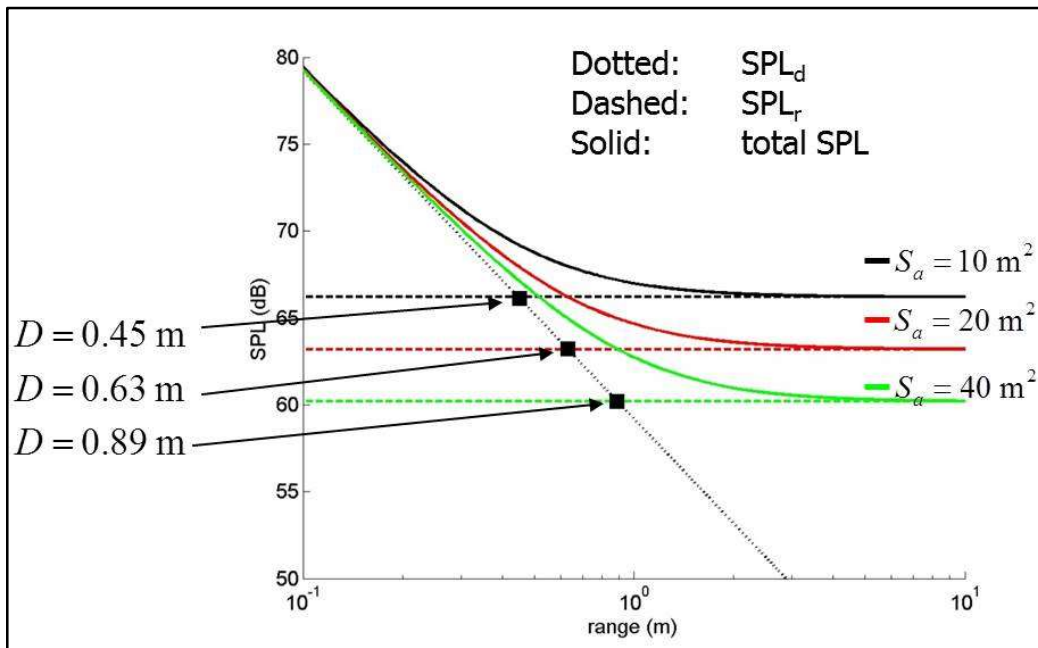
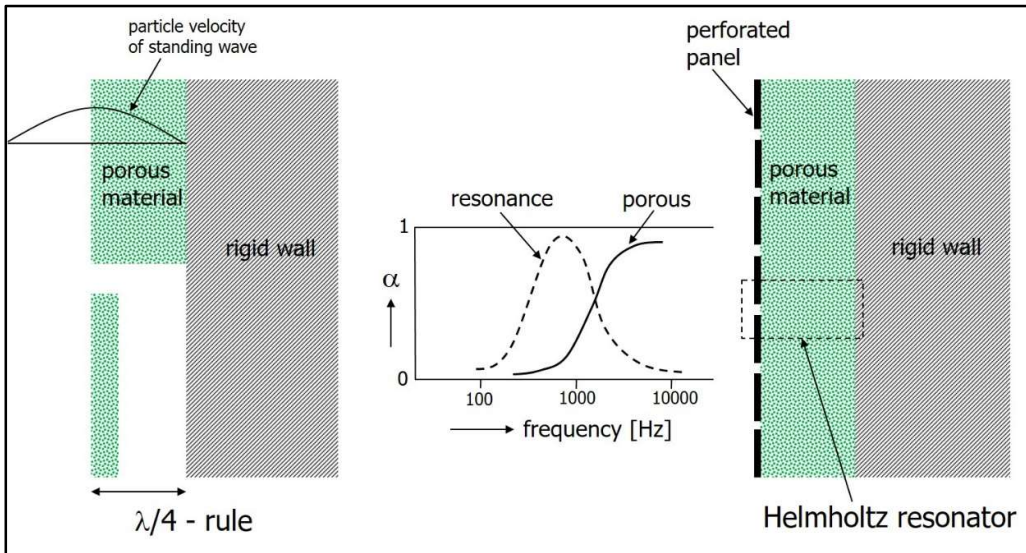


Figure 4.16: Sound pressure level (direct, reverberant and total) as a function of distance (or range) for an enclosure with a volume of  $39 \text{ m}^3$  and for three values of the open window area.

We conclude this section with a brief discussion of sound absorption measures at the walls of an enclosure.

We have learnt that the sound absorption properties of the walls determine both the reverberation time and sound pressure level in an enclosure. Also, we have seen that flat and hard materials are almost perfect reflectors due to the high contrast in acoustic resistance compared to air (see section 3.3). When a considerable sound absorption at the walls is required, usually the walls (and/or ceiling) are covered with a sound absorbing construction. We discuss two different absorbing constructions: the ‘porous absorber’ and the ‘resonant absorber’.



**Figure 4.17:** The ‘porous absorber’ construction (left) and the ‘resonant absorber’ construction (right) on a hard rigid wall. The middle part of the figure shows a typical curve for the frequency behaviour of the absorption coefficient  $\alpha$  for both constructions.

Basically, the first method is accomplished by covering the walls with a porous material, see left part of figure 4.17. The mechanism of sound absorption is that the sound energy is converted into heat by friction, because in such a material the moving air molecules experience frictions at the interior walls of the small and narrow channels in the porous material. Reflections occur at both interfaces, i.e. at the air/porous material interface and at the porous material/hard rigid wall interface. Hence, the incoming sound repeatedly propagates in the absorbing layer, a situation similar to that described in section 4.1. We expect the amount of sound absorption to increase with increasing thickness of the porous layer. Also, it is expected that, for a given layer thickness, high frequency sound is better absorbed than low frequency sound (see also section 3.2). Still, the issue is how thick the layer should be made, since both material costs and space in the enclosure can be limited. Fortunately, there is a simple rule of thumb for the thickness of the layer of absorbing material, given the requirements.

Consider a plane acoustic wave incident on a hard rigid wall (i.e. without the absorbing layer). The plane wave has wavelength  $\lambda$  and impinges perpendicularly on the hard wall. We showed in section 1.4 that, due to the (perfect) reflection, a standing wave results, the particle velocity of which is given by equation 1.29. At the hard wall/air interface the sound pressure is maximum and the corresponding particle velocity is zero. In fact, according to formula 1.29 the particle velocity vanishes at integral multiples of  $\lambda/2$  (i.e. the particle velocity nodes, see also the left part of figure 4.17). In between, the antinodes in velocity, i.e. the positions where particle velocity is maximum, are at  $\lambda/4, 3\lambda/4, 5\lambda/4, \dots$ . Absorption based on friction has the greatest effect on eliminating the standing wave when the porous material is placed at positions where particle velocity is highest. Hence, to absorb

sound with a wavelength  $\lambda$ , a layer of porous material with a thickness of at least  $\lambda/4$  is needed. This is called the ' $\lambda/4$ -rule of thumb'.

The middle part of figure 4.17 shows a typical curve of the dimensionless absorption coefficient  $\alpha$  as a function of frequency. The curve will shift to the left, i.e. towards lower frequencies, for an increasing thickness of the porous layer.

Note: The part of the porous material closest to the wall hardly contributes to the elimination of the wave, since particle velocity there is close to zero. Hence, a layer of porous material of only a few cm thick, placed on an air cavity in such a way that the construction has a total thickness of  $\lambda/4$ , has virtually the same effect as a full  $\lambda/4$ -layer. Such a construction, indicated in the lower left part of figure 4.17, can save costs as less porous material is needed.

Note: Sound absorption in porous materials is a complex phenomenon and depends not only on thickness and frequency, but also on material properties like porosity, flow velocity and the so-called structure factor (i.e. the shape of the pores).

The  $\lambda/4$ -rule shows that, with a construction of a porous material (e.g. mineral wool) with a thickness of about 6 cm, frequencies above 1.5 kHz can be effectively absorbed. Sounds with frequencies higher than about 5 kHz are absorbed anyhow by clothes, curtains and carpets.

Sound absorption for frequencies below 1.5 kHz is not efficient, since, according to the  $\lambda/4$ -rule, the required layer thicknesses of porous material become too large and hence unpractical. A solution to this is to place a perforated panel at a certain distance from the hard rigid wall, see right part of figure 4.17. This will form a large amount of so-called 'Helmholtz resonators', the physics of which is extensively discussed in section 4.3. For now it suffices to state that here each resonator is consisting of the volume of air in each hole of the panel and the adjacent air in the cavity between panel and rigid wall (as indicated by the dashed rectangle in figure 4.17). This system behaves as a mass-spring system, the resonance frequency of which is the frequency to be absorbed. In section 4.3 it is explained that this resonance frequency depends on the geometric parameters of the Helmholtz resonator, i.e. perforation size and cavity thickness. The resonance frequency is however considerably lower than that based on the  $\lambda/4$ -rule for a given cavity thickness. Porous material is usually inserted in the cavity between panel and wall, resulting in a frequency broadening of the resonance. The middle part of the figure shows a typical curve of the dimensionless absorption coefficient  $\alpha$  as a function of frequency for this resonance absorber. Typically, frequencies in the band 0.3 – 1.5 kHz can be absorbed efficiently with this technique. The specific absorption band depends of course on the geometric parameters of the perforated panel, the cavity thickness and the porous material properties.

Note: The same technique of resonance sound absorption is used in turbofan engines. In this aerospace engineering application, the technique is called 'acoustic lining', see section 4.3.

Note: The absorption coefficient  $\alpha$  of both techniques described here depends on the grazing angle of incidence of the sound wave. In general,  $\alpha$  increases with decreasing grazing angle.

Note: The coefficient  $\alpha$  of a sound absorbing construction is often measured in a so-called reverberation chamber, a room designed to create a diffuse sound field. Reverberation chambers are quite large and have hard walls, hence the reverberation time in the chamber is high. Now,  $\alpha$  is determined by measuring the reverberation time in the chamber without and with a sample of the sound absorbing construction under investigation. From the difference in reverberation time one determines the absorption increase, and hence  $\alpha$ , using Sabine's formula (equation 4.48). Using broadband noise as a sound source, this can be done for various frequency bands.

Note: For enclosures that are relatively small and for which the wall absorption coefficients are high (i.e. approaching the range 0.5 - 1), the reverberation time according to Sabine (equation 4.48) is not valid. Then the formula due to Eyring is more appropriate, which reads

$$T_{60} = -\frac{V}{6S \ln(1-\bar{\alpha})}$$

with  $\bar{\alpha} = \frac{S_a}{S}$  the average absorption coefficient.  $S_a = \sum_i \alpha_i S_i$  is the open window area (equation 4.39) and  $S = \sum_i S_i$  is the real total wall area. It is easily verified that Eyring's formula reduces to Sabine's formula when  $\bar{\alpha}$  is small, i.e. close to 0, as then  $-\ln(1-\bar{\alpha}) \approx \bar{\alpha}$ .

#### 4.3 Propagation in ducts – acoustics filters

The acoustic filters discussed here have the purpose to reduce the noise level in a duct, e.g. an engine exhaust or a ventilation system, or to reduce the noise radiating from the end of a duct. Abrupt changes in the cross-sectional area of a duct can significantly reduce the noise level in the duct, since part of the sound incident on the junction is reflected back to the source. This is called 'reactive attenuation'. In the following we assume that the wavelength is large compared to the duct diameter. Hence, we may assume 1D propagation in the duct (as described by plane waves).

First, we consider a single change in cross-sectional area, see figure 4.18.

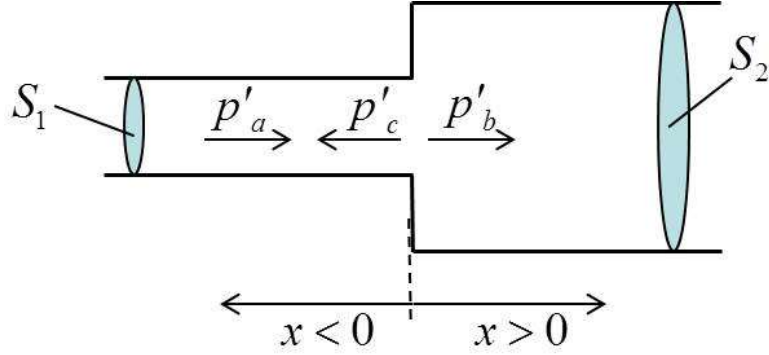


Figure 4.18: A duct with a single change in cross-sectional area.

In the duct with cross-sectional area  $S_1$  (for  $x < 0$ ) there is a harmonic plane wave  $p'_a$  propagating in the positive  $x$ -direction. At the junction at  $x = 0$  the wave is partly reflected and partly transmitted. The three harmonic plane waves are given by

$$\begin{aligned} p'_a &= Ae^{i\omega(t-x/c)} \\ p'_b &= Be^{i\omega(t-x/c)} \\ p'_c &= Ce^{i\omega(t+x/c)} \end{aligned} \quad (4.55)$$

with  $\omega$  the radial frequency and  $c$  the sound speed (in air). Note that the reflected wave  $p'_c$  is propagating in the negative  $x$ -direction. At  $x = 0$  we impose the boundary condition of continuity of pressure, i.e.  $p'_a + p'_c = p'_b$  (with  $p'_b$  the transmitted wave). This immediately gives the following relation between the amplitudes of the plane waves:

$$A + C = B. \quad (4.56)$$

A second boundary condition is provided by the necessary continuity of mass flow (in kg/s) at the junction, i.e.

$$\rho S_1 (v_a + v_c) = \rho S_2 v_b \quad (4.57)$$

with  $\rho$  the static density of the medium in the duct (air) and  $S_2 (> S_1)$  the cross-sectional area of the duct for  $x > 0$ .  $v_a, v_b$  and  $v_c$  are the particle velocities corresponding to the incoming, transmitted and reflected wave, respectively. Using  $v = \pm \frac{p'}{\rho c}$  for plane waves, continuity of mass flow at  $x = 0$  becomes

$$\rho S_1 \left( \frac{Ae^{i\omega t}}{\rho c} - \frac{Ce^{i\omega t}}{\rho c} \right) = \rho S_2 \frac{Be^{i\omega t}}{\rho c} \quad (4.58)$$

which simplifies to

$$S_1 (A - C) = S_2 B. \quad (4.59)$$

The two equations in  $A$ ,  $B$  and  $C$  can easily be solved for the relative amplitude of the transmitted wave (the ‘transmission factor’  $T = \frac{B}{A}$ ) and the relative amplitude of the reflected wave (the ‘reflection factor’  $R = \frac{C}{A}$ ). We obtain

$$T = \frac{B}{A} = \frac{2S_1}{S_1 + S_2} \quad (4.60)$$

and

$$R = \frac{C}{A} = \frac{S_1 - S_2}{S_1 + S_2}. \quad (4.61)$$

Note that  $1 + R = T$  (same as in section 3.3).

For this filter the attenuation, i.e. transmission loss, is determined by the ratio of the power  $W_a$  (in Watt) of the incoming wave and the power  $W_b$  of the transmitted wave. The attenuation in power watt level  $\Delta\text{PWL}$  (in dB) is hence given by

$$\Delta\text{PWL} = 10 \log \left[ \frac{W_a}{W_b} \right] = 10 \log \left[ \frac{p_{e,a}^2 S_1}{\rho c} \frac{\rho c}{p_{e,b}^2 S_2} \right] \quad (4.62)$$

which reduces to

$$\Delta\text{PWL} = 10 \log \left[ \frac{A^2 S_1}{B^2 S_2} \right] = 10 \log \left[ \frac{\left( 1 + \frac{S_2}{S_1} \right)^2}{4 \frac{S_2}{S_1}} \right] \quad (4.63)$$

i.e. fully determined by the ratio  $\frac{S_2}{S_1}$  of the cross-sectional areas. As an example,  $\Delta\text{PWL} = 5$

dB for  $\frac{S_2}{S_1} = 10$ . It is easily shown that the attenuation is independent of the wave direction.

We further note that we can verify that energy is conserved, i.e.  $S_1 (A^2 - C^2) = S_2 B^2$ .

We now consider a double change in cross-sectional area as shown in figure 4.19. The intake duct ( $x < 0$ ) and outflow duct ( $x > \ell$ ) have cross-sectional area  $S_1$  and the expansion chamber ( $0 < x < \ell$ ) has a cross-sectional area  $S_2$ . We still assume that the wavelength is large compared to both duct diameters.

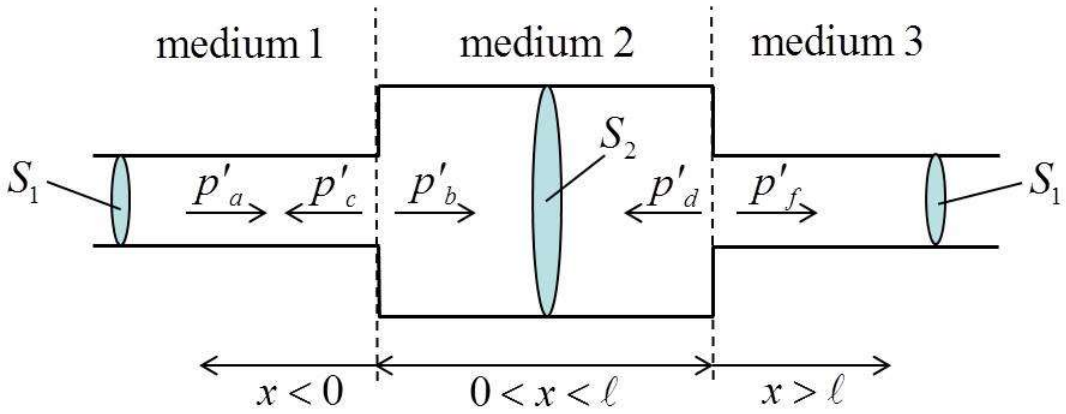


Figure 4.19: A duct with a double change in cross-sectional area.

This is a good model for a so-called ‘muffler’ or single expansion chamber as applied in engine exhausts, see figure 4.20.



Figure 4.20: Examples of single expansion chambers in practice.

Mathematically, this problem is very similar to that treated in section 4.1. The incoming plane harmonic wave at the intake is  $p'_a$  and at both junctions there are reflected and transmitted waves, i.e.  $p'_c$  and  $p'_b$  at the junction at  $x=0$  and  $p'_d$  and  $p'_f$  at the junction at  $x=\ell$ . Actually, these are the result of an infinite number of reflections and transmissions at both junctions. The reflection factor for the junction at  $x=0$  (going from ‘medium 1’ to ‘medium 2’) is given by

$$R_{12} = \frac{C}{A} = \frac{S_1 - S_2}{S_1 + S_2} \quad (4.64)$$

whereas the reflection factor for the junction at  $x=\ell$  (going from ‘medium 2’ to ‘medium 3’) is given by

$$R_{23} = \frac{D}{B} = \frac{S_2 - S_1}{S_1 + S_2}. \quad (4.65)$$

The transmission factors for the junction at  $x=0$  and that at  $x=\ell$  are

$$T_{12} = \frac{B}{A} = \frac{2S_1}{S_1 + S_2} \quad (4.66)$$

and

$$T_{23} = \frac{F}{B} = \frac{2S_2}{S_1 + S_2} \quad (4.67)$$

respectively. We can use the result of section 4.1 (equation 4.4), i.e. the total transmission factor is given by

$$T = \frac{F}{A} = \frac{T_{12} T_{23} e^{i\phi_2}}{1 + R_{12} R_{23} e^{2i\phi_2}} \quad (4.68)$$

with the phase delay (for normal incidence) given as  $\phi_2 = k_2 h_2 = \frac{\omega\ell}{c}$ . After some algebraic manipulation (and using Euler's equation  $e^{ix} = \cos x + i \sin x$ ) we obtain

$$\frac{1}{T} = \frac{A}{F} = \cos\left(\frac{\omega\ell}{c}\right) - i \frac{1}{2} \left[ \frac{S_1}{S_2} + \frac{S_2}{S_1} \right] \sin\left(\frac{\omega\ell}{c}\right). \quad (4.69)$$

Hence, transmission loss TL (in dB) is

$$TL = 10 \log \left| \frac{A}{F} \right|^2 = 10 \log \left[ \cos^2\left(\frac{\omega\ell}{c}\right) + \frac{1}{4} \left[ \frac{S_1}{S_2} + \frac{S_2}{S_1} \right]^2 \sin^2\left(\frac{\omega\ell}{c}\right) \right] \quad (4.70)$$

which can be simplified to

$$TL = 10 \log \left[ 1 + \frac{1}{4} \left[ \frac{S_1}{S_2} - \frac{S_2}{S_1} \right]^2 \sin^2\left(\frac{\omega\ell}{c}\right) \right]. \quad (4.71)$$

Note that TL is maximal and equal to  $TL_{max} = 10 \log \left[ 1 + \frac{1}{4} \left( \frac{S_1}{S_2} - \frac{S_2}{S_1} \right)^2 \right]$  at the frequencies  $f = \frac{c}{4\ell}, \frac{3c}{4\ell}, \frac{5c}{4\ell}, \dots$ . TL = 0 dB (i.e. no attenuation) for the frequencies  $f = 0, \frac{c}{2\ell}, \frac{2c}{2\ell}, \frac{3c}{2\ell}, \dots$ .

Figure 4.21 shows TL as a function of frequency  $f = \frac{\omega}{2\pi}$  for  $\frac{S_2}{S_1} = 10$  and  $\ell = L_2 = 0.5$  m (blue solid and dashed line).

At the beginning of this section we stated that we assume 1D propagation in the duct, i.e. wavelength is large compared to duct diameter. The dashed line therefore indicates the

frequency region where the wavelength becomes smaller than 5 times the diameter of the intake duct (which was taken to be 10 cm for these calculations). With this somewhat arbitrary boundary, the solid line in figure 4.21 is indicating the region of validity of the model. The value of TL for the corresponding single change in cross-sectional area (i.e. 5 dB) is also indicated for comparison (horizontal black line).

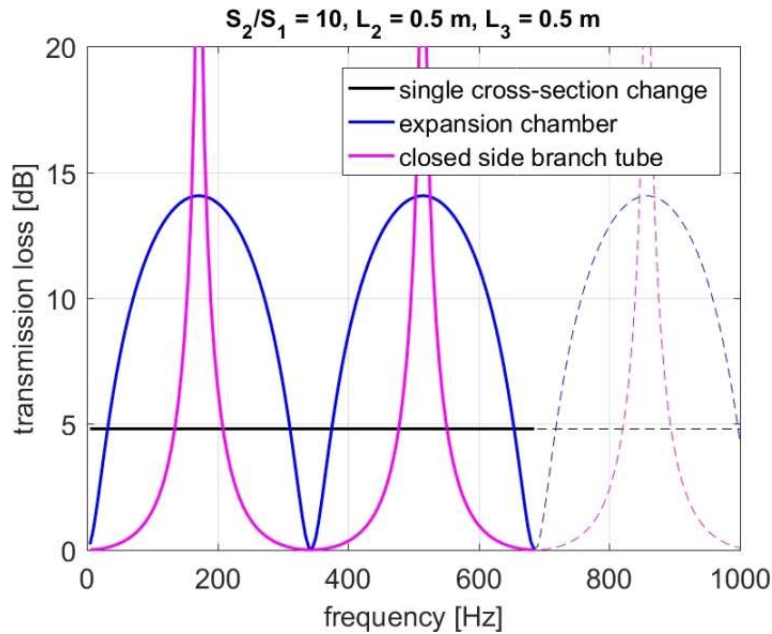


Figure 4.21: Calculated transmission loss as a function of frequency for a duct with a single change in cross-sectional area (black line), a duct with a double change in cross-sectional area (blue line) and a duct with a closed side branch tube (pink line). The duct parameters are given in the title of the graph.

An acoustic filter similar to the muffler is the ‘closed side branch tube’ shown in figure 4.22.

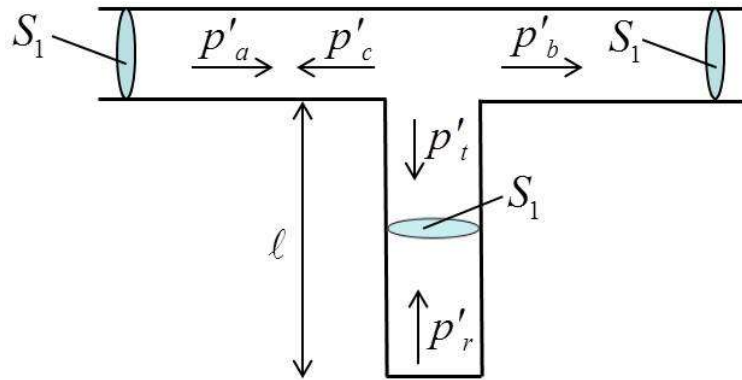


Figure 4.22: A duct with a closed side branch tube.

The side branch tube has a length  $\ell$  and the cross-sectional area is everywhere the same (and equal to  $S_1$ ). The formula for transmission loss is now given by (without derivation)

$$TL = 10 \log \left| \frac{A}{B} \right|^2 = 10 \log \left[ 1 + \frac{1}{4} \tan^2 \left( \frac{\omega \ell}{c} \right) \right]. \quad (4.72)$$

As for the single expansion chamber, the transmission loss is maximal at the frequencies  $f = \frac{c}{4\ell}, \frac{3c}{4\ell}, \frac{5c}{4\ell}, \dots$ . However, now  $TL_{\max} = \infty$ , i.e. the incident sound wave is completely cancelled at these frequencies. Figure 4.21 shows  $TL$  as a function of frequency for  $\ell = L_3 = 0.5$  m (pink line). Also, the frequencies where no attenuation occurs are the same as those for the single expansion chamber.

Finally, we discuss the so-called Helmholtz resonator, an acoustic filter based on resonance. It is a container of air with a small opening (called neck). We assume that all dimensions of the resonator are small compared to the wavelength. Because of the ‘springiness’ of the air in the container, a volume of air in and near the neck can vibrate on it, see figure 4.23 (middle part). Hence, such a system behaves as a mass-spring system, see right part of figure 4.23.

A well-known example of a Helmholtz resonator is an empty bottle: the air inside the bottle vibrates when you blow across the top and a fairly loud tonal sound is produced (figure 4.23, left part).

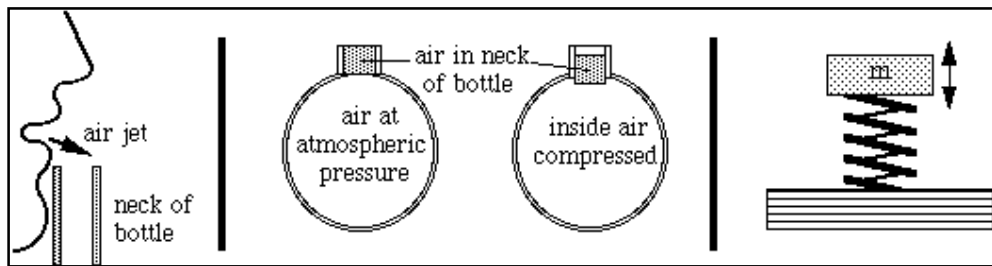


Figure 4.23: The Helmholtz resonator at work.

Figure 4.24 (top picture) shows the sound spectrum measured when we blow across the top of an empty beer bottle. A strong peak at a frequency of around 200 Hz is observed. Reducing the gas volume in the beer bottle (by leaving it half full) causes a shift to a higher frequency (bottom picture of figure 4.24). This will be explained further on.

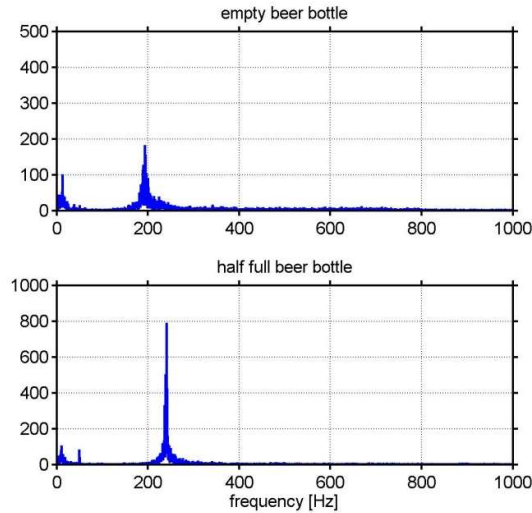


Figure 4.24: Sound spectrum measured when we blow across the top of an empty beer bottle (upper figure) and a half full beer bottle (lower figure).

We have already seen an important application of Helmholtz resonators in the previous section. The applications of Helmholtz resonators are however numerous. For instance, the air in the body of a guitar acts like a Helmholtz resonator (actually Helmholtz resonance plays a role in all string instruments). Here we are interested in the Helmholtz resonator as an acoustic filter that can attenuate sound in a duct. Therefore, we consider the geometry shown in figure 4.25.

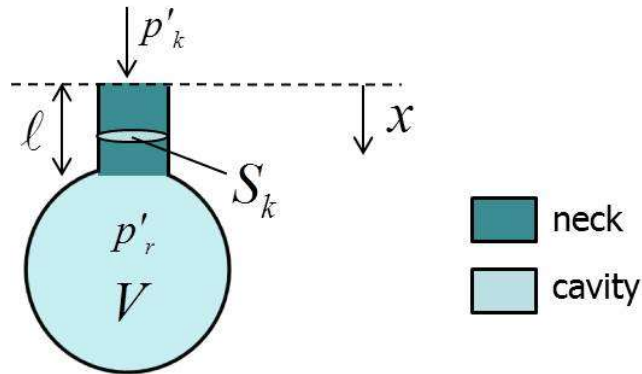


Figure 4.25: Geometry of the Helmholtz resonator.

Assume the sound field outside the resonator is  $p'_k = K e^{i\omega t}$ . This field forces the air in the neck to move back and forth. The resulting density variation in the cavity is

$$\rho'_r = \frac{\rho_\infty S_k x}{V} \quad (4.73)$$

with  $V$  the volume of the cavity,  $S_k$  the cross-sectional area of the neck and  $x$  the position of the air mass in the neck (as indicated in the figure). Using Poisson's relation,  $p'_r = c^2 \rho'_r$ , we obtain for the sound field in the cavity

$$p'_r = \frac{\rho_\infty c^2 S_k x}{V}. \quad (4.74)$$

The total force acting on the air mass in the neck is

$$(p'_k - p'_r) S_k = K S_k e^{i\omega t} - \frac{\rho_\infty c^2 S_k^2 x}{V}. \quad (4.75)$$

Hence, according to Newton's second law, the equation of motion for the mass of the air in the neck is

$$\rho_\infty \ell S_k \frac{d^2 x}{dt^2} + \frac{\rho_\infty c^2 S_k^2}{V} x = K S_k e^{i\omega t} \quad (4.76)$$

with  $\ell$  the length of the neck.

We compare this differential equation with that of (undamped) forced oscillation, i.e.

$$m \frac{d^2 x}{dt^2} + C x = F_0 e^{i\omega t} \quad (4.77)$$

with  $m$  the mass and  $C$  the spring constant. The solution of this equation is

$$x = x_0 e^{i\omega t} \quad \text{with} \quad x_0 = \frac{F_0}{m(\omega_0^2 - \omega^2)} \quad (4.78)$$

where  $\omega_0$  is the resonance frequency given by  $\omega_0 = \sqrt{\frac{C}{m}}$ . Then, in the case of the Helmholtz resonator, we have the solution

$$x = \frac{K e^{i\omega t}}{\rho_\infty \left( \frac{c^2 S_k}{V} - \ell \omega^2 \right)} \quad (4.79)$$

and resonance frequency

$$\omega_0 = c \sqrt{\frac{S_k}{\ell V}} \quad \text{or} \quad f_0 = \frac{c}{2\pi} \sqrt{\frac{S_k}{\ell V}}. \quad (4.80)$$

We note that  $\omega_0 \propto \frac{1}{\sqrt{V}}$ , which explains the higher resonance frequency of a half full beer bottle compared to that of an empty beer bottle (see figure 4.24).

The mass flow  $m_k = \rho_\infty S_k v_k = \rho_\infty S_k \frac{dx}{dt}$  in the neck is

$$m_k = \frac{i\omega S_k K e^{i\omega t}}{\frac{c^2 S_k}{V} - \ell \omega^2}. \quad (4.81)$$

At resonance  $\omega = \omega_0$ ,  $m_k$  (and hence  $p'_r$ ) becomes infinite, which of course is physically impossible. Although there is always some friction,  $m_k$  and  $p'_r$  are still very large at resonance.

We now study the effect of a Helmholtz resonator in a side branch of a duct, see figure 4.26.

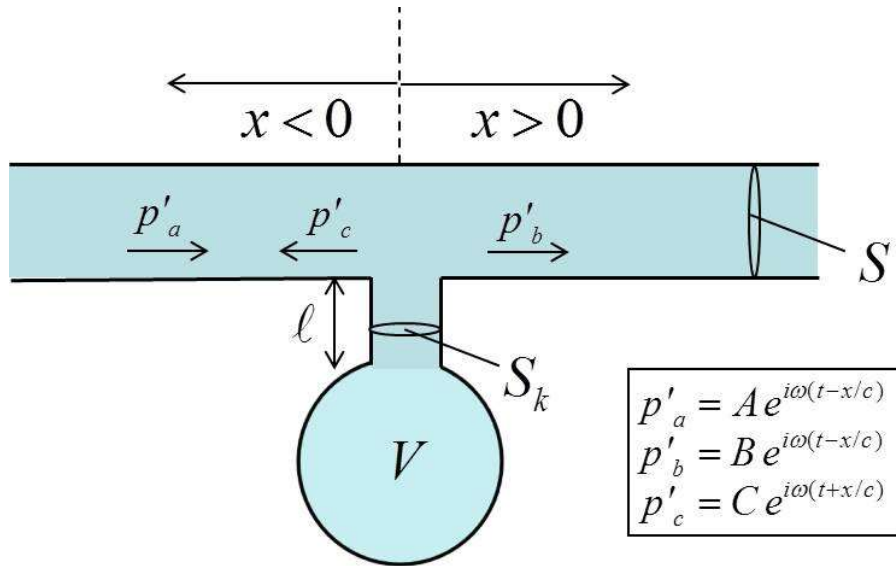


Figure 4.26: The Helmholtz resonator in a side branch of a duct.

We consider an incoming harmonic plane wave  $p'_a$  with amplitude  $A$  (for  $x < 0$ ). The Helmholtz resonator at  $x = 0$  gives rise to a reflected wave  $p'_c$  with amplitude  $C$  (for  $x < 0$ ) and a transmitted wave  $p'_b$  with amplitude  $B$  ( $x > 0$ ). Continuity of pressure at  $x = 0$  gives

$$A + C = B. \quad (4.82)$$

Continuity of mass flow at  $x = 0$  gives

$$\rho_\infty S (v_a + v_c) = m_k + \rho_\infty S v_b \quad (4.83)$$

with velocity  $v = \frac{p'}{\rho_\infty c}$ ,  $S$  the cross-sectional area of the duct and  $m_k$  as above with  $K = B$

(equation 4.81). Hence we obtain

$$\frac{S}{c}(A - C)e^{i\omega t} = \frac{i\omega S_k B e^{i\omega t}}{\frac{c^2 S_k}{V} - \ell \omega^2} + \frac{S}{c} B e^{i\omega t}. \quad (4.84)$$

Substituting  $C = B - A$  in this equation yields

$$\frac{B}{A} = \frac{1}{1 + \frac{1}{2S} \left[ \frac{c}{i\omega V} + \frac{i\omega \ell}{c S_k} \right]^{-1}}. \quad (4.85)$$

The corresponding transmission loss is

$$TL = 10 \log \left( \left| \frac{A}{B} \right|^2 \right) = 10 \log \left( 1 + \frac{1}{4S^2} \frac{1}{\left[ \frac{c}{\omega V} - \frac{\omega \ell}{c S_k} \right]^2} \right). \quad (4.86)$$

Using  $\omega_0^2 = \frac{c^2 S_k}{\ell V}$  we can rewrite the transmission loss as

$$TL = 10 \log \left( 1 + \frac{\frac{VS_k}{4S^2 \ell}}{\left[ \frac{\omega_0}{\omega} - \frac{\omega}{\omega_0} \right]^2} \right). \quad (4.87)$$

So far we have assumed the Helmholtz resonator to be frictionless. Then at resonance  $\omega = \omega_0$ ,  $TL = \infty$ , i.e. the incident sound wave is completely cancelled. Note that the transmission loss function for a Helmholtz resonator in a side branch of the duct is *not periodic* as in the case of the previous two acoustic filters.

An important application of Helmholtz resonators in aerospace engineering is ‘acoustic lining’, which is a special treatment of the duct of a turbofan engine. The acoustic lining material is a perforated or porous sheet covering a series of small cavities, each of which acts as a Helmholtz resonator. The turbofan engine duct is covered by these sheets as shown in figure 4.27. The noise at specific frequencies of the fan can be considerably reduced, provided the dimensions of the Helmholtz resonators are carefully chosen.

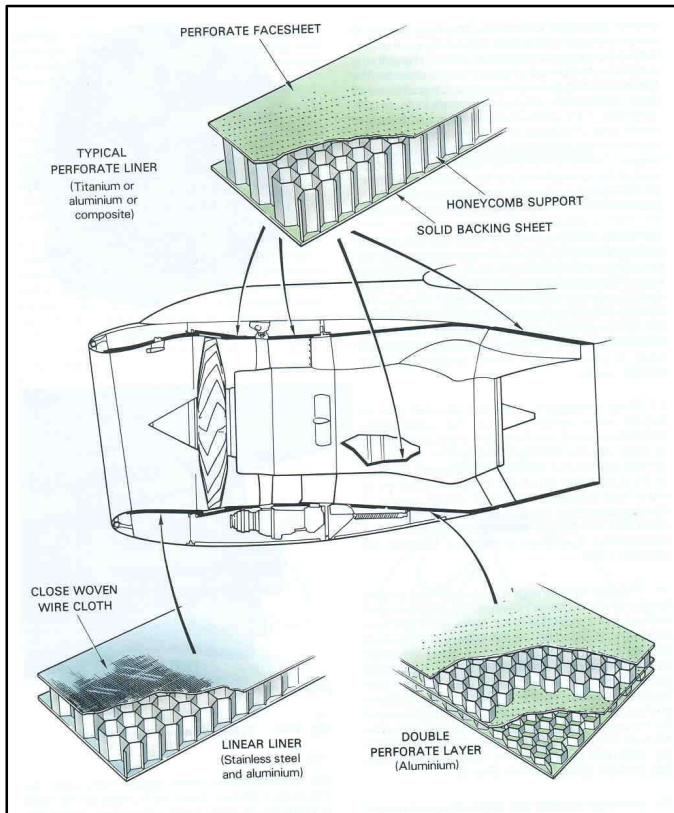


Figure 4.27: Acoustic lining of the duct of a turbofan engine.

#### 4.4 Noise barriers

A noise barrier or noise screen is a solid structure, positioned between source and receiver, which blocks the direct sound path. It can provide a significant reduction in sound pressure level at the receiver position, although in general the sound is not eliminated completely due to diffraction. Still, there can be spaces, called shadow zones, where virtually no sound travels. In this section we only consider thin walls as noise barriers and assume that no sound can pass through the wall.

The acoustic efficiency of a noise barrier (in dB units) is given by

$$\Delta L = L_0 - L_b \quad (4.88)$$

with  $L_0$  and  $L_b$  the SPL values without and with the barrier, respectively. Hence,  $\Delta L$  can be considered as an excess attenuation due to the barrier. Usually, there are three diffracted paths the sound can follow when a barrier is installed between source (S) and receiver (R), see figure 4.28 (sound paths indicated by green lines).

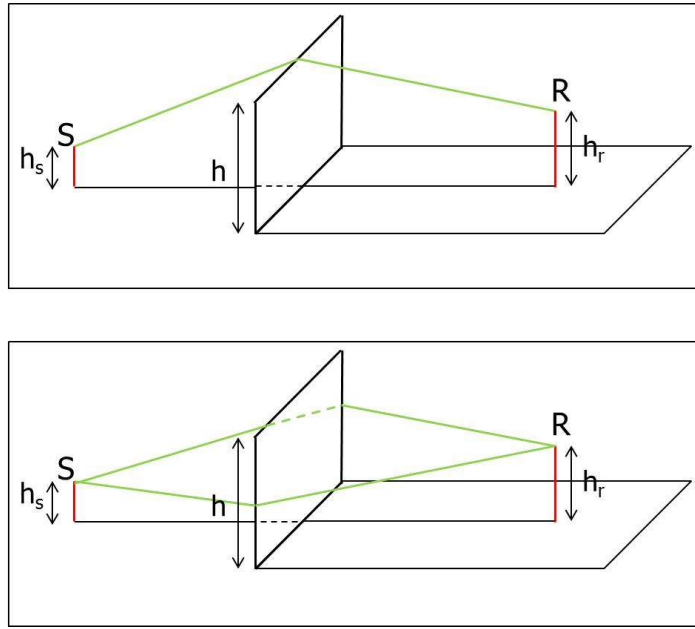


Figure 4.28: Sound path diffracted at the upper edge of a barrier (upper figure) and the sound paths diffracted at the sides of a barrier (lower figure). The diffracted sound paths are indicated by green lines connecting source (S) and receiver (R).

In the upper part of the figure we see the sound path diffracted at the upper edge of the screen. When the barrier is very long this is the only diffracted path that needs to be considered. Diffraction at the sides of the barrier (see lower part of figure 4.28) becomes important when the distance between the source and the screen edge is less than approximately 5 times the effective height. The effective height  $h_{\text{eff}}$  of a noise screen is the length of the upper part of the screen that is above the line of sight connecting source (S) and receiver (R). The line of sight coincides with the direct sound path, see figure 4.29.

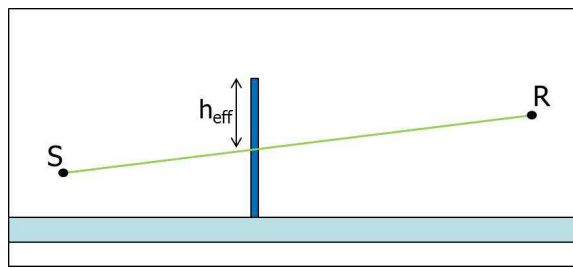


Figure 4.29: Effective height of a noise barrier. The green line connecting source (S) and receiver (R) is the direct sound path, which coincides with the so-called 'line of sight'.

If we only consider the diffraction at the upper edge of the (infinitely long) screen, the excess attenuation can be approximated by the simple empirical Maekawa formula given as

$$\Delta L = 10 \log(3 + 20N) \quad (4.89)$$

where  $N$  is the so-called Fresnel number defined by

$$N = \frac{2(s_2 - s_1)}{\lambda}. \quad (4.90)$$

Here  $s_2$  and  $s_1$  are the length of the diffracted sound path and direct sound path, respectively, and  $\lambda = \frac{c}{f}$  is the wavelength ( $f$  being the frequency and  $c$  the sound speed).

Hence, the Fresnel number is proportional to the ratio of the difference in length of the two sound paths and the wavelength.

As an example we consider the geometry shown in figure 4.30. The noise screen of height  $h$  is positioned at  $x = 0$ . A point source is at the position  $(x, y) = (-d_s, h_s)$  and the receiver is at position  $(x, y) = (d_r, h_r)$ .  $d_s, d_r, h_s, h_r$  and  $h$  are all positive numbers.

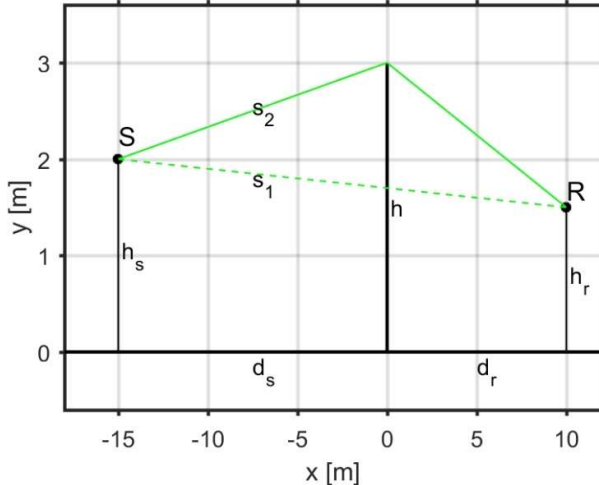


Figure 4.30: Source (S) and receiver (R) position with respect to the noise barrier (of height  $h$ ). The solid green line is the sound path diffracted at the upper edge of the barrier and has length  $s_2$ . The dashed green line is the direct sound path (or line of sight) and has length  $s_1$ .

The length of the direct path is given by

$$s_1 = \sqrt{(d_s + d_r)^2 + (h_s - h_r)^2} \quad (4.91)$$

and the diffracted path is of length

$$s_2 = \sqrt{d_s^2 + (h - h_s)^2} + \sqrt{d_r^2 + (h - h_r)^2}. \quad (4.92)$$

For  $d_s = 15$  m,  $h_s = 2$  m,  $d_r = 10$  m,  $h_r = 1.5$  m and  $h = 3$  m the excess attenuation is calculated as a function of frequency according to equations 4.89 and 4.90, the result of which is depicted in figure 4.31 (blue line).

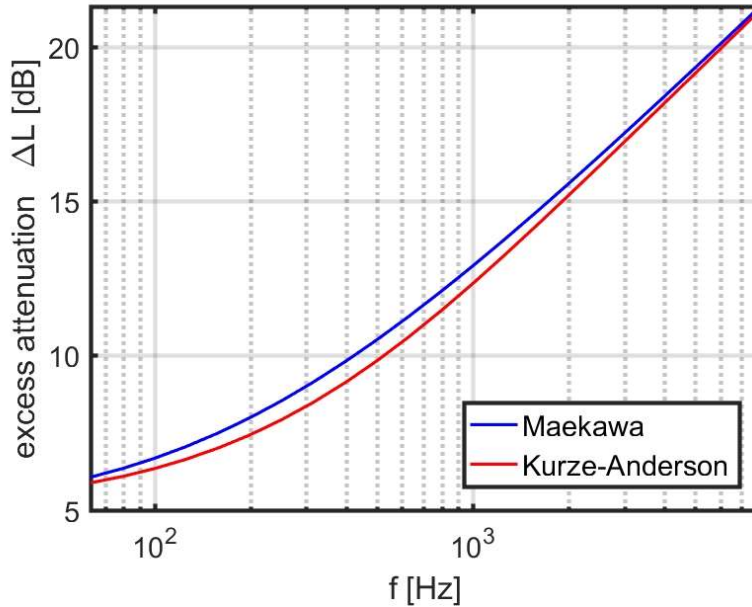


Figure 4.31: Excess attenuation calculated as a function of frequency for the geometry of figure 4.29.

The red line in figure 4.31 indicates the excess attenuation values for the same geometry but now calculated according to the Kurze-Anderson formula, which reads

$$\Delta L = 5 + 20 \log \left( \frac{\sqrt{2\pi N}}{\tanh(\sqrt{2\pi N})} \right). \quad (4.93)$$

This empirical formula is recommended, i.e. more accurate, for Fresnel numbers  $N < 1$ . As observed from the figure, the two curves agree quite well.

As expected the excess attenuation is an increasing function of frequency, since the amount of diffraction decreases with increasing frequency. Consequently, sound screens become more effective at higher frequencies, as already stated in section 1.2.

For  $N = 0$  the Kurze-Anderson formula becomes  $\Delta L = 5$  dB (use  $\tanh x \approx x$  for  $x \rightarrow 0$ ) and also Maekawa's formula then reads  $\Delta L = 10 \log 3 \approx 5$  dB. Hence, when the height of the barrier is tangent to the line of sight, we still get a significant excess attenuation (5 dB).

We further note that for large  $N$  the Kurze-Anderson formula becomes  $\Delta L = 5 + 20 \log(\sqrt{2\pi N}) = 13 + 10 \log N$  (use  $\tanh x \rightarrow 1$  for  $x \rightarrow \infty$ ), the values of which nearly coincide with Maekawa's formula, equation 4.89.

The effect of a noise barrier of height 3 m on the noise spectrum of a typical propeller aircraft is illustrated in figure 6.6 of chapter 6. Shown in that figure is the (A-weighted) spectrum of the aircraft with and without the barrier for the geometry of figure 4.30 of this section. The effect on the overall sound pressure level is a significant reduction of 11 dB. For such a calculation the excess attenuation is calculated separately for each frequency (in this case the 1/3-octave band centre frequencies). Subsequently, the overall (A-weighted) sound pressure level is calculated according to equation 6.8 (see also equation 5.19 or 1.23). We note that whilst the values of  $\Delta L$  at a single frequency depend only on the geometry, the total excess attenuation also depends on the spectrum of the source. The very same barrier will provide a high reduction in overall sound pressure level for noise sources with a lot of energy at high frequencies and a significantly smaller reduction for sources having most energy at low frequencies.

As mentioned above, diffraction at the sides of the barrier (see lower part of figure 4.28) becomes important when the distance between the source and the side edges is less than 5 times the effective height. Then the excess attenuation becomes

$$\Delta L = \Delta L_u - 10 \log \left( 1 + \frac{N}{N_1} + \frac{N}{N_2} \right) \quad (4.94)$$

with  $\Delta L_u$  the excess attenuation as caused by the upper edge alone (which can be evaluated with the Maekawa or Kurze-Anderson formula).  $N_1$  and  $N_2$  are the Fresnel numbers corresponding to the two side edges, respectively, and  $N$  is still the Fresnel number for the upper edge. Note that always  $\Delta L < \Delta L_u$ , i.e. the screen becomes less effective when it is not extending sufficiently far in the lateral direction to prevent diffraction at the side ends.

## Exercises

### Question 1

Consider interior noise of aircraft equipped with turbofan engines. The noise is transmitted to the interior of the fuselage along airborne sound paths, i.e. fan noise and engine exhaust jet noise is incident on the fuselage shell and subsequently transmitted through it into the cockpit and passenger cabin. The fuselage windows are made of Perspex (density 1200 kg/m<sup>3</sup>) and have a thickness of 5 mm. For this question you may assume that the material surrounding the windows is Aluminium (density 2700 kg/m<sup>3</sup>) with a thickness of 2 mm. See also the figure below.



- (a) Use the mass law to determine the normal-incidence transmission loss for sound at 100 Hz through the Perspex window and through the surrounding Aluminium.
- (b) In order to reduce low frequency (~100 Hz) cabin noise, is it useful to make the Perspex window thicker? Or the surrounding Aluminium? Or need both materials to be made thicker at the same time?
- (c) Use the mass law to determine the normal-incidence transmission loss for sound at 1 kHz through the Perspex window and through the surrounding Aluminium.
- (d) In order to reduce cabin noise at frequencies of 1 kHz (and higher), is it useful to make the Perspex window or the Aluminium surroundings thicker? Or both?

### Question 2

A medium-size factory hall is of dimensions 30m x 15m x 7m. The reverberation time  $T_{60}$  is 3 seconds.

- (a) What is the total absorption of this hall?

The desired reverberation time is 1 second, as the hall will be used for lecturing in the near future. The only place where sound absorption measures can be taken is the ceiling.

- (b) What should be the mean absorption coefficient of the ceiling to obtain this required reverberation time?
- (c) What is the change in intensity level of the diffuse (reverberant) sound field?

Question 3

The ‘Concertgebouw’ in Amsterdam has a volume of  $19500 \text{ m}^3$  and a reverberation time of 2.55 s when empty, i.e. when the 2100 available seats are not occupied.

- (a) Calculate the open window area of this concert hall.

Now suppose all seats are occupied and that each person adds  $0.11 \text{ m}^2$  to the open window area.

- (b) Calculate the reverberation time of the ‘Concertgebouw’ when fully occupied.
- (c) Is the fully occupied ‘Concertgebouw’ suitable as concert hall?

Question 4

To study the effectiveness of low frequency sound attenuation in engine exhausts, we consider the single-expansion chamber, see figure 4.19. The diameter of the cylindrical intake tube or duct is 10 cm. Its cross-sectional area is denoted  $S_1$ . The cylindrical outlet duct has an equal cross-sectional area. The expansion chamber has a length  $\ell$  and is also cylindrical in shape with cross-sectional area  $S_2 (> S_1)$ . To simplify calculations for this device one can assume one-dimensional wave motion in the directions of the tube.

- a. Explain that the one-dimensional wave motion assumption requires the tube diameter to be small (say a factor of 5 less) compared to the acoustic wavelength. Up to which frequency is the assumption valid (for the intake tube)?
- b. The single-expansion chamber has two design parameters,  $\ell$  and  $S_2 / S_1$ . Which parameter controls what?
- c. Taking  $\ell = 0.4 \text{ m}$  and  $S_2 / S_1 = 5$ , calculate the Transmission Loss TL as a function of frequency up to 1000 Hz. Make a plot of TL versus frequency. Sketch in the same graph TL for a closed side branch tube of the same length. Which attenuator do you prefer? Explain why.

- d. Suppose we require a single-expansion chamber with a transmission loss of at least 10 dB for all frequencies in between 100 and 600 Hz. Which values for  $\ell$  and  $S_2 / S_1$  would you choose?

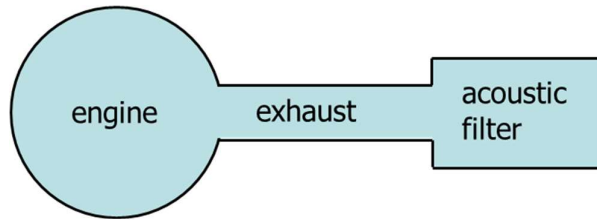
Question 5

Note: These questions can only be answered when the theory of chapter 6 has also been studied.

Consider an engine that produces annoying tonal sound. The noise at the end of the cylindrical engine exhaust consists of two simultaneous tones at frequencies of 400 Hz and 1000 Hz, respectively. Each tonal has a sound pressure level (SPL) of 90 dB.

- (a) Calculate the overall A-weighted sound pressure level.

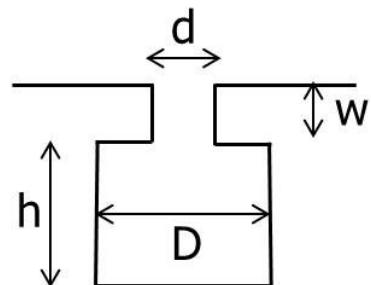
In an attempt to reduce the noise, an acoustic filter is applied at the exhaust exit. The filter consists of a simple single increase in diameter of the exhaust duct by a factor of two, see figure below.



- (b) Calculate again the overall A-weighted sound pressure level, but now after the acoustic filter is applied.

Question 6

A turbofan engine has a main fan with 20 blades operating at 6000 rpm. In order to reduce the radiated noise, it is proposed to line the inlet of the engine with a material composed of cells which act as Helmholtz resonators. The thickness  $w$  of the liner material is 3 mm, i.e.  $w$  is the length of the neck of the resonator, see figure below.



For aerodynamic reasons, the cell opening diameter  $d$  is required to be 2 mm. The depth  $h$  of the cavity of the Helmholtz resonator is equal to 10 mm, whereas its diameter is denoted  $D$ . Both the neck and the cavity are cylindrical in shape. Assume all Helmholtz resonators at the inlet of the engine have the same dimensions.

- (a) Determine  $D$  so that the liner optimally reduces the blade passage frequency of the fan. (Note: you need formula 5.22 for this)
- (b) Does this liner also reduce the higher harmonics of the blade passage frequency?

#### Question 7

Note: Although not needed here, see chapter 5 for the term 'octave band analysis'. In this question the calculations are only required for a single frequency (hence it is not needed to study chapter 5 first).

An octave band analysis of noise measured for a propeller-driven aircraft shows that the noise in the octave band at centre frequency 125 Hz is dominant. The sound pressure level in this band is 77 dB.

This noise is measured under static conditions with a microphone positioned 20 m from the propeller and at a height of 2 m from the ground. The noise originates from the propeller-engine combination and may be considered a point source at a height of 2 m from the ground.

Suppose a thin screen of height 4 m is positioned halfway between the aircraft's propeller and the microphone. It may be assumed that no sound can pass through the screen and that the screen is infinitely long in the direction perpendicular to the line connecting propeller and microphone.

What will be the sound pressure level at the microphone with the screen inserted between aircraft and microphone?

Note: assume that the acoustic efficiency for the centre frequency of the octave band considered is valid for the entire band.

## Chapter 5 Acoustic signal analysis

In this chapter the basics of acoustic signal analysis is treated with emphasis on frequency analysis of aircraft noise data. The basis for this is the Fourier transform, providing the distribution of the sound power of a noise source over frequency. Such an analysis is needed for e.g.

- finding and investigating the dominant source component and hence being able to reduce the noise at the source;
- correcting the measured noise data for the frequency-dependent atmospheric propagation effects (see section 3.2);
- the efficient use of absorbent materials, e.g. in turbofan engines (as we have seen in section 4.3);
- determining perceived loudness (see chapter 6), since the sensitivity of the human ear is very much dependent on frequency.

We conclude this chapter with a brief treatise of some of the technical details of microphones.

### 5.1 Fourier transform – continuous and discrete

Consider a time signal  $x(t)$ . This can be the pressure  $p'(t)$  as recorded by a microphone as a function of time  $t$ . The continuous Fourier transform is given by

$$X(f) = \int_{-\infty}^{\infty} x(t) e^{-2\pi i f t} dt \quad (5.1)$$

with  $f$  the frequency.

The (continuous) inverse Fourier transform is

$$x(t) = \int_{-\infty}^{\infty} X(f) e^{2\pi i f t} df. \quad (5.2)$$

Example 1: If the signal is a pure tone at  $f = f_0$ , i.e.  $x(t) = \cos(2\pi f_0 t)$ , which can be written as

$$x(t) = \frac{e^{2\pi i f_0 t} + e^{-2\pi i f_0 t}}{2} \quad (5.3)$$

then the Fourier transform is

$$X(f) = \frac{1}{2} \delta(f + f_0) + \frac{1}{2} \delta(f - f_0) \quad (5.4)$$

with  $\delta$  the Dirac delta function. Note that  $X(f)$  peaks at  $f = f_0$  (as expected), but also at the ‘negative’ frequency  $f = -f_0$ , hence the Fourier transform is two-sided.

Example 2: For the complex harmonic signal  $x(t) = e^{2\pi i f_0 t}$ , the Fourier transform is  $X(f) = \delta(f - f_0)$ , i.e. one-sided.

Now consider a discrete signal  $x_k, k = 0, \dots, N-1$ , i.e. a continuous signal sampled at  $N$  discrete times with sample ‘distance’  $\Delta t = \frac{1}{f_s}$  with  $f_s$  the sample frequency in Hz.

Note: At a given sample frequency  $f_s$ , the maximum frequency in the signal that can be reconstructed correctly is equal to  $\frac{f_s}{2}$  (i.e. the so-called Nyquist frequency). Higher frequencies in the signal cannot be reconstructed correctly as they are subject to aliasing. Considering signals with band width  $B$  (i.e. the highest frequency in the signal equals  $B$ ), then correct reconstruction of the continuous signal from the samples is only possible if the sample frequency is at least equal to  $2B$  (i.e. the so-called Nyquist rate).

The discrete Fourier transform (DFT) is

$$X_m = \Delta t \sum_{k=0}^{N-1} x_k e^{-2\pi i t_k f_m} \quad (5.5)$$

with  $t_k, k = 0, \dots, N-1$  the discrete times and  $f_m, m = 0, \dots, N-1$  the discrete frequencies. i.e., the discrete frequencies run from 0 to  $f_s$ . The DFT can be written as

$$X_m = \Delta t \sum_{k=0}^{N-1} x_k e^{-2\pi i k \Delta t m \Delta f} \quad (5.6)$$

with  $\Delta f = \frac{f_s}{N} = \frac{1}{N \Delta t}$ . Hence,  $\Delta t \Delta f = \frac{1}{N}$  so that the DFT becomes

$$X_m = \Delta t \sum_{k=0}^{N-1} x_k e^{-2\pi i k m / N}. \quad (5.7)$$

The inverse discrete Fourier transform (IDFT) is

$$x_k = \Delta f \sum_{m=0}^{N-1} X_m e^{2\pi i km/N} = \frac{1}{N\Delta t} \sum_{m=0}^{N-1} X_m e^{2\pi i km/N}. \quad (5.8)$$

## 5.2 Power spectral density and spectrum level

For a continuous signal  $x(t)$ , Parseval's theorem reads

$$\int_{-\infty}^{\infty} [x(t)]^2 dt = \int_{-\infty}^{\infty} |X(f)|^2 df. \quad (5.9)$$

Further, in chapter 1 we defined the effective pressure as (taking  $x(t) = p'(t)$  in units Pa)

$$p_e^2 = \overline{[x(t)]^2} = \frac{1}{T} \int_0^T [x(t)]^2 dt \quad (5.10)$$

with  $T$  a sufficiently large integration time. From these two equations we obtain the so-called 'power spectral density' (in units Pa<sup>2</sup>/Hz)

$$P(f) = \frac{|X(f)|^2}{T} \quad (5.11)$$

where we have implicitly assumed that the Fourier transform  $X(f)$  is now obtained from a finite (but long enough) integration time  $T$ . The power spectral density is normalised according to

$$\int_{-\infty}^{\infty} P(f) df = p_e^2. \quad (5.12)$$

Actually, this is still Parseval's equation, but now in terms of the power spectral density. Note that the integration is also over the negative frequencies.

In the discrete situation the power spectral density is

$$P_m = \frac{|X_m|^2}{T} = \frac{|X_m|^2}{N\Delta t}. \quad (5.13)$$

Note: in the Matlab implementation of the DFT/IDFT the  $\Delta t$  factor is not used. The discrete power spectral density then becomes

$$P_m = \frac{|X_m|^2 (\Delta t)^2}{T} = \frac{|X_m|^2 \Delta t}{N} \quad (5.14)$$

with  $X_m$  the DFT obtained in Matlab.

Example 3: We consider a signal simulated in Matlab: a single tone at 200 Hz with amplitude 1 buried in white noise with standard deviation 1.5. The signal is sampled at a frequency of 1000 Hz and is shown in the upper part of figure 5.1. The length of the signal is  $T = 0.3$  s, hence the number of samples is  $N = 300$ . Note that the tone is hardly visible. The lower part of the figure shows the (discrete) power spectral density  $P_m$  obtained using the formula above.  $P_m$  consists of two contributions: a flat part due to the white noise and two sharp peaks due to the tone. Note that a peak is observed at 200 Hz, but also at  $1000 - 200 = 800$  Hz, since in the DFT the ‘positive’ frequencies are between 0 and  $\frac{f_s}{2}$ , whereas the ‘negative’ frequencies are between  $\frac{f_s}{2}$  and  $f_s$ .

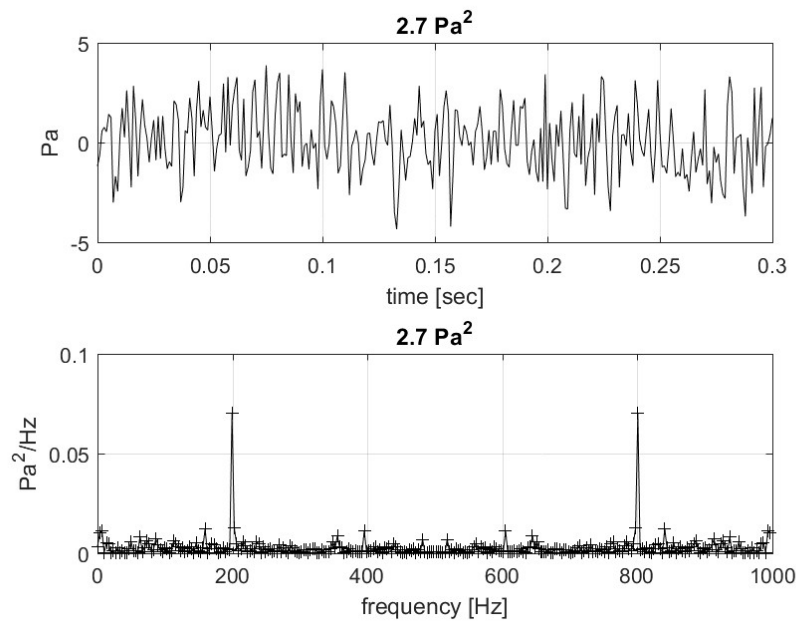


Figure 5.1: Example of a simulated pressure time signal (upper figure) and the corresponding power spectral density (lower figure). The time signal is a tone at 200 Hz buried in noise, sampled at a frequency of 1000 Hz.

In the lower part of figure 5.1 the tone becomes clearly visible, demonstrating the power of this frequency analysis with the Fourier transform.

We also checked Parseval’s theorem. Shown in the figure is the standard deviation squared of the time signal (i.e.  $p_e^2 = 2.7 \text{ Pa}^2$ ) and the value obtained in the frequency domain from the power spectral density (i.e.  $\int_{-\infty}^{\infty} P(f) df = 2.7 \text{ Pa}^2$ ).

Note: The frequency resolution of the power spectral density, i.e. the width of the peaks at half height, is given by  $\delta f = \frac{1}{T} = \frac{1}{N\Delta t}$  (equal to 3.3 Hz in this example), i.e. fully determined by the signal length.

### 5.3 Octave band and 1/3-octave band analysis

Although not strictly needed, the result of a frequency analysis is frequently averaged, i.e. the power spectral density is integrated over a set of bandwidth values. Usually, a constant percentage bandwidth analysis is performed and a distinction is made between octave bands and 1/3-octave bands. In both cases we have a set of centre frequencies  $f_n$  and a set of corresponding lower and upper frequencies ( $f_L$  and  $f_U$ ). The bandwidth values are then equal to  $\Delta f = f_U - f_L$  and the centre frequency is equal to the geometric mean of  $f_L$  and  $f_U$ , i.e.  $f_n = \sqrt{f_U f_L}$  or  $\log f_n = \frac{1}{2} [\log f_L + \log f_U]$ .

Note: the  $\Delta f$  in this section is not the  $\Delta f$  of the previous section.

For octave bands we have a doubling of frequency over the band, i.e.  $f_U = 2f_L$  (hence  $f_n = \sqrt{2}f_L$  and  $f_U = \sqrt{2}f_n$ ), so that the relative bandwidth is

$$\frac{\Delta f}{f_n} = \frac{f_U - f_L}{f_n} = \frac{1}{\sqrt{2}} = 0.71 \quad (5.15)$$

which is indeed a constant. The 14 centre frequencies are given by the simple formula  $f_n = 10^{3n/10}$  for  $n = 1, 2, \dots, 14$ . Band numbers  $n$ , corresponding centre frequencies and bandwidths or pass bands are given in figure 5.2.

band number $n$	centre frequency [Hz]	passband [Hz]	band number $n$	centre frequency [Hz]	passband [Hz]
1	2	1.41 - 2.82	8	250	178 - 355
2	4	2.82 - 5.62	9	500	355 - 708
3	8	5.62 - 11.2	10	1000	708 - 1410
4	16	11.2 - 22.4	11	2000	1410 - 2820
5	31.5	22.4 - 44.7	12	4000	2820 - 5620
6	63	44.7 - 89.1	13	8000	5620 - 11200
7	125	89.1 - 178	14	16000	11200 - 22400

Figure 5.2: Band number, centre frequency and bandwidth (or pass band) for the 14 octave bands.

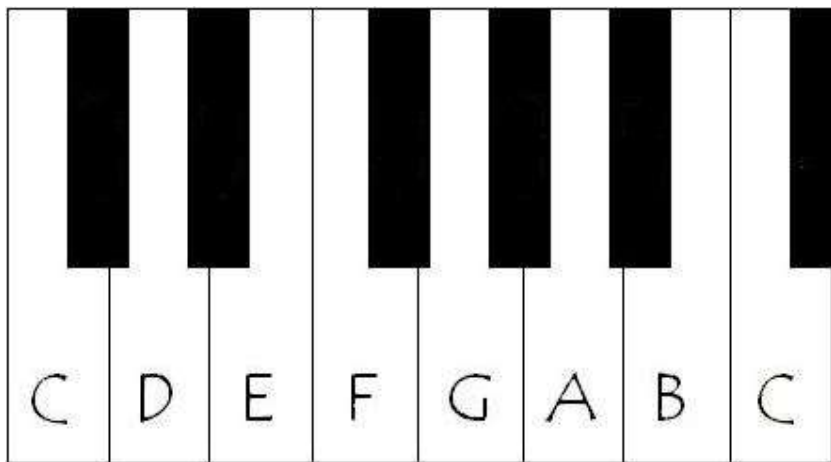
For aircraft noise measurements, frequently a 1/3-octave (or terts-) band analysis is performed. Each octave band is partitioned in 3 bands according to  $f_U = 2^{1/3} f_L$  and hence  $f_U = 2^{1/6} f_n$  and  $f_n = 2^{1/6} f_L$  so that the relative bandwidth now becomes

$$\frac{\Delta f}{f_n} = \frac{f_U - f_L}{f_n} = 2^{1/6} - \frac{1}{2^{1/6}} = 0.23. \quad (5.16)$$

The centre frequencies are given by  $f_n = 10^{n/10}$  for  $n = 1, 2, \dots, 43$ . Figure 5.3 gives band numbers  $n$ , corresponding centre frequencies and bandwidths or pass bands.

Note: The octave is the most fundamental musical interval and has a frequency ratio of exactly 2. In the so-called ‘equally tempered scale’ each octave is divided in 12 half tones, in such a way that the ratio of the frequencies of all subsequent half tones is  $\sqrt[12]{2}$ . The advantage of this scale is that (e.g. on a piano) a certain musical interval is always having the same frequency ratio, independent of the starting half tone of the considered interval. A disadvantage of the equally tempered scale is that, apart from the octave, there are no other perfect intervals such as the perfect fifth (quint) with a frequency ratio of 3/2. In the equally tempered scale a fifth is played as 7 half tones corresponding to a frequency ratio of  $2^{\frac{7}{12}} = 1.4983$ . The deviation of the frequency ratios in the equally tempered scale from that of the perfect ratios is small (and hence the pleasure of music is not disturbed), see table and figure below.

tone	interval	Number of half tones	frequency ratio	
			equally tempered	perfect
c	unison	0	$2^{\frac{0}{12}} = 1$	1
des	minor second	1	$2^{\frac{1}{12}} = 1.0595$	$16/15 = 1.0667$
d	major second	2	$2^{\frac{2}{12}} = 1.1225$	$9/8 = 1.25$
es	minor third (minor thirds)	3	$2^{\frac{3}{12}} = 1.1892$	$6/5 = 1.2$
e	major third (major thirds)	4	$2^{\frac{4}{12}} = 1.2599$	$5/4 = 1.25$
f	fourth	5	$2^{\frac{5}{12}} = 1.3348$	$4/3 = 1.3333$
fis	augmented fourth	6	$2^{\frac{6}{12}} = 1.4142$	$7/5 = 1.4$
g	fifth	7	$2^{\frac{7}{12}} = 1.4983$	$3/2 = 1.5$
as	minor sixth	8	$2^{\frac{8}{12}} = 1.5874$	$8/5 = 1.6$
a	major sixth	9	$2^{\frac{9}{12}} = 1.6818$	$5/3 = 1.6667$
bes	minor seventh	10	$2^{\frac{10}{12}} = 1.7818$	$16/9 = 1.7778$
b	major seventh	11	$2^{\frac{11}{12}} = 1.8877$	$15/8 = 1.875$
c'	octave	12	$2^{\frac{12}{12}} = 2$	2



band number $n$	centre frequency [Hz]	passband [Hz]	band number $n$	centre frequency [Hz]	passband [Hz]
1	1.25	1.12 - 1.41	23	200	178 - 224
2	1.6	1.41 - 1.78	24	250	224 - 282
3	2	1.78 - 2.24	25	315	282 - 355
4	2.5	2.24 - 2.82	26	400	355 - 447
5	3.15	2.82 - 3.55	27	500	447 - 562
6	4	3.55 - 4.47	28	630	562 - 708
7	5	4.47 - 5.62	29	800	708 - 891
8	6.3	5.62 - 7.08	30	1000	891 - 1120
9	8	7.08 - 8.91	31	1250	1120 - 1410
10	10	8.91 - 11.2	32	1600	1410 - 1780
11	12.5	11.2 - 14.1	33	2000	1780 - 2240
12	16	14.1 - 17.8	34	2500	2240 - 2820
13	20	17.8 - 22.4	35	3150	2820 - 3550
14	25	22.4 - 28.2	36	4000	3550 - 4470
15	31.5	28.2 - 35.5	37	5000	4470 - 5620
16	40	35.5 - 44.7	38	6300	5620 - 7080
17	50	44.7 - 56.2	39	8000	7080 - 8910
18	63	56.2 - 70.8	40	10000	8910 - 11200
19	80	70.8 - 89.1	41	12500	11200 - 14100
20	100	89.1 - 112	42	16000	14100 - 17800
21	125	112 - 141	43	20000	17800 - 22400
22	160	141 - 178			

Figure 5.3: Band number, centre frequency and bandwidth (or pass band) for the 43 1/3-octave bands.

The sound pressure level within a specified frequency band (centered at a specified frequency  $f$ ) is called the ‘pressure band level’ PBL (in dB) and is defined according to

$$PBL = 10 \log \left[ \frac{P(f)\Delta f}{P_{e0}^2} \right] = PSL + 10 \log \Delta f \quad (5.17)$$

with

$$PSL = 10 \log \left[ \frac{P(f)}{P_{e0}^2} \right] \quad (5.18)$$

the ‘spectrum’ or spectrum level in units dB/Hz, i.e. the dB value of the power spectral density (in  $\text{Pa}^2/\text{Hz}$ ). The spectrum level is thus the sound pressure level in dB contained within a 1 Hz wide band centred at a specific frequency.

For white noise the spectrum level is a constant, hence the corresponding pressure band levels in the successive octave bands increase with  $10 \log 2 = 3 \text{ dB}$  per octave, see figure 5.4.

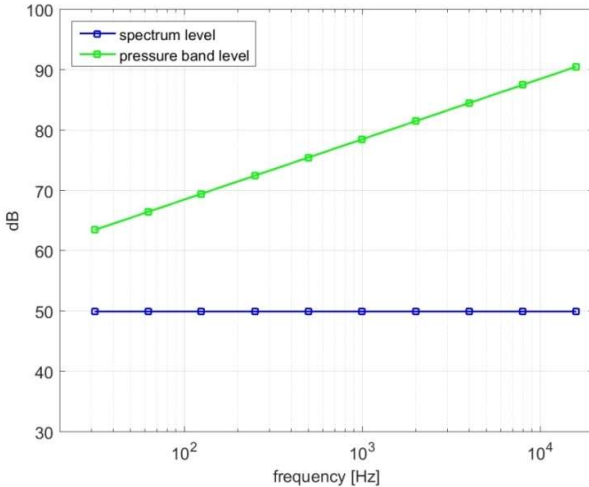


Figure 5.4: Spectrum level for white noise (blue line) and corresponding pressure band levels in the successive octave bands (green line).

#### 5.4 Overall sound pressure level

After an octave or 1/3-octave band analysis, the pressure band levels (in dB) are available for the successive bands. Denoting these as  $SPL(f_i, \theta)$ , with  $\theta$  the angle at which the measurements were taken and  $f_i$  the centre frequency of band  $i$ , the ‘overall sound pressure level’ (in dB) is given by (see also chapter 1, equation 1.23)

$$OSPL(\theta) = 10 \log \sum_{i=1}^n 10^{SPL(f_i, \theta)/10}. \quad (5.19)$$

This should be equal to the overall sound pressure level obtained in the time domain according to

$$OSPL = 10^{10} \log \left( \frac{p_e^2}{p_{e0}^2} \right) \quad (5.20)$$

with the effective pressure squared equal to  $p_e^2 = \frac{1}{T} \int_0^T [x(t)]^2 dt$  and  $p_{e0} = 2 \times 10^{-5}$  Pa.

Strictly speaking, *pressure band levels* are obtained in a (1/3-) octave band analysis. Often, however, these are denoted as sound pressure levels SPL (and not PBL).

## 5.5 Spectrogram

A spectrogram is a 2D image of the spectrum of a sound signal and how it varies with time. The horizontal axis represents time, the vertical axis is frequency and the third dimension indicates the power (represented by a colour scale, often in dB units) at each point in the image. Spectrograms are usually calculated from the time signal using the Fourier transform. A digitally sampled signal, in the time domain, is broken up into chunks of data, which are subsequently Fourier transformed (usually, the chunks of data slightly overlap). Next, the spectrum level (in dB) for each chunk is calculated. Each chunk then corresponds to a vertical line in the image, i.e. a measurement of the spectrum for a specific moment in time (the midpoint of the chunk). The spectra are then ‘laid side by side’ to form the image.

The most important parameter of the spectrogram is the length  $T$  of the data chunks (also called window size). From the above (see e.g. equation 5.13) we know that  $T = N\Delta t$  with

$N$  the number of samples in each chunk (and  $\Delta t = \frac{1}{f_s}$  with  $f_s$  the sample frequency). The

frequency resolution of the DFT is  $\delta f = \frac{1}{T}$ , hence a shorter window will produce more

accurate results in timing, at the expense of frequency resolution. A longer window will provide a better frequency representation, at the expense of precision in timing. Hence, the product of time resolution and frequency resolution is a constant (equal to unity). This is an example of the Heisenberg uncertainty principle: the resolution in two conjugate variables are inversely proportional to each other (e.g. position and momentum of a particle in quantum mechanics).

Figure 5.5 gives an example of a spectrogram of a Boeing 737 flyover. Note the Doppler shifted fan tones.

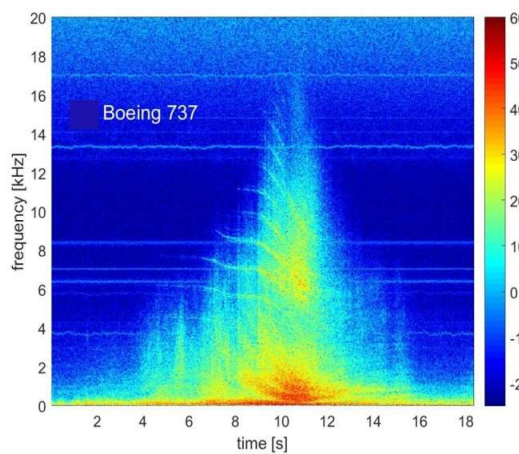
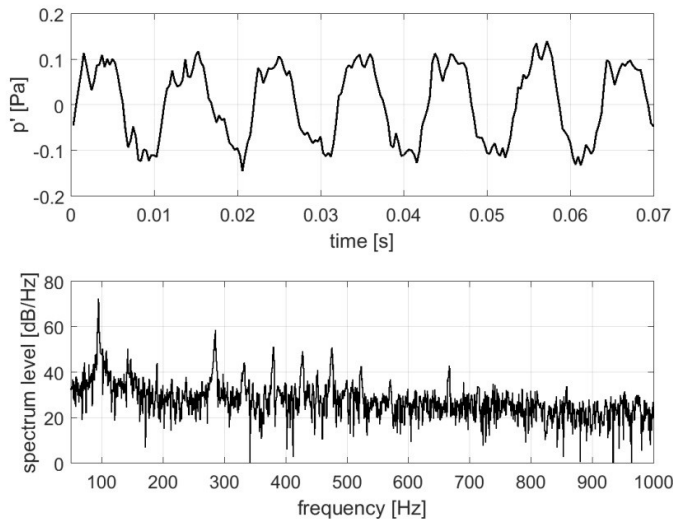


Figure 5.5: Spectrogram measured for a Boeing 737 flyover.

For noise data, aircraft noise in particular, a spectrogram is a very valuable tool. In fact, it is one of the first diagnostic steps in the signal analysis. Further examples are given in the next section.

### 5.6 Aircraft noise measurements - examples

In general, aircraft noise consists of a mixture of broadband noise and tonal noise. A typical spectrum of a small propeller-driven airplane is given in figure 5.6. Also indicated is the pressure time signal  $p'(t)$ . It is obvious that the tonal noise dominates as shown by the high periodicity of the time signal and the strong peaks in the spectrum.



**Figure 5.6:** Pressure time signal (upper figure) and corresponding spectrum level (lower figure) measured for a small propeller-driven airplane.

The frequencies observed are the exhaust firing frequency  $f_e$  and the propeller blade passage frequency  $f_1$  and higher harmonics, i.e. multiples of both  $f_e$  and  $f_1$ . These are given by

$$f_e = N \frac{n}{120} \quad (5.21)$$

and

$$f_1 = B \frac{n_p}{60}, \quad (5.22)$$

respectively (both in Hz). Here,  $N$  is the number of cylinders,  $n$  is the engine rotational speed (in rpm),  $B$  is the number of blades and  $n_p$  is the propeller rotational speed (also in rpm).

For  $B = 2$ ,  $N = 4$  and  $n_p = n = 2400$  rpm, we have  $f_e = f_1 = 80$  Hz. Then the exhaust firing frequency and the propeller blade passage frequency coincide and the spectrum will exhibit peaks at 80 Hz, 160 Hz, 240 Hz, etc. For  $B = 2$ ,  $N = 6$  and  $n_p = n = 2400$  rpm, i.e.  $f_e = 120$  Hz and  $f_1 = 80$  Hz. Now the firing frequency and the blade passage frequency differ and the spectrum will be more complicated although still predominantly tonal.

Note: The blade passage frequency is called the ‘fundamental frequency’. Its higher harmonics, which have frequencies that are integral multiples of the fundamental frequency, are also called ‘overtones’. The figure below shows an example of a sequence of the first 6 harmonics in music notation. Here, harmonic no. 1 is the fundamental (two octaves below ‘middle c’). Harmonic no. 2 is the first overtone (one octave higher than the fundamental) and harmonic no. 3 is the second overtone (3 times the frequency of the fundamental). Hence, this second overtone is a perfect quint higher than the first overtone (i.e. their frequency ratio is 3/2, see note in section 5.3).



Figure 5.7 shows an example of the pressure time signal and corresponding spectrum for an airplane powered by turbofan engines. The broadband noise (due to the jet) is now dominant, although tonal noise is present. The latter is due to the fan for which the above blade passage frequency formula also holds (although now  $B$  is in the order of 20, resulting in a ten times higher  $f_l$  value).

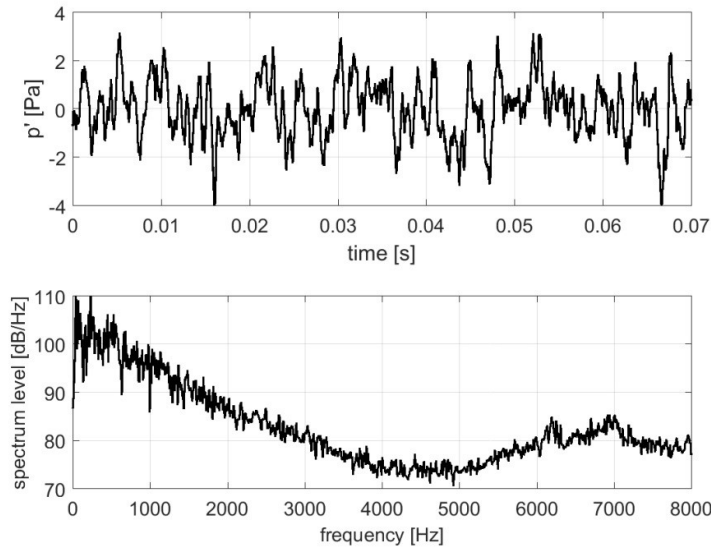


Figure 5.7: Pressure time signal (upper figure) and corresponding spectrum level (lower figure) measured for an airplane powered by turbofan engines.

The spectra shown in figures 5.6 and 5.7 are obtained for a constant bandwidth of 5 Hz, i.e. sufficiently small to not lose any information about the noise characteristics. Figure 5.8 illustrates the effect of an octave and 1/3-octave band analysis. It is clearly observed that wider frequency bands make the individual harmonics less visible, hence information is lost (especially in the case of octave band analysis). It also obvious that reading levels in between the points has become meaningless.

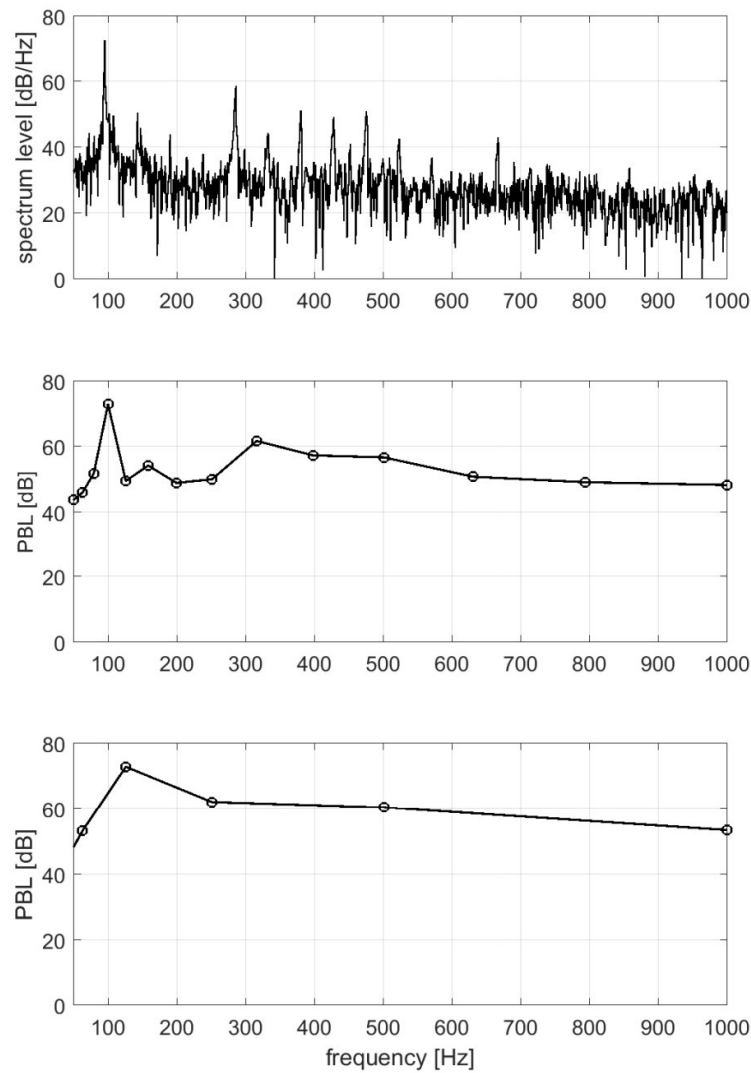


Figure 5.8: Effect of an octave band analysis (lower figure) and a 1/3-octave band analysis (middle figure) on the spectrum of figure 5.6 (shown here again in the upper figure).

The data shown so far are for statically operating airplanes, i.e. the noise is stationary. We will now show data for aircraft ‘flyovers’, i.e. non-stationary noise. Figure 5.9 shows the power spectral density measured for a small propeller-driven airplane in ‘approach’ (top figure) and ‘departure’ situation (bottom figure). Clearly, the tones have been Doppler shifted, but it is not so clear which tone (approaching) is belonging to which tone (departing). However, this becomes very clear when a spectrogram is produced from the data, see figure 5.10.

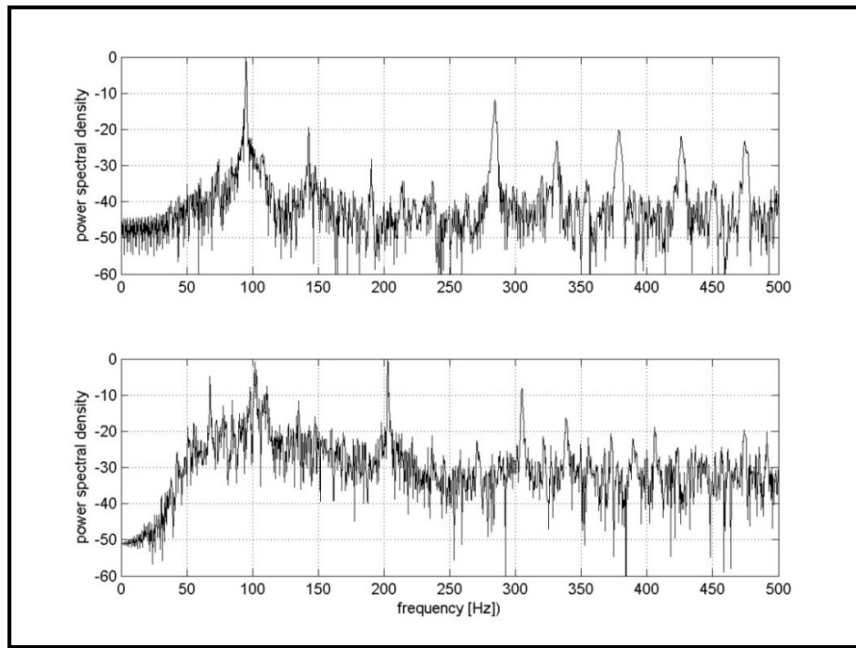


Figure 5.9: Power spectral density in dB (i.e. the spectrum) measured for a small propeller-driven airplane in 'approach' (upper figure) and 'departure' situation (bottom figure).

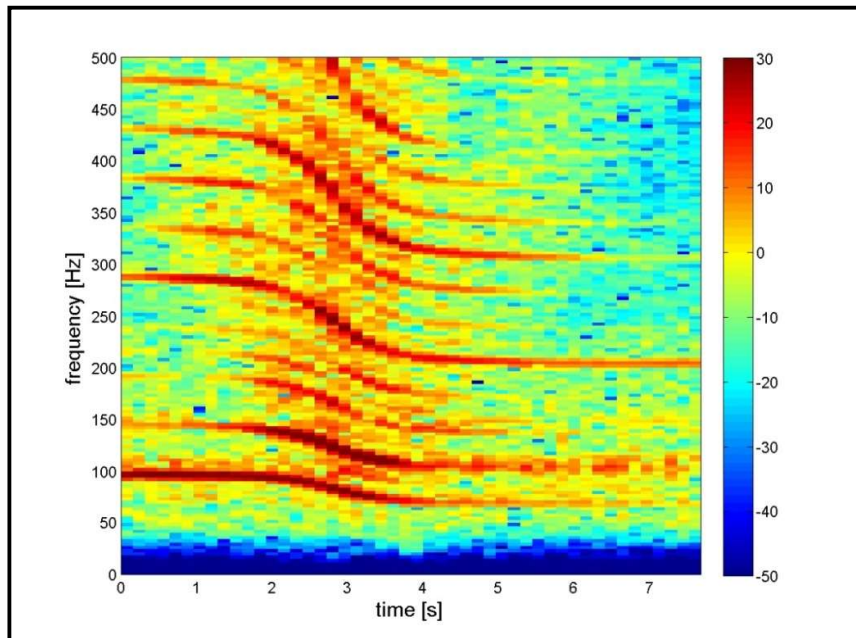
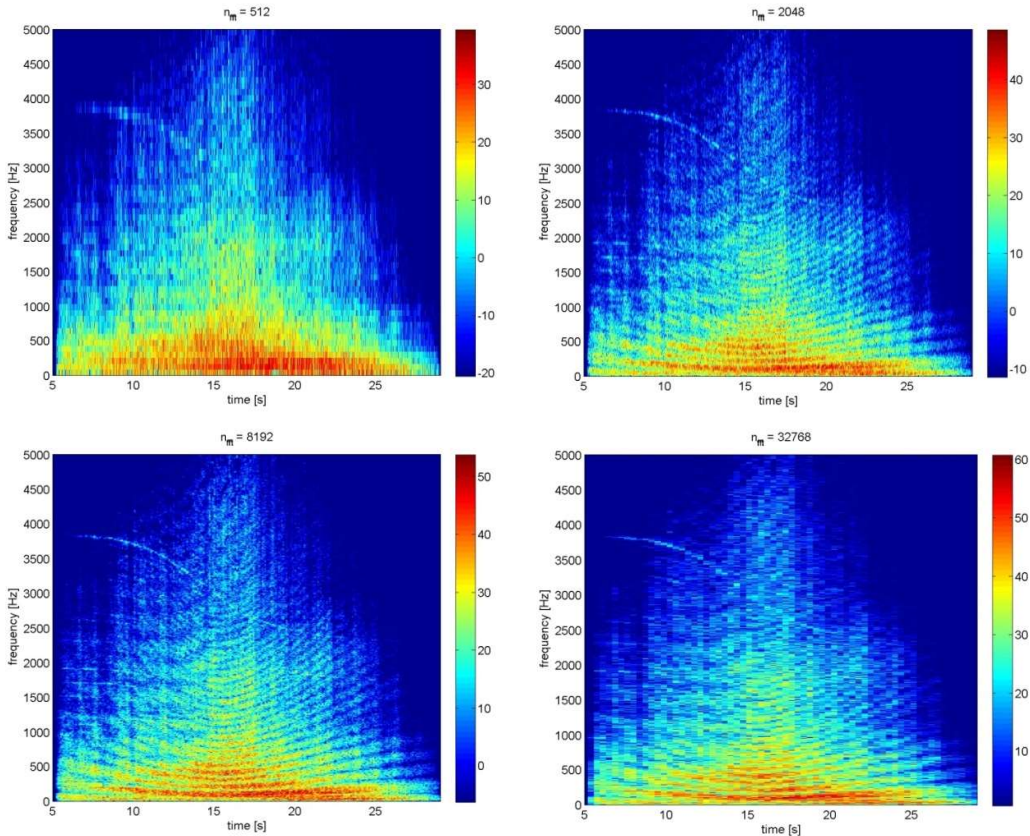


Figure 5.10: Spectrogram produced from the same data as that of figure 5.9.

The Doppler shifted tonals nicely follow the formula  $\frac{f'}{f} = \frac{1}{1 - M \cos \theta}$ , developed in section 1.5. Here,  $f$  is the true frequency,  $f'$  the Doppler shifted frequency,  $M$  the Mach number (equal to  $\frac{V}{c}$  with  $V$  the aircraft velocity) and  $\theta$  as indicated in figure 1.21.

For approach  $\theta = 0^\circ$ , for departure  $\theta = 180^\circ$  and  $\theta = 90^\circ$  when the aircraft is overhead.

Figure 5.11 shows spectrograms of the noise from a flyover of an aircraft equipped with jet engines. The spectrograms are for the same data, however various values for the length  $T$  of the data chunks are chosen to illustrate the effect on time resolution and frequency resolution.



**Figure 5.11:** Spectrograms of noise data obtained for a flyover of an aircraft equipped with jet engines. In the title of the four figures the chosen value for the window size ( $n_{\text{fft}} = N$ ) is indicated.

The data chunk length  $T$  is here parameterised by the FFT size  $n_{\text{fft}}$ , which simply equals the number  $N$  of samples in each chunk. Table 5.1 gives the values for time resolution and frequency resolution in the spectrogram using the formulas developed in the previous section. For this dataset the sample frequency  $f_s = \frac{1}{\Delta t}$  equals 44.1 kHz.

Table 5.1

$N$ or $n_{fft}$	time resolution $T = \frac{n_{fft}}{f_s}$ (s)	frequency resolution $\delta f = \frac{f_s}{n_{fft}}$ (Hz)
512	0.012	86.1
2048	0.046	21.5
8192	0.186	5.38
32768	0.743	1.35

Apparently, for having sufficient resolution both in time and frequency, the precise value of  $N$  is not very critical, provided a value in between 2048 and 8192 is chosen in this case. In general, it is advised to test several values of  $N$  to find the best result. The spectrogram clearly shows the non-stationarity of the signal, i.e. the highest sound pressure levels are at overhead position for all frequencies. Further, note the Doppler shifted fan tone at a frequency of about 3000 Hz. As already mentioned in section 3.5, the interference pattern due to the ground effect is also clearly present.

A spectrogram basically provides measurements of SPL as a function of frequency and angle (angle  $\theta$  converted from time). As explained in chapter 3, these values can be corrected to the SPL values at the source (at 1 m). Subsequently, these data can be used for the validation of aircraft noise models, provided the airplane operational conditions, such as position, engine setting, landing gear position and flap angle, are accurately known. Also, it is then recommended to perform the measurements in low wind conditions with minimal atmospheric refraction. Finally, the aircraft noise measurements have to be corrected for the noise background levels.

## 5.7 Microphones

A microphone is a device that converts the sound pressure into a measurable electrical signal. A microphone is constructed in such a way that there is a linear relationship between the electrical signal and the acoustic signal. An influence of the microphone on the sound field to be measured is, of course, undesirable and should hence be minimised. Many technical implementations of microphones exist. Of interest here are non-directional devices that directly measure (sound) pressure. Such a device is the so-called condenser microphone that we will discuss here.

Basically, the condenser microphone is a capacitor or condenser consisting of two parallel plates, one of which is very light and flexible (the membrane or diaphragm). The second plate is a stiff electrode positioned very close to the membrane (and isolated from it). A schematic of the condenser microphone is given in figure 5.12.

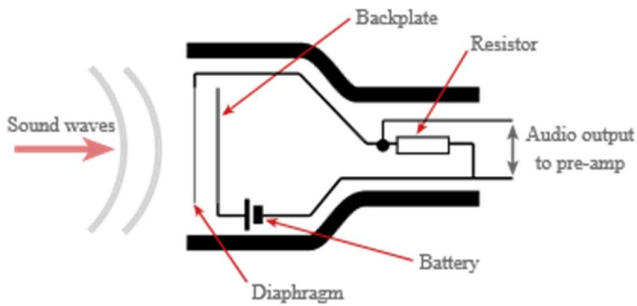


Figure 5.12: The condenser microphone.

A pressure change will cause the membrane to bend, which changes the capacitance of the condenser. The capacitor is charged and this charge  $Q_0$  is kept constant by a suitable electrical circuit. Hence, the varying capacitance will result in a varying voltage across the condenser plates. Let the voltage and capacitance of the condenser at rest be  $U_0$  and  $C_0$ ,

respectively. The capacitance of a parallel plate condenser is  $C_0 = \epsilon \frac{A}{d}$  with  $A$  the area of

the membrane,  $d$  the distance between the plates and  $\epsilon$  the permittivity of space (i.e. the air between the plates). The capacitance of the condenser in a sound pressure field is  $C = \epsilon \frac{A}{d + \delta}$  with  $\delta$  the variation in distance between the plates, i.e. the deflection of the

membrane. The corresponding voltage is  $U_0 + u$  with  $u$  the variation in voltage. Hence, in a pressure field we have

$$U_0 + u = \frac{Q_0}{C} = \frac{Q_0}{\epsilon A} (d + \delta) = \frac{Q_0}{C_0} \left(1 + \frac{\delta}{d}\right) = U_0 \left(1 + \frac{\delta}{d}\right) \quad (5.23)$$

and thus

$$u = U_0 \frac{\delta}{d} \quad (5.24)$$

i.e. a linear relationship between the variation in voltage  $u$  and the deflection  $\delta$  of the membrane. We note that a condenser microphone needs an external power supply ( $U_0$ ), which can be regarded as a disadvantage. However, condenser microphones are used when high quality measurements are required.

Note: Microphones, based on piezo-electricity, are more robust and simpler to use than condenser microphones. A piezo-electric material is a solid which generates an electric charge in response to an applied mechanical load (e.g. due to the sound wave). Still, for accurate measurements condenser microphones are being used.

We now have to investigate the relation between the sound pressure  $p'$  and the deflection  $\delta$  of the membrane, i.e. the mechanical properties of the condenser microphone. Basically, the mechanics of a condenser microphone can be considered as a mass-spring system: the membrane is the mass  $m$ , the air layer between membrane and electrode is the spring

(spring constant  $k$ ), whereas some damping is provided by air friction in this layer (damping constant  $b$ ). Like in section 4.3 we are dealing with the problem of forced oscillation, the governing differential equation of which reads

$$m \frac{d^2x}{dt^2} + b \frac{dx}{dt} + kx = F_0 e^{i\omega t} \quad (5.25)$$

with  $x(t)$  the instantaneous deflection of the membrane and  $F_0 e^{i\omega t}$  the sinusoidal driving force as delivered by an acoustic wave with frequency  $\omega$ . Introducing the resonance frequency  $\omega_0 = \sqrt{\frac{k}{m}}$  and the static deflection  $x_0 = \frac{F_0}{k}$ , the solution is given as

$$x(t) = x_0 \frac{e^{i\omega t - \phi}}{\sqrt{\left(1 - \left(\frac{\omega}{\omega_0}\right)^2\right)^2 + \left(\frac{1}{Q} \frac{\omega}{\omega_0}\right)^2}} \quad (5.26)$$

with

$$\tan \phi = \frac{\frac{1}{Q} \frac{\omega}{\omega_0}}{1 - \left(\frac{\omega}{\omega_0}\right)^2}. \quad (5.27)$$

$Q$  is the so-called quality factor given by  $Q = \sqrt{\frac{mk}{b^2}}$ .

Figure 5.13 shows the ratio of the peak value  $x_{\max}$  of  $x(t)$  and the static deflection  $x_0$  as a function of reduced frequency  $\frac{\omega}{\omega_0}$  for various values of  $Q$  (low  $Q$  means high damping, high  $Q$  means low damping).

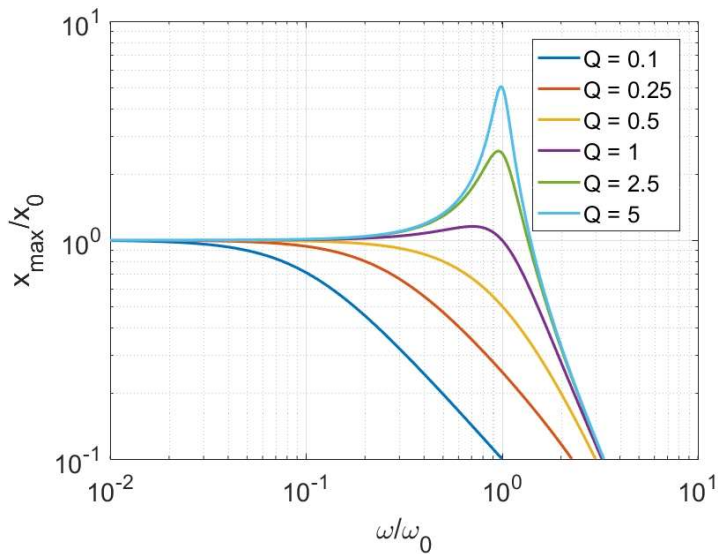


Figure 5.13: Relative amplitude of a damped mass-spring system as a function of reduced frequency for various values of the quality factor.

From the figure it is observed that the deflection of the membrane is independent of frequency (and equal to the static value  $x_0$ ) over a wide frequency range. Around the resonance frequency a significant increase occurs for values of  $Q$  larger than unity. For

frequencies higher than the resonance frequency the value of  $\frac{x_{\max}}{x_0}$  decreases quickly with

increasing frequency. For a condenser microphone this has the following implication: the voltage variation  $u$  (which directly proportional to the membrane deflection  $\delta$ , see equation 5.24) is directly proportional to the sound pressure  $p'$  at the membrane for frequencies lower than the resonance frequency.

The sensitivity  $\frac{u}{p'}$  of a condenser microphone is typically 50 mV/Pa and is governed by the

spring constant  $k$  of the air layer between membrane and electrode. Lowering  $k$  results in an increase in sensitivity (see formula above for the static deflection), but reduces the useful frequency range of the microphone as this will decrease the resonance frequency  $\omega_0$ . Note that a factor of 2 reduction in  $\omega_0$  results in a factor of 4 decrease of  $k$  and hence a factor of 4 increase in sensitivity.

The membrane of the microphone can be made very thin and hence very light. Membranes of a few micrometres thick are applied, resulting in high resonance frequencies up to 70 kHz or higher for microphones with a diameter of approximately 25 mm. Reducing stiffness (i.e. lowering  $k$ ) can be achieved by e.g. perforating the electrode. This also varies the damping constant  $b$ . In this way microphones can be manufactured that satisfy very narrow tolerances on sensitivity and frequency characteristics.

As mentioned at the beginning of this section, the influence of the microphone on the sound field to be measured should be minimised. However, a sound field is markedly disturbed when in that sound field an object is placed with sizes not small compared to the wavelength of the sound and if the acoustic resistance ( $\rho_\infty c$ ) of the object is different from that of the medium surrounding it. This will definitely occur for microphones (the object in the sound field) at high frequencies. The resulting reflections cause the pressure on the membrane to be higher than the pressure of the undisturbed sound field (see also section 1.4, standing waves). Hence, the microphone will give a too high response. This effect is dependent on the propagation direction of the sound field with respect to the membrane's plane. Further, the effect can be influenced by a mechanical attachment such as a diffuser.

The effect of the reflection at the membrane of a microphone (with a 13 mm diameter membrane) is illustrated in figure 5.14 for various angles of incidence of the sound. It is observed that the effect is largest for incoming sound that is perpendicular to the plane of the membrane ( $0^\circ$  in the figure) and smallest for sound with a propagation direction parallel to the membrane's plane ( $90^\circ$ ). Also indicated in the figure is a separate curve for diffuse (random incidence) sound. These so-called free field correction curves need to be added to the pressure sensitivity of the microphone. (We note that we have to pay attention to this angular dependence of the microphone response in aircraft flyover measurements as then the incidence angle is continuously varying).

As seen in figure 5.13, the frequency behaviour of this pressure sensitivity is very much dependent on the quality factor  $Q$  and hence on the damping constant  $b$ . This offers the possibility to compensate the increase in sensitivity at higher frequencies (due to reflections) with the decrease in mechanical sensitivity (see curves in figure 5.13 for  $Q < 1$ ) by accurately adjusting the damping constant  $b$ . This results in a flat frequency response up to frequencies far above the resonance frequency. In practice this compensation is implemented for two situations: normally incident sound ( $0^\circ$ ) and random incidence sound.

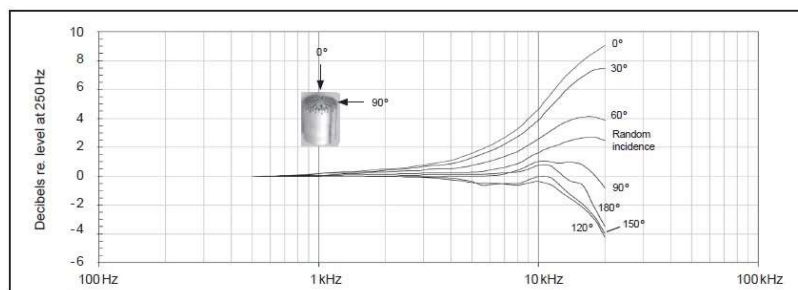


Figure 5.14: Effect of reflection at the membrane of a 13 mm microphone for various angles of incidence of the sound (the so-called free field correction curves). An incidence angle of  $0^\circ$  corresponds to incoming sound that is perpendicular to the plane of the membrane, whereas  $90^\circ$  corresponds to sound with a propagation direction parallel to the membrane's plane.

Manufacturers calibrate the sensitivity of their microphones before delivery. A careful calibration (and regular check) is mandatory for most applications discussed in these lecture notes. An example of such calibration data is shown in figure 5.15. The lower curve is the above mentioned mechanical sensitivity in which the effect of damping is clearly observed. The upper curve is the so-called free field sensitivity (shown here for normal incidence, i.e. 0°). It is clearly observed that the reflection effects at high frequency (see figure 5.14) are nicely compensated by the carefully chosen damping constant.

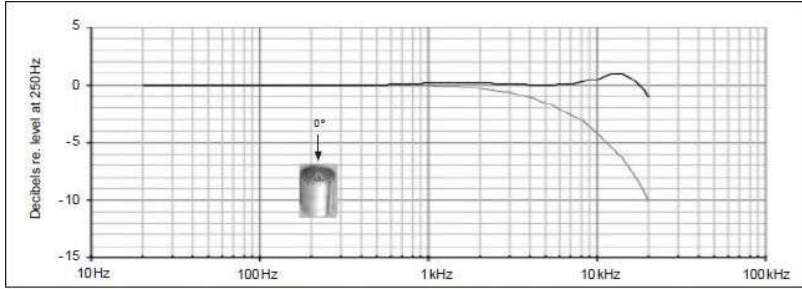


Figure 5.15: Upper curve: sensitivity at 0° angle of incidence (in dB units) of a 13 mm microphone (relative to the sensitivity at 250 Hz). This flat response is the result of a compensation of the high-frequency reflection effects (see figure 5.14) by the high-frequency pressure sensitivity at relatively low Q (the lower curve in this figure).

The calibration data are given in dB units relative to the sensitivity at 250 Hz. Indeed, manufacturers usually determine the absolute sensitivity at a single frequency. Further, the pressure sensitivity (lower curve in figure 5.15) is determined as a function of frequency at a single sound pressure level. For determining the absolute sensitivity use is made of a reference sound source with an exactly known sound level. The most reliable sound source for this is the so-called pistonphone (a mechanical device that basically consists of a moveable piston). The obtained absolute sensitivity at 250 Hz of the microphone of figure 5.15 amounts to 50 mV/Pa, corresponding to -26 dB re 1 V/Pa).

According to equation 1.13 the sound pressure level in dB (here denoted by  $L$  instead of SPL) is given by

$$L = 20 \log \left( \frac{p_e}{p_{e0}} \right). \quad (5.28)$$

Hence, for obtaining  $L$  using a microphone first the effective pressure needs to be determined according to equation 1.4:

$$p_e = \left[ \frac{1}{T} \int_0^T [p'(t)]^2 dt \right]^{1/2}. \quad (5.29)$$

For the integration time  $T$  usually fast averaging (called mode  $F$  with  $T = 0.125$  s) or slow averaging (called mode  $S$  with  $T = 1$  s) can be chosen. These modes reasonably agree with the direct perception of the human ear that has an integration time of about 30 – 50 ms.

The obtained sound pressure level can be integrated over longer times according to

$$L_{\text{eq,T}} = 10 \log \left[ \frac{1}{T} \int_0^T 10^{\frac{L(t)}{10}} dt \right]. \quad (5.30)$$

This is the so-called equivalent sound level, which is treated in section 6.4 as one of the frequently-used noise metrics. Here  $L(t)$  is the instantaneous sound level, obtained using equations 5.28 and 5.29. Hence, the integration time  $T$  in this equation 5.30 is not the same as the  $T$  of equation 5.29 (usually much longer: from a few seconds to e.g. a 24 hour period).

Note: In formula 6.9 for the equivalent sound level as introduced in section 6.4,  $L(t)$  is replaced by  $L_A(t)$ , the instantaneous A-weighted sound pressure level. This A-weighting is also treated in chapter 6.

Note: A special type of microphone is the so-called ‘electret’ microphone. It is a condenser microphone with the same principle of working, i.e. an acoustic wave results in changes in capacity which in turn gives changes in the voltage across the plates. The relatively high supply voltage to maintain the constant charge  $Q_0$  on the plates (typically 50 V in the case of the condenser microphones described above) is not needed for an electret device, since the plates are made of a special dielectric material that is permanently charged. Only a few volts from a small battery are required for the integrated preamplifier. Today, electret microphones are applied in mobile devices such as cell phones and laptops, as they are cheap (about 2 €) and small (the cylindrically-shaped electrets have a typical cross section and thickness of about 5 mm, see picture below).



*Exercises*

Question 1

From a spectrogram obtained from a flyover of an aircraft equipped with turbo fan engines (each with 24 blades) we derived the frequencies of the third, fourth, fifth and sixth harmonic of the fan:  $f_3 = 3450$  Hz,  $f_4 = 4660$  Hz,  $f_5 = 5860$  Hz,  $f_6 = 6980$  Hz. Determine the frequency of the first harmonic ( $f_1$ ) and the corresponding fan RPM.

Question 2

A sound is measured by a FFT analyser, which uses a sample frequency of 20 kHz. At each measurement 4096 data samples are taken (FFT size). Calculate the corresponding frequency resolution.

Question 3

Explain briefly why music is usually recorded digitally at a sample frequency of 44.1 kHz.

Question 4

A small propeller-driven airplane is operating statically on the ground. The propeller is two-bladed and its rotational speed is 1800 rpm. What is the second overtone of the blade passage frequency of the propeller?

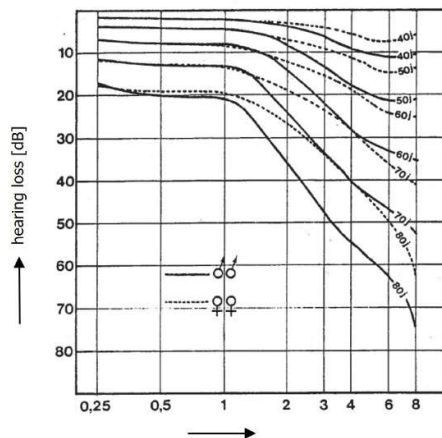
## Chapter 6 Noise metrics

### 6.1 Equal loudness contours and overall loudness

The loudness of a sound as perceived by humans depends not only on the sound pressure level SPL, but also on frequency. The solid black line in figure 6.1 indicates the limits of audibility in terms of frequency and SPL. As mentioned in chapter 1 the audible frequencies range from 20 Hz to 20 kHz. The lower part of the solid line indicates the threshold of hearing, whereas the upper part of the line indicates the threshold of pain. Both thresholds depend on frequency, e.g., a 100 Hz tone must be about 40 dB higher in SPL than that of a 1000 Hz tone in order to be equally loud (at the threshold of hearing). Figure 6.1 also indicates the areas of speech and music in terms of frequency and SPL.

Note: The minimum around 3.5 kHz is due to an outer ear (i.e. in the auditory canal) resonance phenomenon. The ear canal is approximately  $\ell = 2.5$  cm in length and can be considered as a tube that is open at one end. The first resonance frequency of an half-open tube is given by  $f = c / (4\ell)$ , which equals  $340/0.1 = 3400$  Hz. This resonance makes sounds at frequencies around 3400 Hz louder, hence lowering the threshold of hearing below that at 1 kHz (i.e. from 0 dB at 1 kHz to almost -10 dB at 3.4 kHz).

Note: Hearing loss is caused by a number of factors, including ageing and exposure to noise. There is a progressive loss of hearing with aging, predominantly at the higher frequencies, i.e. when people get older the threshold of hearing moves upward (typically 30 dB at 4 kHz for a 60 year old man, see figure below). Noise-induced hearing loss also results in elevated hearing thresholds, again predominantly at the higher frequencies. This loss is largest in the band 2 – 6 kHz, with a peak in hearing loss at 4 kHz of possibly several tens of dB, depending on the noise exposure. Noise-induced hearing loss depends on both SPL and exposure duration (the greater SPL and/or duration, the greater the loss). Hearing loss is quantified by a so-called ‘audiogram’, which is a graph of the measured threshold of hearing at a standardised set of frequencies in the range 125 Hz – 8 kHz. Audiograms are used for diagnosis of the type of hearing loss.



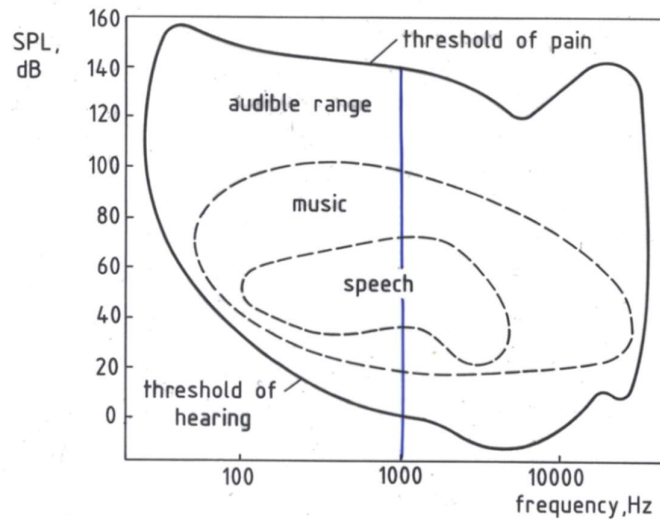


Figure 6.1: Limits of audibility in terms of frequency and sound pressure level (solid line). Also indicated are the areas of speech and music (dashed lines).

Based on sound juries, i.e. a large number of test listeners, the loudness levels of tones have been established, see figure 6.2. The solid lines are so-called equal loudness contours. The unit of loudness is the 'phon', the definition of which is as follows: a tone (or narrowband noise) has a loudness level of  $X$  phons if it is equally loud as a tone with a SPL of  $X$  dB at 1 kHz. For the loudness concept 1 kHz is thus the reference frequency, i.e. at 1 kHz the phon scale coincides with the SPL scale. The 0 phon contour corresponds to the threshold of hearing, whereas the 120 phon contour corresponds to the threshold of pain.

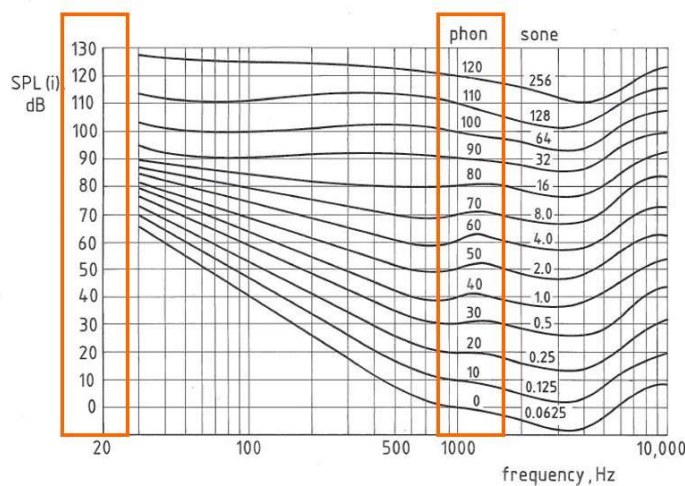


Figure 6.2: Equal loudness contours in terms of frequency and sound pressure level. Each contour is labelled by its phon value and corresponding sone value.

The sensitivity of the human ear decreases significantly with decreasing frequency below 1 kHz, but the contours are less dependent on frequency for high phon levels than for low phon levels. We can read from the contours that at 40 phon a 100 Hz tone must be 24 dB higher than the SPL at 1000 Hz. However, at 70 phon a 100 Hz tone must be only 9 dB higher than the SPL at 1000 Hz.

An increase of loudness with 10 phon is perceived as being twice as loud. This is reflected in the ‘sone’ scale of loudness. Denoting loudness in sone by  $s$  and loudness level in phon by  $p$ , the relation between  $s$  and  $p$  is given by

$$s = 2^{(p-40)/10} \quad (6.1)$$

i.e. the reference loudness level of 40 phon corresponds to 1 sone. Equation 6.1 can also be written as

$$p = 40 + 10 \log s = 40 + 33.3 \log s \quad (6.2)$$

The overall loudness of more complex sounds than tones, e.g., broadband noise, is computed as follows. The overall loudness  $S$  in sone is given by

$$S = s_{\max} + F \left( \left( \sum_{i=1}^n s_i \right) - s_{\max} \right) \quad (6.3)$$

with  $s_i$  the sone values in the subsequent frequency bands,  $s_{\max}$  the maximum sone value and  $F$  the so-called ‘masking factor’. Equation 6.3 thus accounts for ‘masking’, i.e. the phenomenon that one frequency component can make it harder or impossible to hear another frequency component. The masking factor  $F$  equals 0.3 for octave bands and 0.15 for 1/3-octave bands, respectively. The overall loudness level  $L_L$  in phon is given cf. equation 6.2, i.e.

$$L_L = 40 + 33.3 \log S. \quad (6.4)$$

## 6.2 Equal noisiness contours and perceived noise level

For aircraft noise often ‘perceived noise level’ is used instead of (overall) loudness level. Figure 6.3 presents the so-called equal noisiness curves, also obtained with sound juries and similar to the equal loudness curves in sone (see figure 6.2). Noisiness is expressed in the unit ‘noy’ instead of sone.

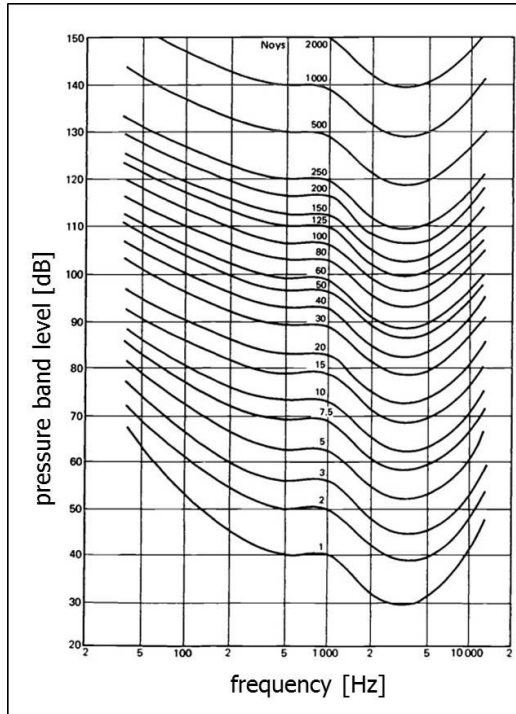


Figure 6.3: Equal noisiness curves in terms of frequency and pressure band level. Each curve is labelled by its noy value.

The overall noy value is given by

$$N = n_{\max} + F \left( \left( \sum_{i=1}^n n_i \right) - n_{\max} \right) \quad (6.5)$$

with  $n_i$  the noy values in the subsequent 1/3-octave bands,  $n_{\max}$  the maximum noy value and  $F$  the masking factor (which is equal to 0.15 here as this analysis is only performed for 1/3-octave bands). Perceived noise level  $L_{\text{PN}}$  (in units PNdB) is again given by equation 6.2, i.e.

$$L_{\text{PN}} = 40 + 33.3 \log N. \quad (6.6)$$

We note that sometimes a tone correction or penalty is applied to account for increased noisiness due to tones present in the (aircraft) noise data. Then the so-called 'tone corrected perceived noise level'  $L_{\text{TPN}}$  (in units TPNDB) is obtained.

### 6.3 A-weighting and overall A-weighted sound pressure level

For the measurement of loudness of a noise signal, first the sound pressure levels in the various frequency bands are determined (according to the method described in chapter 5). Subsequently, the SPL values in e.g. the 1/3-octave bands are weighted according to one of the curves depicted in figure 6.4. Curve A, based on the equal loudness contour at 40 phon (see figure 6.2), is the most widely applied weighting function and is called A-weighting. Other weighting functions are being used: B-weighting based on the equal loudness contour at 70 phon, C-weighting based on the equal loudness contour at 100 phon and D-weighting based on the equal noisiness contour at 40 noy (see figure 6.3). We note that the weighting functions are only frequency dependent and do not account for loudness to be dependent on both frequency and SPL (see figure 6.2).

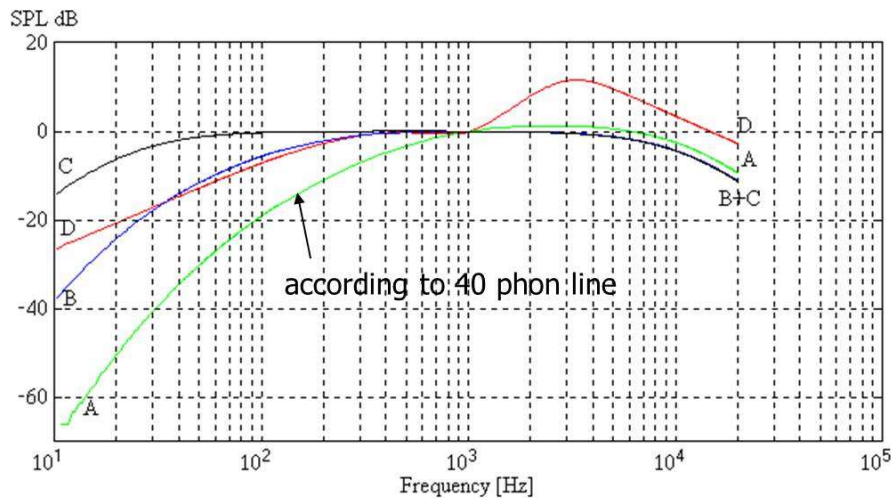


Figure 6.4: A-, B-, C- and D-weighting functions.

The A-weighting function  $\Delta L_A$  is given by

$$\Delta L_A = -145.528 + 98.262 \log f - 19.509 (\log f)^2 + 0.975 (\log f)^3 \quad (6.7)$$

and is graphically depicted in figure 6.5 for the 1/3-octave band centre frequencies.

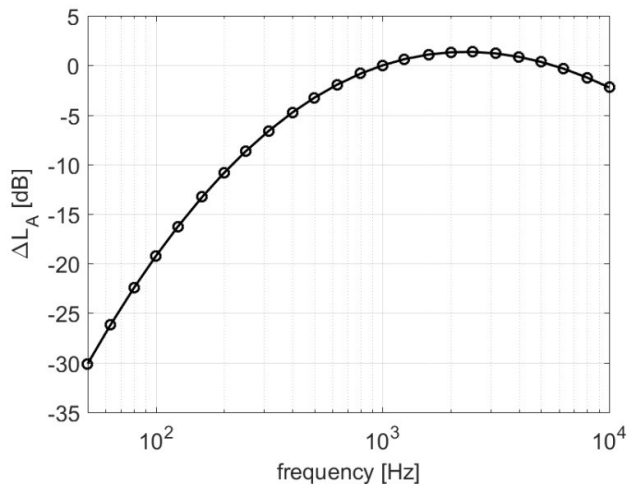


Figure 6.5: A-weighting function according to equation 6.7 (solid line). The circles indicate the positions of the 1/3-octave band centre frequencies.

The overall A-weighted sound pressure level  $L_A$  (in units dBA) is subsequently determined according to

$$L_A = 10 \log \sum_i 10^{\frac{SPL(i)+\Delta L_A(i)}{10}} \quad (6.8)$$

where the summation is over the frequency bands (represented by index  $i$ ). Note the similarity between this equation and that for the overall sound pressure OSPL introduced in chapter 5 (equation 5.19).

Figure 6.6 shows the effect of A-weighting of a 1/3-octave band spectrum measured for a typical propeller aircraft. The effect of A-weighting on the overall sound pressure level is a 7 dB reduction (OSPL = 126.7 dB and  $L_A$  = 119.6 dBA).

Note: Also indicated is the spectrum (blue line) calculated for the situation of a noise barrier in between source (i.e. the propeller engine) and receiver. For this calculation the geometry of figure 4.30 is used and the Maekawa formula, equation 4.89, is used for the calculation of the excess attenuation for each 1/3-octave band centre frequency.

Figure 6.7 shows two completely different aircraft noise spectra (the two black curves). In spectrum 1 the low frequencies dominate, whereas in spectrum 2 the high frequencies dominate. However, their OSPL is exactly the same, i.e. 84.5 dB. The effect of A-weighting (red curves) is completely different, as A-weighting has much more effect at the low frequencies (high frequencies are more annoying). Therefore,  $L_A$  = 74.2 dBA for spectrum 1 (a reduction of more than 10 dB), whereas  $L_A$  = 84.7 dBA for spectrum 2 (i.e. A-weighting has hardly any effect).

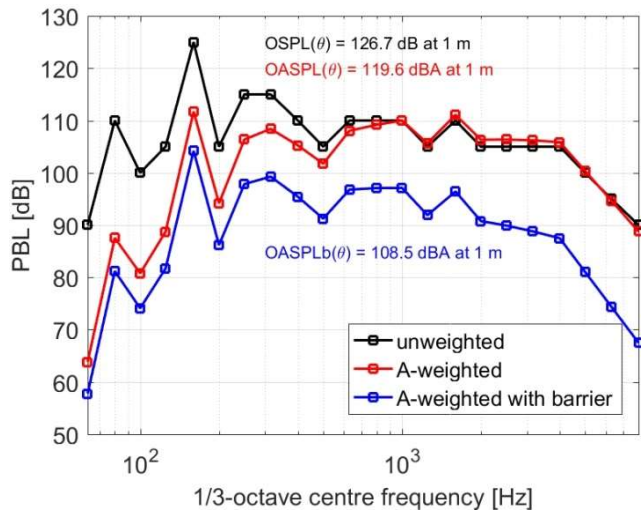


Figure 6.6: Black curve: 1/3-octave band spectrum measured for a typical propeller aircraft. The red curve is the 1/3-octave band spectrum after A-weighting. The blue curve is the A-weighted 1/3-octave band spectrum calculated for the situation of a noise barrier in between source, i.e. the propeller engine, and receiver (using the geometry of figure 4.30).

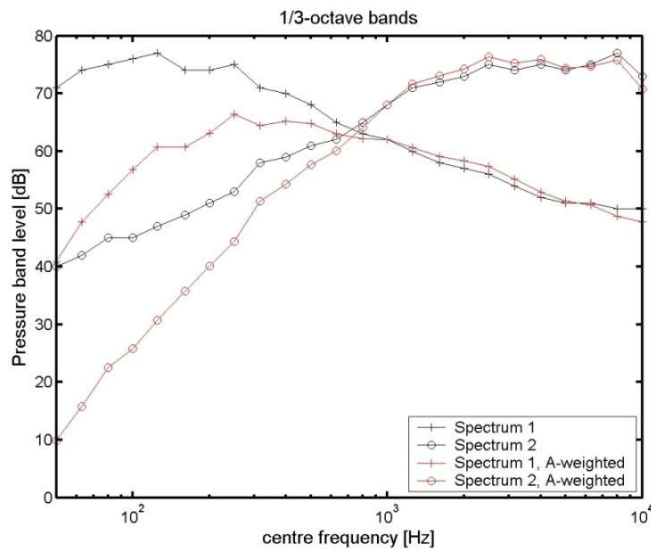


Figure 6.7: A noise spectrum with low frequencies dominating (black curve, spectrum 1) and a noise spectrum with high frequencies dominating (black curve, spectrum 2). The red curves show the effect of A-weighting.

#### 6.4 Sound exposure level\*

In the previous sections of this chapter we have discussed noise metrics for stationary noise signals only. For non-stationary signals, e.g. from aircraft flyovers, the effect of the duration of the noise signal has to be taken into account in some way, although we could simply quantify the maximum overall A-weighted sound pressure level  $L_{A,\max}$ . However, the human ear is not only sensitive to the maximum noise level, but is also sensitive to the

duration of a noise event. Hence, two events may have the same  $L_{A,\max}$ , but the one event may be more annoying due to a longer duration. Figure 6.8 shows a typical noise event from an aircraft flyover where the instantaneous overall A-weighted sound pressure level  $L_A(t)$  is plotted as a function of time  $t$ .

Note: The values of the function  $L_A(t)$  are obtained for say every 0.1 seconds of the noise data. These data chunks of 0.1 seconds long are Fourier transformed and then, for each data chunk, the SPL values in the 1/3-octave bands are obtained and subsequently A-weighted. Subsequently, the instantaneous overall A-weighted sound pressure level is determined according to equation 6.8 (for each data chunk of 0.1 second).

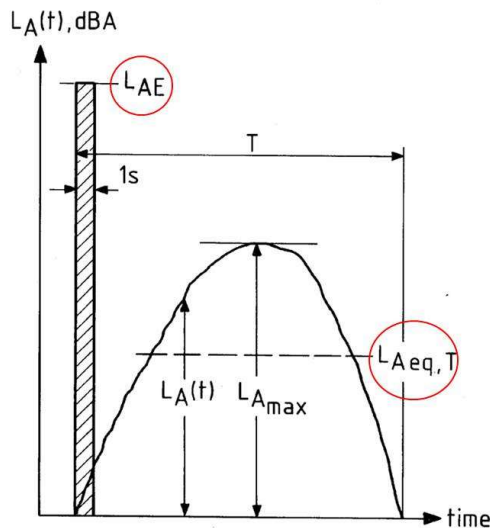


Figure 6.8: Typical noise event from an aircraft flyover where the instantaneous overall A-weighted sound pressure level  $L_A(t)$  is plotted as a function of time. Also indicated are the maximum overall A-weighted sound pressure level  $L_{A,\max}$ , the equivalent A-weighted sound level  $L_{A\text{eq},T}$  (dashed line) and the sound exposure level  $L_{AE}$  (shaded area).

The ‘equivalent A-weighted sound level’ (EAL) is a noise metric that integrates  $L_A(t)$  over time according to

$$L_{A\text{eq},T} = 10 \log \left[ \frac{1}{T} \int_0^T 10^{\frac{L_A(t)}{10}} dt \right]. \quad (6.9)$$

The units of this metric is dBA and the integration time  $T$  is chosen such that it covers the time interval during which  $L_A(t)$  is not more than 10 dBA below the maximum value  $L_{A,\max}$ . The integration time  $T$  is then known as the ‘10 dBA down time’. A larger value than 10 dBA is not needed as only the highest levels of  $L_A(t)$  contribute significantly to the integral.

The so-called ‘sound exposure level’ SEL (also in units dBA) removes the dependence on integration time  $T$  and is given by

$$L_{AE} = 10 \log \left[ \frac{1}{T_1} \int_0^T 10^{\frac{L_A(t)}{10}} dt \right] \quad (6.10)$$

with  $T_1 = 1$  second. Integration time  $T$  is chosen in the same way as that for EAL. SEL is commonly used for aircraft noise events. Both EAL (or  $L_{A,eq,T}$ ) and SEL (or  $L_{AE}$ ) are indicated in figure 6.8. As can be seen from the figure, EAL is a sort of average  $L_A$  value, whereas SEL is the one-second long steady level that contains as much energy as the varying level over the full event.

The relation between EAL and SEL is given by

$$L_{A,eq,T} = L_{AE} - 10 \log \left( \frac{T}{T_1} \right). \quad (6.11)$$

As  $T$  is often larger than  $T_1$  (= 1 second),  $L_{AE}$  is greater than  $L_{A,eq,T}$ .

The process of determining the SEL of two noise events is further illustrated in figure 6.9. The first event has a higher  $L_{A,max}$  than the second event (78 dBA compared to 74 dBA), but the second event has a longer duration. As a result the SEL of the second event is higher than that of the first event (87 dBA compared to 82 dBA). Hence, a noise event with a higher  $L_{A,max}$  can have a lower SEL than a longer event with a lower  $L_{A,max}$ .

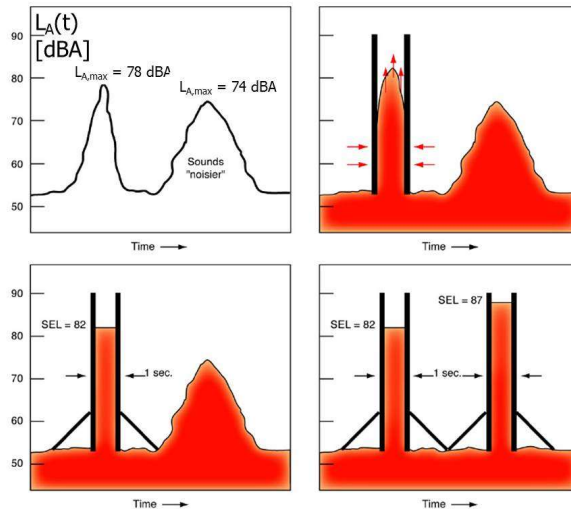


**Figure 6.9: Illustration of the process of determining sound exposure level for two noise events with different  $L_{A,max}$  and different duration.**

Another time-integrated noise metric is the ‘effective perceived noise level’, which is based on the instantaneous perceived noise level  $L_{PN}(t)$  (equation 6.6), or its tone-corrected version  $L_{TPN}(t)$ . It is given as

$$L_{\text{EPN}} = 10 \log \left[ \frac{1}{T_{10}} \int_0^T 10^{\frac{L_{\text{PN}}(t)}{10}} dt \right]. \quad (6.12)$$

For this metric  $T_{10}$  is chosen to be 10 seconds. A practical numerical implementation of this formula is given by

$$L_{\text{EPN}} \approx 10 \log \left[ \frac{\Delta t}{T_{10}} \sum_{k=t_1}^{t_2} 10^{\frac{L_{\text{PN}}(k)}{10}} \right] \quad (6.13)$$

where the instantaneous  $L_{\text{PN}}(t)$  function is sampled every  $\Delta t = 0.5$  second from  $t_1$  to  $t_2$  (with integration time  $T = t_2 - t_1$  corresponding to a '10 PNdB down time').  $L_{\text{EPN}}$  is expressed in units EPNdB.

## 6.5 Day-night average level

In this section we treat the most frequently used metrics for total noise exposure. Such metrics are capable to quantify the impact of noise in airport communities due to air traffic activities. The metrics treated here provide a way to describe the noise dose for a 24 hour period. They are based on  $L_A$  and/or SEL and can incorporate weighting factors depending on the time of the day, evening or night the noise events take place.

The 'day-night average level' DNL (in units dBA) is defined as

$$L_{\text{DN}} = 10 \log \left[ \frac{1}{86400} \int_0^{86400} w(t) 10^{\frac{L_A(t)}{10}} dt \right] \quad (6.14)$$

i.e. a formula similar to the single-event metric  $L_{A_{\text{eq},T}}$  (equation 6.9). Here, the averaging is over a period of 24 hours, i.e. 86400 seconds. As before,  $L_A(t)$  is the instantaneous A-weighted sound level (in dBA). The weighting factors or penalties are as follows:  $w = 1$  (0 dB) for noise events occurring in the time window 07:00 – 23:00 (i.e. during day-time) and  $w = 10$  (10 dB) for noise events in the time window 23:00 – 07:00 (i.e. during night-time). This means that each night event is counted ten times. The 'day-evening-night average level'  $L_{\text{DEN}}$  is defined in the same way as  $L_{\text{DN}}$ , but now an extra penalty of  $w = \sqrt{10}$  (5 dB) is added for the evening period 19:00 – 23:00.

Figure 6.10 gives a typical example of how aircraft noise events are distributed over time during a full 24 hour period. Figure 6.11 zooms in on a few noise events around 22:00 (going from day to night) and illustrates the effect of the penalty for a night event. Also the resulting  $L_{\text{DN}}$  value is indicated.

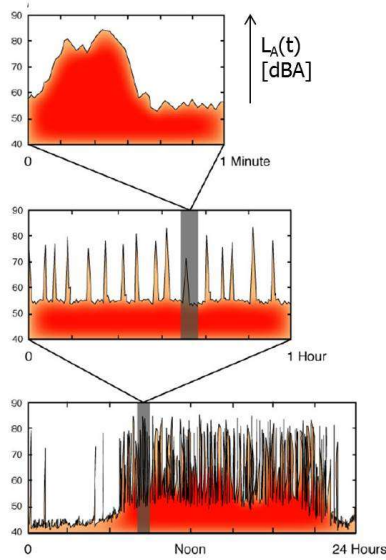


Figure 6.10: Typical distribution of aircraft noise events over a full 24 hour period (bottom figure). The middle figure is a zoomed in version for one hour. The upper figure is a further zoomed in version for one minute where only one event is left. Plotted on the y-axis is the instantaneous overall A-weighted sound pressure level  $L_A(t)$ .

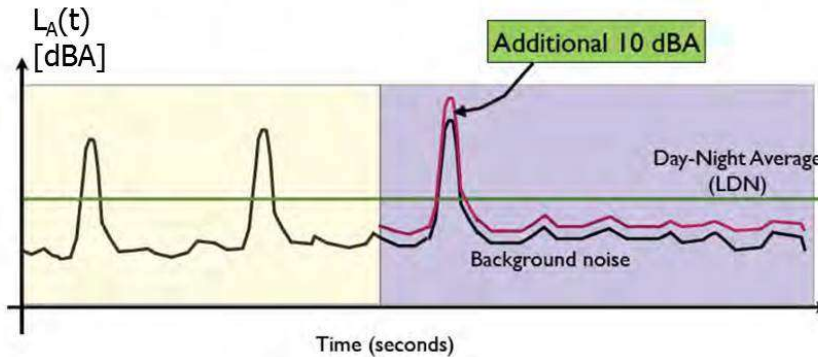


Figure 6.11: Aircraft noise events around 22:00 when going from day (yellow area) to night (purple area) and illustration of the effect of the penalty for a night event (red line). Also indicated are the background noise level and the resulting  $L_{DN}$  value (green horizontal line).

For non-stationary noise events, e.g. landings and take-offs of aircraft at airports, it is convenient to use the corresponding SEL values (when available). Then equation 6.14 becomes

$$L_{DN} = 10 \log \left[ \frac{1}{86400} \sum_{i=1}^N 10^{(SEL_i + W_i)/10} \right] = -49.4 + 10 \log \left[ \sum_{i=1}^N 10^{(SEL_i + W_i)/10} \right] \quad (6.15)$$

with  $SEL_i$  the SEL value of the  $i^{\text{th}}$  noise event,  $W_i$  the corresponding penalty in dB and  $N$  the number of noise events in the 24 hour period.

Note: Often the  $L_{DEN}$  metric is used for a period of a full year. It can then be written as

$$L_{DEN} = 10 \log \left( \sum_{i=1}^{N_d} 10^{\frac{SEL_i}{10}} + \sum_{j=1}^{N_e} 10^{\frac{SEL_j+5}{10}} + \sum_{k=1}^{N_n} 10^{\frac{SEL_k+10}{10}} \right) - 75.0$$

where  $N_d$ ,  $N_e$  and  $N_n$  are the number of (detected) aircraft noise events during day-time, evening-time and night-time, respectively.  $SEL_i$ ,  $SEL_j$  and  $SEL_k$  are the corresponding sound exposure levels of the day-time, evening-time and night-time, respectively. Also, the so-called  $L_{night}$  is an important metric. It is computed for the aircraft noise events during night-time only (without applying the 10 dBA penalty). For a period of a full year it is given as

$$L_{night} = 10 \log \left( \sum_{k=1}^{N_n} 10^{\frac{SEL_k}{10}} \right) - 70.2$$

We illustrate  $L_{DN}$  calculations with two examples. Figure 6.12 shows three situations having the same  $L_{DN}$  value of 65 dBA. In the three situations only day events are considered, i.e.  $W = 0$  dB. In situation 1 there is only one event with a SEL value of 114.4 dBA. The DNL becomes

$$L_{DN} = SEL - 10 \log(86400) = 114.4 - 49.4 = 65 \text{ dBA} .$$

In situation 2 there are 10 events all with the same SEL value but 10 dBA lower than that of situation 1. Then

$$L_{DN} = 104.4 + 10 \log 10 - 49.4 = 65 \text{ dBA} .$$

In situation 3 there are 100 events all with the same SEL value but now 20 dBA lower than that of situation 1. Then we have

$$L_{DN} = 94.4 + 10 \log 100 - 49.4 = 65 \text{ dBA}$$

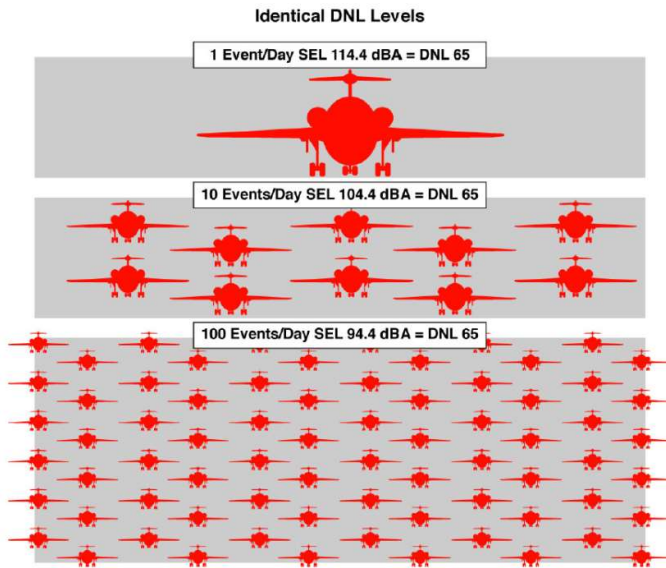


Figure 6.12: Three different situations with the same resulting  $L_{DN}$  value of 65 dBA. From top to bottom the number of aircraft events during day time is 1, 10 and 100, respectively, whereas at the same time the SEL value for each event is 114.4, 104.4 and 94.4 dBA, respectively.

In the second example we consider ten aircraft noise events occurring at an airport in a 24 hour period. Eight events occur during day time and two events occur during night time. Figure 6.13 shows the  $L_A(t)$  curve. Also indicated are the SEL values for each event.

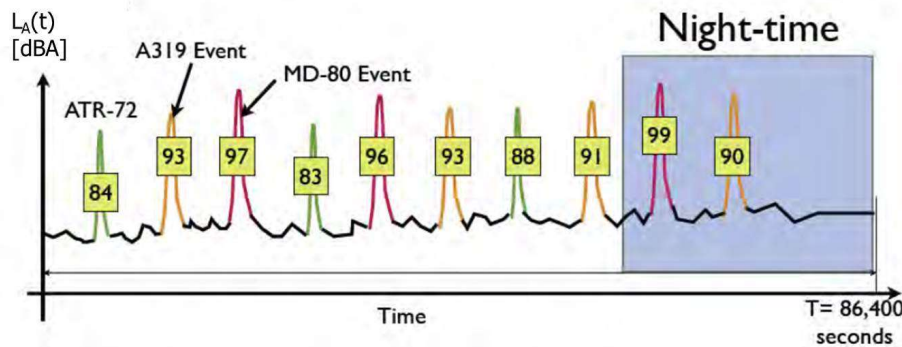


Figure 6.13: An example of 10 aircraft noise events, 8 of which occur during day time and 2 during night time. For each event its SEL value is indicated in the yellow boxes.

The DNL value for this situation is calculated as follows:

$$L_{DN} = -49.4 + 10 \log \left( 10^{\frac{84}{10}} + 10^{\frac{93}{10}} + 10^{\frac{97}{10}} + 10^{\frac{83}{10}} + 10^{\frac{96}{10}} + 10^{\frac{93}{10}} + 10^{\frac{88}{10}} + 10^{\frac{91}{10}} + 10^{\frac{(99+10)}{10}} + 10^{\frac{(90+10)}{10}} \right)$$

the result of which is  $L_{DN} = 61$  dBA . Note the penalty of 10 dB for the last two events.

The day-(evening-)night average level correlates well with community annoyance. This is illustrated in figure 6.14, which shows the percentage of highly annoyed people as a function of  $L_{DEN}$ . The figure shows so-called ‘dose-response’ relations based on extensive surveys held among communities. Typically, 30 % of the population is highly annoyed by aircraft noise at  $L_{DEN} = 55$  dBA, although large differences for different airports can occur.

Note: Also non-acoustic factors, such as demographic, social and personal, can influence the perceived noise annoyance.

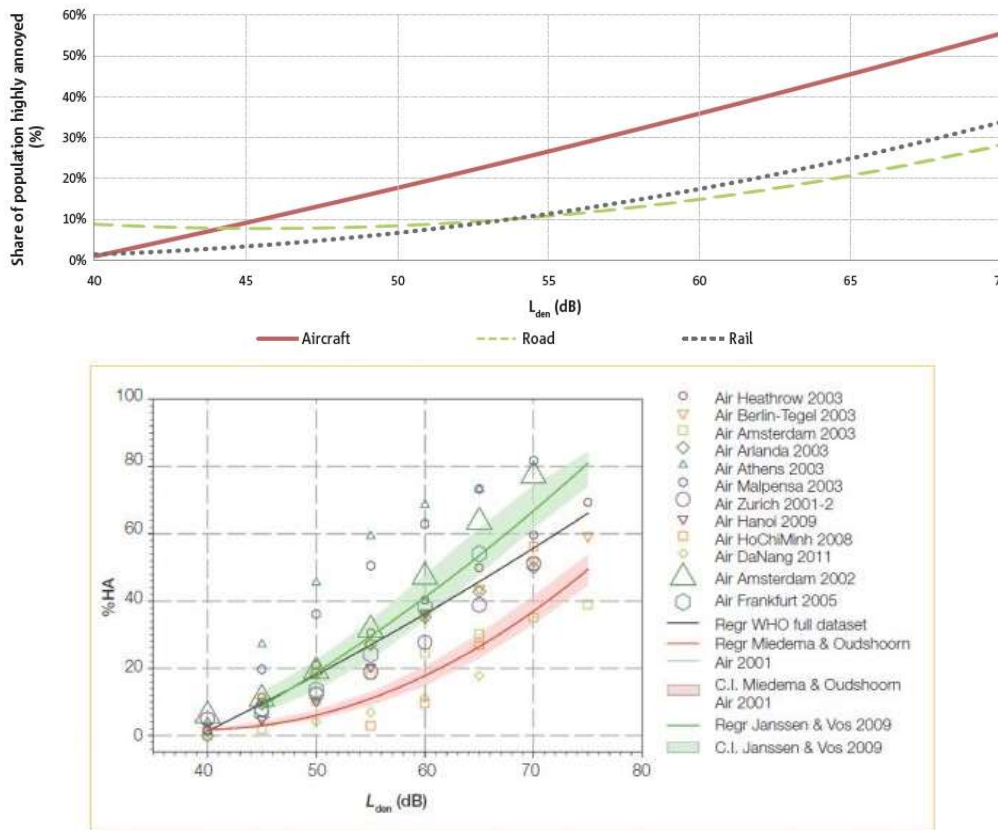


Figure 6.14: Top figure: Estimated percentage of highly annoyed people versus  $L_{DEN}$  by noise from aircraft, road and rail. Bottom figure: Percentage of highly annoyed people versus  $L_{DEN}$  by noise from aircraft for various airports.

## 6.6 Noise contours

Noise contours are lines on the ground where some noise metric has a constant value. A distinction is made between single-event noise contours (or footprints) and multi-event noise contours. Figure 6.15 shows a noise contour of a single noise event, in this case an

aircraft taking off. Along the solid line a metric like  $L_{A,\max}$  or SEL has a constant value. The various phases of take-off (thrust setting, landing gear and flap position), see figure 6.16, are reflected in the shape of the contour.

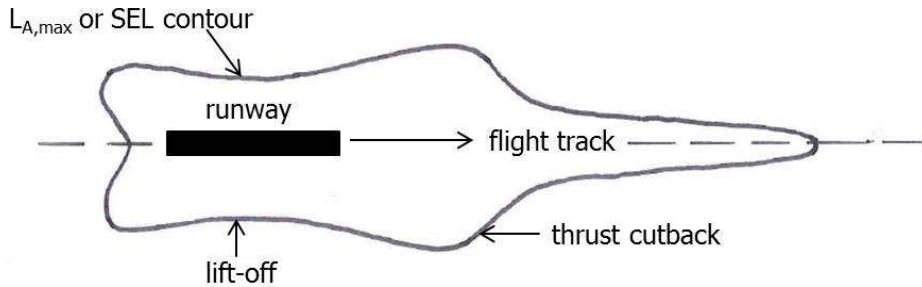


Figure 6.15: Typical noise contour of an aircraft taking off. The various phases of take-off are also indicated.

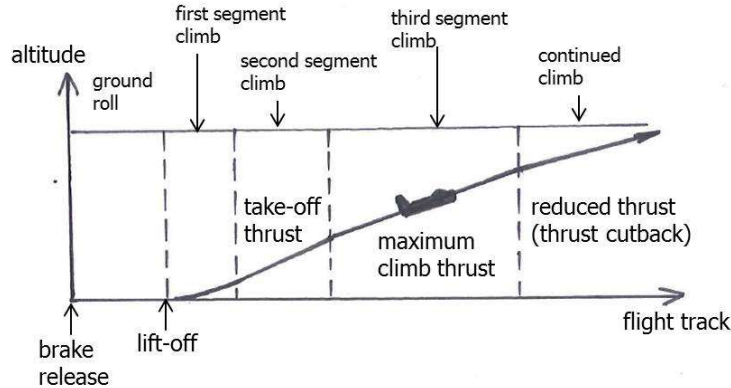


Figure 6.16: The various phases of take-off.

As an example of multi-event noise contours, figure 6.17 shows the  $L_{DEN}$  contours from 40 dBA to 65 dBA (in steps of 2.5 dBA) for the area around Schiphol airport. To get an idea of the amount of annoyance, this map can be converted to ‘percentage of annoyed people’ using the curve of figure 6.14.

Noise contours, either single-event or multi-event, are being used for developing noise abatement procedures, noise assessment around airports (and the related enforcement of environmental laws) and land use planning.

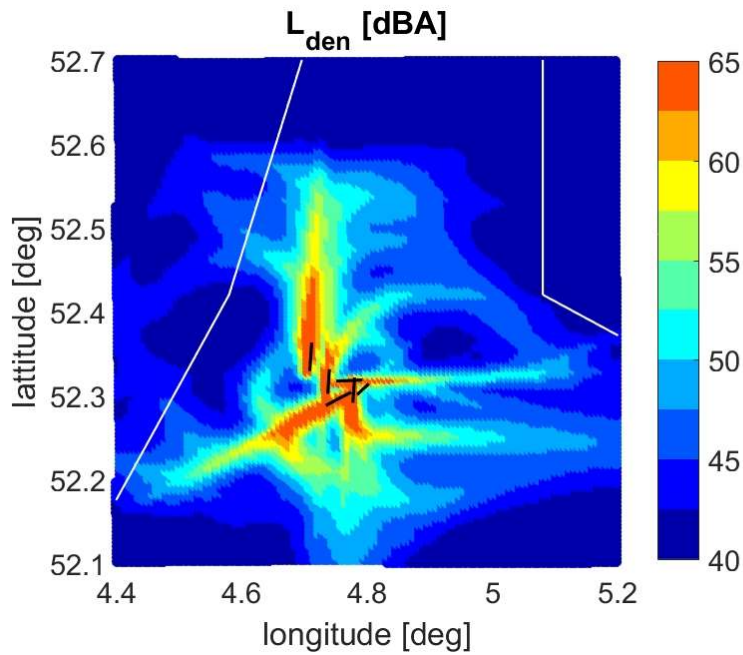


Figure 6.17: Modelled  $L_{\text{DEN}}$  contours for Schiphol area.

We conclude this section with a remark on noise certification of aircraft. This certification is done for each new aircraft by measuring the  $L_{\text{EPN}}$  value (equation 6.12) at the three positions indicated in figure 6.18. These positions are denoted ‘lateral’, ‘flyover’ and ‘approach’, respectively. The certification data for the Boeing 747-400 and the Boeing 777-200 are shown in figure 6.19. These data comprises noise measurements for 377 Boeing 747-400 aircraft and 184 Boeing 777-200 aircraft, respectively. In the figure the mean  $L_{\text{EPN}}$  value and its standard deviation, both in units EPNdB, are indicated. The newer Boeing 777 (in service from 1995) shows significantly lower noise levels compared to the older Boeing 747 (in service from 1969). An explanation for this is partly provided in exercise 2 of chapter 9.

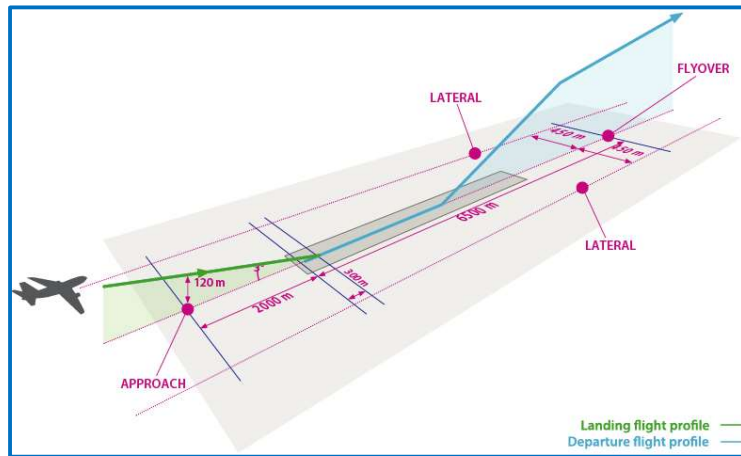


Figure 6.18: The three positions ('lateral', 'flyover' and 'approach') for aircraft noise certification.

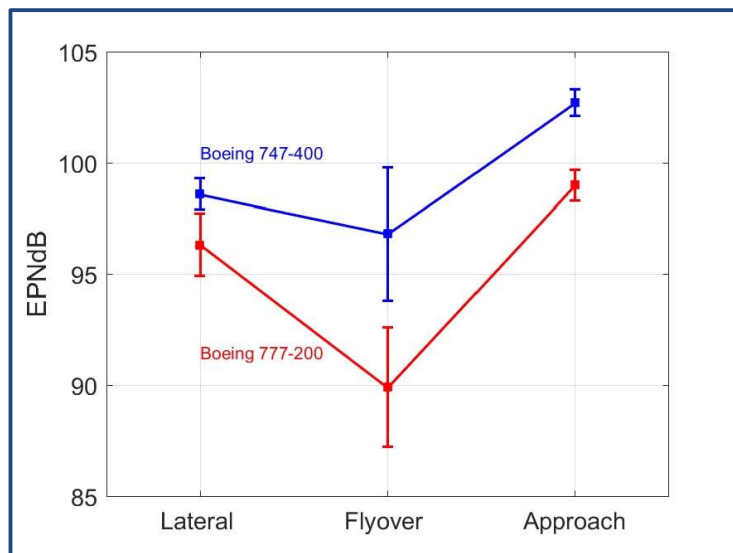


Figure 6.19: Noise certification data for the Boeing 747-400 and the Boeing 777-200.

## 6.7 Dutch aircraft noise model NRM\*

This section describes the model used for predicting aircraft noise in The Netherlands, for Schiphol Airport in particular. The model is called ‘Nederlands Rekenmodel’ (NRM) and uses tables containing data of the following type:

- Classification of aircraft types into classes;
- Flight profiles for each class;
- Noise data for each class (in the form of noise-power-distance (NPD) tables).

These three input data sets are subsequently discussed below.

### 6.7.1 Aircraft classification

Aircraft classes are specified that represent multiple aircraft types with comparable weight and noise characteristics. Aircraft are subdivided into nine weight categories based on their Maximum Take-Off Weight (MTOW) as shown in table 6.1. To exclude small, mostly propeller driven aircraft from the calculations, a threshold has been set at 6000 kg MTOW.

Table 6.1

Weight category	MTOW range (x1000 kg)
1	6-15
2	15-40
3	40-60
4	60-100
5	100-160
6	160-230
7	230-300
8	300-400
9	>400

Since only including weight does not account for technological progress in aircraft design, each weight category is linked to four noise categories based on the aircraft certified noise levels (see section 6.6). These certified noise levels are measured during the certification flight and corrected for atmospheric conditions, following the procedure prescribed by the International Civil Aviation Organisation (ICAO). The ICAO certification measurement setup for the complete landing- and take-off cycle is shown in figure 6.18. For expressing the certification measurements, use is made of the Effective Perceived Noise Level  $L_{EPN}$ , see section 6.4.

The sum of the measurements taken at all certification locations, in units EPNdB, is used to assign an aircraft to a noise class. The sum of the certification measurements of an aircraft is compared to the representative aircraft of the weight class considered. The difference in certified noise level, denoted  $\Delta EPNdB$ , determines the noise class of the aircraft.

Since the noise levels for new aircraft types are generally lower than the representative aircraft within the same weight class, the resulting values for  $\Delta\text{EPNdB}$  are negative. In case of a non-negative value, the aircraft type will automatically be assigned to noise class 1. The four noise classes and corresponding ranges in  $\Delta\text{EPNdB}$  are shown in table 6.2.

Table 6.2

Noise class	range
1	$\Delta\text{EPNdB} > 0$
2	$0 \geq \Delta\text{EPNdB} > -9$
3	$-9 \geq \Delta\text{EPNdB} > -18$
4	$\Delta\text{EPNdB} \leq -18$

Combining the 9 weight categories with the 4 noise classes, 36 aircraft classes are set up, each having one representative aircraft (or a representative aircraft of another noise class with a correction of several dB). A complete overview of the classes and representative aircraft, compiled by NLR, is shown in table 6.3. Because of this representation, noise characteristics are assumed to be independent of the actual configuration and engine type.

Table 6.3

Weight category	Noise class	Noise class	Noise class	Noise class
	1	2	3	4
1	BAe-3100 Jetstream 31	BAe-3100 Jetstream 31	BAe-3100 Jetstream 31	BAe-3100 Jetstream 31
2	Fokker F-28 Fellowship	Fokker F-27 Friendship	Fokker 100	Fokker 70
3	Boeing 737-200	DC-90-30 (-3 dB)	Boeing 737-300 HWFAP	BAe-146-200
4	Boeing 737-200	Boeing 737-300	Boeing 737-300 HWFAP	MD-90
5	DC-8-63	Airbus A-310-203 (+3 dB)	Airbus A-310-203	Boeing 757-200/ RB211-535E4
6	DC-8-63	Boeing 767-300 ER (+3 dB)	Boeing 767-300 ER	Boeing 787-8
7	DC-10-30 (+3 dB)	DC-10-30	DC-10-30 (-3 dB)	Boeing 777-200
8	Boeing 747-200B	Boeing 747-300	Boeing 747-400	Boeing 777-300ER
9	-	-	-	Airbus A380-861

The full list including all aircraft types landing and departing from Schiphol Airport is also available. Each aircraft type is represented by one of the representative aircraft of table 6.3. The dominant category 4/3, which accounts for most of the flights on Schiphol, is shown in table 6.4, which illustrates that most of the operational B737s and A320s are placed in this class.

*Table 6.4*

Aircraft ICAO code	Full name
A306	Airbus A-300B4-600
A319	Airbus A-319, ACJ
A320	Airbus A-320
A321	Airbus A-321
B734	Boeing 737-400 for companies KLM/KLC/TRA/MPH/AHR
B736	Boeing 737-600
B737	Boeing 737-700, BBJ
B738	Boeing 737-800, BBJ2
B739	Boeing 737-900
MD81	McDonnell Douglas MD-81
MD82	McDonnell Douglas MD-82
MD87	McDonnell Douglas MD-87
MD88	McDonnell Douglass MD-88

The aircraft types listed in table 6.4 are represented by the same 737-300, using the ‘HardWall Forward Acoustic Panel acoustic engine modification’ (HWFAP).

#### 6.7.2 Flight profile

For each aircraft class, flight profiles and noise-power-distance (NPD) tables have been constructed. When the aircraft class has been set, the flight profile is selected based on the chosen procedure and the distance of the flight. This profile gives height, flight speed and corresponding thrust setting versus distance for various distance segments. Since these profiles are determined for ideal situations, the real flight profile will in most cases deviate from this, for example because of pilot input, engine transients and actual aircraft configuration.

The flight procedures have been divided into 3 categories, i.e. ‘start’, ‘landing’ and ‘circuit’. The start category consists of 9 procedures, including standard ICAO procedures, but also airport specific procedures like ‘derated’ take-off thrust or ‘Noise Abatement Departure Procedures’ (NADP). The latter are designed for noise reduction and used by several airlines. The landing category has 3 procedures, consisting of aircraft settings being ‘normal instrument approach’, ‘low power low drag approach’ and ‘reduced flap approach’. The normal instrument approach uses the standard landing configuration, whereas ‘low power low drag’ and ‘reduced flap approach’ use adjusted aircraft settings to reduce the emitted noise. The used take-off and landing procedures are shown in table 6.5 and 6.6, respectively.

*Table 6.5*

Take-off code	Procedure
00	'Other than 01-08'
01/02	Derated start
03	ICAO-B start
04	Derated start with changed flap settings
05	ICAO-A start
06	NADP2 start, climb 1.500 ft
07	NADP2 start, climb 1.000 ft
08	NADP2 start, climb 800 ft

*Table 6.6*

Landing code	Procedure
10	3° glide angle, normal instrument approach
11	3° glide angle, low power low drag
12	3° glide angle, reduced flap approach

Next, the class number of the flight is determined. For take-off, the class number represents the distance of the flight, based on the destination. In case of landing the class number gives additional information about the landing procedure, like the initial approach height, in case of 'step approach' or the 'continuous descent approach' (CDA). The class numbers for take-off and landing are given in table 6.7 and 6.8, respectively.

*Table 6.7*

Take-off class-number	Distance $D$ to destination [km]
00	$D \leq 750$
01	$750 < D \leq 1500$
02	$1500 < D \leq 3000$
03	$D > 3000$

*Table 6.8*

Landing class-number	Procedure information
00	Initial approach altitude 2000 ft
01	Initial approach altitude 3000 ft
09	Continuous descent approach

For each procedure/class combination (see previous 4 tables), flight profiles have been determined. As an example, a Boeing 747-400 flying from Schiphol to Paris using the NADP2 procedure 06 is considered. The ICAO code of this airplane is B744 which is listed in weight category/noise class 8/3. This corresponds to NPD table 039, see section 6.7.3. Since the distance from Schiphol to Paris is under 750 km, this flight is placed in class 00. The full administration number of this flight for noise calculations will thus be 0390600. Corresponding to this number, the flight profile table of this specific flight is shown in table 6.9.

Table 6.9

SEGMENT	W (m)	H (m)	H (ft)	T (kN)	GAM (deg)	V (m/s)
1	0.0	0.0	0.0	948.19	0.0	41.57
2	1305.6	0.0	0.0	794.60	10.8	84.06
3	3695.7	457.2	1500.0	810.78	4.3	86.53
4	4000.5	480.2	1575.5	680.16	4.3	95.22
5	5536.0	596.2	1956.1	661.25	4.2	117.06
6	9314.2	871.8	2860.3	631.90	4.1	135.07
7	10264.6	939.2	3081.3	625.68	4.3	141.73
8	11275.1	1014.6	3328.8	619.83	8.3	149.21
9	18926.6	2133.6	7000.0	661.37	7.6	157.01
	25799.5	3048.0	10000.0	695.30		

The data in this table is used to reconstruct the flight path and corresponding thrust settings for each segment of the path. A plot of height profile and thrust settings, with respect to the distance from take-off, is shown in section 6.7.4 (figure 6.25).

### 6.7.3 NPD data

The noise data corresponding to a representative aircraft (see section 6.7.1) are listed in a NPD table consisting of the overall A-weighted sound pressure levels in dBA for pre-determined source-receiver distances (here denoted  $s$  in m) and engine settings (in thrust force (kN) or fan rotational speed (rpm)). The NPD table for the example of the previous

section (i.e. 039, which is representative for the B744, B77L and B77W) is shown in table 6.10. Noise levels at other distances and thrust settings than those listed in the NPD table are calculated by linear interpolation. The NPD data does not include any noise directivity effects, i.e. an aircraft is represented as an omnidirectional point source.

*Table 6.10*

s (m)	THRUST (kN)							
	106.76	177.93	266.89	355.86	432.12	584.62	737.14	889.64
61.0	99.11	99.72	102.12	103.24	103.92	105.57	107.91	112.46
120.1	92.10	92.71	94.78	96.09	96.85	98.86	101.48	105.93
152.4	89.64	90.25	92.16	93.51	94.27	96.41	99.12	103.55
192.0	87.22	87.84	89.59	91.00	91.76	94.01	96.83	101.23
243.8	84.63	85.24	86.83	88.39	89.15	91.47	94.36	98.78
304.8	82.23	82.82	84.28	85.90	86.66	89.05	92.00	96.44
381.0	79.83	80.42	81.74	83.37	84.12	86.57	89.58	94.03
487.7	76.96	77.52	78.76	80.51	81.25	83.76	86.83	91.31
609.6	74.37	74.90	76.08	77.86	78.61	81.17	84.29	88.78
960.1	68.80	69.30	70.37	72.25	73.06	75.72	78.90	83.42
1828.8	60.19	60.63	61.61	63.71	64.64	67.42	70.69	75.30

The full list of NPD table numbers and their corresponding representative aircraft is given in table 6.11.

Table 6.11

NPD	Representative aircraft
001	CESSNA 310 R
010	MBB BO-105
012	SIKORSKY S-76B
014	SIKORSKY S-61
026	DOUGLAS DC-8-63 met hushkit
035	BOEING 747-200B
036	BOEING 747-300
039	BOEING 747-400
045	BOEING 727-200ADV quiet nacelle
055	DOUGLAS DC-10-30
060	FOKKER F-28
066	DOUGLAS DC-9-30
067	BOEING 737-200ADV quiet nacelle
069	BOEING 737-300
072	JETSTREAM 31
074	BRITISH AEROSPACE BAe-146-200
079	FOKKER F-27
081	AIRBUS A-310
082	FOKKER 100
083	BOEING 767-300ER
084	BOEING 777-200IGW
085	BOEING 777-300ER
086	MCDONNEL-DOUGLAS MD-90
087	BOEING 757-200/RB211-535E4 motoren
088	FOKKER 70
094	AIRBUS A380-861
095	BOEING 787-8
469	BOEING 737-300HWFAP

The data of NPD table 039 is visualised in figure 6.20 by plotting the overall A-weighted sound pressure levels  $L_A$  (in dBA) as a function of  $20 \log s$  for the various thrust settings.

This enables the verification of the spherical spreading law, i.e.  $L_A = PWL' - 10.8 - 20 \log s$  (equation 3.8), where  $PWL'$  is an overall power watt level of the source with A-weighting accounted for. For the larger distances, however, the curves deviate from straight lines due to atmospheric absorption (see section 3.2).

Assuming atmospheric absorption to be negligible at the first four distances ( $s < 200$  m), we can linearly fit these NPD data to retrieve the  $PWL'$ -values for the various thrust settings. The results are shown in figure 6.21 revealing an increasing  $PWL'$  for increasing thrust (as expected).

A similar analysis has been performed for NPD table 469, which is representative for the aircraft A319, A320, A321, B734, B736, B737, B738 and B739. The results are shown in figures 6.22 and 6.23, respectively. Note that the thrust values are now in rpm.

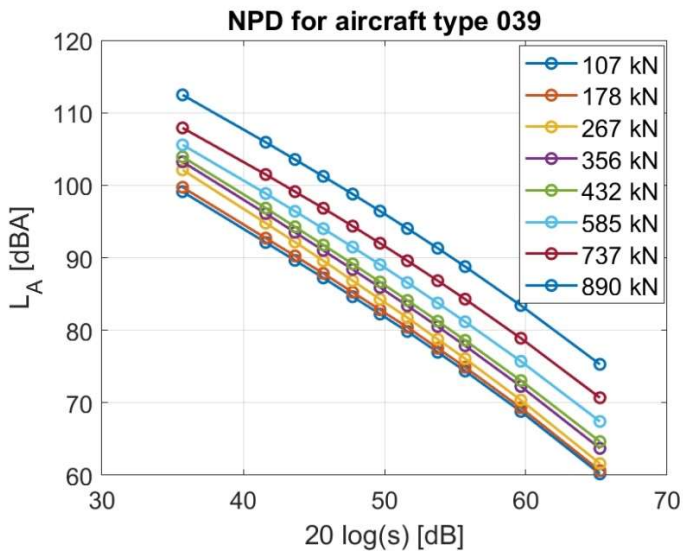


Figure 6.20: Data of NPD table 039.

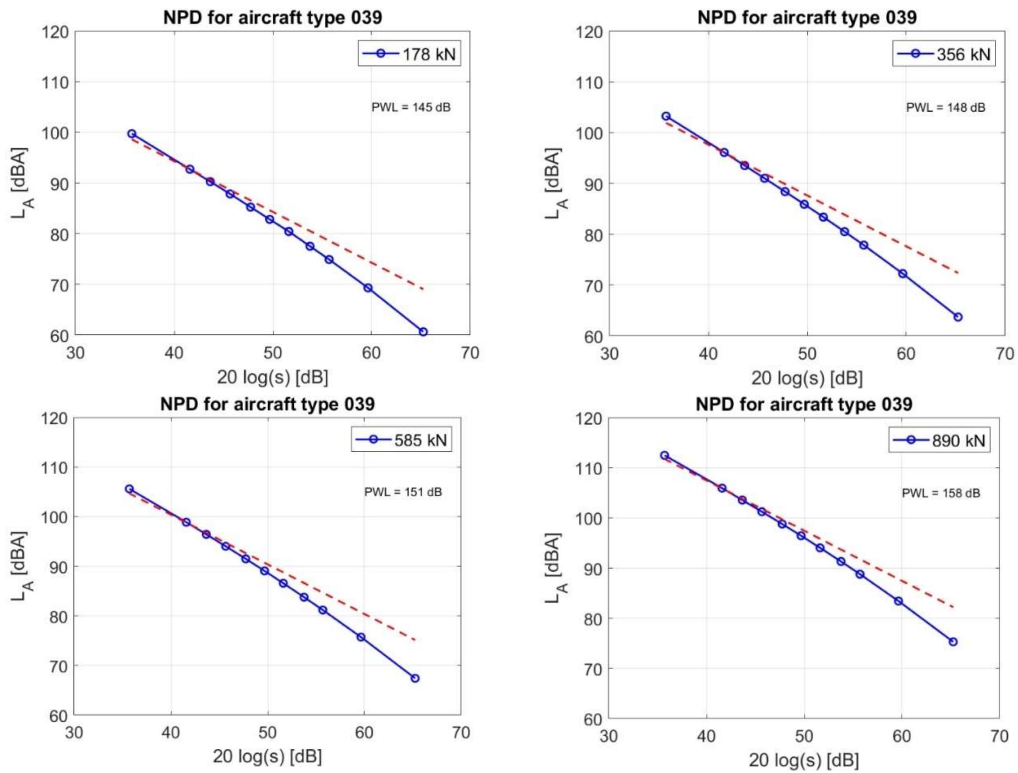


Figure 6.21: Data of NPD table 039 for 4 selected thrust settings (blue lines). Also indicated are linear fits through the first 4 data points (red dashed lines) to retrieve the power watt levels  $PWL'$  of the source.

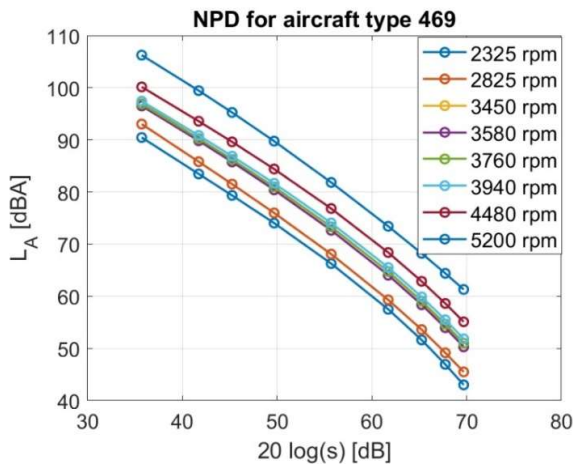


Figure 6.22: Data of NPD table 469.

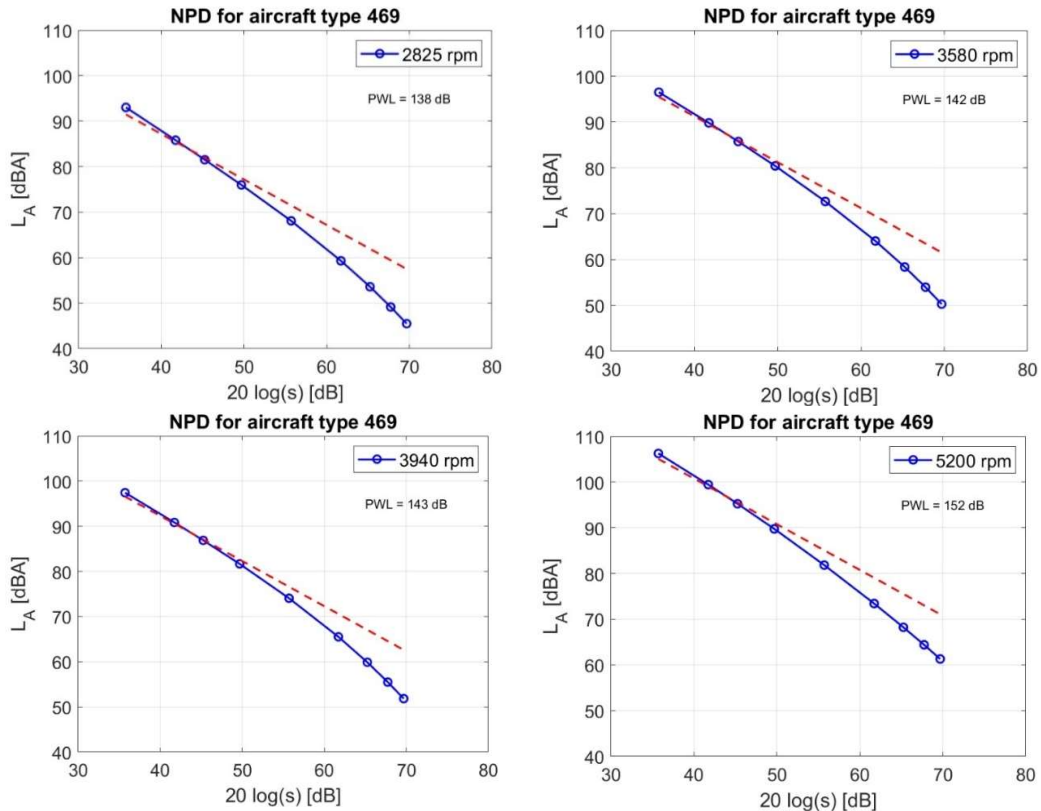


Figure 6.23: Data of NPD table 469 for 4 selected thrust settings (blue lines). Also indicated are linear fits through the first 4 data points (red dashed lines) to retrieve the power watt levels  $PWL'$  of the source.

#### 6.7.4 Lateral attenuation

The overall A-weighted sound pressure levels  $L_A$  obtained from the NPD tables by interpolation (as outlined in the previous section) are corrected for the so-called effect of lateral sound attenuation  $\Delta L_T$ , i.e. contours calculated with NRM show  $L_A - \Delta L_T$  values.  $\Delta L_T$  (in dBA) takes into account the effect of the ground (assumed to be a flat sand surface covered by grass), meteorological effects (wind- and temperature gradients and near surface turbulence) and the effect of directionality of the aircraft sound (to a certain extent). The latter can be caused by shielding of e.g. engine noise by the wings of the aircraft. In NRM, the lateral sound attenuation  $\Delta L_T$  is calculated using simple empirical formulas. First, the ground attenuation  $\Delta L_G$  (in dBA) is calculated as a function of source-receiver distance  $s$  (in m) according to

$$\Delta L_G = \begin{cases} 0 & 0 \leq s < 50 \\ 0.0163s - 0.815 & 50 \leq s < 400 \\ 16.1847^{10} \log s - 36.4086 & 400 \leq s < 2300 \\ 18 & s \geq 2300 \end{cases}$$

The distance  $s$  is depicted in figure 6.24a showing the geometry of the problem. Figure 6.24b shows a graph of  $\Delta L_G$  versus  $s$ . Measurements have indicated that the total lateral attenuation  $\Delta L_T$  is also a strong function of the elevation angle  $\beta$  (see figure 6.24a). In NRM,  $\Delta L_T$  is modelled as

$$\Delta L_T = \begin{cases} \Delta L_G(s)f(\beta) + g(\beta) & 0 \leq \beta < 20^\circ \\ g(\beta) & 20^\circ \leq \beta \leq 90^\circ \end{cases}$$

where the dimensionless formula  $f(\beta)$  is given as

$$f(\beta) = \begin{cases} 5.471\left(\frac{\pi\beta}{180}\right)^2 - 4.774\left(\frac{\pi\beta}{180}\right) + 1 & 0 \leq \beta < 20^\circ \\ 0 & 20^\circ < \beta \leq 90^\circ \end{cases}$$

and the function  $g(\beta)$  (in dBA), representing the shielding effects, is given by

$$g(\beta) = 3\left(1 - \sqrt{\sin \beta}\right).$$

The functions  $f(\beta)$  and  $g(\beta)$  are graphically depicted in figures 6.24c and 6.24d, respectively. Note that, due to the function  $f(\beta)$ , the ground attenuation effect  $\Delta L_G$  vanishes for  $\beta > 20^\circ$ . Further, it can be seen that the shielding effect is maximally 3 dBA.

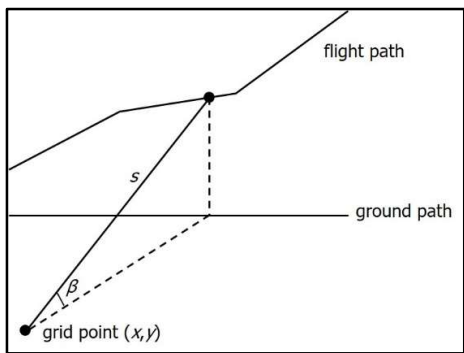


Figure 6.24a: Geometry showing source-receiver distance  $s$  and elevation angle  $\beta$ .

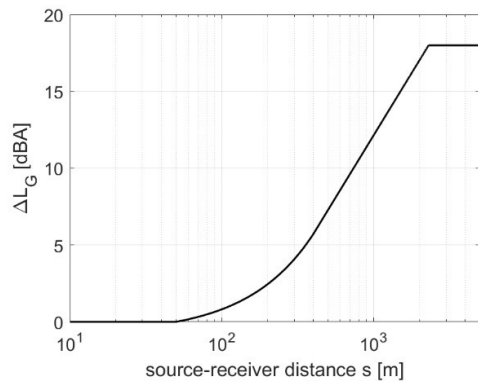


Figure 6.24b: Ground attenuation versus source-receiver distance.

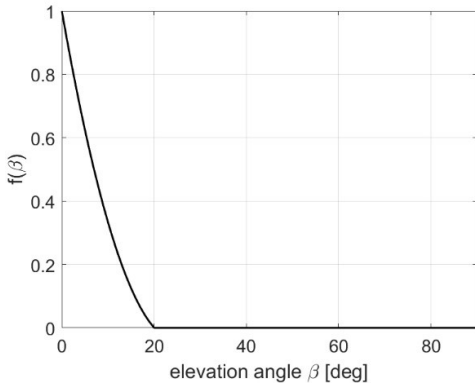


Figure 6.24c: The function  $f(\beta)$ .

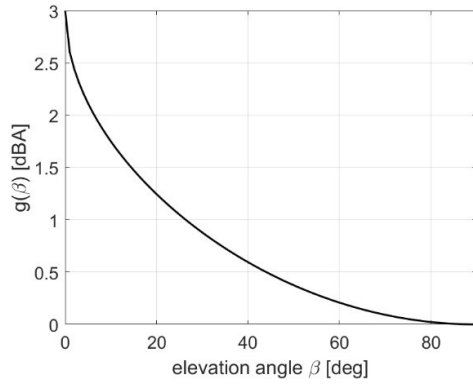


Figure 6.24d: The function  $g(\beta)$ .

### 6.7.5 A case study

This section shows noise contours calculated with NRM for aircraft departures and landings according to various flight procedures. Noise contours of sound exposure level SEL (or  $L_{A,\max}$ ) are calculated as follows.

First, a grid on the ground is defined around the flight path, where the  $x$  coordinate is parallel to the flight path and the  $y$  coordinate perpendicular to it. Given a fixed grid point  $(x, y)$ , the instantaneous distance and thrust setting are determined from the given flight profile as a function of time. This time along the flight profile is obtained using the ground velocity in the profile table (e.g. table 6.9). In the current implementation of NRM a time step of 1 second is chosen. Subsequently, the instantaneous  $L_A$  is calculated as a function of time by linear interpolation of the data in the relevant NPD table. Then from the obtained  $L_A$  versus time curve either SEL or  $L_{A,\max}$  is determined according to the method described in section 6.4. This calculation procedure is repeated for each grid point defined.

Flight profiles and corresponding SEL contours for the B747-400 (NPD table 039) are presented in figure 6.25 for start procedure 06 (and take-off class 00 and 03) and procedure 07 (also for take-off class 00 and 03). The effect of changing procedure 06 to 07 is hardly observed. A marked difference is however observed when the take-off class number is changed from 00 (distance to destination < 750 km) to 03 (distance to destination > 3000 km). The higher SEL values for the larger  $x$  values are mainly due to the lower heights in the flight profile.

Figure 6.26 shows flight profiles and corresponding SEL contours for the B747-400 for landing procedure 10 and 12, both for landing class 00 and 09. Again, in this case the difference in procedure has no effect. The landing class, however, has a pronounced effect on the noise contour, i.e. a more favourable situation in noise exposure is obtained for the continuous descent approach (class 09).

Figure 6.27 shows the effect of changing to a smaller aircraft type, i.e. the B737-300 (NPD table 469). The results are presented for two different take-off profiles (0600 and 0602) and two different landing profiles (1000 and 1009). Note that for the same take-off and landing procedure/class, different flight profiles have to be chosen when aircraft type is changed.

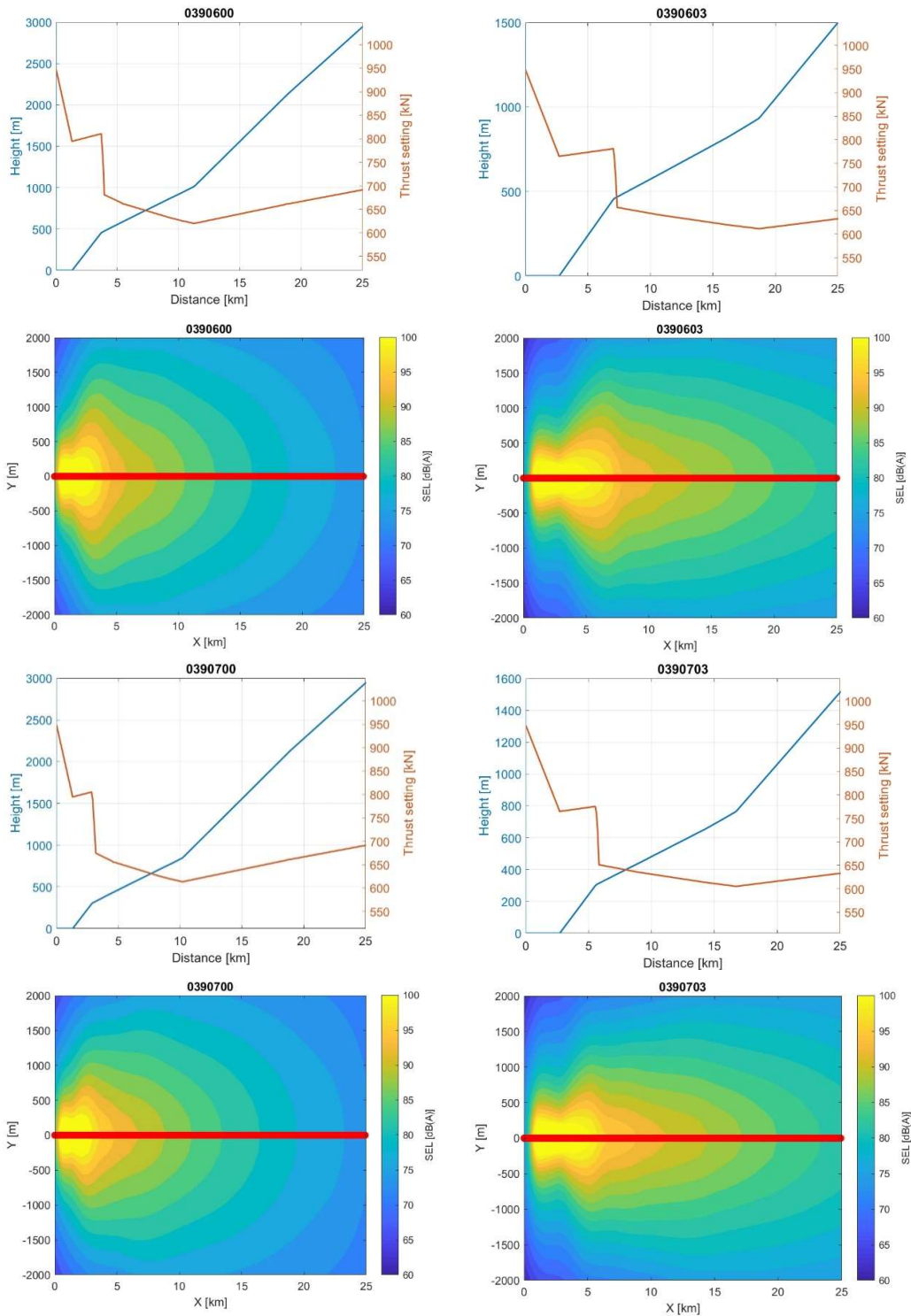


**Figure 6.25: Flight profiles and corresponding SEL contours for the B747-400 for two different start procedures (06 and 07) and two different take-off classes (00 and 03).**

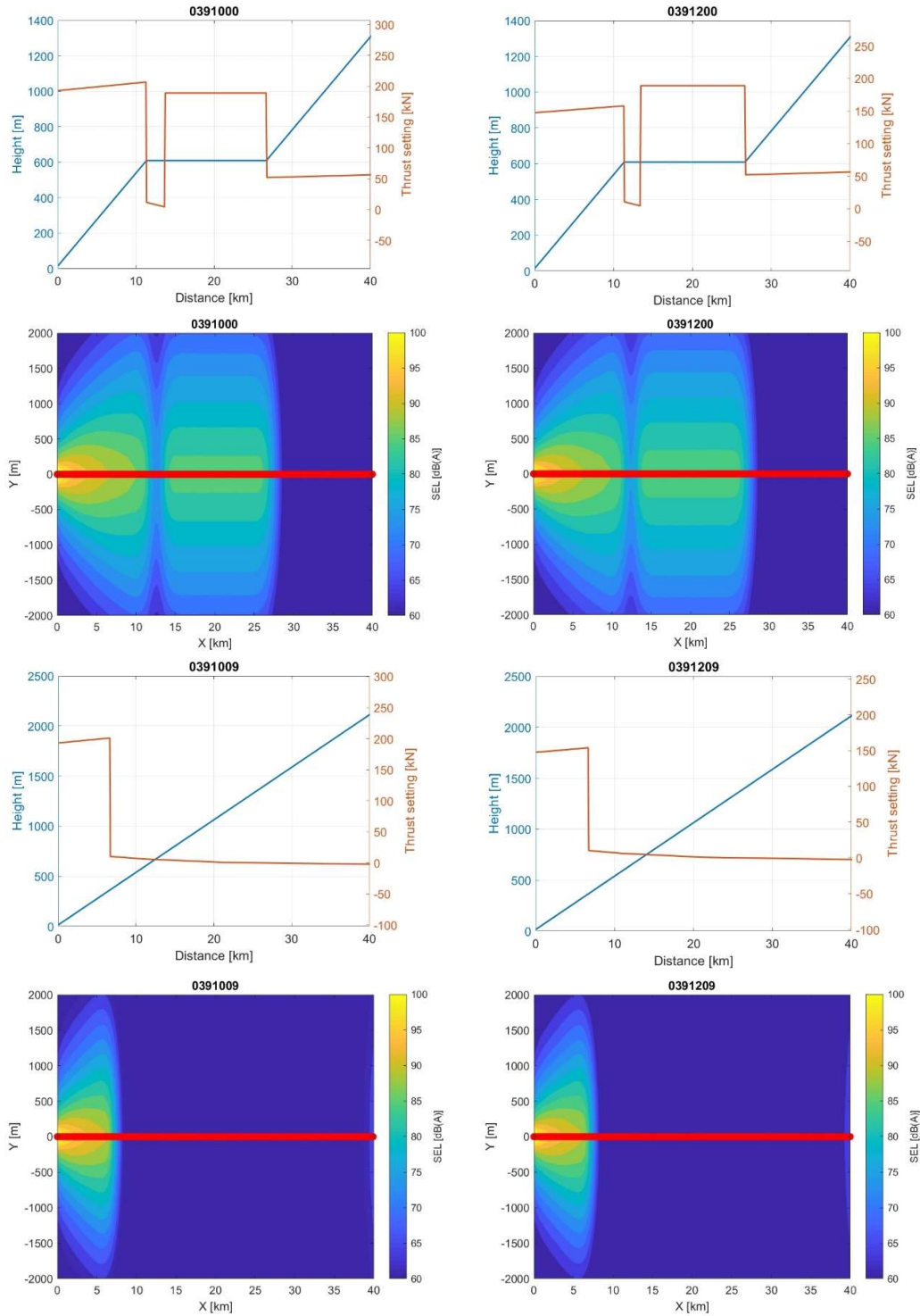
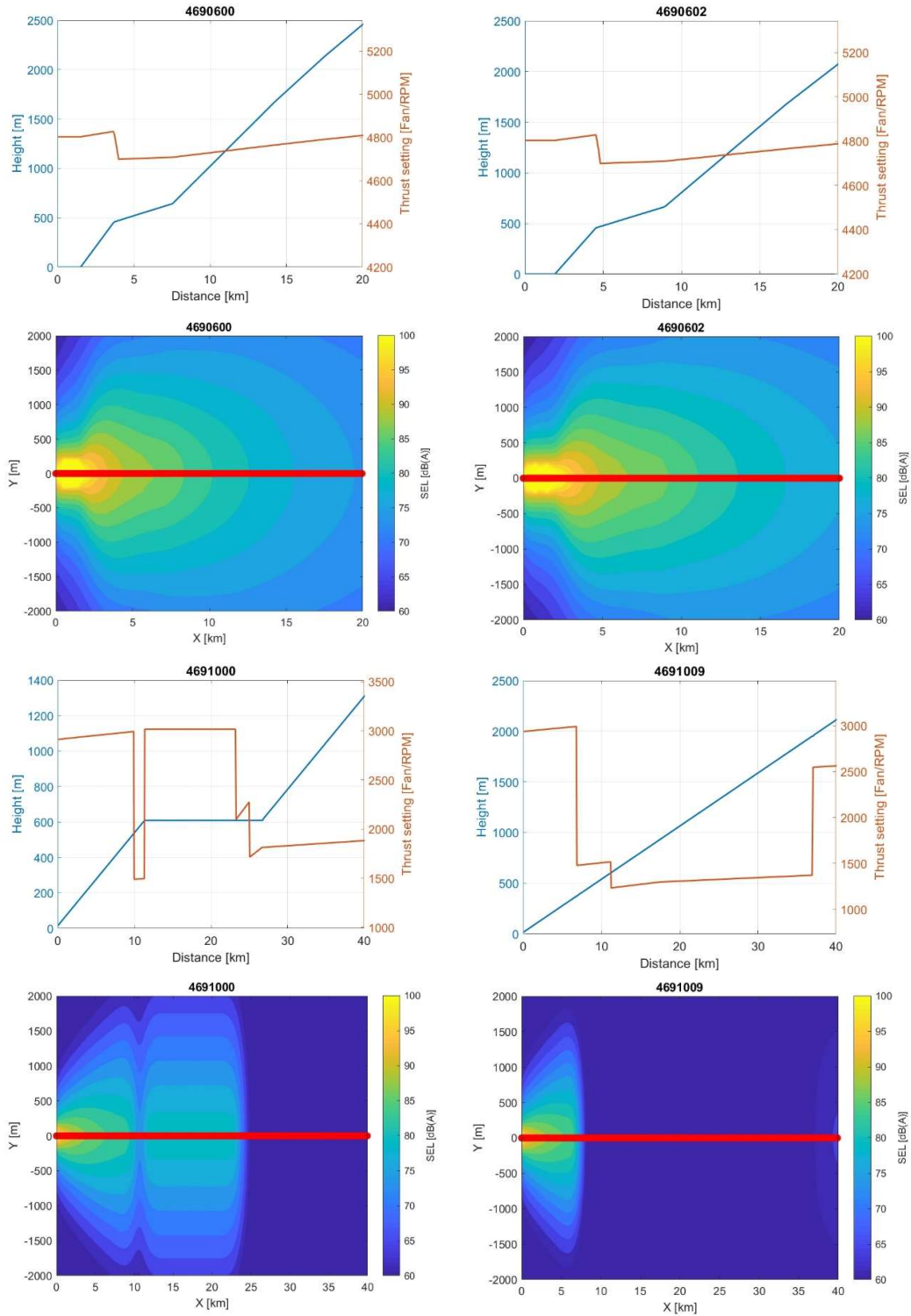


Figure 6.26: Flight profiles and corresponding SEL contours for the B747-400 for two different landing procedures (10 and 12) and two different landing classes (00 and 09).



**Figure 6.27: Flight profiles and corresponding SEL contours for the B737-300 for two different take-off procedures (0600 and 0602) and two different landing procedures (1000 and 1009).**

## 6.8 Psychoacoustic Annoyance and Sound Quality Metrics

Even though the conventional sound metrics  $L_{A,\max}$  or SEL are typically employed for environmental noise law enforcement (see the noise contour examples from section 6.7.5) and certification purposes, recent studies show that sounds can be perceived in practice as considerably more annoying if tonal noise and/or high-frequency noise are present, despite having the same SEL value as sounds without tones or high-frequency noise. Therefore, it is questionable to only use these conventional indicators to predict and assess noise annoyance around airports (and potential abatement procedures), since they do not fully capture the sound properties responsible for the perceived annoyance.

To address this issue there have been recent efforts to incorporate more representative and accurate perception-based sound quality metrics (SQMs) into the aircraft noise assessment. These metrics were originally developed within the field of ‘psychoacoustics’, i.e. the scientific study of sound perception and audiology. These SQMs provide sensation magnitudes instead of stimulus magnitudes, i.e. they describe the hearing sensation instead of the purely physical magnitude, such as the sound pressure or the sound pressure level. Therefore, these new metrics are expected to better capture the human ear behaviour and be more accurate in predicting annoyance.

The five most common SQMs are:

- **Loudness** is the subjective perception of the magnitude of a sound, which corresponds to the overall sound intensity. The calculation of loudness has been standardized within the ISO norm 532–1 using Zwicker’s method. The unit of this metric is the *sone* in linear scale or the *phon* in logarithmic scale, see section 6.1.
- **Tonality** measures the perceived strength of the unmasked tonal energy within a sound. There are different methods to estimate tonality, but Aures’ method is the most widely-used. The unit of this metric is the *tonality unit (t.u.)*.
- **Sharpness** is a measure of the high frequency content of a sound. A sound is, therefore, perceived to be *sharper* when it has more high frequency content than low frequency content. In particular, frequencies higher than 2700 Hz are weighted more heavily by a weighting function. This metric is usually calculated with the method suggested by von Bismark and has the unit of *acum*.
- **Roughness** refers to rapid loudness fluctuations in the frequency range between 50 Hz and 90 Hz. This is typically important for propeller-driven aircraft and rough sounds similar to a lawnmower noise. The method by Daniel and Weber is generally used to estimate roughness with the unit of *asper*.
- **Fluctuation strength**, similarly to roughness, assesses fluctuations in loudness but it gives more importance to slow temporal amplitude modulations, having its maximum value for fluctuations of approximately 4 Hz. Hence, this metric is more relevant for sound sources that rotate slower than propellers, such as wind turbines.

The method by Fastl and Zwicker is normally employed to calculate this metric with the unit of *vacil*.

Figure 6.28 provides a graphical representation of the SQMs from more (left) to less relevance (right) in the perceived noise annoyance of aircraft noise, where loudness is usually the dominant metric. Several authors (e.g. Fastl and Zwicker, More, Di et al.) have tried to combine these SQMs into a single global metric, such as the Psychoacoustic Annoyance (PA) metric to estimate noise annoyance.



Figure 6.28: Sound quality metrics (SQMs) ordered from more relevant (left) to less relevant (right) in the perceived noise annoyance of aircraft noise.

Given the highly subjective nature of noise annoyance, the estimated noise annoyance by the SQMs is validated with dedicated psychoacoustic listening experiments in a controlled environment with low background noise levels and reduced sound reflections. In these experiments, human subjects listen to different sound stimuli and provide their subjective opinion on the perceived noise annoyance for each stimulus (typically in a 11-point scale, from not annoying at all (zero) to extremely annoying (ten)). As in most human perception studies, it is essential to have a statistically significant and diverse test subject population (e.g. in age, background, etc.) in order to extract relevant conclusions.

This type of research is gaining interest in the last years and an increasing number of psychoacoustic listening facilities are being developed. Figure 6.29 depicts the AuraLab facility at Empa (Swiss Federal Laboratories for Materials Science and Technology) on the left and the newly-developed Psychoacoustic Listening Laboratory at the faculty of Aerospace Engineering of TU Delft on the right.



Figure 6.29: AuraLab facility at Empa for psychoacoustic listening experiments (left) and the newly-developed Psychoacoustic Listening Laboratory at TU Delft (right).

## Exercises

### Question 1

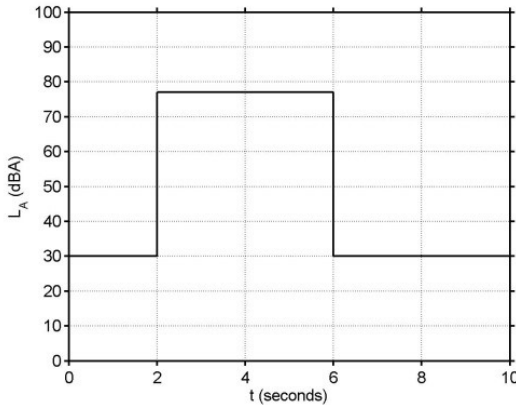
A broadband noise signal is band-pass-filtered with pass band 178 Hz – 562 Hz. The pressure band level or sound pressure level  $SPL(i)$  in the successive one-third octave band is a constant equal to 80 dB, i.e. the noise spectrum of the signal in this pass band is a constant (see also the table below).

- (a) Calculate the overall sound pressure level (OASPL).
- (b) Calculate the corrected band levels  $L_A(i)$  when A-weighting is applied. First, determine the weighting corrections  $\Delta L_A(i)$  for the one-third octave centre frequencies  $f_i$ . Your calculated values for  $L_A(i)$  can be put in the table.
- (c) Calculate the overall A-weighted sound pressure level  $L_A$  (OASPL).
- (d) Assume the sound pressure levels in the given one-third octave bands to be mainly due to tones at the corresponding centre frequencies  $f_i$ . Then find the loudness levels  $p$  of these tones expressed in phon from figure 6.2. Calculate the corresponding loudness levels  $s$  in sone. Your values for  $p$  and  $s$  can be put in the table too.
- (e) Calculate the overall sone value  $S$  and the corresponding total loudness level  $L_L$  in phon.
- (f) For noise from airplane flyovers, perceived noise level  $L_{PN}$  is used instead of  $L_A$  or  $L_L$ . For this we need the noisiness values  $n$  corresponding to the sound pressure levels in the given one-third octave bands. These values of  $n$  have already been given in the table (but can also be determined from figure 6.3). Calculate the overall noy value  $N$  and the corresponding perceived noise level  $L_{PN}$ .

1/3-octave band nr <i>i</i>	Centre frequency <i>f<sub>i</sub></i> [Hz]	SPL( <i>i</i> ) [dB]	$\Delta L_A(i)$ [dB]	$L_A(i)$ [dBA]	Loudness level <i>p</i> [phon]	Loudness level <i>s</i> [sone]	Noisiness <i>n</i> [noy]
23	200	80					13
24	250	80					14
25	315	80					15
26	400	80					16
27	500	80					16

### Question 2

Consider the noise event in the figure below. The duration of the event is 4.0 seconds, whereas the corresponding constant  $L_A$  level is 77 dBA. The background level is 30 dBA.



- (a) Calculate the Sound Exposure Level (SEL) of this event.
- (b) Calculate the day-night average level  $L_{DN}$  for the situation that this event occurs 50 times during day time *and* that the event occurs 5 times during night time.

### Question 3

A machine in a factory hall produces noise in the following pattern: (the SPL values were measured at the position where the machine is operated)

period	type of noise	Sound Pressure Level SPL
during the 1st second	tonal noise at 100 Hz	89 dB
during the 2nd second	tonal noise at 100 Hz and 1000 Hz simultaneously	89 dB (100 Hz) and 70 dB (1000 Hz)
during the 3rd second	tonal noise at 1000 Hz	70 dB
during the 4th second	no sound (silence)	

This 4 second pattern is continuously repeated. Calculate the Equivalent A-weighted Sound Level (EAL or  $L_{A\text{ eq},T}$ ) in dBA.

#### Question 4

An octave band analysis of noise measured for a small propeller-driven aircraft gives the following results:

centre frequency [Hz]	pressure band level [dB]
63	53
125	73
250	62
500	60
1000	53

The noise is measured under static conditions of the aircraft. The microphone is positioned 20 m from the propeller of the aircraft and is at a height of 2 m from the ground. The noise originates from the propeller and the engine and may be considered a point source at a height of 2 m from the ground. The noise outside the five octave bands given in the above table is negligible.

- (a) Calculate the Overall Sound Pressure Level and the Overall A-weighted Sound Pressure Level (as measured at the microphone position).

A thin screen of height 3 m is positioned halfway between the aircraft's propeller and the microphone. It is assumed that no sound can pass through the screen and that the screen is infinitely long in the lateral direction.

- (b) Calculate the acoustic efficiency (i.e. excess attenuation in dB) due to the screen for the five frequencies given in the table above.
- (c) Calculate the Overall A-weighted Sound Pressure Level (as measured at the microphone position) for the situation with the screen between aircraft and microphone. Assume that the acoustic efficiencies calculated for the centre frequencies of the octave bands are valid for these entire bands.

#### Question 5

A point source in air radiates a tone at a frequency of 500 Hz with a PWL of 57 dB. At this frequency the absorption coefficient due to friction and molecular relaxation is 3.0 dB/km. The threshold of hearing at 500 Hz is 8.0 dB. Refraction effects due to temperature and wind gradients can be ignored.

What is the maximum distance from the source at which the tone is just audible by a human observer?

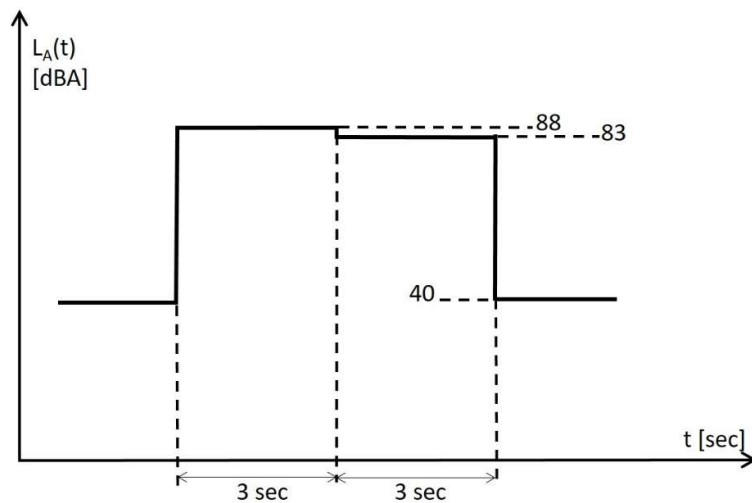
Question 6

A microphone system at a certain position around Schiphol airport measures a background level of 40 dBA, i.e. the instantaneous A-weighted SPL due to background (non-aviation) noise is a constant and equal to 40 dBA.

What is the  $L_{DEN}$  due to this background noise?

Question 7

Consider an aircraft noise event shown in the figure, where the instantaneous A-weighted sound pressure level  $L_A(t)$  in dBA is plotted versus time  $t$  (in seconds). The constant background level is 40 dBA. What is the Sound Exposure Level SEL of this event?



## Chapter 7 Directional acoustic sources

Directionality of an acoustic source was already briefly discussed in chapter 1. It is also of importance to aircraft noise as most aircraft noise sources tend to be directional, see figure 1.24. In this chapter we treat the topic quantitatively. We start with the directional radiation patterns of some elementary sound sources, i.e. the monopole, dipole and quadrupole source. Monopole sources are not directional, but they form the basis for the dipole and quadrupole source. Moreover, it is shown that more complicated sound sources, e.g. loudspeakers, can be constructed from monopoles. The dipole and quadrupole source are the simplest directional sound sources that are also relevant for aircraft noise sources, as they represent an idealized directional pattern for propeller noise and jet noise, respectively.

### 7.1 Monopole, dipole and quadrupole source

A monopole source is a mechanical device consisting of a small sphere of radius  $a$  whose surface oscillates harmonically in the radial direction, see figure 7.1. The velocity at the sphere's surface is given by

$$v(a, t) = v_0 e^{i\omega t}. \quad (7.1)$$

Such a harmonic pulsating sphere will produce the spherical harmonic sound wave given by

$$p(r, t) = \frac{A}{r} e^{i(\omega t - kr)} \quad (7.2)$$

with  $k = \frac{\omega}{c} = \frac{2\pi}{\lambda}$  the wavenumber (see section 2.4).

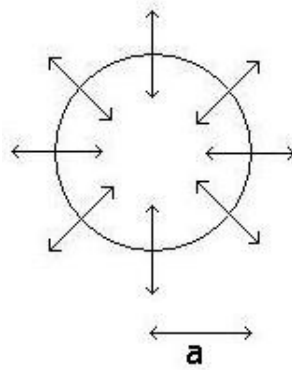


Figure 7.1: The monopole source: a simple pulsating sphere.

We will now determine the unknown parameter  $A$ , the amplitude of the sound wave (at 1 m from the source), in terms of the mechanical parameters of the source, i.e. radius  $a$  and

velocity amplitude  $v_0$ . The relation between sound pressure and particle velocity for a spherical wave, as derived in chapter 2, is

$$v_r(r,t) = \frac{1}{\rho_\infty c} p(r,t) \left[ 1 + \frac{c}{i\omega r} \right]. \quad (7.3)$$

Substituting  $r = a$  we should obtain the velocity at the surface of the sphere as imposed by equation 7.1. Hence

$$v_r(a,t) = \frac{1}{\rho_\infty c} \frac{A}{a} e^{i(\omega t - ka)} \left[ 1 + \frac{c}{i\omega a} \right] = v_0 e^{i\omega t} \quad (7.4)$$

from which the amplitude  $A$  is directly obtained as

$$A = \rho_\infty c v_0 a \frac{e^{ika}}{\left[ 1 + \frac{1}{ika} \right]}. \quad (7.5)$$

We consider so-called ‘point monopoles’, i.e. the circumference of the source is small compared to the wavelength:

$$2\pi a \ll \lambda \quad \text{or} \quad ka \ll 1 \quad (7.6)$$

Then, using  $e^{ika} \approx 1$ , the amplitude becomes

$$A = i\rho_\infty c v_0 a^2 k = i\rho_\infty c \frac{Q}{4\pi} k \quad (7.7)$$

where we have introduced the volume velocity  $Q = 4\pi a^2 v_0$ .

The sound pressure from a point monopole source is thus given by

$$p(r,t) = i\rho_\infty c \frac{Qk}{4\pi r} e^{i(\omega t - kr)} = i\rho_\infty \frac{\omega Q}{4\pi r} e^{i(\omega t - kr)}. \quad (7.8)$$

We note that the square of the effective pressure can be written as  $p_e^2 = \frac{p_{\max}^2}{2} = \frac{|p|^2}{2}$ .

Hence, the intensity becomes

$$I(r) = \frac{|p|^2}{2\rho_\infty c} = \frac{\rho_\infty c}{32\pi^2} \left( \frac{Qk}{r} \right)^2. \quad (7.9)$$

When we integrate this expression over a sphere of radius  $r$ , i.e. multiplying the intensity  $I(r)$  with the surface of a sphere with radius  $r$ , we obtain the radiated power  $W$  given by

$$W = \rho_\infty c \frac{Q^2 k^2}{8\pi} = \frac{\rho_\infty Q^2 \omega^2}{8\pi c} \quad (7.10)$$

i.e. proportional to the frequency squared.

A dipole source consists of two monopole sources of equal strength but opposite phase, see figure 7.2. We consider point monopoles ( $ka \ll 1$ ) and we assume the monopoles are separated by a distance  $d$  small compared to the wavelength, i.e.  $kd \ll 1$ . We determine the total sound pressure in the ‘far field’, i.e. we may assume that the two lines connecting the monopoles and the observation point (the two red arrows in figure 7.3) are parallel. In addition, we ignore the weak dependence of the amplitude of the sound pressure on the position of the monopoles. This far field approximation is also called the ‘Fraunhofer approximation’. The phase difference can however not be ignored.

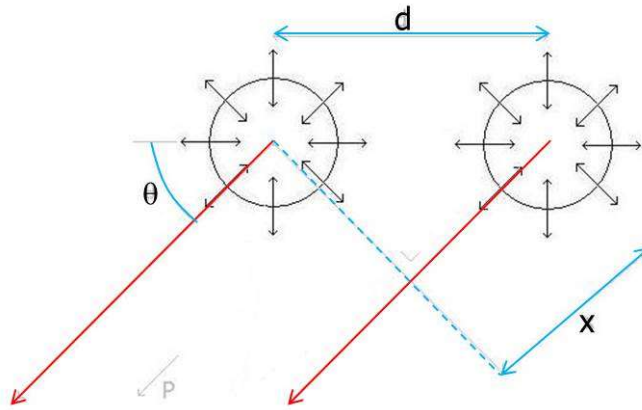


Figure 7.2: The dipole source: two closely spaced monopoles in antiphase.

With  $\theta$  the angle between the dipole axis and the line connecting the dipole and the observation point  $P$ , the total sound pressure is given by

$$p(r, \theta, t) = i\rho_\infty \frac{\omega Q}{4\pi r} \left[ -e^{i(\omega t - kr)} + e^{i(\omega t - k(r+x))} \right] \quad (7.11)$$

with  $x = d \cos \theta$ . Equation 7.11 can be rewritten as

$$p(r, \theta, t) = i\rho_\infty \frac{\omega Q}{4\pi r} e^{i(\omega t - kr)} \left[ -1 + e^{-ikx} \right] \quad (7.12)$$

with  $-1 + e^{-ikx} \approx -ikx = -ikd \cos \theta$ . Hence, we obtain

$$p(r, \theta, t) = \frac{\rho_\infty \omega^2 Q}{c} \frac{d \cos \theta}{4\pi r} e^{i(\omega t - kr)} = \rho_\infty c \frac{Q k^2}{4\pi r} d \cos \theta e^{i(\omega t - kr)}. \quad (7.13)$$

The corresponding intensity at distance  $r$  and angle  $\theta$  is

$$I(r, \theta) = \frac{|p|^2}{2\rho_\infty c} = \frac{\rho_\infty c Q^2 k^4 d^2 \cos^2 \theta}{32\pi^2 r^2}. \quad (7.14)$$

Of importance is that the directional radiation pattern follows a  $\cos^2 \theta$  dependence, i.e. in the directions normal to the dipole axis ( $\theta = 90^\circ, 270^\circ$ ) the sound pressure is zero (see also figure 7.4).

The total radiated power of the dipole is given by

$$W = \int_0^\pi I(r, \theta) 2\pi r^2 \sin \theta d\theta = \frac{\rho_\infty Q^2 \omega^4 d^2}{24\pi c^3} \quad (7.15)$$

i.e. proportional to the frequency to the fourth power.

A quadrupole source consists of two dipole sources of equal strength but opposite phase. As can be seen in figure 7.3, the two dipoles do not lie along the same line, i.e. we have four monopoles with alternating phase at the corners of a rectangle. Again we consider point monopoles ( $ka \ll 1$ ) and we assume that the monopoles are separated by distances  $d$  and  $D$ , which are both small compared to the wavelength, i.e.  $kd \ll 1$  and  $kD \ll 1$ . Further, the total sound pressure in the ‘far field’ is considered.

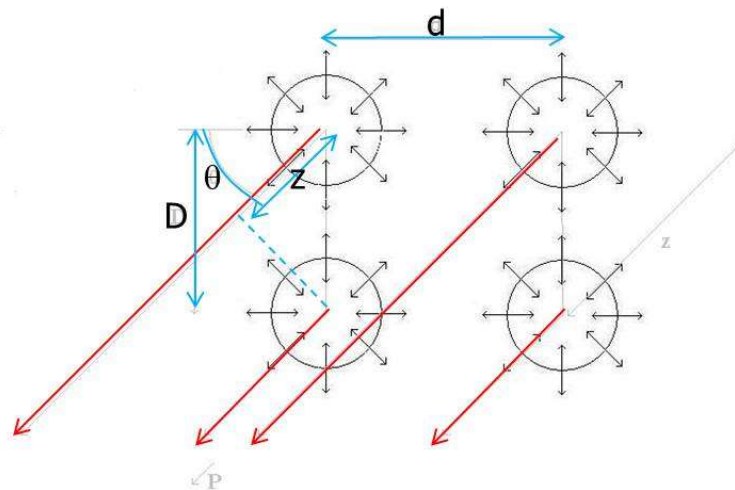


Figure 7.3: The quadrupole source: two closely spaced dipoles in antiphase.

With  $\theta$  the angle as indicated in the figure, the total sound pressure of the quadrupole is given by

$$p(r, \theta, t) = \rho_\infty c \frac{Qk^2}{4\pi r} d \cos \theta \left[ e^{i(\omega t - kr)} - e^{i(\omega t - k(r+z))} \right] \quad (7.16)$$

with  $z = D \sin \theta$ . Equation 7.16 can be rewritten as

$$p(r, \theta, t) = \rho_\infty c \frac{Qk^2}{4\pi r} d \cos \theta e^{i(\omega t - kr)} \left[ 1 - e^{-ikD \sin \theta} \right] \quad (7.17)$$

with  $1 - e^{-ikD \sin \theta} \approx ikD \sin \theta$ . Hence we obtain

$$p(r, \theta, t) = i\rho_\infty c \frac{Qk^3}{8\pi r} dD \sin(2\theta) e^{i(\omega t - kr)} \quad (7.18)$$

where we have used  $\sin(2\theta) = 2\sin\theta\cos\theta$ .

The corresponding intensity at distance  $r$  and angle  $\theta$  is

$$I(r, \theta) = \frac{|p|^2}{2\rho_\infty c} = \frac{\rho_\infty c Q^2 k^6 d^2 D^2 \sin^2(2\theta)}{128\pi^2 r^2}. \quad (7.19)$$

The directional radiation pattern now follows a  $\sin^2(2\theta)$  dependence, i.e. in the directions  $\theta = 0^\circ, 90^\circ, 180^\circ$  and  $270^\circ$  the sound pressure is zero. Figure 7.4 shows the radiation patterns (for the intensity) for all three types of sources treated so far.

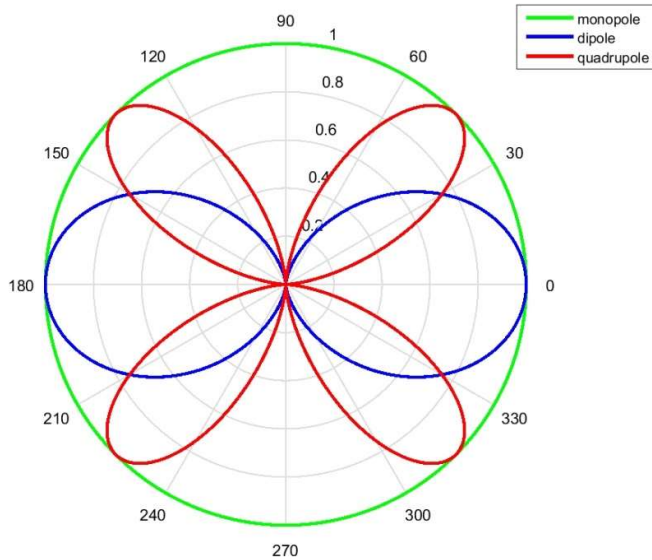


Figure 7.4: Directional radiation pattern of the monopole, dipole and quadrupole source.

The total radiated power of the quadrupole is given by

$$W = \int_0^\pi I(r, \theta) 2\pi r^2 \sin \theta d\theta = \frac{\rho_\infty Q^2 \omega^6 d^2 D^2}{60\pi c^5} \quad (7.20)$$

i.e. proportional to frequency to the sixth power.

## 7.2 Line array of monopoles and the continuous line array

Using the mathematical technique of the previous section we will now derive the directional radiation pattern of an array of  $n$  in-phase point monopoles (all with the same strength  $Q$ ), see figure 7.5. The spacing between the monopoles is  $d$  and the length of the array is then  $L = (n - 1)d$ .

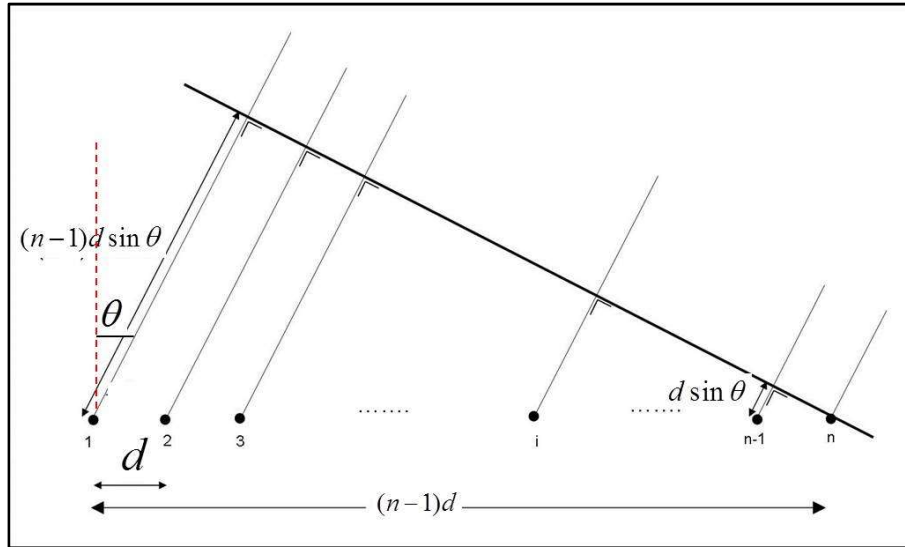


Figure 7.5: The array of  $n$  in-phase monopoles.

We consider an observation point at a far distance  $r \gg L$  from monopole 1. Then the distances to the other monopoles is given by  $r - (j - 1)d \sin \theta$  for  $j = 1, 2, \dots, n$ . In the far field or Fraunhofer approximation the total sound pressure at distance  $r$  and angle  $\theta$  is given by

$$p(r, \theta, t) = \frac{i\omega\rho_\infty Q}{4\pi r} e^{i(\omega t - kr)} \sum_{j=1}^n e^{ik(j-1)d \sin \theta}. \quad (7.21)$$

For the summation in this equation we use the geometric series

$$\sum_{j=1}^n e^{ik(j-1)d \sin \theta} = \frac{1 - e^{nikd \sin \theta}}{1 - e^{ikd \sin \theta}} \quad (7.22)$$

which can be written as

$$n e^{\frac{i(n-1)kd \sin \theta}{2}} \frac{\sin\left(n \frac{kd \sin \theta}{2}\right)}{n \sin\left(\frac{kd \sin \theta}{2}\right)}$$

where we have used the complex expression for the sine function, i.e.  $\sin x = \frac{e^{ix} - e^{-ix}}{2i}$ .

Hence, the total sound pressure becomes

$$p(r, \theta, t) = \frac{i\omega\rho_\infty nQ}{4\pi r} e^{i(\omega t - kr)} e^{\frac{i(n-1)kd\sin\theta}{2}} \frac{\sin\left(\frac{nkd\sin\theta}{2}\right)}{n\sin\left(\frac{kd\sin\theta}{2}\right)}. \quad (7.23)$$

The directional characteristics of the corresponding intensity is contained in the function

$$\left[ \frac{\sin\left(\frac{nkd\sin\theta}{2}\right)}{n\sin\left(\frac{kd\sin\theta}{2}\right)} \right]^2 \quad (7.24)$$

which can also be written as

$$\left[ \frac{\sin\left(\frac{n\pi d\sin\theta}{\lambda}\right)}{n\sin\left(\frac{\pi d\sin\theta}{\lambda}\right)} \right]^2. \quad (7.25)$$

In figure 7.6 we have plotted this directional radiation pattern for  $n = 3$  and  $n = 5$ . In the upper two subplots the separation between the monopoles is taken as half the wavelength, i.e.  $d = \frac{\lambda}{2}$ , whereas the lower two subplots are for the situation that  $d = \lambda$ .

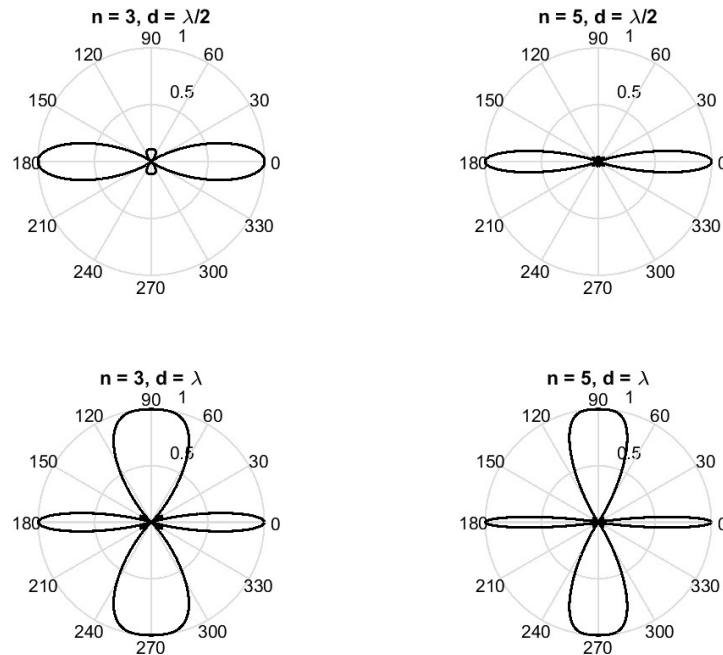


Figure 7.6: Directional radiation pattern of arrays of 3 (left figures) and 5 (right figures) in-phase monopoles. In the upper two figures the spacing between the monopoles is  $\lambda/2$ , whereas in the lower two figures the spacing is  $\lambda$ .

These arrays are designed to steer the sound into a particular direction. Indeed, the radiation pattern shows a narrow beam in the desired direction  $\theta = 0^\circ$ . Because of the symmetry a second beam is created at  $\theta = 180^\circ$ , which cannot be avoided. Also visible are so-called ‘side lobes’, beams in other ‘wrong’ directions, but much smaller in amplitude. When  $n$  increases, the beam width narrows and the side lobe level decreases.

Apparently, for  $d = \frac{\lambda}{2}$  there are only main beams in the two desired directions. For  $d = \lambda$ , however, sound is also projected (with the same amplitude) into the ‘wrong’ directions  $\theta = 90^\circ, 270^\circ$ . These undesired beams are called ‘grating lobes’. As in the case  $d = \lambda$  the array is effectively longer, the beam width in the desired directions is smaller than that for  $d = \frac{\lambda}{2}$ .

We now discuss the related problem of the ‘continuous line array’. Mathematically, this means that the monopole separation distance is taken infinitely small, i.e.  $d \rightarrow 0$ , while keeping the array length  $L = (n-1)d$  finite, i.e. then  $n \rightarrow \infty$ . Such an array is practically realized by a vibrating surface, which has a length  $L$  in one direction and a very small size in the other direction.

The argument  $\frac{nkd \sin \theta}{2}$  in the nominator of the directional function, equation 7.24, then

becomes  $\frac{kL \sin \theta}{2}$ . The denominator of equation 7.24 becomes

$$n \sin\left(\frac{kd \sin \theta}{2}\right) \approx n \frac{kd \sin \theta}{2} \approx \frac{kL \sin \theta}{2}, \text{ where we have used } \sin x \approx x \text{ for } x \ll 1. \text{ Hence,}$$

the directional radiation pattern of the continuous line array is given by

$$\left[ \frac{\sin\left(\frac{kL \sin \theta}{2}\right)}{\frac{kL \sin \theta}{2}} \right]^2. \quad (7.26)$$

In figure 7.7 we have plotted this directional radiation pattern for  $L = \lambda$  and  $L = 2\lambda$ , respectively. The radiation pattern of a continuous line array never shows grating lobes.

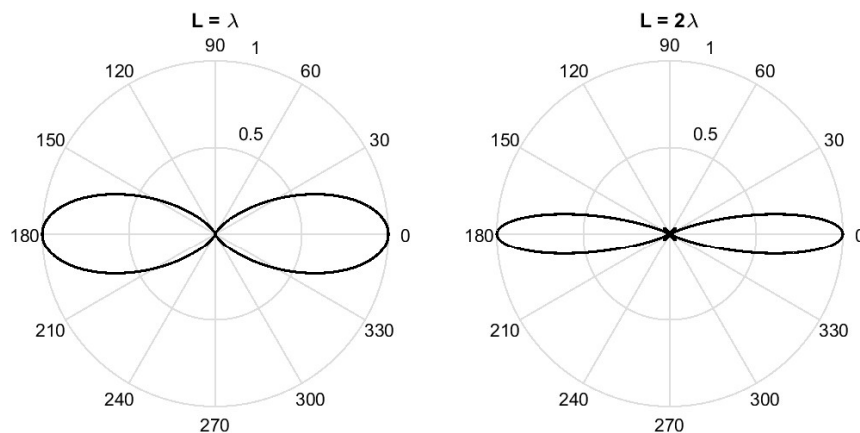


Figure 7.7: Directional radiation pattern of a continuous line array with length equal to  $\lambda$  (left figure) and length equal to  $2\lambda$  (right figure).

The beam width of the lobe at  $\theta = 0^\circ$  can be determined as follows. The first zero of equation 7.26 left or right of the peak at  $\theta = 0^\circ$  is at  $\frac{kL \sin \theta_0}{2} = \pi$ . Assuming  $\theta$  to be small

(hence  $\sin \theta \approx \theta$ ) and using  $k = \frac{2\pi}{\lambda}$ , we obtain  $\theta_0 = \frac{\lambda}{L}$ . Hence, the beam width is

$$2\theta_0 = 2 \frac{\lambda}{L} \quad (7.27)$$

We note that for beamforming (chapter 8) it is more usual to define the beam width as the width at half maximum. Then the beam width is just half of this, i.e.  $\frac{\lambda}{L}$ .

In figure 7.8 we have plotted the function  $\left[ \frac{\sin x}{x} \right]^2$ . From this figure (blue line) it can be observed that the highest side lobe level (at  $x = 1.43\pi$ ) equals 0.0472 (or -13 dB). Also indicated in the figure is a directional function involving a Bessel function, which is needed for the next section.

We note that the physics of the continuous line array discussed here is exactly equal to that of optical Fraunhofer diffraction at a single 1D slit of length  $L$ .

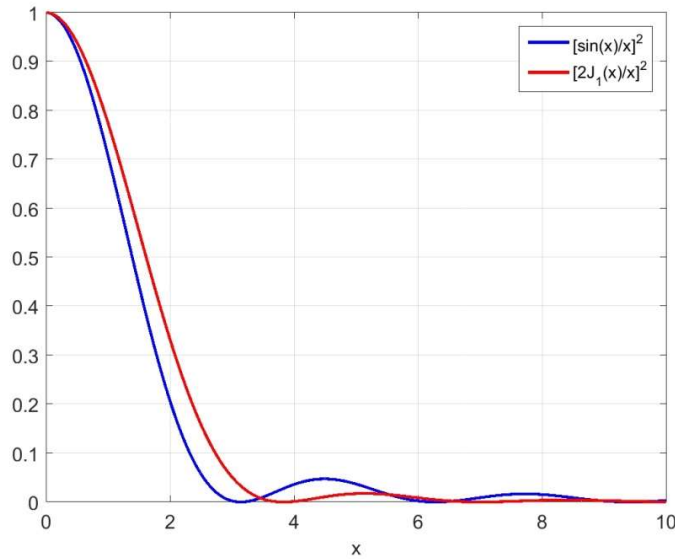


Figure 7.8: Plot of the directional functions  $[\sin(x)/x]^2$  and  $[2J_1(x)/x]^2$ , relevant for the 1D continuous line array and the 2D continuous circular array, respectively.

### 7.3 Rayleigh integral and loudspeakers

We conclude this chapter with a general method for determining the directional radiation pattern of 2D continuous sources. The active vibrating surface of the source has an area  $A$  and is mounted in an infinite rigid baffle. The dimensions of  $A$  are not necessarily small compared to the wavelength  $\lambda$ . The basis for the method is again the monopole expression (equation 7.8)

$$p(r,t) = \frac{i\rho_\infty\omega}{4\pi r} v_0 dA e^{i(\omega t - kr)} \quad (7.28)$$

where we have replaced the volume velocity  $Q$  by  $dQ = v_0 dA$ , i.e. we will position a monopole of strength  $dQ$  at an infinitesimally small area  $dA$  of the total area  $A$  of the vibrating surface of the source.  $v_0$  is the velocity amplitude valid for that part  $dA$  of the surface. Populating the entire area of the vibrating surface with such monopoles, we obtain for the sound pressure at distance  $r$  from the source the so-called ‘Rayleigh integral’ given as

$$p(r,t) = \frac{i\rho_\infty\omega}{2\pi} \int_A \frac{v_0 e^{i(\omega t - kr)}}{r} dA. \quad (7.29)$$

We note that each of the monopoles is radiating from a rigid, reflecting, plane and not from free space. The sound pressure due to any one of the baffled monopoles is therefore twice that of an equivalent monopole in free space. Again we employ the far field or Fraunhofer approximation, i.e. we ignore the weak dependence of the amplitude of the sound pressure

on the position of the monopoles. The  $\frac{1}{r}$  – dependence can thus be taken out of the integral. In addition, we assume  $v_0$  to be the same for the entire surface  $A$ . Hence, it can also be taken out of the integral. We thus assume that all monopoles have the same surface velocity and phase. Rayleigh’s integral then becomes

$$p(r,t) = \frac{i\rho_\infty\omega v_0 e^{i\omega t}}{2\pi r} \int_A e^{-ikr} dA. \quad (7.30)$$

We apply this equation to a circular piston membrane mounted in an infinite rigid baffle, which is a good model for loudspeakers. We note that the problem of Fraunhofer diffraction at a circular aperture in optics is solved by exactly the same physics.

The left part of figure 7.9 shows a side view of the geometry of the problem where we consider an observation point in the far field at an angle  $\theta$  with respect to the axis normal to the vibrating membrane or disk. The distance from the centre of the disk to the observation point is  $r$  and  $a$  is the radius of the disk. The right part of the figure shows a top view of the vibrating circular disk where we indicated a polar coordinate system  $(w, \varphi)$ . We consider an elemental infinitesimally small surface confined by  $(w, w+dw)$  and

$(\varphi, \varphi + d\varphi)$ . The area of this elemental surface is equal to  $w dw d\varphi$  and the distance from the elemental surface to the observation point is given as  $r - w \sin \theta \cos \varphi$ .

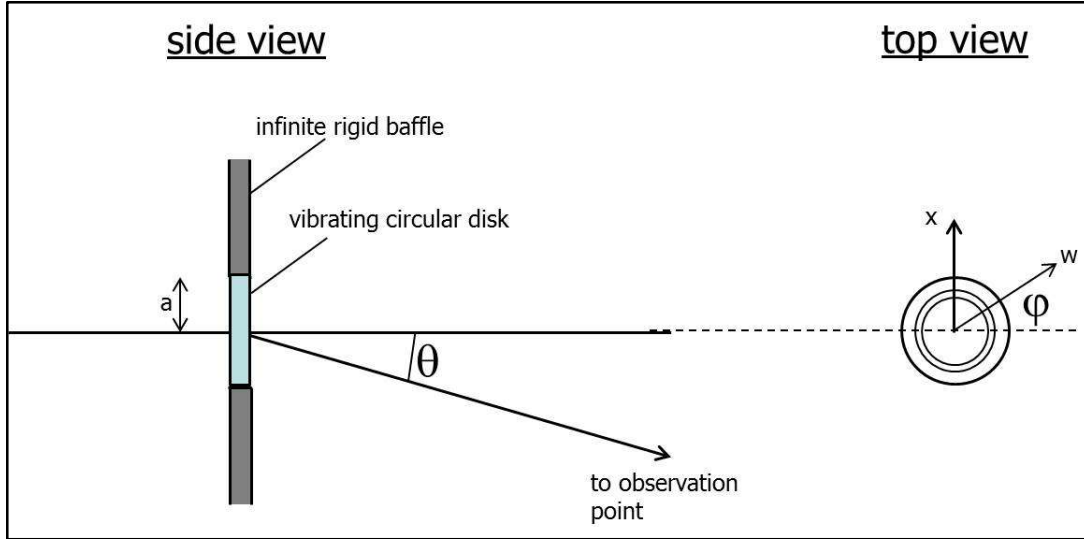


Figure 7.9: Side (left) and top view (right) of the geometry of the problem of the vibrating circular disk mounted in an infinite rigid baffle.

Equation 7.30 then becomes

$$p(r, t) = \frac{i\rho_\infty \omega v_0 e^{i\omega t}}{2\pi r} \int_{w=0}^a \int_{\varphi=0}^{2\pi} e^{-ik(r - w \sin \theta \cos \varphi)} w dw d\varphi \quad (7.31)$$

which can be rewritten as

$$p(r, t) = \frac{i\rho_\infty \omega v_0 e^{i(\omega t - kr)}}{2\pi r} \int_{w=0}^a w \left[ \int_{\varphi=0}^{2\pi} e^{ikw \sin \theta \cos \varphi} d\varphi \right] dw. \quad (7.32)$$

The integral over variable  $\varphi$  is well-known from calculus and is equal to  $2\pi J_0(kw \sin \theta)$  with  $J_0$  the zeroth order Bessel function of the first kind. The remaining integral then is

$$2\pi \int_{w=0}^a w J_0(kw \sin \theta) dw. \quad (7.33)$$

With a change of variables according to  $w' = kw \sin \theta$  this can be written as

$$\frac{2\pi}{(k \sin \theta)^2} \int_{w'=0}^{ka \sin \theta} w' J_0(w') dw'. \quad (7.34)$$

We will now use the following recursion relation for Bessel functions of the first kind:

$$x^n J_n(x) = \int_0^x s^n J_{n-1}(s) ds. \quad (7.35)$$

Using the special case  $n=1$ , equation 7.34 becomes

$$\frac{2\pi}{(k \sin \theta)^2} (ka \sin \theta) J_1(ka \sin \theta) = \frac{2\pi a}{k \sin \theta} J_1(ka \sin \theta). \quad (7.36)$$

The Rayleigh integral, equation 7.32, can now be written as

$$p(r,t) = \frac{i \rho_\infty \omega v_0 e^{i(\omega t - kr)}}{2\pi r} 2\pi a^2 \frac{J_1(ka \sin \theta)}{ka \sin \theta}. \quad (7.37)$$

With  $Q = \pi a^2 v_0$ , the volume velocity of the disk, this reads

$$p(r,t) = \frac{i \rho_\infty \omega Q}{2\pi r} e^{i(\omega t - kr)} \left[ \frac{2J_1(ka \sin \theta)}{ka \sin \theta} \right]. \quad (7.38)$$

The directional function  $\left[ \frac{2J_1(x)}{x} \right]^2$  (with  $x = ka \sin \theta$ ) is plotted in figure 7.8. From this figure (red line) it can be observed that the highest side lobe level (at  $x = 1.635\pi$ ) equals 0.0175 (or -18 dB).

The first zero of this function is at  $x = ka \sin \theta_0 = 1.22\pi$ . Assuming  $\theta$  to be small (hence  $\sin \theta \approx \theta$ ) and using  $k = \frac{2\pi}{\lambda}$ , we obtain  $\theta_0 = 1.22 \frac{\lambda}{2a}$ . Hence, the beam width is

$$2\theta_0 = 1.22 \frac{\lambda}{a}. \quad (7.39)$$

When the beam width is defined as the width at half maximum, the beam width is  $1.22 \frac{\lambda}{2a}$  with  $2a$  the diameter of the disk.

In figure 7.10 we have plotted the directional radiation pattern,  $\left[ \frac{2J_1(ka \sin \theta)}{ka \sin \theta} \right]^2$ , for three values of  $a$ , i.e.  $a = \frac{\lambda}{9}, \frac{\lambda}{3}$  and  $\lambda$ . For  $a = \frac{\lambda}{9}$ , corresponding to  $ka \approx 0.7 < 1$ , the radiation

pattern is virtually non-directional (as if the membrane is acting as a single non-directional monopole). For the larger values of  $a$ , corresponding to  $ka \approx 2$  and  $6$ , the radiation pattern is really directional.

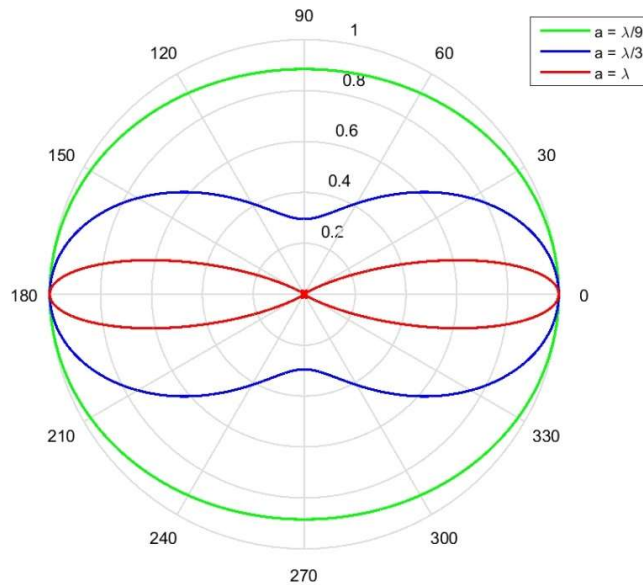


Figure 7.10: Directional radiation pattern of the vibrating circular disk for three values of the disk radius  $a$  relative to the wavelength  $\lambda$ .

For loudspeakers this has the following implications. We do not use the same loudspeaker, e.g. a large woofer, to produce both low and high frequencies, as you would notice a severe drop-off in the loudness of the higher frequencies as you step away from in front of the speaker. Hence, well-designed loudspeaker systems do not send all frequencies through the same speaker.

*Exercises*

Question 1

Consider an ‘array’ of two point monopoles separated by a distance  $d$  equal to  $\frac{\lambda}{2}$ . Give the formula for the directional radiation pattern. Sketch a polar plot of the radiation pattern. Sketch the polar plot of the radiation pattern of the dipole in the same figure for comparison.

Question 2

Consider a loudspeaker, which can be regarded as a circular vibrating membrane with a diameter of 12 cm, mounted in an infinite rigid baffle. Is this loudspeaker suitable for tonal sound with a frequency of 500 Hz? And for a tone of 5000 Hz? Explain why.

## Chapter 8 Acoustic imaging\*

In this chapter we consider arrays of receivers (microphones). The response of such an array can be made dependent on the direction of an incoming sound wave. This can be desirable, since it allows for estimating the direction from which a signal arrives ('acoustic imaging') and the unwanted noise from other directions is reduced. The directional sensitivity of a microphone array depends on the size of the array relative to the wavelength of the incoming sound. We will show that for low frequencies around say 100 Hz, the required size is several tens of meters, whereas for very high frequencies (e.g. around 1 MHz, i.e. medical imaging frequencies), a size of a few cm suffices.

For the theory developed in this chapter, the following assumptions are made:

- The signals are narrow band (or even single frequency);
- In section 8.1 and 8.2, we only consider the 'far field' situation, i.e. the sound source is at a large enough distance from the array, such that the wave front at the array's position can be considered as plane.

Concerning the second assumption, we will derive now what a far enough distance means. Consider, as shown in figure 8.1, a receiving array with length  $L$  and a point source at distance  $r$  on the acoustic axis of the array. The point source transmits spherical waves. These can be considered plane at the position of the array if the phase of the sound impinging in the middle of the array is sufficiently close to the phase of the sound that arrives at the end of the array. This phase difference should be about an order of magnitude smaller than  $360^\circ$ .

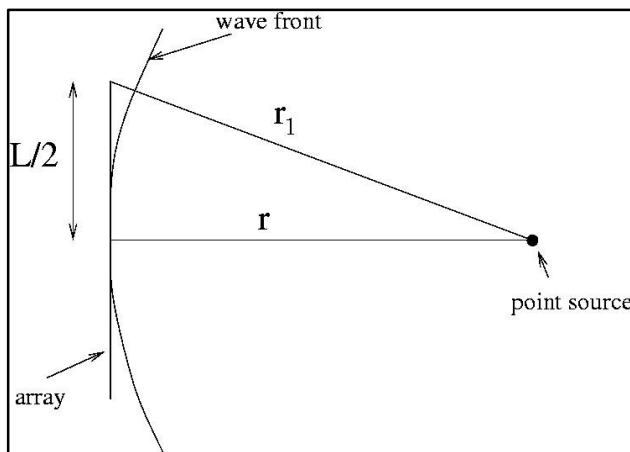


Figure 8.1: Receiving array of length  $L$  and a point source at distance  $r$  on the acoustic axis of the array. Also indicated is the acoustic wave front from the point source at the position of the array.

According to Pythagoras theorem

$$\left(\frac{L}{2}\right)^2 + r^2 = r_1^2 \quad (8.1)$$

with  $r_1$  the distance of the point source to end of the array. Assuming  $r_1 \approx r$ , we can approximate the distance difference  $r_1 - r$  by

$$r_1 - r = \frac{r_1^2 - r^2}{r_1 + r} = \frac{\left(\frac{L}{2}\right)^2}{r_1 + r} \approx \frac{L^2}{8r}. \quad (8.2)$$

We now define the Fresnel or Rayleigh distance  $r = r_F$  as the distance at which the distance difference equals  $\frac{\lambda}{8}$ , corresponding to a  $45^\circ$  phase difference between the sound impinging on the end of the array and the sound impinging on the middle of the array. Hence, we have

$$\frac{\lambda}{8} = \frac{L^2}{8r_F} \quad (8.3)$$

or

$$r_F = \frac{L^2}{\lambda} \quad (8.4)$$

i.e. the Rayleigh distance is dependent on frequency. A source at distance  $r > r_F$  is in the so-called ‘far field’ (or Fraunhofer zone). This source is located at a sufficiently large distance of the array, such that the incoming wave front can be considered as plane. For this case the theory as treated in sections 8.1 and 8.2 is sufficiently accurate. A source at a distance  $r < r_F$  is said to be located in the ‘near field’.

A microphone array can be steered electronically (‘beam steering’), such that the maximum response of the array can be obtained in each direction. The basic principle of this technique, denoted by ‘beamforming’, is discussed now.

### 8.1 Principle of beamforming\*

The basic principle behind the beamforming technique consists of combining the signals of all microphones by ‘delay and sum’. In figure 8.2 a plane wave front impinges on an array that consists of two (omni-directional) microphones. It is clear that the output of the array (after summation) will be maximal if the wave fronts are parallel to the array, i.e. if the wave fronts come from the direction perpendicular to the array.

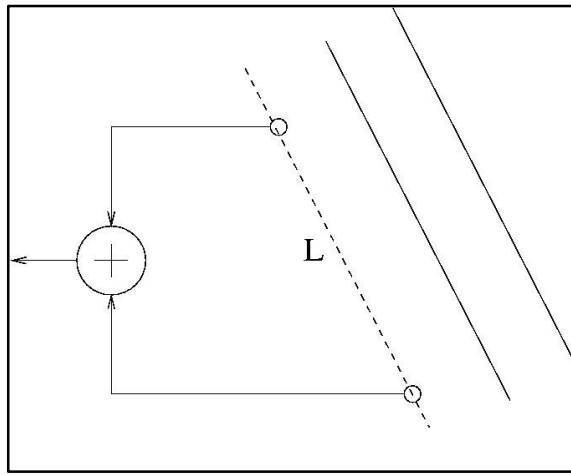


Figure 8.2: Plane wave fronts impinging on an array that consists of two point receivers. The wave fronts are parallel to the array, i.e. parallel to the line connecting the two receivers.

If the distance  $L$  between the two microphones, is larger than the wavelength  $\lambda$ , then the combined signal (here simply the summed signal) is strongly dependent on the direction the sound is coming from (this will be quantified in section 8.2).

Now consider the situation depicted in figure 8.3 (note that  $L$  is defined differently).

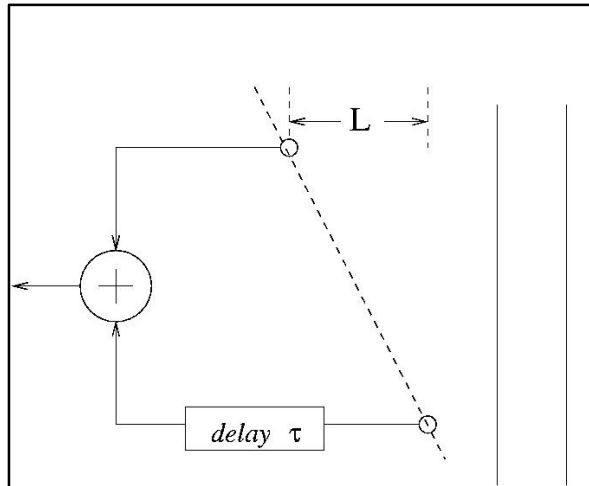


Figure 8.3: Plane wave fronts impinging on an array that consists of two point receivers. The wave fronts are not parallel to the array, i.e. not parallel to the line connecting the two receivers.

The output of this array can be maximised for the indicated direction (i.e. the vertical wave fronts) by applying an electronic delay  $\tau$  on the lower microphone of  $\tau = \frac{L}{c}$ , with  $c$  the sound speed. This is what we call ‘beam steering’, i.e. steering of the array in a desired direction. The usability of the technique, however, depends on the response of the array on wave fronts from other (than the desired) directions. Directions can exist for which the

response also adds maximally. These directions are denoted by the term ‘grating lobes’ ( see section 8.2).

We will now take a quantitative look at the beamsteering technique. We consider figure 8.4.

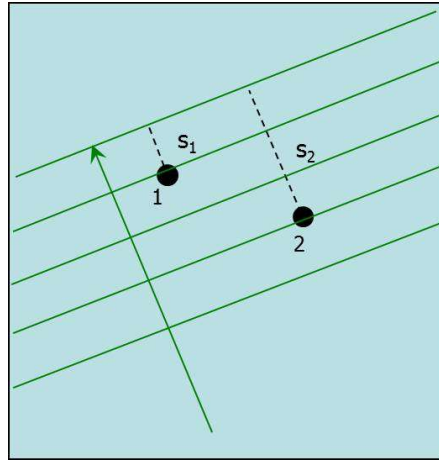


Figure 8.4: Two microphones (black dots) positioned in space where there is a plane wave field (green lines).

For a harmonic wave the signal on microphone 1 can be written as

$$A_1 \cos \omega(t + t_1) = A_1 \cos(\omega t + \phi_1) \quad (8.5)$$

where the phase is

$$\phi_1 = \omega t_1 = 2\pi f \frac{s_1}{c} = 2\pi \frac{s_1}{\lambda} \quad (8.6)$$

with  $s_1$  the distance as indicated in the figure. The signal received on microphone 2 is

$$A_2 \cos \omega(t + t_2) = A_2 \cos(\omega t + \phi_2) \quad (8.7)$$

with phase

$$\phi_2 = 2\pi \frac{s_2}{\lambda}. \quad (8.8)$$

We note that  $A_1$  and  $A_2$  can be used to weight the different signals, see section 8.2.

Using the goniometric relation  $\cos(a+b) = \cos a \cos b - \sin a \sin b$ , we obtain for the sum signal

$$(A_1 \cos \phi_1 + A_2 \cos \phi_2) \cos \omega t - (A_1 \sin \phi_1 + A_2 \sin \phi_2) \sin \omega t \quad (8.9)$$

which can be written as

$$Q_1 \cos \omega t - Q_2 \sin \omega t = \sqrt{Q_1^2 + Q_2^2} \cos(\omega t + \phi) \quad (8.10)$$

with

$$\begin{aligned} Q_1 &= A_1 \cos \phi_1 + A_2 \cos \phi_2 \\ Q_2 &= A_1 \sin \phi_1 + A_2 \sin \phi_2 \end{aligned} \quad (8.11)$$

and  $\varphi = \tan\left(\frac{Q_2}{Q_1}\right)$ .

The function  $\sqrt{Q_1^2 + Q_2^2}$  is called the 'directional response function' and the expressions for  $Q_1$  and  $Q_2$ , equation 8.11, form the basis for the next section.

## 8.2 1D beamforming \*

Figure 8.5 shows a line array of equidistant microphones. The distance or spacing between the succeeding microphones is  $d$ , whereas the number of microphones is  $N$  (taken to be uneven for the moment). Microphone 0 is taken as the reference. The coefficients  $a_n$  represent the weights that can be applied to the received signals. A plane wave front impinges on the array at an angle  $\theta$ .

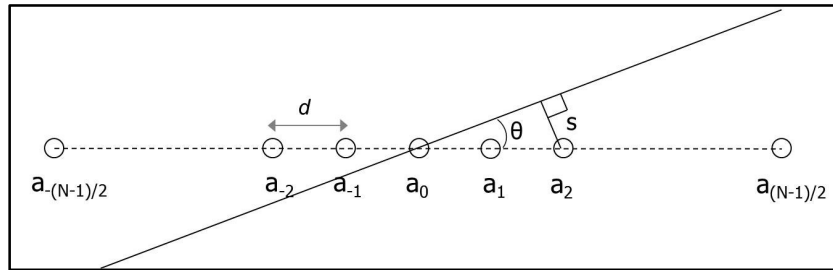


Figure 8.5: Line array of  $N$  equidistant microphones. Also indicated is a plane wave front impinging on the array at an angle  $\theta$ .

At microphone 1 the signal arrives  $t_1$  seconds earlier, at microphone 2 the signal arrives  $t_2$  earlier, etc. We have

$$\sin \theta = \frac{s_1}{d} = \frac{s_2}{2d} = \dots \quad \text{with} \quad t_1 = \frac{s_1}{c}, t_2 = \frac{s_2}{c}, \dots \quad (8.12)$$

The corresponding phase difference for microphone 1 (with respect to that of microphone 0) is

$$\phi_1 = \omega t_1 = 2\pi f \frac{s_1}{c} = \frac{2\pi}{\lambda} s_1 = \left( \frac{2\pi}{\lambda} \sin \theta \right) d . \quad (8.13)$$

Introducing the ‘projected’ wavenumber

$$K = \frac{2\pi}{\lambda} \sin \theta \quad (8.14)$$

we can write for the phase difference for microphone  $n$

$$\phi_n = nKd \quad \text{for } n = -\frac{(N-1)}{2}, \dots, -2, -1, 0, 1, 2, \dots, \frac{(N-1)}{2} . \quad (8.15)$$

Using equation 8.11 of the previous section we find for  $Q_1$  and  $Q_2$  for the situation of the line array

$$\begin{aligned} Q_1 &= a_0 + (a_1 + a_{-1}) \cos Kd + (a_2 + a_{-2}) \cos 2Kd + \dots + \left( a_{\frac{N-1}{2}} + a_{-\frac{N-1}{2}} \right) \cos \left( \frac{N-1}{2} \right) Kd \\ Q_2 &= (a_1 - a_{-1}) \sin Kd + (a_2 - a_{-2}) \sin 2Kd + \dots + \left( a_{\frac{N-1}{2}} - a_{-\frac{N-1}{2}} \right) \sin \left( \frac{N-1}{2} \right) Kd \end{aligned} \quad (8.16)$$

The sum signal of the array is given by equation 8.10 and  $D(K) = \sqrt{Q_1^2 + Q_2^2}$  is the directional response function.

Considering only symmetrical arrays, i.e.  $a_{-n} = a_n$ , then  $Q_2 = 0$ . If we also take all weights equal to 1, then

$$D(K) = 1 + 2 \cos Kd + 2 \cos 2Kd + \dots + 2 \cos \left( \frac{N-1}{2} \right) Kd . \quad (8.17)$$

Using  $\cos x = \frac{e^{ix} + e^{-ix}}{2}$  and the expression for the sum of a geometric series we obtain

$$D(K) = \frac{1 - e^{\frac{iK(N+1)d}{2}}}{1 - e^{iKd}} + \frac{1 - e^{-\frac{iK(N+1)d}{2}}}{1 - e^{-iKd}} - 1 \quad (8.18)$$

which can be written as

$$D(K) = \frac{-e^{\frac{iKd}{2}} + e^{\frac{iKn}{2}}}{-e^{\frac{-iKd}{2}} + e^{\frac{iKd}{2}}} + \frac{e^{\frac{iKd}{2}} - e^{\frac{-iKn}{2}}}{e^{\frac{iKd}{2}} - e^{\frac{-iKd}{2}}} + \frac{-e^{\frac{iKd}{2}} + e^{\frac{-iKd}{2}}}{e^{\frac{iKd}{2}} - e^{\frac{-iKd}{2}}} \quad (8.19)$$

or

$$D(K) = \frac{e^{\frac{iKd}{2}} - e^{-\frac{iKd}{2}}}{e^{\frac{iKd}{2}} - e^{-\frac{iKd}{2}}} = \frac{\sin\left(\frac{Kd}{2}\right)}{\sin\left(\frac{NKd}{2}\right)}. \quad (8.20)$$

It turns out that this expression is also valid for even  $N$ .

For  $Kd \rightarrow 0$ , i.e.  $\theta = 0^\circ$ ,  $D(K) = N$ . Hence, we normalize the function by  $N$  and write

$$D(K) = \frac{\sin\left(\frac{NKd}{2}\right)}{N \sin\left(\frac{Kd}{2}\right)}. \quad (8.21)$$

We will now examine this important function. Figure 8.6 shows a plot of  $D(K)$  as a function of  $\frac{Kd}{2}$  for  $N = 5$  and  $N = 6$ .

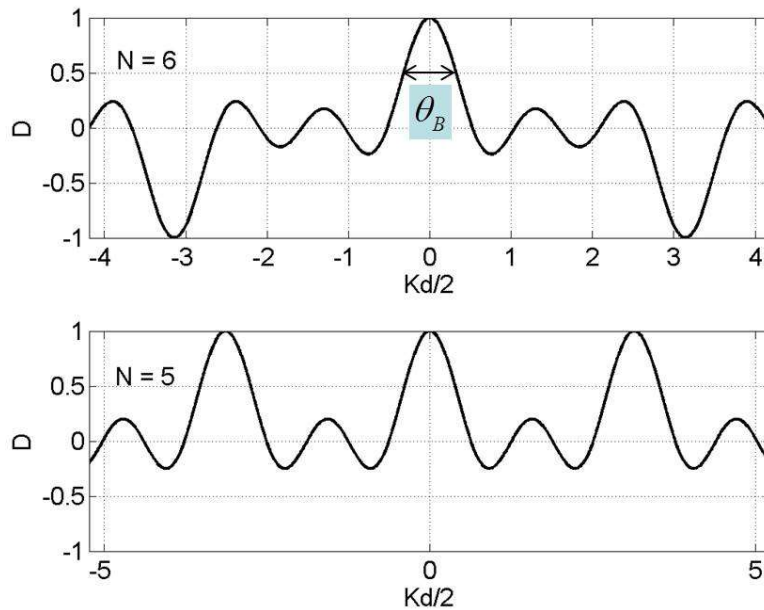


Figure 8.6: Directional response function, equation 8.21, for a line array with 6 and 5 equidistant microphones.

$D(K)$  has the following properties:

- If  $\frac{Kd}{2} = 0$ ,  $D(K)$  is maximal, i.e. 1. This peak is called the 'main lobe'.
- If  $\frac{NKd}{2} = n\pi$ ,  $n = 1, 2, \dots$ , then  $D(K) = 0$ .

- If  $\frac{Kd}{2} = n\pi$ ,  $n = 1, 2, \dots$ , then  $D(K)$  is also maximal. These peaks (either +1 or -1) are called 'grating lobes'.
- The height of the first 'side lobe', i.e. the smaller peak closest to the main lobe, is 0.22 (-13 dB).

It is clear that in the example of figure 8.6 several peaks of amplitude 1, i.e. the maximum value, are present. The question is, however, whether these occur when  $D$  is plotted as a function of angle  $\theta$  (from  $-90^\circ$  to  $+90^\circ$ ). This undesired effect will be examined later. First, we derive a practical formula for the angular width of the main lobe.

The zeros left and right of the main lobe are at  $\frac{Kd}{2} = \pm \frac{\pi}{N}$ . That is why we define a 'beam width'  $\theta_B$  according to the equations  $\frac{Kd}{2} = \pm \frac{\pi}{2N}$ . Using the definition of  $K$  we have

$$\frac{Kd}{2} = \frac{2\pi d}{2\lambda} \sin\left(\frac{\theta_B}{2}\right) = \frac{\pi}{2N} \quad (8.22)$$

or

$$\theta_B = 2 \sin^{-1} \frac{\lambda}{2Nd} \approx 2 \sin^{-1} \frac{\lambda}{2L} \quad (8.23)$$

where we have used for the array length  $L = (N-1)d \approx Nd$ . For sufficiently large  $L$  (i.e.  $\theta_B$  is sufficiently small) we obtain the simple but very practical result

$$\theta_B = \frac{\lambda}{L}. \quad (8.24)$$

Note that the obtained  $\theta_B$  is in radians. The width of the main lobe is called the 'angular resolution' of the array.

We will now determine the condition on the microphone spacing  $d$  for which there are no grating lobes, i.e. the condition that there are no angles  $\theta$  in the range from  $-90^\circ$  to  $+90^\circ$  for which  $D$  is also maximal (i.e. equal to 1), next to the main peak at  $\theta = 0^\circ$ .

The first grating lobes are at  $\frac{Kd}{2} = \pm \pi$ . Suppose that  $d = \lambda$ , then this equation becomes

$\pi \sin \theta = \pm \pi$ , the solution of which is  $\theta = \pm 90^\circ$ . This means that when  $d = \lambda$  there are two grating lobes, but they are at the utmost angles. Now assume  $d = \frac{\lambda}{2}$  then we have

$\frac{\pi}{2} \sin \theta = \pm \pi$  and this equation has no solutions, i.e. there are no grating lobes. The condition for which there are no grating lobes is therefore

$$d < \lambda. \quad (8.25)$$

This condition will be more stringent when beam steering is applied (see further).

For the extreme situation that the number of microphones becomes infinite while keeping the array length  $Nd$  finite (i.e.  $N \rightarrow \infty, d \rightarrow 0, Nd$  finite), the directional response function becomes

$$D(K) = \frac{\sin\left(\frac{NKd}{2}\right)}{N \sin\left(\frac{Kd}{2}\right)} = \frac{\sin\left(\frac{KL}{2}\right)}{N \sin\left(\frac{KL}{2N}\right)}. \quad (8.26)$$

Using  $\sin x \approx x$  for  $x \ll 1$ , the dominator of this function becomes  $\frac{KL}{2}$  for  $N$  very large.

Hence,

$$D(K) = \frac{\sin\left(\frac{KL}{2}\right)}{\frac{KL}{2}}. \quad (8.27)$$

This directional response function has never grating lobes. Further, knowing that  $K = \frac{2\pi}{\lambda} \sin \theta = k \sin \theta$ , we note that this is the same equation as that obtained in chapter 7 for the continuous line array of monopoles (see equation 7.26).

As already mentioned in the introduction, an array can be steered electronically such that the maximum response of the array can be obtained in any direction. The steering occurs by applying a delay on the signals of each of the microphones. This is called ‘beam steering’. For a beam in the direction  $\theta_s$  the required delay  $\tau_s$  for microphone  $n$  equals

$$\tau_s = \frac{nd}{c} \sin \theta_s. \quad (8.28)$$

The corresponding phase is

$$\phi_s = \omega \tau_s = \frac{2\pi f}{c} nd \sin \theta_s = \frac{2\pi}{\lambda} \sin \theta_s nd. \quad (8.29)$$

Defining  $K_s = \frac{2\pi}{\lambda} \sin \theta_s$ , this can be written as

$$\phi_s = K_s nd. \quad (8.30)$$

It is easily shown that the directional response function for a line array, steered in the  $\theta_s$  direction, is

$$D(K) = \frac{\sin\left(\frac{N(K - K_s)d}{2}\right)}{N \sin\left(\frac{(K - K_s)d}{2}\right)}. \quad (8.31)$$

We have seen that for a line array with no steering and with  $d = \lambda$ , the grating lobes are at  $\theta = \pm 90^\circ$ . If we now steer the array to  $\theta_s$ , the grating lobe equation is

$$(K - K_s) \frac{d}{2} = \pm m\pi \quad \text{for} \quad m = 1, 2, \dots \quad (8.32)$$

or

$$\sin \theta = \sin \theta_s \pm m \frac{\lambda}{d} \quad \text{for} \quad m = 1, 2, \dots \quad (8.33)$$

This equation has no solutions, i.e. there are no grating lobes, if

$$d \leq \frac{\lambda}{2}. \quad (8.34)$$

Note: If we steer the array (with  $d = \frac{\lambda}{2}$ ) in the utmost direction  $\theta_s = 90^\circ$ , then the grating lobe is at  $\theta = -90^\circ$ .

As an example we consider an array of length  $L = 7.5\lambda$  and consisting of  $N = 8$  microphones. The microphone spacing is thus  $d = 1.07\lambda$ . Figure 8.7 shows plots of the absolute value of the directional response function  $D$  as a function of angle  $\theta$ . The graph on the left is for the un-steered array ( $\theta_s = 0^\circ$ ) and the graph on the right for a steering angle  $\theta_s = 30^\circ$ . In both cases there is a grating lobe (at  $69.2^\circ$  for  $\theta_s = 0^\circ$  and  $-25.8^\circ$  for  $\theta_s = 30^\circ$ , respectively).

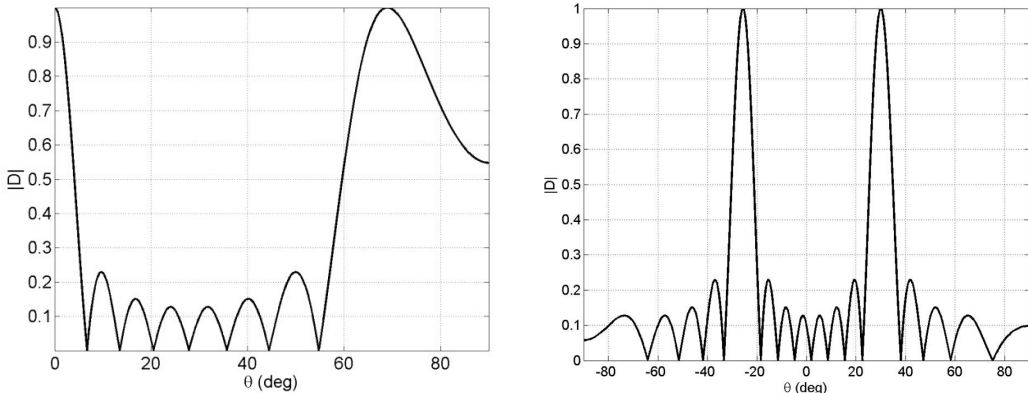


Figure 8.7: Absolute value of the directional response function as a function of angle for a line array with 8 microphones and a microphone spacing of  $1.07\lambda$ . The left figure is for the un-steered array and the right figure is for the array steered in the direction  $30^\circ$ .

As a second example we consider an array of the same length  $L = 7.5\lambda$ , but now consisting of  $N = 16$  microphones. The microphone spacing is thus  $d = \frac{\lambda}{2}$ . We steer the array in the direction  $\theta_s = 60^\circ$ . Figure 8.8 shows  $|D|$  as a function of  $\theta$  for  $\theta = -180^\circ$  to  $+180^\circ$ . Because of the symmetry there is a beam at  $\theta_s = 60^\circ$  (as required) and at  $\theta_s = 120^\circ$ . However, the latter beam is not a grating lobe.

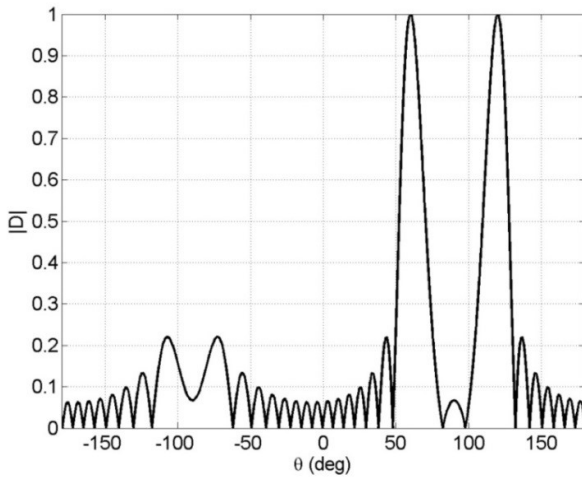


Figure 8.8: Absolute value of the directional response function as a function of angle for a line array with 16 microphones and a microphone spacing of  $0.5\lambda$ . The array is steered in the direction  $60^\circ$ . Because of the symmetry there is also a beam at  $120^\circ$ .

The directional response function can also be presented in the form of a polar plot. The left part of figure 8.9 shows the polar plot on a linear scale ( $|D|$  versus  $\theta$ ), whereas the right part of figure 8.9 shows the polar plot on a dB scale (dynamic range 40 dB) to enhance the side lobe pattern.

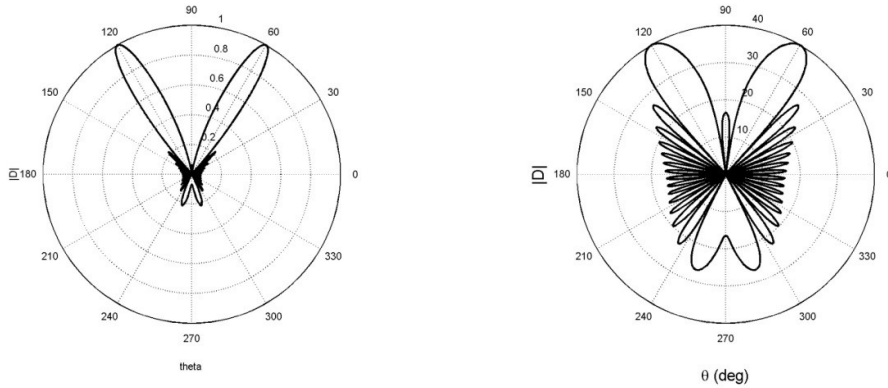


Figure 8.9: Polar plots of the directional response function of figure 8.8, both on a linear scale (left) and a dB scale (right).

From the grating lobe equation 8.33 we can deduce that, for arbitrary microphone spacing  $d$ , the maximum steering angle up to which no grating lobes occur is given by

$$\theta_{s,\max} = \sin^{-1}\left(\frac{\lambda}{d} - 1\right) \quad (8.35)$$

i.e. grating lobes do not occur at all for  $d \leq \frac{\lambda}{2}$ , but do occur for all steering angles for  $d \geq \lambda$ .

A practical formula for the beam width of a steered array is obtained as follows. The equation from which the beam width of an un-steered array was determined is  $\frac{Kd}{2} = \pm \frac{\pi}{2N}$ . This equation now becomes  $\frac{Kd}{2} = \frac{K_s d}{2} \pm \frac{\pi}{2N}$ . We define the beam width for the steered array as  $\theta_{B,s} = \theta_2 - \theta_1$ . Then according to equation 8.14,  $\theta_1$  and  $\theta_2$  are determined by the equations

$$\begin{aligned} \sin \theta_1 &= \sin \theta_s - \frac{\lambda}{2Nd} \\ \sin \theta_2 &= \sin \theta_s + \frac{\lambda}{2Nd} \end{aligned} \quad (8.36)$$

Hence,

$$\sin \theta_2 - \sin \theta_1 = \frac{\lambda}{Nd} \quad (8.37)$$

or

$$\sin\left(\frac{\theta_2 - \theta_1}{2}\right) \cos\left(\frac{\theta_2 + \theta_1}{2}\right) = \frac{\lambda}{N2d}. \quad (8.38)$$

With  $\frac{\theta_2 + \theta_1}{2} \approx \theta_s$  and  $N2d \approx 2L$ , this equation becomes

$$\sin\frac{\theta_{B,s}}{2} \approx \frac{\lambda/2L}{\cos\theta_s} \approx \frac{\sin(\theta_B/2)}{\cos\theta_s} \quad (8.39)$$

with  $\theta_B$  the beam width of the un-steered array ( $\theta_s = 0^\circ$ ), see equation 8.23. For small beam widths ( $L$  large) this equation can further be approximated to

$$\theta_{B,s} = \frac{\theta_B}{\cos\theta_s} \quad (8.40)$$

i.e. again a simple but very practical result (compare with equation 8.24).

Grating lobes are highly undesirable, but also side lobes can have a detrimental effect on array performance. Consider again figure 8.9. There are no grating lobes, but the highest side lobe level is only 13 dB less than the main lobe. This means that sound with a certain strength that enters the array at the main lobe results in an array output that is just as high as a signal resulting from sound with a 13 dB higher level that enters the array at an angle where the highest side lobe occurs. In other words, weak signals in the main lobe cannot be discriminated from a 13 dB stronger signal from a different direction. This effect can be highly undesirable. The solution is side lobe reduction by applying weights ( $a_n$ ) to the received microphone signals. Well-known weighting functions are the so-called ‘Hanning’ and ‘Hamming’ weighting, see figure 8.10 for an array with 16 microphones. Note that the outer microphone signals are heavily attenuated by this type of weighting.

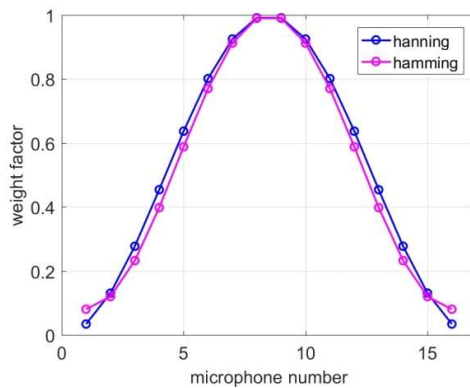
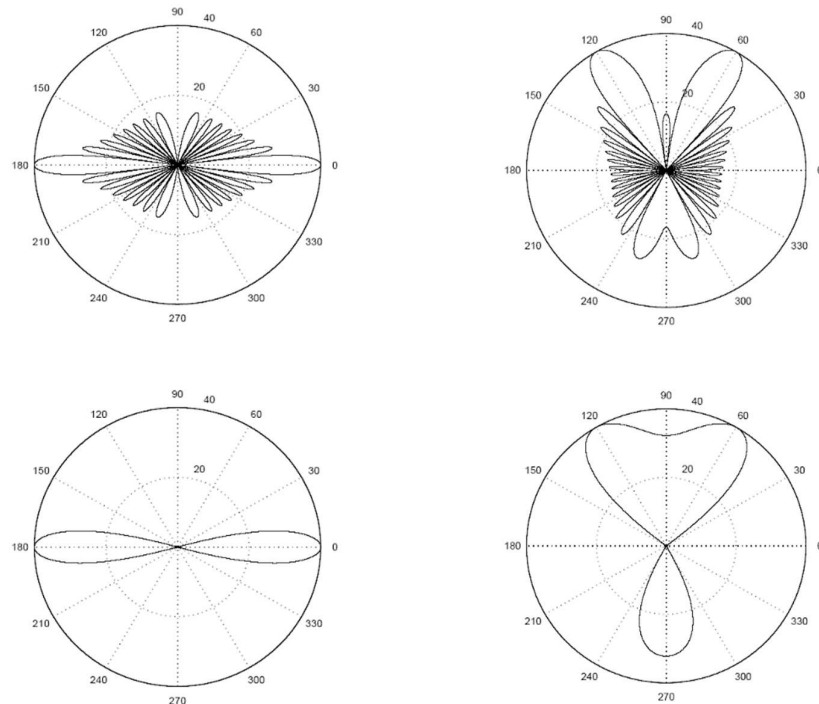


Figure 8.10: Hanning and Hamming weighting functions for a 16-element array.

Figure 8.11 shows polar plots of the directional response function in dB for the 16 microphone array with  $d = \frac{\lambda}{2}$ , with (bottom figures) and without weighting (top figures). The plots on the left are for ‘no steering’, whereas the plots on the right are for  $\theta_s = 60^\circ$ . The side lobe suppression is impressive. The price paid for this is a broadening of the main lobe, i.e. angular resolution gets somewhat worse.



**Figure 8.11:** Polar plots of the directional response function in dB for an array with 16 microphones and a spacing of  $0.5\lambda$ , without weighting (top figures) and with weighting (bottom figures). Left figures: no steering. Right figures: steering angle is  $60^\circ$ .

The analytical formulas derived for the directional response functions, e.g. equation 8.31, are useful for getting an idea of the performance of a specific array with a certain length (aperture) and microphone spacing. Performance indicators then are angular resolution, side lobe level and grating lobe presence as a function of frequency. In other words, these formulas are useful for designing an array for a specific application, prior to the actual beamforming (i.e. acoustic imaging) of the acoustic data. The beamforming of real data is quite straightforward and goes as follows.

Delay and sum beamforming is easily implemented in the frequency domain. Assume we have  $N$  microphone signals  $x_n(t_k)$ ,  $n=1,\dots,N$ , sampled in the time domain at discrete times  $t_k$ . After Fourier transforming we obtain  $X_n(f_k)$ ,  $n=1,\dots,N$  with  $f_k$  the discrete frequencies (see chapter 5). Now suppose that we have a signal  $x(t)$  with Fourier transform

$X(f)$ . Then the Fourier transform of the delayed signal  $x(t - \tau)$  is  $X(f)e^{-2\pi if\tau}$ . Hence, the delay and sum beamformer is implemented as

$$\sum_{n=1}^N X_n(f_k) e^{-2\pi i f_k \tau_n} \quad (8.41)$$

with

$$\tau_n = \frac{d}{c} n \sin \theta_s \quad (8.42)$$

for the case of a line array with microphone spacing  $d$ , steered in the direction  $\theta_s$ . For a fixed frequency  $f_k$  the beamformer output is

$$B(\theta_s, f_k) = \left| \sum_n X_n(f_k) e^{-2\pi i f_k \tau_n} \right|^2 \quad (8.43)$$

i.e. a real function of the two variables  $\theta_s$  and  $f_k$ . This can be written as

$$B(\theta_s, f_k) = \mathbf{g}^* (\mathbf{X} \mathbf{X}^*) \mathbf{g} = \mathbf{g}^* \mathbf{C} \mathbf{g} \quad (8.44)$$

with  $\mathbf{g}$  the steering vector with components  $g_n = e^{-2\pi i f_k \tau_n}$ ,  $n = 1, \dots, N$  and  $\mathbf{X}$  the data vector with components  $X_n(f_k)$ ,  $n = 1, \dots, N$ . The superscript \* denotes the conjugate transpose (i.e. if  $\mathbf{X}$  is column vector with complex numbers, then  $\mathbf{X}^*$  is a row vector containing the complex conjugates of the components of  $\mathbf{X}$ ).  $\mathbf{C} = \mathbf{X} \mathbf{X}^*$  is called the  $N \times N$  data covariance matrix. Usually, the dB value of  $B$  is presented, i.e.  $10 \log(B(\theta_s, f_k))$ .

### 8.3 2D beamforming\*

The implementation of delay and sum beamforming for the 2D situation is very similar to that of the 1D situation. The microphones are now in a 2D configuration and we define a 2D scan plane at a certain distance parallel to the plane of the microphone array, see figure 8.12. We assume possible sources to be in the defined scan plane.

Note: In this section the far field assumption is (see beginning of this chapter) is abandoned.

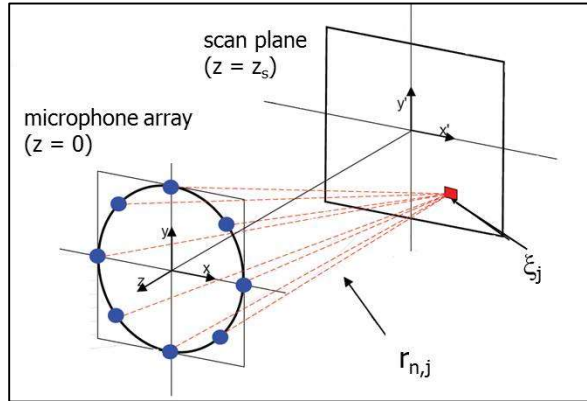


Figure 8.12: Geometry for 2D beamforming.

The beamformer output can now be written as

$$B(\xi_j, f_k) = \frac{\mathbf{g}^* (\mathbf{X} \mathbf{X}^*) \mathbf{g}}{\|\mathbf{g}\|^2} \quad (8.45)$$

with  $\xi_j = (x_j', y_j')$  the position vector of grid point  $j$  in the scan plane. The steering vector  $\mathbf{g}$  has now components

$$g_n(\xi_j, f_k) = \frac{e^{-j2\pi f_k \left( \frac{r_{n,j}}{c} \right)}}{r_{n,j}} \quad (8.46)$$

with the distance from position  $j$  in the scan plane to microphone  $n$  given by

$$r_{n,j} = \sqrt{(x_n - x_j')^2 + (y_n - y_j')^2 + z_s^2}. \quad (8.47)$$

Here,  $(x_n, y_n)$  is the position of microphone  $n$  (in the plane  $z=0$ ) and the scan positions are in the plane  $z=z_s$ , i.e. the distance between the scan plane and the plane of the microphone array is  $z_s$ .

$\frac{r_{n,j}}{c}$  represent the delay  $\tau_n$  of equation 8.43. The only difference between equation 8.45 and 8.44 is that we now normalize the steering vector by its length  $\|\mathbf{g}\|$ . The steering vector given in equation 8.46 implicitly assumes a monopole source model to describe the sound pressure field. Also, the source is assumed to be non-moving. For aircraft flyovers, this is a valid approximation when the airplane noise source is directly above the microphone array (provided a sufficiently small time interval is taken for the Fourier transform).

We will now present some simulations for sound sources at 8 m distance from a microphone array consisting of 32 microphones. The microphones are situated within a circle of radius 1 m, i.e. the array aperture is 2 m. In the first simulation we have two sources, simultaneously radiating at 2000 Hz. The first source is at the position (0,0) in the scan plane and the second source is at the position (-2.5 m,0). The microphone signals are simulated in the time domain accounting for the time delays dependent on the microphone positions and the position of the sources (see equation 8.47). Subsequently, equations 8.45 and 8.46 are employed to generate the beamformer output for a scan plane of size 9 m x 9 m.

The positioning of the microphones within the available aperture is not so obvious for the 2D situation as it is for the 1D situation. In fact, still quite some research is carried out to find the best 2D microphone configuration. Perhaps the most obvious array configuration is a cross consisting of two perpendicular 1D arrays as shown in the top left plot of figure 8.13. In this simple configuration, 16 microphones are positioned along the  $x$ -axis and the other 16 microphones along the  $y$ -axis. The corresponding beamformer output is shown in the top right plot of the figure on a dB scale. It is observed that the beamformer is capable of resolving the two sources, however the side lobes are quite high and abundant. According to equation 8.24 the angular resolution of a 1D array is  $\theta_B = \frac{\lambda}{L}$  with  $L$  the array aperture in one dimension. Because of the array being 2D, a more accurate formula for the angular resolution is given by  $\theta_B = 1.22 \frac{\lambda}{L}$ , i.e. the beam width of a vibrating circular disk (with diameter  $L$ ) as treated in section 7.3. The spatial resolution in the scan plane is then given by

$$\theta_B z_s = 1.22 \frac{cz_s}{fL} \quad (8.48)$$

provided the source is not too far away from the origin (0,0) in the scan plane. This formula is known as ‘Rayleigh’s criterion’ for the spatial resolution and is indicated in the beamform output plot by the dashed red circle (the diameter of which is 0.83 m in this case). Hence, it is not a surprise that the beamformer is capable of resolving two sources that are separated by 2.5 m.

The left middle plot of figure 8.13 shows a configuration where the available 32 microphones are positioned along concentric circles. The outer circle has a radius of nearly 1 m, i.e. the microphones stay within the available array aperture of 2 m. The corresponding

beamformer output is shown in the middle right plot of the figure. Fortunately, the side lobes are lower and less abundant, while the two sources are still resolved with virtually the same resolution.

The lower left plot of figure 8.13 shows a frequently used configuration where the microphones are positioned along a spiral. For this particular case, the beamformer performance, shown in the lower right plot of the figure, is similar to that of the concentric circles configuration.

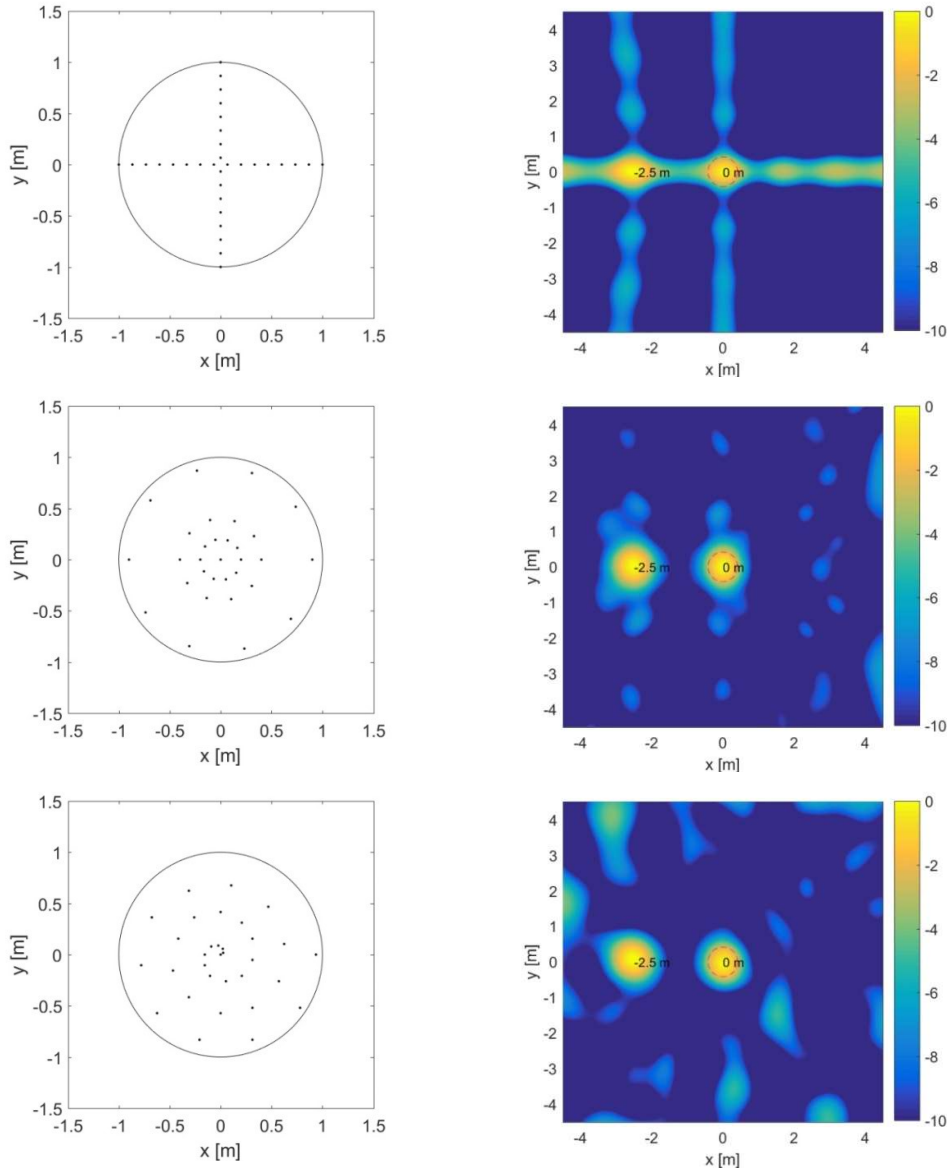


**Figure 8.13:** 2D microphone configurations (left) and corresponding beamformer outputs in dB (right). Two sources separated by 2.5 m and at 8 m from the array are considered. The sources simultaneously radiate at 2000 Hz.

In the second simulation we further investigate the spatial resolution of the 2 m aperture array consisting of 32 microphones. We select the configuration with the microphones

positioned along concentric circles, see left middle plot of figure 8.13. Again we simulate two sources, both radiating at 2000 Hz, at 8 m from the array. The first source is still fixed at the position (0,0) in the scan plane. The other source is at the  $x$ -axis but now with a varying distance to the fixed source at (0,0). Figure 8.14 shows the beamformer output for decreasing separation of the two sources, starting from 1.25 m to 0.5 m in steps of 0.25 m. It is clearly observed that when the source separation is below the Rayleigh limit (0.83 m in this case, see above), the beamformer is not capable anymore of resolving the two sources.

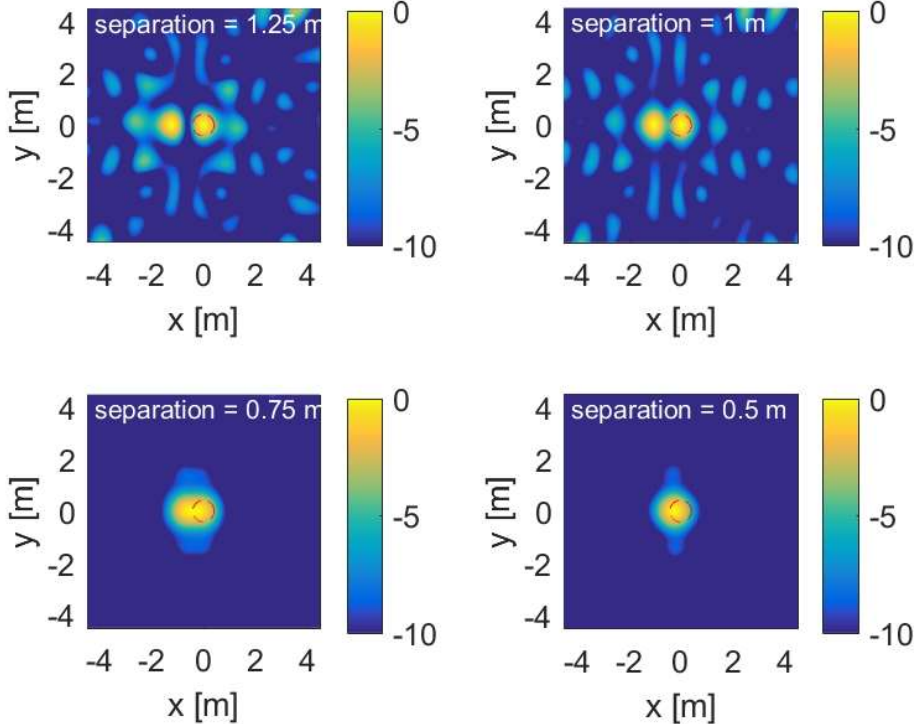


Figure 8.14: Beamformer outputs (in dB) for the configuration with microphones along concentric circles, see left middle plot of figure 8.13. Two sources at 8 m from the array are considered. The sources simultaneously radiate at 2000 Hz. The source separation is subsequently decreased from 1.25 m to 0.5 m in steps of 0.25 m.

We mentioned above that for the angular resolution of a 2D array with aperture  $L$  we use the formula  $\theta_B = 1.22 \frac{\lambda}{L}$ , i.e. the beam width of a vibrating circular disk (see section 7.3). To be more precise, the beam width of the vibrating circular disk should be equal to the beam width of a circular array of the same size that is densely populated with microphones. This

means that the directional response function of such an array is  $\frac{2J_1\left(\frac{2\pi}{\lambda} \frac{L}{2} \sin \theta\right)}{\left(\frac{2\pi}{\lambda} \frac{L}{2} \sin \theta\right)}$  (see

equation 7.38 and figure 7.8). In the next simulation we have verified this by simulating a source at the origin (0,0) of the scan plane at 8 m from the array. The frequency of the source is again 2000 Hz. The obtained beamform plot in dB as shown in figure 8.15 is indeed

the projection of this function on the scan plane. The light blue halo around the main peak, representing the circle-symmetric highest side lobes, indeed has a level of -18 dB.

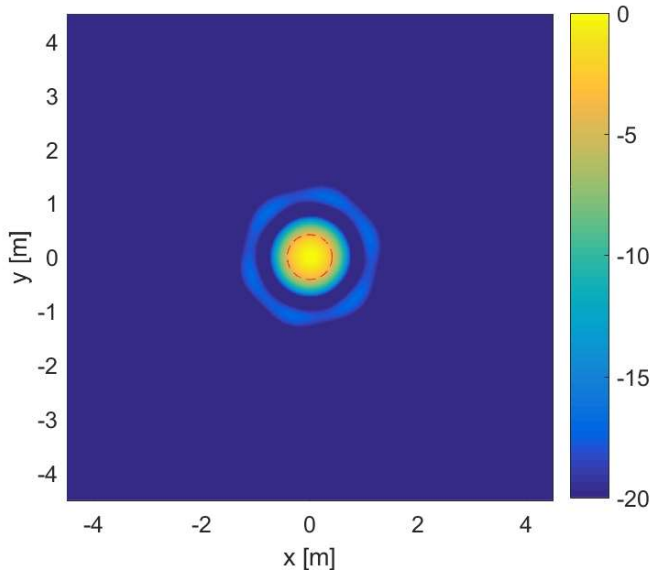


Figure 8.15: Beamformer output (in dB) for a circular array of the same size as that of figures 8.13 and 8.14, but now densely populated with microphones. The source, radiating at 2000 Hz, is at 8 m from the centre of the array.

#### 8.4 Imaging aircraft noise data\*

For the delay and sum beamformer, the spatial resolution at low frequencies can be quite insufficient, whereas at high frequencies the beamform output can show many side and grating lobes. These two effects can be counteracted by averaging the beamform outputs calculated for the distinct frequencies  $f_k$  within a certain band according to

$$B_{\text{incoh}}(\xi_j) = \frac{1}{N_f} \sum_{k=1}^{N_f} B(\xi_j, f_k) \quad (8.49)$$

with  $B(\xi_j, f_k)$  given by equation 8.45 and  $N_f$  the number of frequencies in the band considered. This so-called incoherent averaging over frequencies averages away side and grating lobes that are differently positioned in the beamform outputs at the various frequencies, while at the same time preserving the good resolution at the higher frequencies.

The band-averaged beamform outputs presented here have been obtained by taking the dB value of  $B_{\text{incoh}}$  (after correcting it for the aircraft altitude  $z_s$  by adding  $20 \log z_s$ ). Beamform outputs are shown for the band 1500 – 4500 Hz where airframe noise is expected to be important (see section 9.4, in which figure 9.15 presents a comparison of the measured

spectrum to that calculated with an airframe noise model). The frequency step is 20 Hz as set by the snapshot time of 50 ms used for the Fourier transforming of the data. Hence, 150 frequencies are used for the averaging.

Note: in section 5.2 we have learned that the frequency resolution of a Fourier transform is equal to the inverse of the signal length (or snapshot time as used for the Fourier transforming).

The microphone array used is shown in the left part of figure 8.16. It consists of 32 microphones in a spiral configuration with an array aperture of 1.7 m. The array's spatial resolution according to the Rayleigh criterion is shown in the right part of the figure by the solid line. In this section we show beamform results for landing aircraft with an altitude  $z_s$  of around 65 m (when the aircraft is directly above the array). According to equation 8.48

the solid line in the figure is then given by  $\frac{1.6 \times 10^4}{f(\text{Hz})}$ . Also indicated in the figure are the

shortest distances between the engines and the main landing gear for various types of aircraft (the horizontal dashed lines). We may conclude that for the smaller aircraft (Boeing 737, Fokker 70 and Airbus 321), resolving main landing gear from the engine noise is problematic as landing gear noise is expected to be only present at frequencies below approximately 4500 Hz (see section 9.4). For the other aircraft we may expect to see the main landing gear noise to be separated from the engine noise in the beamform plots. (The somewhat arbitrary lower bound of 1500 Hz is determined by spatial resolution considerations, since below 1500 Hz the array's resolution becomes worse than 10 m).



Figure 8.16: Left figure: Microphone array hardware used for the aircraft flyover measurements (32 microphones in a spiral configuration with an array aperture of 1.7 m). Right figure: Corresponding spatial resolution versus frequency according to the Rayleigh criterion and shortest distances between the engines and the main landing gear for various types of aircraft.

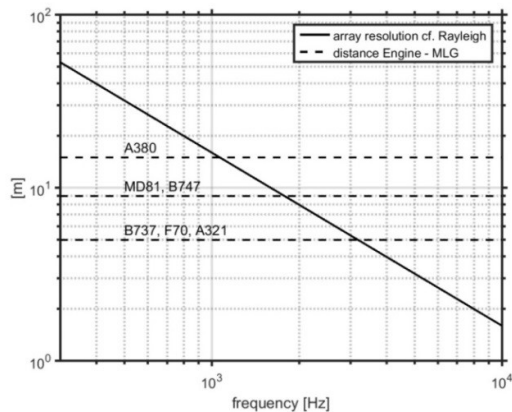


Figure 8.17 shows the beamform output (using equation 8.49 on a dB scale) for a Fokker 70 (left) and an Airbus 380 (right). In each plot we have added the aircraft contour (black solid

lines) on top of the images, including the positions of the landing gear as indicated by the small squares. For the Fokker 70 the spatial resolution is not sufficient to resolve noise from the engines and main landing gear, although the noise from the nose landing gear is clearly resolved. As expected, noise from the engines and main landing gear for the Airbus 380 is indeed resolved.

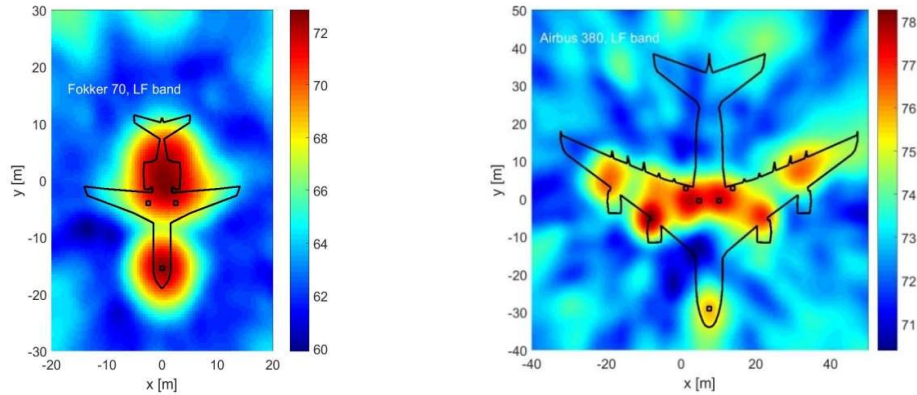


Figure 8.17: Beamformer output for a Fokker 70 (left) and an Airbus 380 (right) flyover (band 1500 – 4500 Hz).

Note: within the 50 ms snapshot the aircraft have moved by a distance of approximately 3.8 m (aircraft velocity is around 70 m/s), which is virtually equal to the resolution of the array at 4500 Hz. The array's resolution in the middle of the frequency band considered amounts to 5.4 m (see figure 8.16), i.e. significantly larger than the distance of 3.8 m flown by the aircraft. Hence, for the 1500 – 4500 Hz band, the 50 ms snapshot time is chosen short enough.

### Exercises

#### Question 1

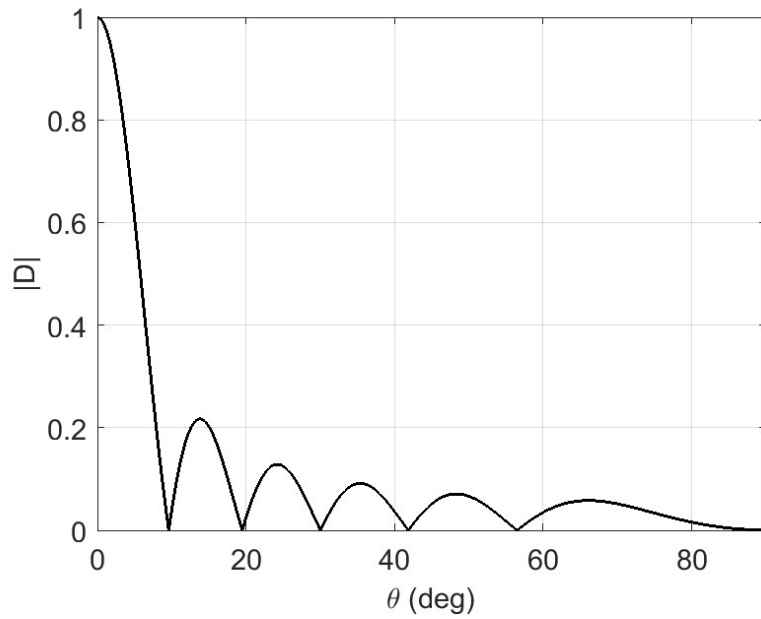
We consider acoustic imaging systems for a wide range of applications, ranging from atmospheric research with infrasound to medical diagnosis with ultrasound. The table below lists a total of five applications, organised from low to high operating frequency. Note that the medium (and hence sound speed  $c$ ) differs for the various applications. Assuming 1D acoustic imaging and given a fixed angular resolution requirement of  $2^\circ$  for all applications, find the required linear array lengths  $L$  and plot these versus the operating wavelengths  $\lambda$  on a log-log scale. Also, give the formula relating  $L$  and  $\lambda$ .

Note: for each application assume that the spacing between the sensors is equal to half the operating wavelength.

<b>Application</b>	<b>Operating frequency</b>	<b>Medium</b>
Atmospheric research with infrasound	10 Hz	Air ( $c = 340 \text{ m/s}$ )
Submarine detection with passive sonar	500 Hz	Water ( $c = 1500 \text{ m/s}$ )
Source identification of aircraft noise	1 kHz	Air ( $c = 340 \text{ m/s}$ )
Seabed mapping in hydrography	500 kHz	Water ( $c = 1500 \text{ m/s}$ )
Medical diagnosis with ultrasound	5 MHz	Water ( $c = 1500 \text{ m/s}$ )

#### Question 2

Consider a continuous line array for which we can assume that it is built up with very many, very closely spaced transducers. The figure below gives for this array the absolute value of the directional response function  $D$  as a function of the angle of incidence  $\theta$  for sound in air ( $c = 340 \text{ m/s}$ ) with a frequency of 1500 Hz.



- a) Determine the length  $L$  of the array.
- b) Calculate the beamwidth of the array using the answer of a). Compare this result with the beamwidth as determined from the figure.
- c) What is the level of the first side lobe in dB.

## Chapter 9 Aircraft noise sources

When discussing noise sources on aircraft a distinction is made between noise from the aircraft engines and noise from the airframe. In the first three sections of this chapter some general properties of these noise sources are subsequently discussed. Regarding engine noise a further distinction is made between propeller noise (section 9.1) and turbo engine noise (such as turbo jet and turbofan noise, see section 9.2). Airframe noise is briefly discussed in section 9.3. In section 9.4 a more detailed treatment of aircraft noise from a modelling perspective is presented. Finally, section 9.5 introduces the topic of aerodynamics, i.e. the study of noise generation of turbulent fluid motion or noise due to aerodynamic forces that interact with surfaces.

### 9.1 General properties of piston engine and propeller noise

The piston engine of a propeller-driven aircraft generates noise proportional to the total power  $P_{br}$  (in Watt) delivered. A very simple empirical formula for the sound pressure level (at 1 m from the source) due to the piston engine is

$$SPL_1 \approx 57 + 14 \log P_{br} \quad (9.1)$$

where the power  $P_{br}$  is given by

$$P_{br} = \frac{NW_i n}{120} \quad (9.2)$$

with  $N$  the number of cylinders,  $W_i$  the work (in Joule) during one thermodynamic cycle (per cylinder) and  $n$  the engine rotational speed (in rpm). Typically,  $W_i \approx 800$  Joule, so that for  $N = 4$  and  $n = 2400$  rpm, the power  $P_{br}$  equals 64 kW. Substituting this in equation 9.1 yields  $SPL_1 = 124$  dB. The noise from the piston engine is mainly tonal, i.e. the observed peaks in the spectrum are at the exhaust firing frequency  $f_e$  and its higher harmonics. The exhaust firing frequency is given by equation 5.21 and with  $N = 4$  and  $n = 2400$  rpm,  $f_e$  equals 80 Hz. Piston engine noise is virtually non-directional.

In addition to the piston engine, also the propeller itself generates noise. The mechanism of propeller propulsion is the backward acceleration of air. Propeller noise, being the result of the periodic propeller motion, is also mainly tonal. Tones occur at the blade passage or fundamental frequency  $f_l$  (see equation 5.22) and its higher harmonics. The rotation of the propeller blades excites a volume of air in the propeller plane at the time a blade is passing. This has two effects on the surrounding volume of air:

- ‘thickness noise’ due to the displacement of the air volume by the passing blade volume;
- ‘loading noise’ due to the lift- and drag generating pressure field on the blade, which, in turn, causes a pressure field in the surrounding air volume.

The thickness noise is dependent on the local velocity. At the blade tips, the relative velocity of a blade section is highest and thus the thickness source is stronger than for blade sections closer to the propeller hub.

Additionally, there is a broadband noise component caused by turbulent flow over the blades. Usually, this propeller noise source is much less dominant than the tonal noise due to thickness and loading noise.

Propeller noise is the subject of current research, an example of which is shown in figure 9.1. Here propeller noise is studied with a microphone array, see chapter 8. When the acoustic imaging algorithm is able to separate the various noise sources (for each frequency band of interest), this should enable the validation of propeller noise model predictions at the component level.



Figure 9.1: Measurement setup for identification of noise sources on a small propeller-driven aircraft (here in static conditions). A mobile array consisting of 112 microphones is visible in the very right part of the photograph.

Figure 9.2 shows a measured spectrum for the aircraft depicted in figure 9.1. It is clearly observed that the tonal noise at the blade passage frequency  $f_1$  and its higher harmonics is indeed dominant. Here  $f_1$  is measured to be 100.5 Hz, which agrees well with equation 5.22 with  $B = 3$  and the given  $n_p = 2010$  rpm.

The maximum value of the sound pressure level of propeller noise (at 1 m from the source) is typically (see figure 1.16 of chapter 1)

$$SPL_1 = PWL - 11 \approx 140 - 11 = 129 \text{ dB} . \quad (9.3)$$

Compare this to the typical value of 124 dB for the noise due to the piston engine (see above).

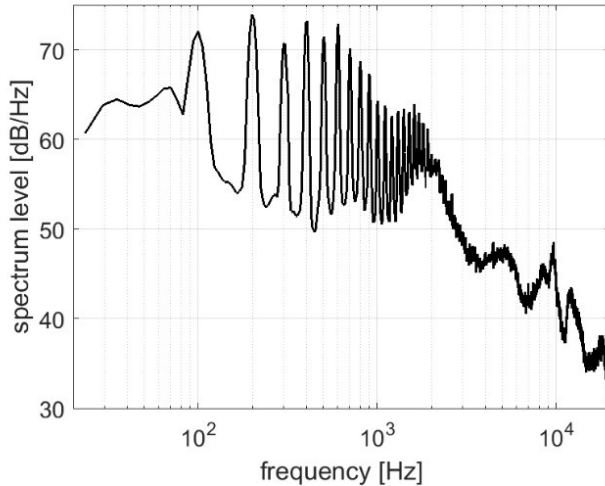


Figure 9.2: Spectrum level measured for the propeller-driven aircraft shown in figure 9.1. Note that the blade passage frequency is 100.5 Hz and that also its higher harmonics are clearly visible.

A very simple empirical (i.e. based on experimental data) ‘model’ for propeller noise is given by the formula

$$SPL_{1,\max} = 83.4 + 15.3 \log P_{br} - 20 \log D + 38.5 M_t - 3(B-2) + 10 \log N_p \quad (9.4)$$

with  $P_{br}$  the engine power in kW,  $D$  the propeller diameter (in m),  $B$  the number of blades (per propeller) and  $N_p$  the number of propellers.  $SPL_{1,\max}$  is the sound pressure level at 1 m from the source in the direction where it is maximal.  $M_t$  is the rotational tip Mach number (for static conditions) given by

$$M_t = \frac{\pi D}{c} \frac{n_p}{60} \quad (9.5)$$

with  $n_p$  the propeller rotational speed (in rpm).

Equation 9.4 gives a limited opportunity for designing a propeller system. As the noise is proportional to  $M_t$ , the noise could be substantially reduced by using smaller propellers (i.e. decreasing  $D$ ) and lowering rotational speed  $n_p$ . To maintain thrust, the number of blades  $B$  have to be increased then. However, this will increase the blade passage frequency  $f_1$  and, consequently, the reduction in perceived noise level might be lost (as higher frequencies are more annoying, see chapter 6). These considerations are to some extent

indicated in figure 9.3 where  $SPL_{1,\max}$  (according to equations 9.4 and 9.5) is plotted as a function of propeller diameter  $D$  for two values of  $n_p$  (1800 and 2400 rpm, respectively). Clearly, starting from  $D = 1.9$  m and  $n_p = 2400$  rpm ( $SPL_{1,\max} = 132$  dB), roughly 10 dB noise reduction can be attained when going to  $n_p = 1800$  rpm and propeller diameters around 1.4 m (as indicated by the red arrow in the figure).

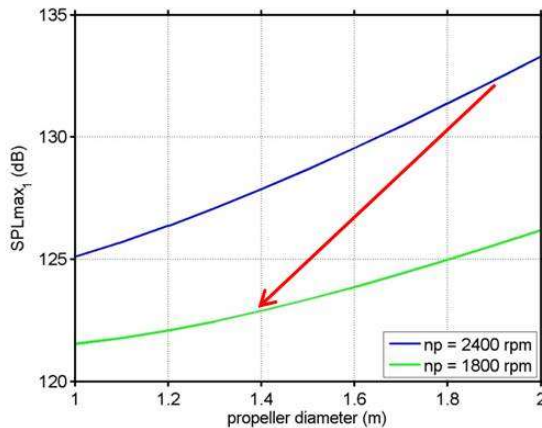


Figure 9.3: Typical value of  $SPL_{1,\max}$  versus propeller diameter  $D$  for two values of the propeller rotational speed  $n_p$ .

## 9.2 General properties of turbo-engine noise

The turbojet engine is an air breathing gas turbine engine. It was developed in the late 1930's, but only after WWII it became a widely used propulsion method for aircraft. A schematic drawing is given in figure 9.4a, showing the different stages of the engine. Each component of the engine, e.g. the compressor, combustor and exhaust jet produces noise. Turbojets are extremely noisy.

The turbofan engine, an advanced version of the turbojet engine, was developed in the 1940's, but came into operation in 1960's. Part of the air intake is used to drive the jet engine in the core, while the other portion is directed separately through a series of compressors and directed through the nozzle without undergoing combustion. Because the jet noise power is proportional to the exhaust flow velocity to the power eight, turbofan engines are much less noisy than turbojet engines.

Note: This will be derived in the aero-acoustics section 9.5 where it will be shown that the acoustic power of jet noise scales as  $\frac{\rho_\infty V^8 D^2}{c^5}$  with  $V$  the exhaust flow velocity and  $D$  the nozzle diameter.

The bypass ratio of a turbofan engine is defined as the ratio between the mass flow rates of air drawn through a fan disk that bypasses the engine core without undergoing combustion,

to the mass flow rate passing through the engine core that is involved in combustion. Figure 9.4b shows the different stages of a high-bypass-ratio turbofan engine. Each component of the engine, i.e. the fan, the compressor, the combustor, the turbine and the exhaust jet, produces noise.

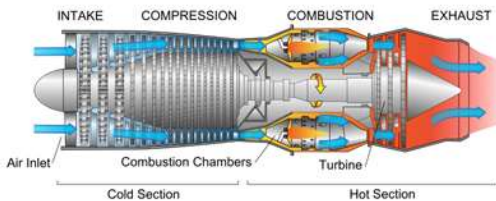


Figure 9.4a: Schematic of a turbojet engine.

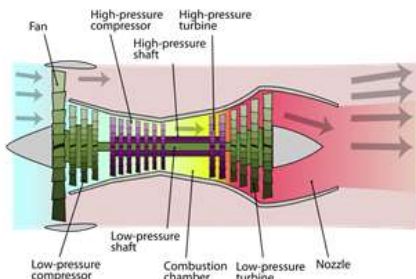


Figure 9.4b: Schematic of a turbofan engine.

Compared to a turbojet engine, a turbofan generates much less jet noise, however noise due to the fan is introduced. The blade passage frequency of the fan is in the range 1 to 2 kHz (compared to a propeller the number of blades is 10 times higher, see equation 5.22). Figure 9.5 shows the various noise contributions and their directivity for a turbojet and a high-bypass ratio turbofan. Because of the different directivity of fan and jet noise, an observer can hear two noise peaks as shown in figure 9.6.

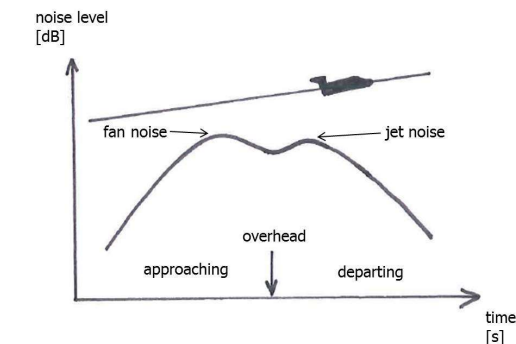
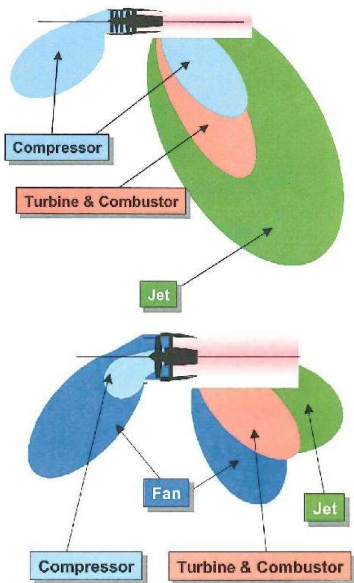


Figure 9.6: Typical noise level as a function of time for a flyover of an aircraft equipped with a turbofan engine.

Figure 9.5: Directionality of the various noise sources for a turbojet engine (top) and a turbofan engine (bottom).

Figure 9.7 shows the decrease in sound pressure level of the exhaust jet as a function of bypass ratio. Currently, at a bypass ratio of around 4, the exhaust jet noise is equal to the fan

noise, assuming the fan noise has been reduced by so-called ‘acoustic lining’. Increasing the bypass ratio will increase the fan noise, which can subsequently be counteracted by acoustic treatment of the fan duct (see figure 9.8, thick red lines). The basic principle of this acoustic lining is treated in section 4.3 (see figures 4.26 and 4.27). Here it suffices to say that this technique consists of covering the fan duct by a large number of small cavities, each of which functions as a Helmholtz resonator that attenuates the sound.

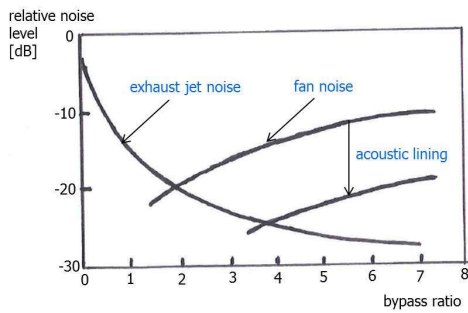


Figure 9.7: Relative noise level as a function of bypass ratio for jet noise and fan noise. Also indicated is the effect of acoustic lining on the fan noise level.

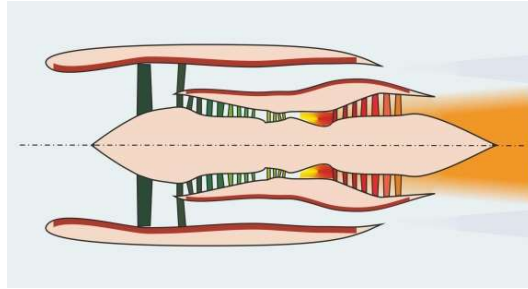


Figure 9.8: Areas in the fan duct (thick red lines) where acoustic lining can be performed.

### 9.3 General properties of airframe noise

Airframe noise is aerodynamic noise generated by the turbulence in the airflow over the outer surface of the airplane. At current, it can have a significant contribution to the total aircraft noise during landing approaches, i.e. when landing gear and aerodynamic devices (leading-edge slats, trailing-edge flaps, spoilers) are deployed. Airframe noise is mostly broadband in nature. The airframe noise power behaves as  $V^5$  or  $V^6$  ( $V$  being the aircraft speed), depending on the compactness of the airframe noise source. For compact sources such as landing gear the noise power is proportional to  $V^6$ , whereas for non-compact sources, such as the clean wing and the slats, the noise power is proportional to  $V^5$ . Further reductions in fan noise will result in airframe noise becoming the dominant noise source during approach and landing. Airframe noise may even be the lower bound on the noise produced by aircraft.

Figure 9.9 shows a typical noise breakdown for approach and take-off conditions. It is clearly observed that airframe noise is important during approach and can be neglected during take-off.

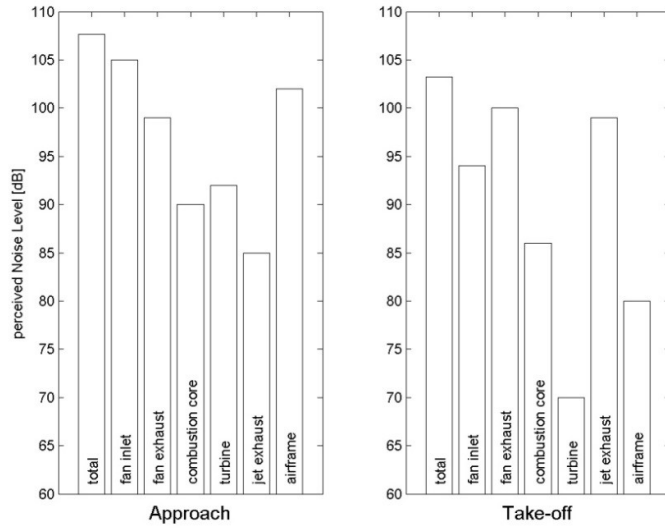


Figure 9.9: Typical noise breakdown for approach (left) and take-off (right) conditions.

#### 9.4 Aircraft noise modelling\*

Various approaches to aircraft noise modelling are employed today, ranging from fully numerical (which is computationally demanding) to fully analytical and semi-empirical. The latter method is addressed in this section. The semi-empirical method of aircraft noise modelling is based on databases containing measured acoustic data, either from wind-tunnel tests (which is necessarily on noise component level) or from full-scale aircraft under varying operational conditions. In addition, the method is partly based on analytical or numerical methods (i.e. a physics-based approach). The combination of measurement-based and physics-based, hence the name semi-empirical, provides a very useful and practical tool for aircraft noise assessment that is sufficiently fast for parameter sensitivity studies.

Here we discuss the ANOPP method, which stands for NASA's Aircraft Noise Prediction Program. The method is illustrated for airframe noise modelling. For engine noise the method is similar<sup>2</sup>. However, engine noise modelling requires a large number of model input parameters, accurate values of which are difficult to obtain. For airframe noise, only the aircraft velocity and the aircraft's geometrical parameters, such as wing and flap area, are needed.

The various airframe noise sources are indicated in figure 9.10. In this section we treat the trailing edge of the clean wing, the leading edge (I.e.) slats, the trailing edge (t.e.) flaps and the main and nose landing gear.

<sup>2</sup> See Ana Vieira, Bieke von den Hoff, Mirjam Snellen and Dick G. Simons, "Comparison of semi-empirical noise models with flyover measurements of operating aircraft", Journal of Aircraft Vol. 59, No. 6, November–December 2022 (paper available on Brightspace).

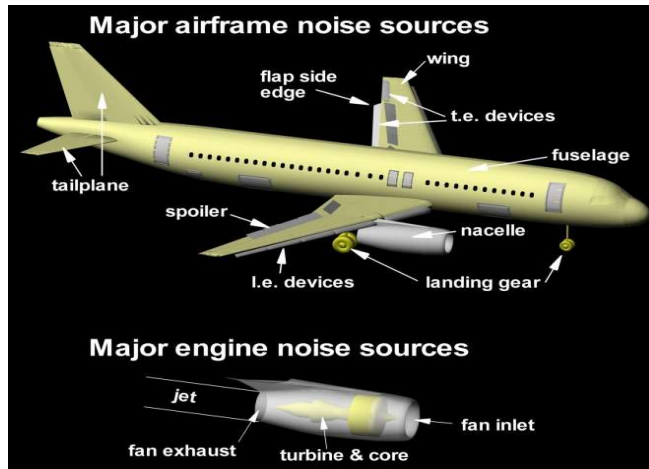


Figure 9.10: The various airframe and engine noise sources.

The general method is that each noise component is modelled according to the formula

$$p_e^2(f, \theta, \phi) = \frac{\rho_\infty c P D(\theta, \phi) F(S)}{4\pi r^2 (1 - M \cos \theta)^4} \quad (9.6)$$

with  $p_e^2$  the effective pressure (in  $\text{Pa}^2$ ) in the various 1/3-octave bands and  $f$  the centre frequencies of the subsequent 1/3-octave bands.  $p_e^2$  is also dependent on  $\theta$  and  $\phi$ , the polar and azimuthal directivity angle, respectively, the definition of which is indicated in figure 9.11. This angular dependence is contained in the dimensionless directivity function  $D(\theta, \phi)$ , which is different for each noise component.

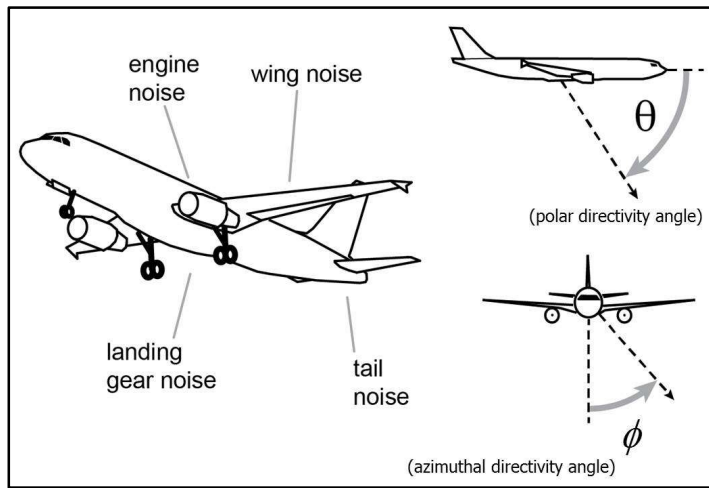


Figure 9.11: Definition of the polar and azimuthal directivity angle.

$p_e^2$  is further proportional to a power function  $P$  (in Watt) and a dimensionless empirical spectral function  $F(S)$ .  $P$  and  $F$  are also different for each noise component.  $S$  is the so-called Strouhal number, which is a dimensionless frequency that is explained below. In

equation 9.6 one recognizes the spherical spreading factor  $\frac{1}{4\pi r^2}$  with  $r$  the distance from the source to the observer (in m).

The factor  $\frac{1}{(1-M \cos \theta)^4}$  is due to the forward motion of the aircraft ( $M = \frac{V}{c}$  is the Mach number with  $V$  the aircraft speed in m/s). It can be derived (not in this lecture) that for a moving monopole or dipole there is this additional directivity factor, which is only dependent on the polar angle  $\theta$  (and Mach number). The effect is substantial as can be seen in figure 9.12 where we plotted this directivity in dB for various values of the Mach number  $M$ . In fact, figure 9.12 shows polar plots of this directivity, i.e.  $10 \log \left( \frac{1}{(1-M \cos \theta)^4} \right) = -40 \log(1-M \cos \theta)$  versus  $\theta$ . The Mach values chosen are relevant for aircraft velocities during approach and landing (when airframe noise is important or even dominant). Note that for  $\theta=90^\circ$  (aircraft overhead) the directivity factor due to forward motion is equal to 1 (0 dB).

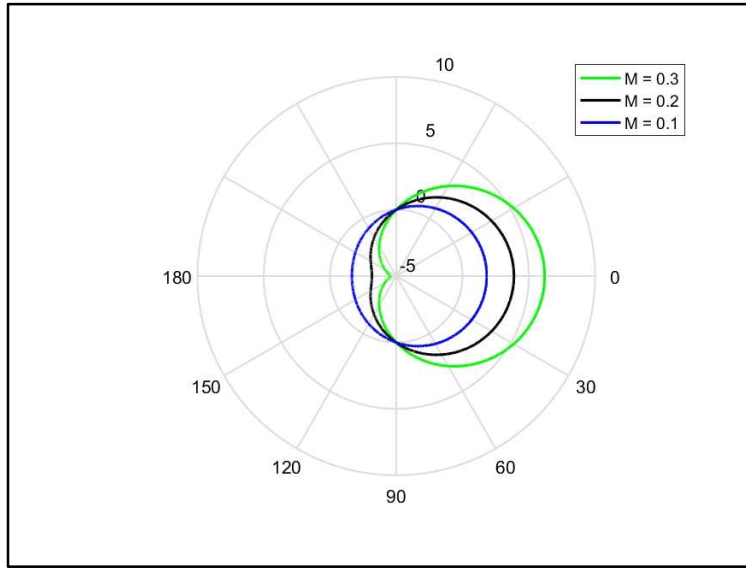


Figure 9.12: Polar plots of the directivity function (in dB) due to forward motion of the aircraft for three values of the Mach number  $M$ .

The power function  $P$  is given as

$$P = K M^a G(\rho_\infty c^3 b_w^2) \quad (9.7)$$

with  $K$  and  $a$  dimensionless constants determined from empirical data.  $G$  is the geometry function (also dimensionless) and  $b_w$  is the total wing span (in m).  $K$ ,  $a$  and  $G$  are different for each noise component.

The dimensionless Strouhal number  $S$  is given by

$$S = \frac{f L (1 - M \cos \theta)}{Mc} \quad (9.8)$$

with  $L$  a length scale characteristic of the particular airframe noise source considered.

Table 9.1 below provides the geometry function  $G$ , the length scale  $L$  and the constants  $K$  and  $a$  for the various airframe noise sources. We also briefly indicated the basic noise mechanism.

*Table 9.1*

Airframe noise source	Basic mechanism	$G$	$L$	$K$	$a$
Trailing-edge clean wing	Convection of the turbulent boundary layer past the trailing edge	$0.37 \frac{A_w}{b_w^2} \left( \frac{\rho_\infty M c A_w}{\mu_\infty b_w} \right)^{-0.2}$	$G b_w$	$4.464 \times 10^{-5}$	5
Leading-edge slats	1. Increment of wing trailing-edge noise. 2. Slat itself produces trailing-edge noise	Same as for wing for the 2 mechanisms	$G b_w$	$4.464 \times 10^{-5}$	5
Trailing-edge flaps	Lift fluctuations due to the incident turbulence on flap	$\frac{A_f}{b_w^2} \sin^2(\delta_f)$	$\frac{A_f}{b_f}$	$2.787 \times 10^{-4}$	6
Landing gear	multi-scale vortex dynamics and the consequent unsteady force applied to the gear components	$n \left( \frac{d}{b_w} \right)^2$	$d$	$4.349 \times 10^{-4}$ (1 and 2 wheels) $3.414 \times 10^{-4}$ (4 wheels)	6

$A_w$  (in  $m^2$ ) and  $b_w$  (in m) are the total wing area and total wing span, respectively.  $A_f$  (in  $m^2$ ),  $b_f$  (in m) and  $\delta_f$  (in degrees) are the total flap area, the total flap span and flap deflection angle, respectively.  $d$  (in m) and  $n$  are the wheel diameter and number of wheels, respectively.  $\mu_\infty$  is the dynamic viscosity of the ambient air, which is equal to  $1.84 \times 10^{-5}$  kg/(m s).

The empirical spectral functions for each airframe noise source are given in table 9.2 and are depicted graphically in figure 9.13. Note the log-log scale.

Table 9.2

Airframe noise source	Spectral function
Clean wing	$F(S) = 0.613(10S)^4 \left[ (10S)^{1.5} + 0.5 \right]^{-4}$
Slats	$F(S) = 0.613(10S)^4 \left[ (10S)^{1.5} + 0.5 \right]^{-4} + 0.613(2.19S)^4 \left[ (2.19S)^{1.5} + 0.5 \right]^{-4}$
Flaps	$F(S) = 0.0480S \quad \text{for } S < 2$ $F(S) = 0.1406S^{-0.55} \quad \text{for } 2 \leq S \leq 20$ $F(S) = 216.49S^{-3} \quad \text{for } S > 20$
Main landing gear ( $n = 2$ )	$F(S) = 13.59S^2 \left( S^2 + 12.5 \right)^{-2.25}$
Main landing gear ( $n = 4$ )	$F(S) = 0.0577S^2 \left( 0.25S^2 + 1 \right)^{-1.5}$

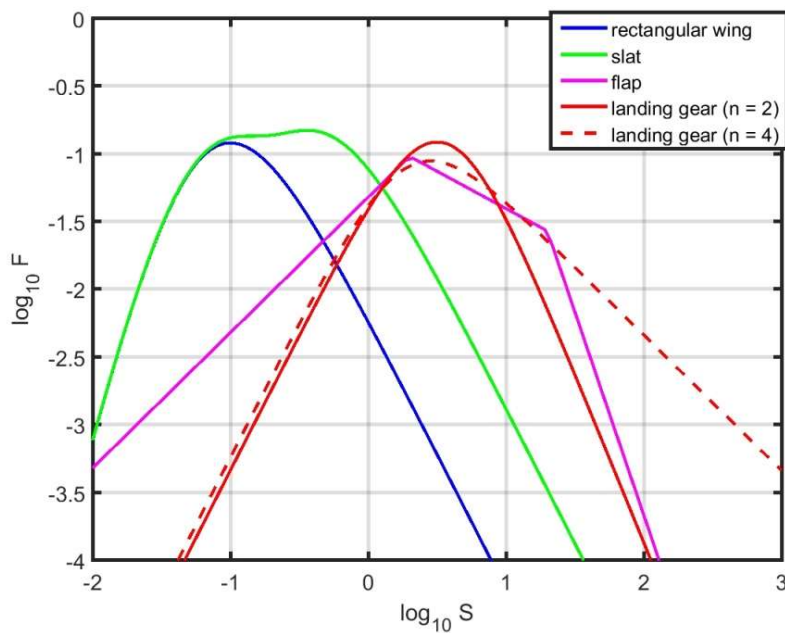


Figure 9.13: Empirical spectral functions for each airframe noise source (see also table 9.2). Note the log-log scale.

The directivity functions for each airframe noise source are given in table 9.3. Figure 9.14 presents polar plots of the directivity functions (log scale) for  $\phi = 0^\circ$  and  $\delta_f = 30^\circ$ .

Table 9.3

Airframe noise source	Directivity function
Clean wing	$D(\theta, \phi) = 4 \cos^2(\phi) \cos^2(\theta/2)$
Slats	$D(\theta, \phi) = 4 \cos^2(\phi) \cos^2(\theta/2)$
Flaps	$D(\theta, \phi) = 3 (\sin \delta_f \cos \theta + \cos \delta_f \sin \theta \cos \phi)^2$
Main landing gear	$D(\theta, \phi) = \frac{3}{2} \sin^2 \theta$

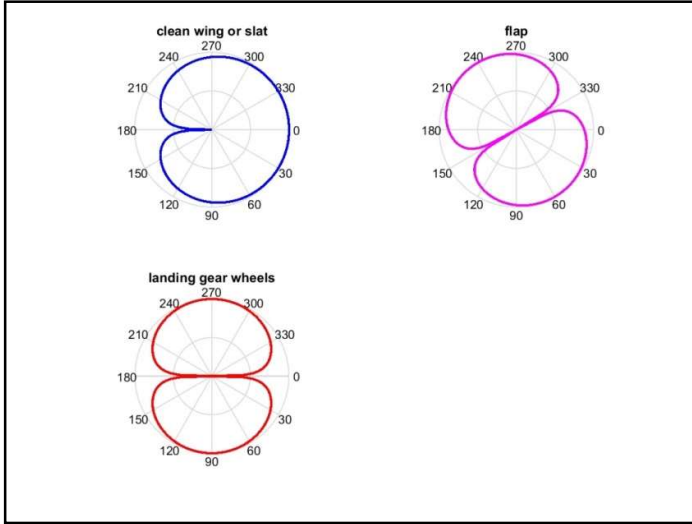


Figure 9.14: Polar plots of the directivity functions for each airframe noise source. Shown is the  $\vartheta$ -dependence for  $\varphi = 0^\circ$  and  $\delta_f = 30^\circ$ .

We now have all the necessary modelling tools for a model-data comparison. In figure 9.15 we compare the measured spectrum level (in units dB/Hz) with the modelled one for two landing aircraft, i.e. a small aircraft (Fokker 70, left part of figure) and a large aircraft (Airbus 380, right part of figure). For the modelling we used  $r = 1$  m, hence the data have been compensated for aircraft altitude. The aircraft are at overhead position ( $\theta = 90^\circ$ ). The colours indicate the spectrum levels at the component level, whereas the smooth black line represents the total modelled spectrum. The black rapidly fluctuating line is the experimental data.

The modelling according to equation 9.6 gives the effective pressure squared in the various 1/3-octave bands. Hence, to obtain the modelled spectrum level we have to correct for the 1/3-octave bandwidths according to equation 5.17. The geometrical data of the two aircraft, including altitude and velocity are given in table 9.4. The landing gear data is provided in table 9.5. Also indicated in the tables are the data for a Boeing 737 landing as this information is needed for one of the assignments of course AE4463P.

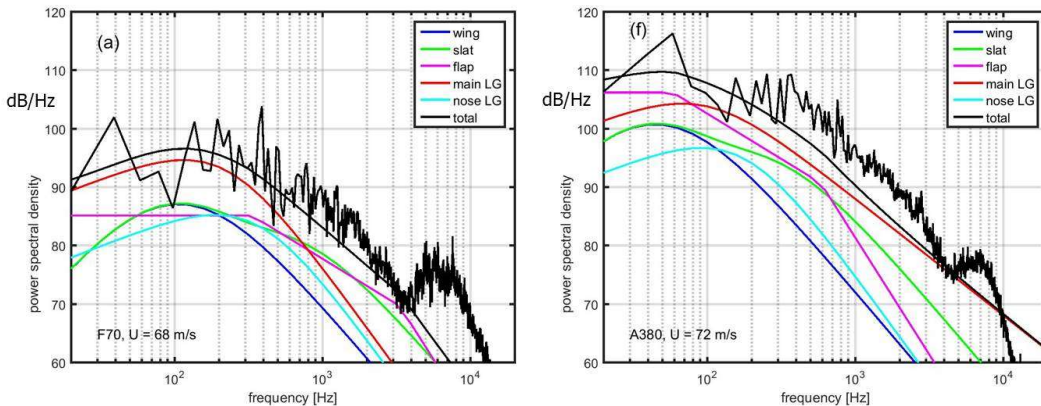


Figure 9.15: Comparison of the measured spectrum with the modelled one for a landing Fokker 70 (left) and a landing Airbus 380 (right).

Table 9.4

Aircraft type	Height (m)	Speed (m/s)	Wing area (m <sup>2</sup> )	Wing span (m)	Flap area (m <sup>2</sup> )	Flap span (m)
Fokker 70	63.5	68	81	28	6.5	16
Boeing 737	70.4	81	130	34	18	17
Airbus 380	64.9	72	753	80	103	42

Table 9.5

Aircraft type	Main landing gear			Nose landing gear		
	Tire diameter (m)	Number of wheels/boggie	Number of boggies	Tire diameter (m)	Number of wheels/boggie	Number of boggies
Fokker 70	1.1	2	2	0.7	2	1
Boeing 737	1.1	2	2	0.7	2	1
Airbus 380	1.5	4	4	1.5	2	1

Note that, according to the model, in the mid-frequency band 1 – 4 kHz, slat and flap noise are dominant for the Fokker 70. For the Airbus 380 the main landing gear noise is dominant. From this model-data comparison we may conclude that for both landing aircraft, airframe noise is important, however a significant contribution from the engines is also present for all frequencies, especially above 4 kHz.

## 9.5 Aero-acoustics

Aero-acoustics studies noise generation of turbulent fluid motion or noise due to aerodynamic forces that interact with surfaces. As such it is a relevant (theoretical) approach to study and model aircraft noise sources. Here we will treat the so-called ‘aero-acoustic analogy’ developed by Lighthill. In this approach the governing equations of motion of the

fluid, mass conservation and momentum conservation (see section 2.1), are reworked into an equation, i.e. Lighthill's equation. This equation reminds us of the classical linear wave equation on the left-hand side and source terms on the right-hand side. With Lighthill's equation, developed in the 1950s, the modern discipline of aero-acoustics has started. As an application we will derive the scaling law for jet noise: noise power proportional to flow velocity to the power eight, see section 9.2.

We start with the conservation of mass and momentum laws, but now without the linearizations performed in section 2.1. The conservation of mass equation 2.1 can be written as

$$\frac{\partial \rho}{\partial t} + \nabla \cdot (\rho \vec{v}) = 0. \quad (9.9)$$

The conservation of momentum equations 2.7, i.e. Euler's equations, can be written in vector form as

$$\rho \frac{\partial \vec{v}}{\partial t} + \rho(\vec{v} \cdot \nabla) \vec{v} + \nabla p = 0 \quad (9.10)$$

where  $(\vec{v} \cdot \nabla) \vec{v}$  is interpreted as the operator  $(\vec{v} \cdot \nabla) = v_1 \frac{\partial}{\partial x_1} + v_2 \frac{\partial}{\partial x_2} + v_3 \frac{\partial}{\partial x_3}$  working on the components  $v_i$  of  $\vec{v}$ . Here we have neglected viscosity, i.e. we consider inviscid fluid motion, as it is generally accepted that the effects of viscosity of the fluid on noise generation are negligible.

We multiply the conservation of mass equation (9.9) by  $\vec{v}$  and obtain

$$\vec{v} \frac{\partial \rho}{\partial t} + \vec{v} (\nabla \cdot (\rho \vec{v})) = 0. \quad (9.11)$$

Subsequently, adding this equation (9.11) to the conservation of momentum equation (9.10) gives

$$\rho \frac{\partial \vec{v}}{\partial t} + \vec{v} \frac{\partial \rho}{\partial t} + \rho(\vec{v} \cdot \nabla) \vec{v} + \vec{v} (\nabla \cdot (\rho \vec{v})) + \nabla p = 0. \quad (9.12)$$

Using the product rule for differentiation we can combine the first two terms of this equation into  $\frac{\partial}{\partial t}(\rho \vec{v})$ . The  $i^{th}$  component of the sum of the third and fourth component is

$$\rho \left( v_1 \frac{\partial v_i}{\partial x_1} + v_2 \frac{\partial v_i}{\partial x_2} + v_3 \frac{\partial v_i}{\partial x_3} \right) + v_i \left( \frac{\partial(\rho v_1)}{\partial x_1} + \frac{\partial(\rho v_2)}{\partial x_2} + \frac{\partial(\rho v_3)}{\partial x_3} \right) \quad (9.13)$$

which, again according to the product rule for differentiation, is equal to

$$\frac{\partial(\rho v_i v_i)}{\partial x_1} + \frac{\partial(\rho v_2 v_i)}{\partial x_2} + \frac{\partial(\rho v_3 v_i)}{\partial x_3} = \nabla \cdot (\rho v_i \vec{v}) \quad (9.14)$$

i.e. the divergence of the vector  $\rho v_i \vec{v}$ .

Equation 9.12 can now be written as

$$\frac{\partial}{\partial t}(\rho \vec{v}) + \nabla \cdot (\rho \vec{v} \vec{v}) + \nabla p = 0 \quad (9.15)$$

where the product  $\rho \vec{v} \vec{v}$  is to be read as a tensor (like a matrix or vector of vectors), which can be written as

$$\rho \vec{v} \vec{v} = \begin{pmatrix} \rho v_1 v_1 & \rho v_2 v_1 & \rho v_3 v_1 \\ \rho v_1 v_2 & \rho v_2 v_2 & \rho v_3 v_2 \\ \rho v_1 v_3 & \rho v_2 v_3 & \rho v_3 v_3 \end{pmatrix}. \quad (9.16)$$

The expression  $\nabla \cdot (\rho \vec{v} \vec{v})$  means that the  $i^{th}$  component of this vector is  $\frac{\partial(\rho v_i v_i)}{\partial x_1} + \frac{\partial(\rho v_2 v_i)}{\partial x_2} + \frac{\partial(\rho v_3 v_i)}{\partial x_3}$ , i.e. the divergence works on a row of  $\rho \vec{v} \vec{v}$  (see equation 9.14).

We now take the partial time derivative  $\frac{\partial}{\partial t}$  of conservation of mass, equation 9.9, and obtain

$$\frac{\partial^2 \rho}{\partial t^2} + \nabla \cdot \left( \frac{\partial}{\partial t}(\rho \vec{v}) \right) = 0 \quad (9.17)$$

where we have reversed the operators  $\frac{\partial}{\partial t}$  and  $\nabla \cdot$  in the second term.

Further, we take de divergence  $\nabla \cdot$  of equation 9.15 and get

$$\nabla \cdot \left( \frac{\partial}{\partial t}(\rho \vec{v}) \right) + \nabla \cdot (\nabla \cdot (\rho \vec{v} \vec{v})) + \nabla \cdot (\nabla p) = 0 \quad (9.18)$$

where  $\nabla \cdot (\nabla p) = \nabla^2 p = \frac{\partial^2 p}{\partial x_1^2} + \frac{\partial^2 p}{\partial x_2^2} + \frac{\partial^2 p}{\partial x_3^2}$  i.e. the Laplace operator on  $p$ . Subtracting equation 9.18 from equation 9.17 results in

$$\frac{\partial^2 \rho}{\partial t^2} - \nabla^2 p = \nabla \cdot (\nabla \cdot (\rho \vec{v} \vec{v})). \quad (9.19)$$

Note that the right-hand side of this equation is a double divergence of a tensor, which results into a scalar (as it should be as the left-hand side of the equation is also scalar). This scalar is

$$\nabla \cdot (\nabla \cdot (\rho \vec{v})) = \sum_{i=1}^3 \frac{\partial}{\partial x_i} \left( \frac{\partial(\rho v_i v_i)}{\partial x_1} + \frac{\partial(\rho v_2 v_i)}{\partial x_2} + \frac{\partial(\rho v_3 v_i)}{\partial x_3} \right) \quad (9.20)$$

and contains nine terms that can be reduced to the six terms

$$\frac{\partial^2}{\partial x_1^2}(\rho v_1^2) + \frac{\partial^2}{\partial x_2^2}(\rho v_2^2) + \frac{\partial^2}{\partial x_3^2}(\rho v_3^2) + 2 \frac{\partial^2}{\partial x_1 \partial x_2}(\rho v_1 v_2) + 2 \frac{\partial^2}{\partial x_1 \partial x_3}(\rho v_1 v_3) + 2 \frac{\partial^2}{\partial x_2 \partial x_3}(\rho v_2 v_3)$$

which can be written in the Einstein summation convention as

$$\nabla \cdot (\nabla \cdot (\rho \vec{v})) = \frac{\partial^2}{\partial x_i \partial x_j}(\rho v_i v_j). \quad (9.21)$$

In this convention it is implicitly assumed that the summation is taken over all possible values of the indices ( $i$  and  $j$  in this case).

Finally, we subtract  $c^2 \nabla^2 \rho$  from both sides of equation 9.19 and we obtain Lighthill's equation

$$\frac{\partial^2 \rho}{\partial t^2} - c^2 \nabla^2 \rho = \nabla \cdot (\nabla \cdot (\rho \vec{v})) + \nabla^2(p - c^2 \rho) \quad (9.22)$$

with  $c$  the sound speed of the medium in its equilibrium state. Lighthill's equation is a wave equation (here for the variable  $\rho$ ) with a source term on the right-hand side, i.e. it is an inhomogeneous wave equation. The first term on the right-hand side describes unsteady convection of flow (also called Reynolds' stress) and the second term describes nonlinear acoustic generation processes. In most cases these nonlinear effects are neglected (see also equation 2.15). Lighthill's equation for the variable sound pressure  $p'$  then is

$$\frac{1}{c^2} \frac{\partial^2 p'}{\partial t^2} - \nabla^2 p' = \nabla \cdot (\nabla \cdot (\rho \vec{v})) \quad (9.23)$$

i.e. the only sources considered are the nonlinear convective effects  $\frac{\partial^2}{\partial x_i \partial x_j}(\rho v_i v_j)$ .

Often a hybrid method for predicting aerodynamic noise using Lighthill's equation is utilized, i.e. the noise generation and propagation are treated separately. In the first step the sound sources (the right-hand side of the equation) are formed using data provided by numerical simulations. The second step consists in solving the wave equation using the simulated source term. The first assumption of Lighthill's approach is thus that the listener (or receiver) is surrounded by quiescent air in which the small acoustic perturbations are accurately described by the homogenous linear wave equation 2.19 (chapter 2). Secondly,

approximations to estimate the source terms, i.e. the right-hand side of equation 9.22, are introduced (ignoring any acoustic wave propagation). Thirdly, the sound production outside the turbulent flow (i.e. the source region) is predicted.

We can obtain a formal solution to an inhomogeneous wave equation using Green's theorem. Consider the inhomogeneous wave equation for the variable sound pressure  $p' = p'(\vec{r}, t)$ , i.e.

$$\frac{1}{c^2} \frac{\partial^2 p'}{\partial t^2} - \nabla^2 p' = q(\vec{r}, t) \quad (9.24)$$

with  $q(\vec{r}, t)$  the source term. The Green function or impulse response  $G(\vec{r}, t, \vec{r}', \tau)$  is defined as the solution to an impulsive point source represented by Dirac delta functions in space and time, i.e.

$$\frac{1}{c^2} \frac{\partial^2 G}{\partial t^2} - \nabla^2 G = \delta(\vec{r} - \vec{r}') \delta(t - \tau). \quad (9.25)$$

The point source is thus at position  $\vec{r}'$  released at time  $\tau$ . It can be shown that Green's function for free space conditions is given as

$$G(\vec{r}, t, \vec{r}', \tau) = \frac{1}{4\pi \|\vec{r} - \vec{r}'\|} \delta\left(t - \tau - \frac{\|\vec{r} - \vec{r}'\|}{c}\right) \quad (9.26)$$

with  $\|\cdot\|$  denoting the length of the vector and  $t - \frac{\|\vec{r} - \vec{r}'\|}{c}$  being the emission time. Now,

by Green's theorem, the solution to the inhomogeneous wave equation with source  $q$  is given by

$$p'(\vec{r}, t) = \int_{\tau=-\infty}^{\infty} \iiint_V \frac{1}{4\pi \|\vec{r} - \vec{r}'\|} \delta\left(t - \tau - \frac{\|\vec{r} - \vec{r}'\|}{c}\right) q(\vec{r}', \tau) d\vec{r}' d\tau \quad (9.27)$$

i.e. the convolution of the source function  $q$  with the Green's function  $G$ . The integration over the spatial coordinates ( $\vec{r}'$ ) is over a volume  $V$  that contains all sources of acoustic energy as described by the function  $q$ . Performing the integration over variable  $\tau$  yields

$$p'(\vec{r}, t) = \iiint_V \frac{1}{4\pi \|\vec{r} - \vec{r}'\|} q(\vec{r}', t - \frac{\|\vec{r} - \vec{r}'\|}{c}) d\vec{r}'. \quad (9.28)$$

We will now apply this formal solution to Lighthill's equation for sound pressure, i.e. for equation 9.23. With only unsteady convection of flow as the source term, i.e.  $q = \nabla \cdot (\nabla \cdot (\rho \vec{v} \vec{v}))$ , we obtain

$$p'(\vec{r}, t) = \iiint_V \frac{\partial^2 (\rho v_i v_j)}{\partial x'_i \partial x'_j} \frac{1}{4\pi \|\vec{r} - \vec{r}'\|} d\vec{r}' \quad (9.29)$$

where  $\frac{\partial^2 (\rho v_i v_j)}{\partial x'_i \partial x'_j}$  in the integrand is evaluated at the retarded time  $t - \frac{\|\vec{r} - \vec{r}'\|}{c}$ .

A basic property of this convolution integral is that derivatives can be interchanged, i.e. equation 9.29 can be written as

$$p'(\vec{r}, t) = \frac{\partial^2}{\partial x_i \partial x_j} \iiint_V \frac{\rho v_i v_j}{4\pi \|\vec{r} - \vec{r}'\|} d\vec{r}'. \quad (9.30)$$

As stated in the introduction of this section, we will apply this equation to derive the scaling law for jet noise. We assume that the sound is mainly produced by the turbulent structures with a typical length scale of the width  $D$  of the jet, see figure 9.16. Hence, the source volume is of the order of  $D^3$ .

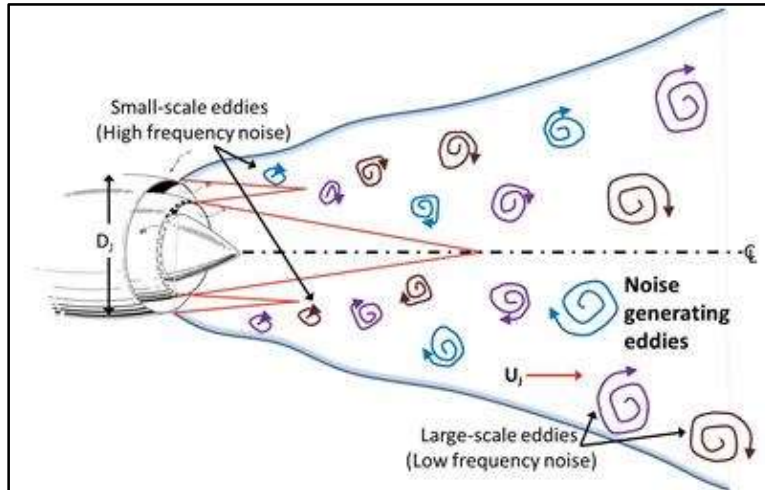


Figure 9.16: Turbulent structures from a jet flow.

Let  $V$  be the jet velocity at the exit of the nozzle of the turbo-engine. As velocities  $v_i \sim V$  and  $\rho \sim \rho_\infty$  we may assume that  $\rho v_i v_j \sim \rho_\infty V^2$ . Further,  $\frac{\partial}{\partial x_i} \sim \frac{V}{cD}$ . Hence, in the far field at the listener the sound pressure is of the order  $\frac{V^2}{c^2 D^2} \frac{\rho_\infty V^2}{r} D^3$  with  $r = \|\vec{r}\|$  (see equation 9.30). Hence, for the effective sound pressure we have

$$p_e \sim \frac{\rho_\infty V^4 D}{c^2 r} \quad (9.31)$$

with corresponding intensity

$$I = \frac{p_e^2}{\rho_\infty c} \sim \frac{\rho_\infty V^8 D^2}{c^5 r^2}. \quad (9.32)$$

The acoustic power of the source  $W = 4\pi r^2 I$  is thus of the order

$$W \sim \frac{\rho_\infty V^8 D^2}{c^5}. \quad (9.33)$$

Strictly, this ‘law’ is only valid for low  $V$  as we have implicitly assumed the source to be compact. Note that this law implies that a dramatic reduction of aircraft jet noise can be achieved by reducing the jet flow velocity  $V$ . (However, if  $V$  is reduced,  $D$  has to be increased to maintain sufficient thrust). Actually, this is the idea of the high-bypass turbofan engines, which have replaced the older turbojet engines (without or with little by-pass flow), see section 9.2. In question 2 of the exercises of this chapter you will practice with this jet noise scaling law for the Boeing 747 and the newer Boeing 777 aircraft.

Note: In the beginning of this section it was mentioned that we only consider inviscid fluid motion (i.e. viscosity vanishes). The conservation of momentum equation (9.10) including viscous effects reads

$$\rho \frac{\partial \vec{v}}{\partial t} + \rho(\vec{v} \cdot \nabla) \vec{v} = -\nabla p + \nabla \cdot \vec{\Xi} \quad (9.34)$$

with  $\vec{\Xi}$  the viscous stress tensor. Then Lighthill’s equation (9.21) would become

$$\frac{\partial^2 \rho}{\partial t^2} - c^2 \nabla^2 \rho = \nabla \cdot (\nabla \cdot (\rho \vec{v})) - \nabla \cdot (\nabla \cdot \vec{\Xi}) + \nabla^2 (p - c^2 \rho) \quad (9.35)$$

where we now have three source terms on the right-hand side of this inhomogeneous wave equation. In this form Lighthill’s equation is exact as no approximations were made in deriving it.

In the Einstein summation convention Lighthill’s equation reads

$$\frac{\partial^2 \rho}{\partial t^2} - c^2 \nabla^2 \rho = \frac{\partial^2}{\partial x_i \partial x_j} T_{ij} \quad (9.36)$$

with  $T_{ij}$  the components of the so-called ‘Lighthill turbulence stress tensor’ given by

$$T_{ij} = \rho v_i v_j - \Xi_{ij} + (p^2 - c^2 \rho) \delta_{ij} \quad (9.37)$$

with  $\delta_{ij}$  the Kronecker delta and  $\Xi_{ij}$  describing the sound generated by viscous effects. However, in practice the effects of viscosity of the fluid on noise generation is neglected:  $\Xi_{ij} = 0$  (i.e. viscosity vanishes).

## Exercises

### Question 1

We consider the major noise sources on-board of a modern medium-range transport aircraft, equipped with turbofan engines. A distinction can be made between engine noise, due to the fan and the jet, and airframe noise, due to the landing gear and leading edge and trailing edge devices. The various noise contributions (as sound pressure levels SPL) on the ground (at a certain representative observer location) are given in the table below for take-off conditions.

Noise source	SPL (dB)	Estimated reduction (dB)
Fan	99	10
Jet	93	6
Landing gear	80	5
Leading edge	75	5
Trailing edge	75	5

(a) Calculate the total SPL due to the engines and that due to the airframe. Also, calculate the total SPL due to all aircraft noise sources.

Promising measures to reduce airframe noise are mesh fairings for landing gear noise, porous devices at the flap edges for trailing edge noise and optimising the setting of the slats for leading edge noise. Sophisticated model calculations have indicated that a 5 dB reduction for each airframe noise source is feasible (see also table).

Promising measures to reduce the fan noise of the engine are a turbofan design for a bypass ratio (bpr) of 15, combined with an improved liner design and optimized fan speed. The higher bpr and a nozzle modification can also reduce the jet noise of the engine. The estimated noise reductions, based on model calculations, are given in the table.

(b) Calculate the total SPL due to the engines, the airframe and due to all aircraft noise sources after the implementation of the noise reduction measures described above.

### Question 2

We consider a trend in aircraft design: the Boeing 777 (in service from 1995) has two (turbofan) engines that provide as much thrust as the four engines of the Boeing 747 (in service from 1969). The Boeing 777 is a more fuel-efficient solution and, as it will turn out in this exercise, also a more quieter aircraft. We assume here that the noise of both aircraft is dominated by jet noise and that the total acoustic power of jet noise is proportional to  $\rho V^8 D^2$  (with  $V$  the exhaust flow velocity and  $D$  the nozzle diameter).

(a) Show that the thrust from a jet engine is proportional to  $\rho V^2 D^2$ .

- (b) Assume that the thrust of the two aircraft are equal and that the nozzle diameter of a B777 engine is twice that of a B747 engine. Determine the ratio of the exhaust flow velocities of the two aircraft.
- (c) Calculate with the above scaling law for jet noise the reduction in jet noise (in dB) of a B777 compared to that of a B747.

The table below provides the origin of the figures listed. The remaining figures have been made by the author.

Figure	Source
1.1	"Physics for scientists & engineers with modern physics" (fourth edition) by D.C. Giancoli
1.2	"Physics for scientists & engineers with modern physics" (fourth edition) by D.C. Giancoli
1.4	"Physics for scientists & engineers with modern physics" (fourth edition) by D.C. Giancoli
1.10	"Elements of aviation acoustics" (second edition, 2007) by G.J.J. Ruijgrok
1.11	"Elements of aviation acoustics" (second edition, 2007) by G.J.J. Ruijgrok
1.12	"Physics for scientists & engineers with modern physics" (fourth edition) by D.C. Giancoli
1.13	<a href="https://www.natuurkunde.nl/vraagbaak/10805">https://www.natuurkunde.nl/vraagbaak/10805</a>
1.14	<a href="https://en.wikipedia.org/wiki/Huygens%20%93Fresnel_principle">https://en.wikipedia.org/wiki/Huygens%20%93Fresnel_principle</a>
1.18	"Elements of aviation acoustics" (second edition, 2007) by G.J.J. Ruijgrok
1.23	"Physics for scientists & engineers with modern physics" (fourth edition) by D.C. Giancoli
1.24	<a href="https://www.nap.edu/read/12928/chapter/7">https://www.nap.edu/read/12928/chapter/7</a>
2.3	"Elements of aviation acoustics" (second edition, 2007) by G.J.J. Ruijgrok
3.7	<a href="http://www.srh.noaa.gov/jetstream/atmos/layers.html">http://www.srh.noaa.gov/jetstream/atmos/layers.html</a>
4.1	"Computational ocean acoustics" (1994) by Jensen et al.
4.13	<a href="http://www.dolmetsch.com/defsr1.htm">http://www.dolmetsch.com/defsr1.htm</a>
4.14	<a href="http://johnsayers.com/Recmanual/Pages/Coefficients.htm">http://johnsayers.com/Recmanual/Pages/Coefficients.htm</a>
4.23	<a href="https://newt.phys.unsw.edu.au/jw/Helmholtz.html">https://newt.phys.unsw.edu.au/jw/Helmholtz.html</a>
4.27	<a href="https://engineering.purdue.edu/~propulsi/propulsion/jets/basics/noise.html">https://engineering.purdue.edu/~propulsi/propulsion/jets/basics/noise.html</a>
5.12	<a href="https://www.electronics-notes.com/articles/audio-video/microphones/condenser-capacitor-microphone.php">https://www.electronics-notes.com/articles/audio-video/microphones/condenser-capacitor-microphone.php</a>
5.14	<a href="https://www.gras.dk/">https://www.gras.dk/</a>
5.15	<a href="https://www.gras.dk/">https://www.gras.dk/</a>
6.1	"Elements of aviation acoustics" (second edition, 2007) by G.J.J. Ruijgrok
6.2	"Elements of aviation acoustics" (second edition, 2007) by G.J.J. Ruijgrok
6.3	"Elements of aviation acoustics" (second edition, 2007) by G.J.J. Ruijgrok
6.8	"Elements of aviation acoustics" (second edition, 2007) by G.J.J. Ruijgrok
6.9	<a href="http://www.broward.org/Airport/NoiseInformation/Documents/PresentationSept2015.pdf">http://www.broward.org/Airport/NoiseInformation/Documents/PresentationSept2015.pdf</a>
6.10	<a href="http://www.broward.org/Airport/NoiseInformation/Documents/PresentationSept2015.pdf">http://www.broward.org/Airport/NoiseInformation/Documents/PresentationSept2015.pdf</a>
6.11	<a href="http://128.173.204.63/courses/cee4674/cee4674_pub/BasicNoiseCalculations.pdf">http://128.173.204.63/courses/cee4674/cee4674_pub/BasicNoiseCalculations.pdf</a>
6.12	<a href="http://www.broward.org/Airport/NoiseInformation/Documents/PresentationSept2015.pdf">http://www.broward.org/Airport/NoiseInformation/Documents/PresentationSept2015.pdf</a>
6.13	<a href="http://128.173.204.63/courses/cee4674/cee4674_pub/BasicNoiseCalculations.pdf">http://128.173.204.63/courses/cee4674/cee4674_pub/BasicNoiseCalculations.pdf</a>
6.14 top	<a href="https://www.easa.europa.eu/eaer/figures-tables/estimated-percentage-people-highly-annoyed-noise-aircraft-road-and-rail">https://www.easa.europa.eu/eaer/figures-tables/estimated-percentage-people-highly-annoyed-noise-aircraft-road-and-rail</a>
6.14 bottom	<a href="https://www.bjmgerard.nl/?p=8137">https://www.bjmgerard.nl/?p=8137</a>
6.15	"Elements of aviation acoustics" (second edition, 2007) by G.J.J. Ruijgrok
6.16	"Elements of aviation acoustics" (second edition, 2007) by G.J.J. Ruijgrok
6.17	Courtesy Michael Arntzen, Schiphol Group
6.18	<a href="https://www.easa.europa.eu/eaer/figures-tables/three-noise-certification-measurement-points">https://www.easa.europa.eu/eaer/figures-tables/three-noise-certification-measurement-points</a>
9.2	"Elements of aviation acoustics" (second edition, 2007) by G.J.J. Ruijgrok
9.4a	<a href="http://www.differencebetween.com/difference-between-turbojet-and-vs-turbofan/">http://www.differencebetween.com/difference-between-turbojet-and-vs-turbofan/</a>
9.4b	<a href="http://www.differencebetween.com/difference-between-turbojet-and-vs-turbofan/">http://www.differencebetween.com/difference-between-turbojet-and-vs-turbofan/</a>
9.5	<a href="https://www.nap.edu/read/12928/chapter/7">https://www.nap.edu/read/12928/chapter/7</a>
9.6	"Elements of aviation acoustics" (second edition, 2007) by G.J.J. Ruijgrok
9.8	<a href="https://www.southampton.ac.uk/engineering/research/themes/acoustics/aeroacoustics.page">https://www.southampton.ac.uk/engineering/research/themes/acoustics/aeroacoustics.page</a>
9.10	<a href="http://blog.nus.edu.sg/a0108344/">http://blog.nus.edu.sg/a0108344/</a>
9.16	<a href="https://www.southampton.ac.uk/engineering/research/projects/prediction_of_aircraft_exhaust_noise.page">https://www.southampton.ac.uk/engineering/research/projects/prediction_of_aircraft_exhaust_noise.page</a>